Universität Rostock Traditio et Innovatio

CERN

Compact Radio-frequency Quadrupoles for Industrial and Medical Applications

DISSERTATION

to attain the degree
Doktor-Ingenieur (Dr.-Ing.)
of the Faculty of Computer Science and Electrical Engineering
of the University of Rostock

put forward by
Hermann W. Pommerenke
born on 25 March 1995 in Rostock, Germany
from Saint-Genis-Pouilly, France

Geneva, 16 August 2020

https://doi.org/10.18453/rosdok_id00002956

Reviewers

Prof. Dr. Ursula van Rienen, University of Rostock, Germany
Dr. Alexej Grudiev, CERN, Geneva, Switzerland
Prof. Dr. Holger Podlech, Goethe University Frankfurt am Main, Germany

Day of submission: 16 August 2020
Day of defense: 28 January 2021

The work leading to this thesis has been sponsored by the Wolfgang Gentner Programme of the German Federal Ministry of Education and Research (grant number 05E15CHA).

That's all it is. You just begin. You do the math. You solve one problem and you solve the next one, and then the next. And if you solve enough problems, you get to come home.

Mark Watney in Andy Weir, *The Martian*

Abstract

The radio-frequency quadrupole (RFQ) is a crucial component of modern linear hadron accelerators. RFQs accelerate proton or ion beams at low energies and have a major impact on the overall beam quality of the accelerator. High frequencies allow for compact and economical RFQ designs that open up many possibilities of application in industry and medicine. The present thesis is motivated by the development of two compact RFQs operating at 750 MHz. Consequently, the thesis is organized into two parts:

The first part lays out radio-frequency (RF) design, measurements, and tuning of the PIXE-RFQ. The PIXE-RFQ is a one-meter long stand-alone accelerator providing 2 MeV protons for non-destructive proton-induced X-ray emission (PIXE) analysis of cultural heritage artwork. Numerical simulation and analytical techniques were used to determine optimum geometric and RF parameters of cavity, tuners, vacuum pumping ports, input power coupler, and diagnostic antennas. Thermo-mechanical and beam dynamics studies are presented to validate the design. Subsequently, RF and bead-pull measurements conducted on the PIXE-RFQ and its components are reported. The RFQ was tuned by means of movable slugs and an improved tuning algorithm, which allows for correcting both field and frequency at the same time. Very good agreement between measurements and design values was observed with regards to frequency, quality factors, and field profile.

The second part of the thesis reports the development of the Carbon-RFQ, which represents a key component of a new linear accelerator for light-ion cancer therapy, accelerating carbon ions to 5 MeV/u. The Carbon-RFQ features trapezoidal vanes. A new semi-analytic approach based on multipole expansion is used to describe the field of the trapezoidal vanes. The RFQ was split into two decoupled RF cavities, whose dipole modes were detuned by means of a novel technique based on length adjustment. The splitting is described both from the RF and the beam dynamics point of view. The Carbon-RFQ study concludes with the RF design of the full structure, including computations of the maximum surface electric field and thermal-mechanical behavior.

Kurzfassung

Der Hochfrequenzquadrupol (RFQ, engl. *radio-frequency quadrupole*) stellt eine essentielle Komponente moderner linearer Hadronenbeschleuniger dar. RFQs beschleunigen Protonen oder Ionen im niederenergetischen Bereich und bestimmen maßgeblich die Strahlqualität im gesamten Beschleuniger. Mit hohen Frequenzen können kompakte und ökonomische RFQ-Entwürfe umgesetzt werden, die viele Anwendungsmöglichkeiten in Industrie und Medizin eröffnen. In der vorliegenden Arbeit wird die Entwicklung zweier kompakter RFQs mit einer Frequenz von 750 MHz beschrieben. Entsprechend ist die Arbeit in zwei Teile gegliedert:

Der erste Teil beschreibt Hochfrequenzdesign (HF-Design), HF-Messungen, und HF-Abstimmung (engl. *tuning*) des PIXE-RFQ. Der PIXE-RFQ ist ein eigenständiger Beschleuniger, der über eine Länge von einem Meter 2 MeV-Protonen für zerstörungsfreie PIXE-Analyse (protoneninduzierte Röntgenemission, engl. *proton-induced X-ray emission*) historischer Kunstwerke liefert. Mithilfe numerischer Simulationen und analytischer Methoden wurden optimale Geometrie- und HF-Parameter des Hohlraumresonators und seiner Komponenten bestimmt. Thermomechanisches Verhalten sowie Strahldynamik wurden simuliert um das HF-Design zu validieren. Anschließend wurden HF- und Störkörpermessungen am PIXE-RFQ und dessen Komponenten durchgeführt. Die HF-Abstimmung des RFQ erfolgte über bewegliche Tuner und einen weiterentwickelten Tuning-Algorithmus, mit dessen Hilfe sowohl Feld als auch Frequenz gleichzeitig korrigiert werden können. Messergebnisse und Entwurfswerte stimmten bezüglich Frequenz, Gütefaktoren und Feldverteilung mit nur geringer Abweichung überein.

Der zweite Teil der Arbeit widmet sich dem Carbon-RFQ, der Kohlenstoffionen auf 5 MeV/u beschleunigt und einen wesentlichen Teil eines vorgeschlagenen Linearbeschleunigers für Krebstherapie darstellt. Der Carbon-RFQ verfügt über trapezförmige Elektroden (engl. *trapezoidal vanes*). Das Feld der Elektroden wird mithilfe einer neuartigen semi-analytischen Methode beschrieben, die auf einer Multipolentwicklung aufbaut. Der Carbon-RFQ wurde in zwei Resonatoren geteilt, deren parasitäre Dipolmoden durch eine neuartige, auf Längenanpassung basierende Methode verstimmt wurden. Die Aufteilung wird aus sowohl HF-technischer als auch strahldynamischer Perspektive diskutiert. Die Studie schließt mit dem HF-Design der gesamten Struktur einschließlich Berechnungen der maximalen Feldstärken und des thermomechanischen Verhaltens.

Acknowledgments

With great pleasure I would like to express my gratitude to the people who have contributed to this thesis in one or the other way, and who supported me along the journey:

- to Ursula van Rienen for the supervision of not only this dissertation, but also of my bachelor and master thesis before. By accepting me as "HiWi" into your working group at University of Rostock, you supported me in taking my first steps into science. Thank you for taking on the challenge of supervising a thesis on radio-frequency quadrupoles.

- to Alexej Grudiev, my supervisor and mentor at the RF Group at CERN. I am grateful for your trust and freedom you gave me in my work, while providing me with guidance and support whenever needed. Your thoroughness and intuitive understanding of the field of RF engineering deeply impress me, and they have left their mark on this thesis and myself.

- to Holger Podlech for his time and effort in taking on the external review of this thesis.

- to my current and former colleagues at CERN and the University of Rostock, namely Vittorio Bencini, Thomas Flisgen, Benjamin Koubek, and Kai Papke, for many fruitful discussions and even more coffees. In particular I would like to thank Johann Heller, who supervised my bachelor and master thesis and inspired me to write my dissertation in accelerator physics.

- to my colleagues at CERN with whom I worked on the RFQs, especially Yves Cuvet, Alessandra Lombardi, and Serge Mathot, for giving valuable input to this thesis and sharing their knowledge with me. Regards also go to the team at the vacuum brazing workshop for helping out with the tuning.

- to Eleanor Davies and Kathrin Krebs for not letting me drown in the sea of bureaucracy.

- to the Wolfgang Gentner Programme of the German Federal Ministry of Education and Research, which financially supported this PhD thesis.

- to my friends with whom I shared school, university, vacations, LAN parties, and Salsarico Biereimer: Andrea, Anja, Alex, Clemens, Felix, Maik, Steffen, Tobias, Yves, Wiebke, especially to my lab partner Tino, and to my best friend since childhood Gustav.
- to my friends from Yachting Club CERN that made my evenings and weekends on Lac Léman a blast, first and foremost Oliver, Bernadett, and Felix. Thank you for an amazing sailing cruise around the Flensburger Förde that ventilated my head during the writing phase.
- meiner Schwester Uta, meinen Eltern, und meinen Großeltern. Ohne eure Liebe und bedingungslose Unterstützung stünde ich nicht dort, wo ich heute stehe.
- por último, a mi novia Ana. Gracias por tu amor y apoyo nutricional sin fin, especialmente durante la fase de escritura. Estoy agradecido de que seas parte de mi vida.

Table of Contents

Acronyms

2D	two-dimensional
3D	three-dimensional
CAD	computer-aided design
CERN	European Organization for Nuclear Research
CW	continuous wave
DSR	dipole stabilization rod
DTL	drift-tube linear accelerator
FEM	finite element method
FF	fringe field region
LEBT	low-energy beam transport line
LHC	Large Hadron Collider
linac	linear accelerator
PEC	perfect electric conductor
PEEK	polyether ether ketone
PIXE	proton-induced X-ray emission
PMC	perfect magnetic conductor
QC	quadrupole cell
RF	radio frequency
RFQ	radio-frequency quadrupole
RM	radial matcher
rms	root mean square
SCDTL	side-coupled drift-tube linear accelerator
SNR	signal-to-noise ratio
STP	standard temperature and pressure
SVD	singular value decomposition
TC	transition cell
TE	transverse electric
TEM	transverse electromagnetic
TM	transvere magnetic
TLM	transmission line model
VNA	vector network analyzer

List of Symbols

Symbol	Unit	Description
$A_{\mu,\nu}$	1	multipole expansion coefficient
$A_{0,1}$	1	RFQ quadrupole term (general)
$A_{1,0}$	1	RFQ acceleration efficiency
a	m	minimum aperture
$a_1, \cdots, a_4$	1	field amplitudes measured in quadrants
$\mathcal{B}$	1	RFQ effective focusing force
$\mathbf{B}$	T	magnetic flux density
b_c	m	cavity dimension
b_1, b_2, b_3	1	quality factor circle parameters
$\mathbf{b}$	1	vector
C	F	capacitance
C'	F/m	shunt capacitance per unit length
C_e	F	shunt capacitance of RFQ end
C_{tot}	F	total shunt capacitance of end segment
$\mathbb{C}$	—	complex numbers
c	m/s	speed of light in vacuum
c_c	m	cavity dimension
D	1	circle diameter in complex plane
D^S	1	dipole component, first polarization
D^T	1	dipole component, second polarization
D^S_{trg}, D^T_{trg}	1	dipole component target value
δD^S, δD^T	1	relative errors in dipole component
$\mathbf{D}$	C/m^2	electric flux density
d	1	duty cycle
$\mathbf{E}$, E	V/m	electric field strength
E_0	V/m	average longitudinal electric field
E_{acc}	V/m	accelerating electric field
E_s	V/m	surface electric field
$E_{s,max}$	V/m	maximum surface electric field
E_K	V/m	Kilpatrick limit
e	1	Euler's number
$F_{\mu,\nu}$	1	multipole basis function

Symbol	Unit	Description
$\mathbf{F}$	N	force
f	Hz	frequency
$\bar{f}$	1	normalized frequency
f_0	Hz	resonant frequency (operating mode)
f_{co}	Hz	cutoff frequency
f_{meas}	Hz	measured frequency without correction
f_{rep}	Hz	RF pulse repetition rate
f_{trg}	Hz	target frequency
$\bar{f}_{trg}$	1	normalized target frequency
Δf	Hz	frequency shift, bandwidth
$\Delta \bar{f}$	1	normalized frequency shift
g	m	accelerating gap length
g_c	1	modified Poynting vector coefficient
$\mathbf{H}$, H	A/m	magnetic field strength
H_t	A/m	tangential component of magnetic field
h	$W/m^2/K$	heat transfer coefficient
h_c	$W/m^2/K$	thermal contact conductance
I	A	current
I_b	A	beam current
$\mathcal{I}_n(\cdot)$	1	modified Bessel function of first kind and nth order
$\mathfrak{I}\{\cdot\}$	—	imaginary part
i	1	index
$\mathbf{J}$	A/m^2	electric current density
$\mathbf{J}_s$	A/m	surface electric current density
j	1	index
j	j	imaginary unit
$\mathbf{K}$	1	matrix
k	1	index
k	1/m	wavenumber
k_{co}	1/m	cutoff wavenumber
L	m	cell length
L_{QC}	m	length of quadrupole cell
L_{RFQ}	m	RFQ length
L_{TC}	m	length of transition cell
ΔL	m	RFQ segment length
$\mathcal{L}$	H	inductance
$\mathcal{L}'$	H m	shunt inductance times unit length
$\mathcal{L}'_s$	H/m	series inductance per unit length
$\mathcal{L}_e$	H	shunt inductance of RFQ end
$\mathcal{L}_{tot}$	H	total shunt inductance of end segment
ℓ_{DSR}	m	length of the dipole stabilization rod
$\Delta\ell$	m	coupling loop size
M	1	index

Symbol	Unit	Description
$\mathbf{M}_{\mathrm{e}}$	1, 1/m	TLM matrix of RFQ end
$\mathbf{M}_{\mathrm{RFQ}}$	1, 1/m	TLM matrix of entire RFQ
$\mathbf{M}_{\mathrm{wg}}$	1, 1/m	TLM matrix of waveguide-like RFQ slice
$\mathfrak{m}$	1	modulation
$\mathfrak{m}$	1	index, number of tuners
$\mathfrak{m}_0$	$\mathrm{eV/c^2}$	particle rest mass
N	1	index
$\mathfrak{n}$	1	index
$\mathbf{n}$	1	normal vector
P_0	W	surface power loss
P_{a}	W	pickup antenna power
$\bar{\mathrm{P}}_{\mathrm{a},\mathfrak{i}}^{\mathrm{A}\to\mathrm{A}}$	1	rel. antenna power from antenna-antenna meas.
$\bar{\mathrm{P}}_{\mathrm{a},\mathfrak{i}}^{\mathrm{C}\to\mathrm{A}}$	1	rel. antenna power from coupler-antenna meas.
P_{b}	W	beam power
P_{ex}	W	external power
P_{+}	W	power propagating from generator to coupler
P_{-}	W	power propagating back from coupler to generator
$\mathbf{p}$, p	eV/c	particle momentum
p_{s}	$\mathrm{W/m^2}$	surface power loss density
p_{c}	Pa	contact pressure
$\mathrm{p}_{\mathrm{air}}$	mmHg	air pressure
$\mathrm{p}_{\mathrm{vap}}$	mmHg	vapor pressure
Q	1	quadrupole component
$\mathrm{Q}_{\mathrm{trg}}$	1	quadrupole component target value
$\hat{\mathrm{Q}}_{\mathrm{trg}}$	1	unknown quadrupole component target value
$\delta\mathrm{Q}$	1	relative error in quadrupole component
Q_0	1	unloaded quality factor
$\tilde{\mathrm{Q}}_0$	1	unloaded quality factor with vane modulation
$\mathrm{Q}_{0,\mathrm{2D}}$	1	unloaded quality factor, two-dimensional case
$\mathrm{Q}_0^{\mathrm{prt}}$	1	unloaded quality factor of a port segment
Q_{ex}	1	external quality factor
Q_ℓ	1	loaded quality factor
q	e	particle charge
R	Ω	resistance
R_{c}	m	cavity radius
$\mathrm{R}_{\mu,\nu}$	1	radial scaling factor
$\mathbf{R}$	1	tuning response matrix
$\mathfrak{R}\{\cdot\}$	—	real part
$\mathbb{R}$	—	real numbers
RH	%	relative humidity
$\mathbf{r}$	m	position vector
r	m	radial coordinate

Symbol	Unit	Description
r_0	m	mid-cell aperture
S_{11}	1	reflection coefficient (scattering parameter)
S_{21}	1	transmission coefficient (scattering parameter)
$S_{21}^{Aj\to Ai}$	1	transmission between jth and ith antenna
$S_{21}^{C\to Ai}$	1	transmission between coupler and ith antenna
$\boldsymbol{S}$	W/m^2	Poynting vector
S_c	W/m^2	modified Poynting vector
$\mathcal{S}$	m^2	surface of integration
$\mathbf{s}$	1	vector
T	K	temperature
T_w	K	water temperature
ΔT	K	temperature difference
T_{tr}	1	transit-time factor
$\mathcal{T}$	1	transmission
t	s	time
t_{pls}	s	RF pulse length
t_j	m	position of jth tuner
$\bar{t}_j$	1	position of jth tuner, normalized
$t_{trg,j}$	m	target position of jth tuner
$\bar{t}_{trg,j}$	1	target position of jth tuner, normalized
$\mathbf{t}_{cur}$	m	vector of current tuner positions
$\mathbf{t}_{trg}$	m	vector of target tuner positions
$\Delta\mathbf{t}$	1	vector of tuner adjustments
$\mathbf{U}$	1	orthonormal matrix
$\mathbf{u}$	m	deformation field
V	V	voltage
V_0	V	inter-vane voltage
V_{acc}	V	accelerating voltage
$\boldsymbol{V}$	1	orthonormal matrix
$\mathcal{V}$	m^3	volume of integration
$\boldsymbol{v}, v$	m/s	velocity
v_w	m/s	average water flow speed
W_0	J	energy stored in the electromagnetic field
ΔW	J	change in stored energy
$\mathcal{W}$	eV	kinetic energy
$\mathcal{W}_s$	eV	synchronous energy
$\Delta\mathcal{W}$	eV	energy difference w.r.t. synchronous particle
$\boldsymbol{W}$	1	weighting matrix
w_f	1/Hz	frequency weight
w_t	1/m	tuner normalization constant
$\mathcal{X}$	1	RFQ quadrupole term (two-term potential)
x	m	transverse coordinate
x'	rad	transverse momentum deviation

Symbol	Unit	Description
$\mathbf{x}_{\mathrm{cur}}$	1	vector of current field amplitude samples
$\mathbf{x}_{\mathrm{trg}}$	1	vector of target field amplitude samples
$\tilde{\mathbf{x}}_{\mathrm{trg}}$	1	vector of predicted field corrections
$\Delta\mathbf{x}$	1	vector of field amplitude errors
Y	S	admittance
$\bar{Y}$	1	normalized admittance
Y_e	S	shunt admittance of RFQ end
y	m	transverse coordinate
y'	rad	transverse momentum deviation
Δy	m	penetration of auxiliaries into the cavity
Z_0	Ω	line impedance
Z_{in}	Ω	input impedance
Z_s	Ω	surface impedance
z	m	longitudinal coordinate
z_0, z_1	m	start/end of RFQ segment
z_{up}, z_{dn}	m	position of RFQ upstream/downstream end
α_c	rad	angle of vane support
α_T	1/K	coefficient of thermal expansion
$\tilde{\alpha}$	1	Twiss parameter
$\boldsymbol{\beta}$, β	1	normalized velocity
β_c	1	coupling coefficient
$\tilde{\beta}$	various	Twiss parameter
Γ	1	reflection coefficient
Γ_{ds}	1	refl. coeff. in detuned-short position
Γ'_{ds}	1	refl. coeff. in detuned-short position, corrected
$\boldsymbol{\Gamma}$	1	vector of reflection coefficient samples
γ	1	relativistic mass factor
$\tilde{\gamma}$	various	Twiss parameter
δ_{pass}	1	numerical convergence error
ε_0	F/m	vacuum permittivity (electric constant)
ε_r	1	relative permittivity
$\tilde{\varepsilon}$	various	rms emittance
ϑ	rad	azimuthal coordinate
κ	1	field enhancement
λ	m	wavelength
μ	1	multipole expansion longitudinal index
μ_0	T m/A	vacuum permeability (magnetic constant)
μ_r	1	relative permeability
ν	1	multipole expansion azimuthal index
ρ	$\mathrm{C/m^3}$	electric charge density
ρ_ℓ	m	vane tip longitudinal radius of curvature
ρ_t	m	vane tip transverse radius of curvature
$\boldsymbol{\Sigma}$	1	diagonal matrix of singular values

Symbol	Unit	Description
σ	S/m	electric conductivity
σ_0	rad	transverse phase advance per focusing period
σ_k	1	singular value of tuning response matrix
σ_{vM}	Pa	von Mises equivalent stress
σ_W	eV	rms energy spread
σ_x, σ_y	m	transverse rms beam envelopes
Φ	V	electric potential
Φ_{16}	V	sixteen-term potential function
Φ_{FEM}	V	potential computed by means of FEM
ϕ	rad	phase
ϕ_s	rad	synchronous phase
$\Delta\phi$	rad	phase shift, phase difference w.r.t. sync. particle
ω	rad/s	angular frequency
$\bar{\omega}$	1	normalized angular frequency
ω_0	rad/s	resonant angular frequency (operating mode)
ω_{co}	rad/s	cutoff angular frequency
$\Delta\omega$	rad/s	angular frequency shift, bandwidth
$\boldsymbol{\nabla}$	1/m	Nabla operator
∇^2	$1/m^2$	Laplace operator

List of Figures

List of Tables

1 Introduction

Particle accelerators are high-technological developments that emerged from twentieth-century science and technology. They fulfill the purpose of accelerating charged particles to relativistic velocities (near speed of light) and high energies using electromagnetic fields. Established as a major driving force in fundamental nuclear and high-energy physics research, particle accelerators have gained increasing importance in industry and medicine with a broad variety of applications. The radio-frequency quadrupole (RFQ) is a special type of linear accelerator that accelerates protons or ions at low energies, and represents an essential component of modern linear accelerator designs. A high operating frequency allows for compact and economic RFQ designs, opening up a broad variety of applications in industry and medicine. The present thesis is centered around the development of two RFQs operating at 750 MHz: The PIXE-RFQ embodies a stand-alone accelerator with a length of only one meter that provides protons for ion beam analysis of cultural heritage artwork. The Carbon-RFQ is part of a linear accelerator design proposal for particle cancer therapy by means of carbon ions.

In the following three sections, linear accelerators and RFQs in particular are introduced in their historical context, and the two above-mentioned applications are discussed in detail. Section 1.4 outlines the thesis and states its contributions to the field of accelerator physics.

1.1 Linear Accelerators & RFQs

The term linear accelerator, or linac, refers to accelerators in which time-dependent electromagnetic fields accelerate charged particles along a straight line [1]. Contrarily, in circular machines such as synchrotrons and cyclotrons, the particles gain energy over many turns. While the first accelerator to use time-dependent fields was proposed by Ising in 1924 [2], generally the drift-tube linac (DTL) developed and demonstrated by Widerøe in 1927 [3] is considered the first radio-frequency (RF) linear accelerator.

Widerøe applied a time-alternating voltage to an array of drift tubes, where two subsequent tubes each have opposite polarity (Fig. 1.1). The lengths of the drift tubes increase with the particle velocity, such that the particles arrive at ev-

ery gap at the correct time when the electric field has the correct orientation for acceleration. Large numbers of particles are grouped into so-called bunches in order to achieve acceptable beam currents. The thereby established use of time-varying electromagnetic fields overcomes the limitation of electrostatic particle accelerators (Van de Graaff [4] or Cockcroft-Walton accelerators [5]), in which the final energy depends on the overall potential difference. By 1931, a DTL with 30 tubes was built, which accelerated mercury ions to an energy[1] of 1.26 MeV with an RF voltage of only 42 kV [6].

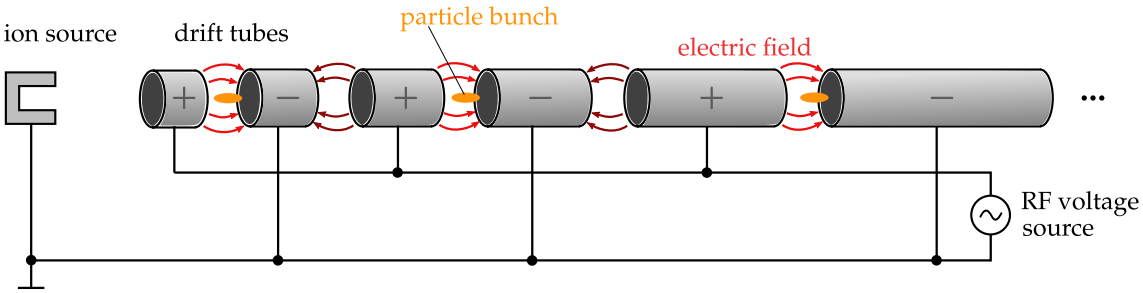

Figure 1.1: Sketch of the Widerøe drift-tube linac (DTL). A time-alternating voltage is applied to an array of drift-tubes, where two subsequent tubes each are charged with opposite polarity. The total acceleration provided by the electric fields in the gaps between two drift-tubes is not limited by some overall potential difference.

Since the development of the Alvarez-DTL from 1946 onwards [7, 8], modern linacs use RF electromagnetic fields resonating in room-temperature or superconducting cavities to provide accelerating forces, with frequencies ranging from few MHz to several tens of GHz. Various types of accelerating RF cavities have been developed for different particle types, energies, frequencies, and applications [1, 9, 10].

A special type of RF linear accelerator is the RFQ (radio-frequency quadrupole linac). An RFQ accelerates hadrons, i.e. protons or ions, at low energies (1 % to 6 % of the speed of light [1]). In 1969, Kapchinsky and Teplyakov first presented the RFQ principle [11]. They proposed to introduce a spatial sinusoidal-like modulation to the geometries of the four electrodes of an RF quadrupole. Thereby introducing a longitudinal electric field component, not only transverse focusing, but also acceleration was achieved. The introduction of adiabatic bunching soon followed in a second publication [12]. As one of the main advantages of the RFQ over other low-energy RF accelerators, adiabatic bunching converts a large portion of a continuous input beam into a train of stable bunches while minimizing space-charge effects [13], maintaining high beam quality. The RFQ is considered a major innovation in the field of linear accelerators [1]. Nowadays, it is usually the first RF accelerating structure in a hadron accelerator complex, as the beam

[1] In accelerator physics (and other fields), energy and mass of the particles are commonly given in units of electron-volt, or eV. One electron-volt is the kinetic energy that electrons or other particles with unit charge gain upon being accelerated by a potential difference of 1 V. The energy of ions is often given normalized to their number of nucleons in units of eV/u.

quality achieved at low energies is a crucial contributor to the overall accelerator performance. A photograph of the inside of an RFQ is depicted in Fig. 1.2. The RFQ is described in detail in Section 2.3.

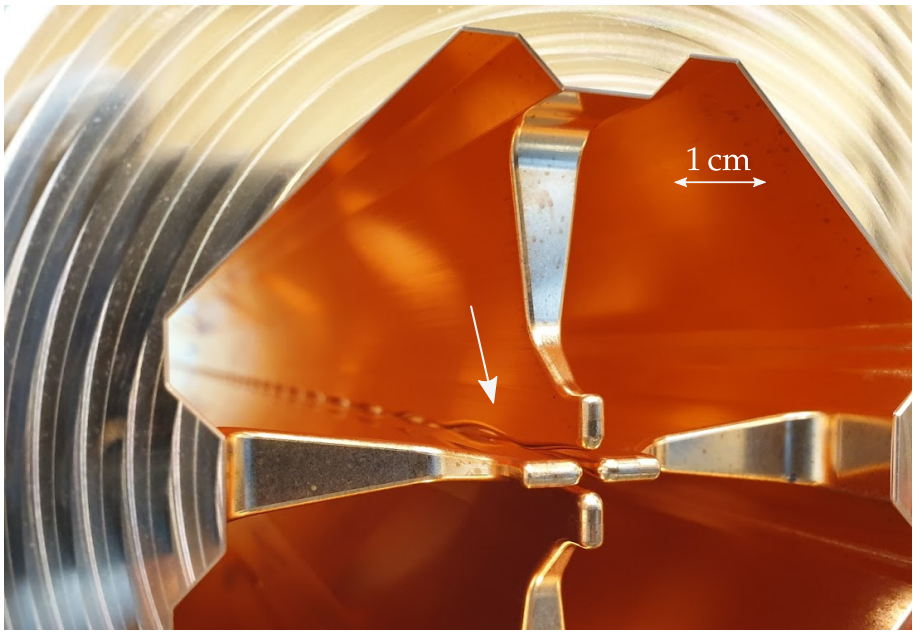

Figure 1.2: Photograph of the inside of the PIXE-RFQ cavity operating at 750 MHz. The four electrode support structures, so-called vanes, are visible in the foreground. The electrode tips with sinusoidal-like modulation are indicated by a white arrow.

Linear accelerators offer several advantages over circular machines. They can produce high-energy, high-intensity beams with sought-after qualities such as small beam size and low energy spread. Further characteristics include easy inclusion of strong focusing, simpler injection and extraction, high average beam currents (operation at any duty cycle up to continuous wave), and avoidance of cumulative errors (the particles pass every linac component only once) [1]. The main disadvantage compared to circular machines is a consequence of the latter: Since the energy gain per unit length in a linac is limited by the maximum surface electric field that can be sustained at a given RF breakdown rate, the linac length and thus cost increase linearly with its total energy gain. Therefore, facilities achieving very high beam energies commonly combine different types of accelerators. For instance, in the main accelerator complex of the European Organization for Nuclear Research (CERN), protons are brought to 160 MeV by a linear accelerator (Linac4), and from there accelerated through a sequence of synchrotrons of increasing diameter until they reach 7 TeV in the Large Hadron Collider (LHC) synchrotron [14].

Stimulated by radar developments during World War II, the availability of high-power RF sources immensely increased in the 1950s, supporting a rapid growth of research and development in the field of accelerator physics [10]. With high-energy particle beams, interactions between elementary particles can be an-

alyzed and smallest structures can be resolved. Two beams brought to collision recreate conditions comparable to the Big Bang in the laboratory with the purpose of proving existence of elementary particles and measuring their properties. By directing the beam onto a target, a large variety of secondary particle beams is obtained. Synchrotron radiation can be generated by guiding the beam through a suitable lattice of magnets. Through this, high-intensity light sources of various spectral properties can be constructed. The largest particle accelerators are essential instruments in basic research, in particular nuclear and high-energy particle physics. A notable example is given by the LHC, a synchrotron with 27 km circumference located at CERN near Geneva, Switzerland. The world's longest linacs are the Linear Collider (3 km, shut down in the 2000s) at Stanford National Accelerator Laboratory (SLAC), USA [15], and the European X-Ray Free-Electron Laser Facility (European XFEL) at Deutsches Elektronen-Synchrotron (DESY) in Hamburg, Germany, featuring superconducting RF cavities over a length of 2.1 km [16]. Smaller accelerators have become crucial instruments in—besides basic research—a broad variety of applications, for instance in fusion research and reactor fuel breeding, ion implantation, semi-conductor industry, radiography, ion beam analysis, isotope production, chemistry, material sciences, medicine, radiotherapy, microsurgery, or food sterilization, to name only a small selection [1, 10, 17].

A high operating frequency f allows for compact designs, which make linacs and RFQs in particular economically attractive with regards to many of the applications mentioned above. Specifically, both transverse cross section and length decrease as f increases, reducing cost of construction. Moreover, the RF power consumption scales as $f^{-1/2}$ in normal conducting cavities [1]. (However, this can not always be translated to RFQ designs with higher RF efficiency because of aperture requirements [18].) The present thesis is centered around the development of two RFQs operating at 750 MHz: the PIXE-RFQ as a stand-alone accelerator for ion beam analysis, and the Carbon-RFQ as low-energy part of a linear accelerator for particle cancer therapy. Both applications and the respective RFQs are introduced in the following two sections.

1.2 Ion Beam Analysis: The PIXE-RFQ

In ion beam analysis, protons or ions of a few MeV/u are used for material characterization, with the proton-induced X-ray emission analysis (PIXE) [19, 20] being the most widely used ion beam analysis technique. Developed in the 1950s, and first applied in the 1970s, PIXE analysis is a spectrographic technique, where a 2 MeV to 4 MeV proton[2] beam stimulates the emission of X-rays of specimen atoms. Measuring the emitted spectrum allows for the quantitative, highly sensitive, and simultaneous determination of elements in the material, with detection

[2]Sometimes, α-particles (helium nuclei) are used instead of protons in PIXE analysis [20].

limits reaching the order of 10^{-7} [20]. Both solid, liquid, and aerosol filter samples may be analyzed. Because of its non-destructive character, PIXE analysis is used in many fields, including (but not limited to) chemistry, medicine, atmospheric and environmental sciences, search for mineral resources, material sciences, quality control, fisheries, forensics, and—in this particular case—the analysis of cultural heritage artwork.

Conventional PIXE facilities feature cyclotrons or electrostatic (tandem) Van de Graaff accelerators. Such machines require significant space, infrastructure, and operating staff, and are thus installed only in dedicated centers (see e.g. Refs. [21–26], to name a few). However, because of a variety of reasons, for instance cost and feasibility, size, conservation stage, or immobility of e.g. a fresco, it is often not desirable or acceptable to move the masterpiece to the facility. Contrarily, a small RFQ can provide protons at the required energy over a length of just one meter, offering the possibility to bring the accelerator to the artwork instead.

A compact high-frequency RFQ for PIXE analysis, called PIXE-RFQ [27–31], was developed and built at CERN within the context of the MACHINA project (Movable Accelerator for Cultural Heritage In situ Non-destructive Analysis, [31, 32]), a collaboration between CERN and Istituto Nazionale di Fisica Nucleare (INFN), Florence, Italy. The aim of the project is to build the first transportable system for *in situ* PIXE ion beam analysis, allowing employment in museums, restoration centers, or even in the field. A CAD model of the MACHINA setup is shown in Fig. 1.3. In addition to the PIXE-RFQ, it consists of an RF proton source and a low-energy beam transport line including a Faraday cup [33] installed before the RFQ. The high-energy beam transport line downstream of the RFQ consists of two permanent quadrupole magnets allowing to shift the position of minimum beam spot size, and a beam degrader featuring different foils on a rotating disc to reduce the beam energy for differential PIXE analysis.

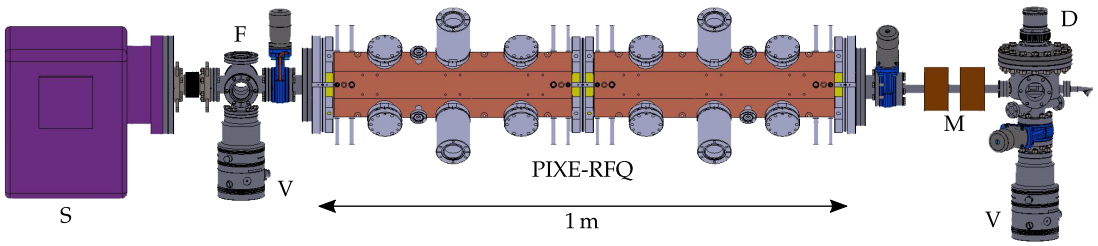

Figure 1.3: CAD model of the MACHINA setup with the PIXE-RFQ at the center (slightly elevated side view). Also shown are the RF proton source (S), the low-energy beam transport line with Faraday cup (F), the high-energy beam transport line comprising two permanent quadrupole magnets (M), a second Faraday cup, and a beam degrader (D), as well as two vacuum turbo pumps (V). Graphics adapted from Ref. [31] with courtesy of S. Mathot.

The development of the PIXE-RFQ started in 2017 at CERN, supported by the CERN Knowledge Transfer fund. It operates at a frequency of 750 MHz, accelerating protons to 2 MeV over a length of one meter. Both design and con-

struction profited from the experience gained with the Linac4-RFQ [34–39] of the LHC injector complex, and the CERN High-frequency RFQ for medical applications (HF-RFQ) [18, 27, 28, 40–43], which has been commissioned in 2018 [43] and represents the first RFQ worldwide[3] to operate at 750 MHz. As of July 2020, design, construction, as well as low-power RF measurements and tuning of the PIXE-RFQ have been completed. It is now *en route* to high-power RF and beam commissioning as the world's smallest RFQ to date.

1.3 Particle Cancer Therapy: The Carbon-RFQ

Particle accelerators represent important instruments in modern medicine and medical physics. Next to biomedical research, radioisotope production, and medical imaging, to name a few, they have grown essential in oncotherapy [45].

Effective cancer treatment requires a highest possible killing rate of tumor cells, while the damage to healthy tissue has to be minimized. The killing rate depends on the amount of energy deposited by the radiation upon interaction with the tissue, called treatment dose. The dose is shown in Fig. 1.4 for four types of radiation as a function of penetration into water [46], which in this context is very similar to biological tissue. The energy deposition mechanism strongly depends on the particle type: After a short build-up, the dose deposited by high-energy photons (X-rays) decays exponentially. The interaction of charged particles with matter is characterized by the stopping power, which may be calculated as a function of the particle energy by means of the Bethe formula [47, 48]. Electrons have a short range, releasing almost all of their energy over the first few centimeters, while beyond only a minimum dose is deposited through secondary electrons generated by bremsstrahlung. Electrons of much higher energies are necessary to provide deeper dose deposition. For hadrons such as protons and carbon ions, the stopping power increases dramatically at low energies, such that these particles deposit the largest fraction of their energy in a small region close to the end of their path through the tissue.

The stopping region is known as the Bragg peak (Fig. 1.4). This behavior allows for concentrating the treatment dose deposited by hadron beams in a small target area, minimizing damage to healthy tissue compared to X-ray treatment (Fig. 1.5). Furthermore, as hadrons travel a nearly linear path through matter, the depth of the Bragg peak, and thus the location of maximum deposited energy, can be controlled by means of the initial particle energy. With a sharper and more intense Bragg peak, carbon ions feature a more advantageous energy deposition behavior (Fig. 1.4) compared to protons. Less dose is released before reaching the high-dose region. Furthermore, the Relative Biological Effectiveness (RBE) of carbon ions is by a factor of two to three higher than that of protons, meaning

[3] In fact, already in 1995 the TERA Foundation (Terapia con Radiazioni Adroniche) proposed a proton-therapy linac comprising a 750 MHz RFQ [44], however, the project was abandoned because of construction-related challenges that could not be met by the technology of the time [18].

that they are more effective at killing cells [49]. Carbon ions are thus particularly suited for treating radio-resistant tumors.

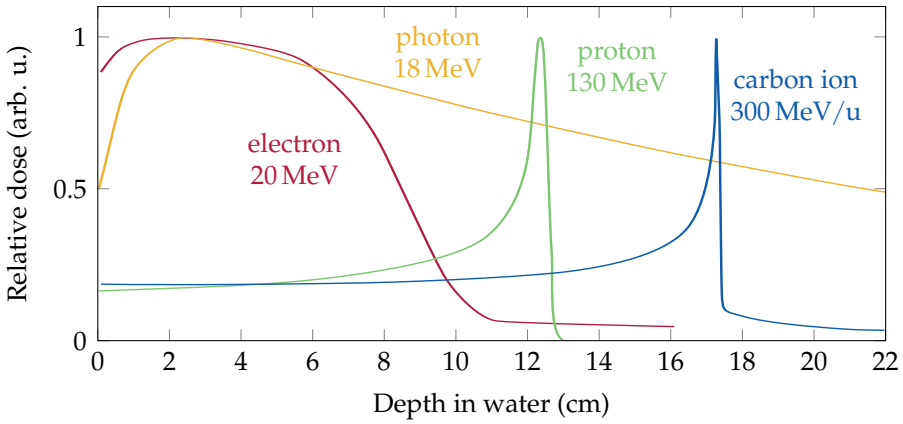

Figure 1.4: Relative dose deposition by different types of radiation penetrating into water (very similar to biological tissue). The peak of the proton and carbon ion curves is known as the Bragg peak. Figure adapted from Ref. [46].

Studies showed that 15 % of the patients treated with conventional radiotherapy in Europe would have profited from hadron therapy, and for 3 % a treatment by means of carbon ion beams would have been particularly beneficial [51, 52]. The hadron therapy market is continuously expanding because of the advantages that this treatment brings. As of June 2020, 103 particle therapy facilities are in operation worldwide, with an additional 38 under construction, and 27 facilities in the planning stage [53]. Almost 220 000 patients were treated with proton beams, and nearly 40 000 underwent carbon ion therapy [53]. The main hindrance to the application and growth of hadron therapy over conventional radiotherapy is given by the cost of the respective technologies. For radiotherapy, X-rays can be produced using an electron beam (around 10 MeV) obtained from a few meter long high-frequency linac. Protons and ions however feature a by three orders of magnitude larger mass and must be accelerated to energies of several hundred MeV/u. The required infrastructure increases the cost of a proton beam treatment to roughly three times that of radiotherapy [52]. Carbon ion therapy is even more expensive because of higher final energies and the lower charge-to-mass ratio that is unfavorable in terms of acceleration.

Presently, three types of particle accelerators can be used for hadron therapy: cyclotrons, synchrotrons, and linacs. Being the latest technology proposed for hadron therapy, linear accelerators produce high-quality pulsed beams at high repetition rates compared to cyclotrons or synchrotrons. The output energy—and thus the depth of the high-intensity dose deposition given by the Bragg peak—can be modulated by switching off parts of the accelerating structures, resulting in rapid energy switching times given by the linac repetition rate. With the first proposal dating back to 1991 [54, 55], proton therapy linacs have reached industrialization phase—two machines are presently under construction or commis-

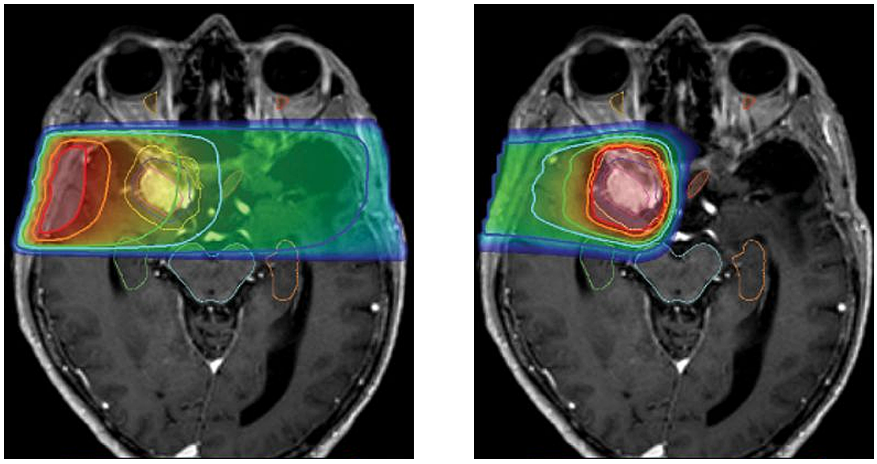

(a) X-ray beam **(b)** Proton beam

Figure 1.5: Magnetic resonance image of a skull of a patient with brain tumor (light area). The overlay shows the dose deposited by conventional X-ray therapy (a) and by a proton beam (b). The phenomenon observed as the Bragg peak (Fig. 1.4) allows for concentrating the treatment dose at the tumor location, minimizing damage to healthy tissue in front and behind (b). Figure taken from Emory Proton Therapy Center [50].

sioning [56–58]. Carbon ion linacs, however, are still at a conceptual design stage, a notable example being the Compact Carbon Ion Linac (ACCIL) [59] developed at Argonne National Laboratory, USA. Thus, it is important to explore new solutions tailored to reduce size and cost of the accelerator, easing the transition to industrialization.

As one of the most recent proposals, Bencini proposed the design of a 3 GHz "bent linac" for carbon ions (Fig. 1.6) in Ref. [52]. A key goal of the study was to improve the aspect ratio of the usually unfavorable linac footprint, such that it would better fit into a hospital facility without affecting the treatment beam properties. In the low energy section of the machine, fully stripped carbon ions ($^{12}C^{6+}$) are produced by the ion source (TwinEBIS, operating at CERN [60]), propagated through a suitable low-energy beam transport line (LEBT) [61], and matched into the RFQ, which represents the first RF accelerating structure. The RFQ—called Carbon-RFQ—has the critical role of shaping the carbon ion beam and prepare it for injection into the following accelerating structures.

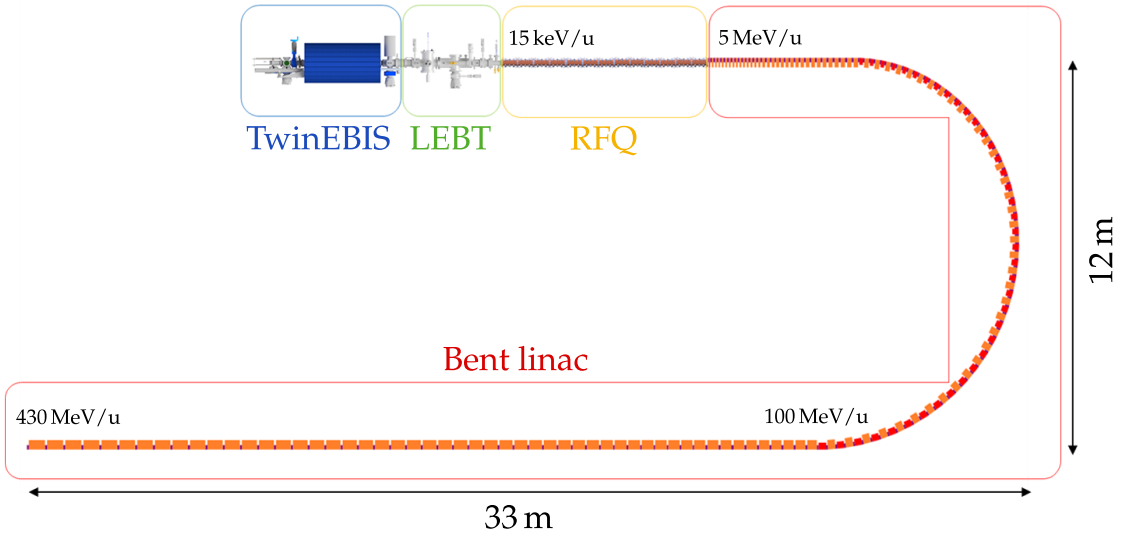

Figure 1.6: Concept of the bent linac consisting of the TwinEBIS carbon ion source, a LEBT, the Carbon-RFQ, and a linac comprising a fixed energy section with interlaced dipole magnets up to 100 MeV/u, followed by a modulated energy section up to 430 MeV/u. The Carbon-RFQ represents the first RF accelerating structure. Figure adapted from Ref. [52] with courtesy of V. Bencini.

1.4 Structure and Novel Contributions of the Thesis

The present thesis is organized as follows: Chapter 2 provides the reader with the theoretical concepts useful for the understanding of the thesis. After briefly presenting textbook knowledge on electromagnetic theory, the RFQ principles of operation are explained from a beam dynamics and an RF point of view. Chapter 2 is completed by a review of previous RFQs with respect to maximum achieved electromagnetic field strengths, justifying the design choices of the two RFQs discussed in the thesis.

Two parts form the main thesis body: Chapters 3 and 4 are dedicated to the PIXE-RFQ, whereas the development of the Carbon-RFQ is covered in Chapter 5. RF design, measurements, and tuning of the PIXE-RFQ were carried out by the author. Chapter 3 reconstructs the RF design process, including 2D and 3D geometry optimization and the design of power coupler and RFQ auxiliaries. The RF design was validated by both thermal and beam dynamics simulations, which are subsequently discussed. In Chapter 4, the low-power RF measurements performed on the PIXE-RFQ are presented. A large portion of this chapter is dedicated to the RFQ tuning, where frequency and field distribution were corrected by means of repeated bead-pull measurements and adjustment of movable slug tuners.

Chapter 5 covers the studies carried out for the Carbon-RFQ for hadron cancer therapy. The general RFQ parameters and an initial design with standard vanes were presented by Bencini in Ref. [52]. The RFQ was subsequently modified to feature trapezoidal vanes. Extending the multipole potential function description

commonly used for RFQs, a semi-analytic method was developed by the author to describe the 3D electric field of the trapezoidal electrodes. The RF design of the Carbon-RFQ, which consists of two independent RF cavities, was carried out by the author, including the detuning of parasitic dipole modes by means of length adjustment, which was implemented for the first time. Chapter 5 also details the beam matching over the drift between the two cavities, which is the result of joint efforts of Bencini and the author.

Finally, the thesis is concluded in Chapter 6 and a brief outlook is given.

To the best knowledge of the author, the present thesis contains the following novel contributions, part of which have been previously published by the author in Refs. [29, 30, 62]:

- An overview-study on field limitations in RFQs. Publications on a range of commissioned or designed RFQs have been evaluated with regards to maximum surface electric field, frequency, and RF pulse lengths. Various derived quantities have been analyzed to find a figure of merit suitable to predict RFQ breakdown performance besides the Kilpatrick limit.

- The RF design of two compact RFQs operating at 750 MHz based on the design of the High-frequency RFQ for medical applications (HF-RFQ) [27], the first RFQ to operate at this frequency. The RF cavities of the one-meter long proton PIXE-RFQ and of the nearly five-meter long Carbon-RFQ were developed by the author. Using both numerical and analytical techniques, relevant RF parameters were computed and mechanical dimensions were provided for machining. The RF designs of the two RFQs have been published in Refs. [30] and [62], respectively.

- The low-power RF measurements and tuning of the PIXE-RFQ. Various components of the PIXE-RFQ and then the full assembly were measured by means of a vector network analyzer and the bead-pull perturbation technique during and after construction. Resonant frequency, quality factors, coupling coefficient, and field components were assessed and the diagnostic pickup antennas were calibrated. The field of the RFQ was tuned by means of repeated bead-pull measurements and a novel tuning algorithm (see next point).

- Further improvement of the tuning algorithm developed by Koubek for the HF-RFQ [63]. The RFQ response matrix recording the field sensitivity to movement of the piston tuners was augmented, such that not only field distribution, but also the resonant frequency can be tuned at the same time. The PIXE-RFQ has been tuned successfully using the new iteration of the algorithm in much fewer tuning steps.

- The sixteen-term potential function as a semi-analytic method to describe the electric fields of RFQs with trapezoidal electrodes. By extending the

commonly used eight-term potential function to sixteen terms, the field of trapezoidal RFQ electrodes, commonly computed numerically, can be approximated by a weighted sum with precomputed coefficients. Repetitive 3D electrostatic simulations are avoided, considerably speeding up the design process. Furthermore, 3D field maps can be generated rapidly from the potential function to perform particle tracking with a code of choice. A similar approach has been published by Li early 2020 [64], however, only the longitudinal on-axis field was considered there by means of five additional terms. The sixteen-term potential function was used for the beam dynamics design of the Carbon-RFQ [62].

- Dipole-mode detuning by means of length adjustment. In a four-vane RFQ, the frequency separation between the operating mode and parasitic dipole modes can be increased by using the RFQ length as a free parameter. The length can be adjusted to the desired value by removing or adding accelerating cells, or by adding a symmetric channel without altering output energy. As other dedicated detuning techniques are not necessary, mechanical complexity and RF power loss are reduced. A conceptual study on this method was carried out for the PIXE-RFQ by the author in Ref. [30], and it was implemented for the two cavities of the Carbon-RFQ for the first time [62].

2 Foundations

Chapter 2 provides the reader with the theoretical concepts that form the basis for the understanding of the present thesis. Section 2.1 summarizes relevant textbook knowledge on electromagnetic theory. A brief comment on numerical treatment of electromagnetic fields is given in Section 2.2. The RFQ principle of operation is explained in detail from a beam dynamics and an RF point of view in Section 2.3. The chapter is completed by a review of previously designed RFQs with respect to maximum electromagnetic field strengths achieved during commissioning. The review fulfills the purpose of justifying the design choices of the two RFQs discussed in the thesis.

2.1 Electromagnetic Theory

This section briefly presents important concepts and formulas from the theory of electromagnetic fields. The section is largely based on the explanations given in the textbooks [10, 65–69]. For a deeper insight, the reader is referred to these publications.

2.1.1 Maxwell's Equations

Classical electrodynamics are governed by Maxwell's equations. Introduced in the nineteenth century by Maxwell [70] to unify laws of electric and magnetic phenomena, they have been reformulated by other scientists into their nowadays commonly known form. The differential representation in the most general case reads:[4]

$$\boldsymbol{\nabla} \times \mathbf{H}(\mathbf{r}, t) = \frac{\partial}{\partial t}\mathbf{D}(\mathbf{r}, t) + \mathbf{J}(\mathbf{r}, t), \tag{2.1}$$

$$-\boldsymbol{\nabla} \times \mathbf{E}(\mathbf{r}, t) = \frac{\partial}{\partial t}\mathbf{B}(\mathbf{r}, t), \tag{2.2}$$

$$\boldsymbol{\nabla} \cdot \mathbf{D}(\mathbf{r}, t) = \rho(\mathbf{r}, t), \tag{2.3}$$

$$\boldsymbol{\nabla} \cdot \mathbf{B}(\mathbf{r}, t) = 0, \tag{2.4}$$

[4] Throughout this thesis, bold-face characters identify vector or matrix-valued quantities.

where the Nabla operator $\boldsymbol{\nabla}$ is used to express curl and divergence. $\mathbf{H}$ and $\mathbf{E}$ denote the magnetic and electric field strengths, $\mathbf{B}$ and $\mathbf{D}$ the corresponding flux densities, ρ the electric charge density and $\mathbf{J}$ the electric current density, while spatial and time dependence are indicated by $\mathbf{r}$ and t, respectively. Sometimes it is advantageous to use Maxwell's equations in their integral representation. With the help of Gauss' and Stokes' integral theorems [71], Eqs. (2.1)–(2.4) are rewritten as

$$\oint_{\partial\mathcal{S}} \mathbf{H}(\mathbf{r},t)\mathrm{d}\mathbf{s} = \iint_{\mathcal{S}} \left(\frac{\partial}{\partial t}\mathbf{D}(\mathbf{r},t) + \mathbf{J}(\mathbf{r},t)\right) \mathrm{d}\mathcal{S}, \tag{2.5}$$

$$-\oint_{\partial\mathcal{S}} \mathbf{E}(\mathbf{r},t)\mathrm{d}\mathbf{s} = \iint_{\mathcal{S}} \frac{\partial}{\partial t}\mathbf{B}(\mathbf{r},t)\mathrm{d}\mathcal{S}, \tag{2.6}$$

$$\oiint_{\partial\mathcal{V}} \mathbf{D}(\mathbf{r},t)\mathrm{d}\mathcal{S} = \iiint_{\mathcal{V}} \rho(\mathbf{r},t)\mathrm{d}\mathcal{V}, \tag{2.7}$$

$$\oiint_{\partial\mathcal{V}} \mathbf{B}(\mathbf{r},t)\mathrm{d}\mathcal{S} = 0. \tag{2.8}$$

Here, $\mathcal{S}$ and $\mathcal{V}$ are the surface and volume of integration, while $\partial\mathcal{S}$ and $\partial\mathcal{V}$ identify their respective boundaries.

The field strengths and flux densities are linked by the constitutive relations incorporating the properties of matter:

$$\mathbf{B}(\mathbf{r},t) = \mu_0\mu_r(\mathbf{r},t)\mathbf{H}(\mathbf{r},t), \tag{2.9}$$

$$\mathbf{D}(\mathbf{r},t) = \varepsilon_0\varepsilon_r(\mathbf{r},t)\mathbf{E}(\mathbf{r},t), \tag{2.10}$$

where $\mu_r(\mathbf{r},t)$ is the relative magnetic permeability and $\varepsilon_r(\mathbf{r},t)$ denotes the relative electric permittivity. The zero-indexed quantities refer to the permeability and permittivity of vacuum, also known as magnetic and electric constant, respectively. The electric current density is composed of three contributions: an impressed current density related to external sources, a convective current density representing free moving charges, and an Ohmic current density proportional to the material conductivity σ. Throughout this thesis only the Ohmic current density is relevant, such that

$$\mathbf{J}(\mathbf{r},t) = \sigma(\mathbf{r},t)\mathbf{E}(\mathbf{r},t). \tag{2.11}$$

For the most general cases, μ_r, ε_r, and σ are functions of both space and time (or frequency), and take tensor form for anisotropic materials. However, this thesis focuses on evacuated structures bounded by well-conducting surfaces, i.e. $\mu_r = \varepsilon_r = 1$ in the domain of interest—with the notable exception being the measurements conducted under air in Chapter 4. While for both vacuum and air $\sigma = 0$, it assumes very large values in the surrounding metal, which is generally approximated as an ideal conductor with $\sigma \to \infty$.

In absence of free charges, and assuming harmonic time-dependence in the form of $e^{j\omega t}$, Eqs. (2.1)–(2.4) become

$$\boldsymbol{\nabla} \times \mathbf{H}(\mathbf{r}, \omega) = j\omega\varepsilon_0 \mathbf{E}(\mathbf{r}, \omega), \tag{2.12}$$

$$-\boldsymbol{\nabla} \times \mathbf{E}(\mathbf{r}, \omega) = j\omega\mu_0 \mathbf{H}(\mathbf{r}, \omega), \tag{2.13}$$

$$\boldsymbol{\nabla} \cdot \mathbf{E}(\mathbf{r}, \omega) = 0, \tag{2.14}$$

$$\boldsymbol{\nabla} \cdot \mathbf{H}(\mathbf{r}, \omega) = 0, \tag{2.15}$$

where $\omega = 2\pi f$ denotes the angular frequency, and f is the (ordinary) frequency. By combining Eqs. (2.12) and (2.13) to eliminate either $\mathbf{H}$ or $\mathbf{E}$, and incorporating either Eq. (2.14) or Eq. (2.15), respectively, the well-known Helmholtz equations of the electric or magnetic fields arise:

$$\left(\nabla^2 + k^2\right)\mathbf{E}(\mathbf{r}, \omega) = \mathbf{0}, \tag{2.16}$$

$$\left(\nabla^2 + k^2\right)\mathbf{H}(\mathbf{r}, \omega) = \mathbf{0}. \tag{2.17}$$

Here, ∇^2 is the Laplace operator, and $k = 2\pi/\lambda$ denotes the wavenumber, the reciprocal of the wavelength λ. The two equations equally describe electromagnetic waves of one particular frequency $\omega = kc$, with $c = 1/\sqrt{\varepsilon_0\mu_0}$ denoting the speed of light in vacuum, and represent time-independent forms of the more general wave equations.

If the frequency is low and the wavelength becomes large compared to the geometry of interest, the right hand side of Eq. (2.13) vanishes in the so-called quasi-static approximation. The electric field then becomes curl-free and can be described as the gradient of an electrostatic potential Φ:

$$\mathbf{E}(\mathbf{r}, t) = -\boldsymbol{\nabla}\Phi(\mathbf{r}) \cos(\omega t + \phi), \tag{2.18}$$

where Φ satisfies the Laplace equation[5]

$$\nabla^2 \Phi(\mathbf{r}) = 0, \tag{2.19}$$

and ϕ is the phase of the electric field oscillation. If the electric and magnetic fields are spatially well-separated, one can take advantage of the mathematically simpler quasi-static approximation to calculate the electric field even at high frequencies. For example, the electric field between the RFQ electrodes is well-described by a electro-quasistatic potential, that is discussed in detail in Section 2.3.

From here on, the indication of space or time dependence of the physical quantities is omitted in favor of a more compact notation, and only emphasized when appropriate.

[5]The potential Φ obeys the Laplace equation in the absence of free charges. For a non-zero charge density ρ, it satisfies the more general, inhomogeneous Poisson equation: $\nabla^2 \Phi(\mathbf{r}) = \rho(\mathbf{r})$.

2.1.2 Electromagnetic Fields in Resonant Cavities

RF cavities are realized by enclosing the electromagnetic fields inside a volume bounded by conducting walls, such that standing or traveling waves are established. On a boundary of infinite conductance ($\sigma \to \infty$), denoted as perfect electric conductor (PEC), the fields are subject to

$$\mathbf{n} \times \mathbf{E} = \mathbf{0} \quad \text{and} \quad \mathbf{n} \cdot \mathbf{H} = 0 \quad \text{on} \quad \partial\mathcal{V}_{\text{PEC}}, \tag{2.20}$$

with $\mathbf{n}$ indicating the boundary normal. Perfect conductors do not exist in reality, however, Eq. (2.20) still holds with negligibly small deviation for boundaries with very high—but finite—conductance. Thus, the surfaces of electric conductors, such as copper and aluminum, are commonly modeled by means of Eq. (2.20). The conditions are interchanged with respect to the field quantities for the perfect magnetic conductor (PMC) boundary, where

$$\mathbf{n} \cdot \mathbf{E} = 0 \quad \text{and} \quad \mathbf{n} \times \mathbf{H} = \mathbf{0} \quad \text{on} \quad \partial\mathcal{V}_{\text{PMC}}. \tag{2.21}$$

PMC boundaries are often used to simplify field calculations by inserting symmetry planes where the field obeys Eq. (2.21).

Imposing Eqs. (2.20), (2.21), or a disjunct combination of both onto Eqs. (2.16) or (2.17) leads to an eigenvalue problem. The electromagnetic fields fulfilling the eigenvalue problem are commonly denoted as the eigenmodes of the cavity, which (for the linear case) are mutually orthogonal. Their corresponding discrete oscillation frequencies are the eigenfrequencies $\omega_n = k_n c$, derived from the eigenvalue k_n^2.

2.1.3 Power Loss and Coupling

Real-world RF resonators are subject to power loss, that steadily reduces the energy W_0 stored in the electromagnetic field. One differentiates between dielectric and magnetic losses, surface losses, external losses, and beam loading.[6] For the low-current RFQs discussed throughout this thesis, only surface and external losses are of practical relevance.

The surface power loss P_0 originating in the ohmic surface resistance is given by

$$P_0 = \iint_{\mathcal{S}} p_s \mathrm{d}\mathcal{S}, \tag{2.22}$$

where

$$p_s = \frac{1}{2}\Re\{Z_s\}\,\mathbf{J}_s \cdot \mathbf{J}_s^\star = \frac{1}{2}\Re\{Z_s\}\,H_t^2 \tag{2.23}$$

[6] In high-current accelerators, the power supplied to the beam becomes relevant in comparison to the other losses, a mechanism that is known as beam loading [1]. While not being an issue for the low-current RFQs developed in this thesis, beam loading has to be considered for high-current RFQs [72–78].

is known as the surface power loss density, proportional to the square of the Ohmic surface current density $\mathbf{J}_s$, or, with $\mathbf{J}_s = \mathbf{n} \times \mathbf{H}$, the tangential magnetic field H_t. The surface impedance[7]

$$Z_s(\omega) = (1 - j)\sqrt{\frac{\omega\mu_0}{2\sigma}} \tag{2.24}$$

increases with the RF frequency. For annealed copper at 750 MHz, the surface impedance amounts to $\Re\{Z_s\} = 7.14\,\mathrm{m\Omega}$.

The power loss of an eigenmode is commonly quantified by the unloaded quality factor

$$Q_0 = \frac{\omega_0 W_0}{P_0}, \tag{2.25}$$

a measure of the energy lost by the electromagnetic field per oscillation period, normalized to the total energy W_0 stored in the electromagnetic field of the eigenmode:

$$W_0 = \frac{\varepsilon_0}{2}\iiint_{\mathcal{V}} \mathbf{E}\cdot\mathbf{E}^\star \mathrm{d}\mathcal{V} = \frac{\mu_0}{2}\iiint_{\mathcal{V}} \mathbf{H}\cdot\mathbf{H}^\star \mathrm{d}\mathcal{V}. \tag{2.26}$$

One or more input power couplers supply the required power to the cavity. In the broadest sense, an antenna couples the cavity to a waveguide, which in turn is connected to an RF generator, that one assumes to be perfectly matched. In analogy to the definition of the unloaded Q_0 [Eq. (2.25)], the external quality factor

$$Q_{ex} = \frac{\omega_0 W_0}{P_{ex}} \tag{2.27}$$

is defined as the quotient of stored energy W_0 and P_{ex}, the power transmitted through the waveguide.[8] Surface and external power loss are combined in the loaded quality factor Q_ℓ. While in the most general cases Q_ℓ comprises all the possible power loss contributions mentioned above, in the context of this thesis

$$\frac{1}{Q_\ell} = \frac{1}{Q_0} + \frac{1}{Q_{ex}}. \tag{2.28}$$

Figure 2.1 shows the equivalent circuit model of an RF resonator with a single input coupler [1, 67]. The cavity is modeled as an RLC circuit, where the shunt resistance R represents the surface losses, $\mathcal{L}$ is the inductance representing the magnetic field in the cavity and C identifies the capacitance associated with the electric field. For the RFQ, the capacitance is determined by the four electrodes form-

[7] The stated formula (2.24) is valid for good conductors, whose surface roughness is significantly smaller than the skin depth $\delta_s = \sqrt{2/(\omega\mu_0\sigma)}$. A surface roughness in the same order of magnitude as δ_s has to be considered with an appropriate impedance model [79]. A high-quality surface finish becomes more crucial with increasing frequency.

[8] More precisely, P_{ex} is the power radiated by the cavity through the waveguide when the RF generator is turned off [1].

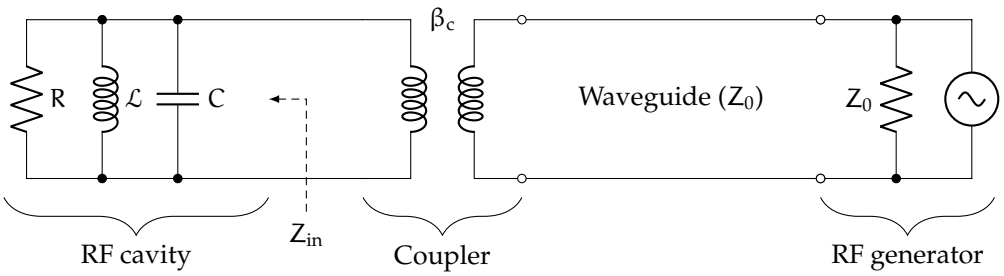

Figure 2.1: Equivalent RLC circuit of an RFQ cavity connected to the matched RF generator via waveguide and power coupler. The coupler is modeled as a transformer with a coupling strength β_c.

ing the quadrupole channel. The coupler is represented by a transformer with a coupling strength β_c, connected to a waveguide with a line impedance[9] Z_0 and an RF generator that is matched to the waveguide.[10] The unloaded quality factor is related to the lumped circuit elements by $Q_0 = \omega_0 RC$, where $\omega_0^2 = 1/(\mathcal{L}C)$. The coupling strength is given as the ratio between the power P_{ex} transmitted through the coupler to the power P_0 lost on the interior cavity walls:

$$\beta_c = \frac{P_{ex}}{P_0} = \frac{Q_0}{Q_{ex}} \tag{2.29}$$

The cases of $\beta_c > 1$, $\beta_c < 1$ and $\beta_c = 1$ are referred to as over-coupled, under-coupled, and critically coupled, respectively.

Considering not only the coupling strength itself, but also an offset $\Delta\omega$ between the natural resonance frequency of the cavity ω_0 and the RF source frequency, the reflection coefficient $\Gamma = S_{11}$ is given by

$$\Gamma = \frac{Z'_{in} - Z_0}{Z'_{in} + Z_0} = \frac{\beta_c - 1 - 2jQ_0\Delta\omega/\omega_0}{\beta_c + 1 + 2jQ_0\Delta\omega/\omega_0}, \tag{2.30}$$

where $Z'_{in} = \beta_c Z_{in}$ is the cavity input impedance

$$Z_{in} = \frac{R}{1 + 2jQ_0\Delta\omega/\omega_0} \tag{2.31}$$

transformed into the generator circuit. The reflection becomes zero only for the case of critical coupling ($\beta_c = 1$) and exact frequency match ($\Delta\omega = 0$). The power loss P_0 in the walls of the cavity is proportional to V_0^2, the squared cavity voltage, which in turn is fixed by beam dynamics requirements. Thus, the required

[9] Typically $Z_0 = 50\,\Omega$ or $75\,\Omega$.

[10] In practise, a circulator is installed between the cavity and the generator. It directs power reflected from the cavity in case of mismatch away from the generator into a matched load.

feeding power P_+ and power reflected back into the waveguide P_- amount to[11]

$$P_+ = \frac{P_0}{1-|\Gamma|^2}, \quad P_- = \frac{P_0}{1/|\Gamma|^2-1}. \tag{2.32}$$

2.1.4 Slater's Perturbation Theorem

The resonant frequency of an RF cavity changes when its geometry is perturbed, for example through the displacement of cavity walls caused by heat-induced deformation, or the introduction of a perturbing object. For adiabatic changes, the change in frequency $\Delta\omega$ is proportional to the change in energy.[12] This fact is quantified by Slater's cavity perturbation theorem [83]:

$$\frac{\Delta\omega}{\omega_0} = \frac{\iiint_{\Delta\mathcal{V}} \left(\mu_0 H^2 - \varepsilon_0 E^2\right) \mathrm{d}\mathcal{V}}{\iiint_{\mathcal{V}} \left(\mu_0 H^2 + \varepsilon_0 E^2\right) \mathrm{d}\mathcal{V}}, \tag{2.33}$$

where $\Delta\mathcal{V}$ denotes the small volume that is removed from the cavity. E and H are the amplitudes of the unperturbed electric and magnetic fields, respectively, at the location of $\Delta\mathcal{V}$. Slater's theorem states that the frequency increases if a volume containing a strong magnetic field is removed from the cavity, and decreases if the volume contains a strong electric field. With $\omega_0^2 = 1/(\mathcal{L}C)$, removing the volume corresponds to lowering the inductance and increasing the capacitance [1].

The perturbation theorem forms the theoretical basis for understanding the effect of thermal deformation on the RFQ. Furthermore, it provides the foundation of the RF field measurements [84], as well as frequency and field adjustments by means of tuners introduced into the RFQ cavity, that are discussed in Chapter 4.

2.1.5 Relativistic Particles in Electromagnetic Fields

Being low-energy accelerators, RFQs typically accelerate beams with velocities in the range of 1 % to 6 % of the speed of light [1]. While the equations of classical mechanics still deliver useful approximations, relativistic effects cannot be neglected for high-precision designs even at these velocities. Consider a particle with a rest mass m_0, carrying a charge q, and traveling at a velocity $\boldsymbol{v}$. With the speed of light c, it is customary to define a normalized velocity

$$\boldsymbol{\beta} = \boldsymbol{v}/c, \tag{2.34}$$

[11] P_- differs from P_{ex} in that it is defined for the case of an active generator, which emits the power P_+ toward the cavity. $P_- = P_{ex}$ if the generator is turned off and the fields inside the cavity are decaying—the case which defines P_{ex} [1].

[12] Also known as as Boltzmann-Ehrenfest theorem, this proportionality holds for any linear oscillator with adiabatically changing parameters [80–82].

and a relativistic mass factor

$$\gamma = 1/\sqrt{1-\beta^2}. \tag{2.35}$$

The relativistic momentum then reads

$$\mathbf{p} = \boldsymbol{\beta}\gamma m_0 c, \tag{2.36}$$

and the kinetic energy amounts to

$$\mathcal{W} = (\gamma - 1) m_0 c^2, \tag{2.37}$$

A charged particle traveling through an electromagnetic field experiences a change of its momentum $\mathbf{p}$ by means of the Lorentz force:

$$\frac{d}{dt}\mathbf{p} = \mathbf{F} = q\left(\mathbf{E} + \boldsymbol{v} \times \mathbf{B}\right). \tag{2.38}$$

Two components contribute to the Lorentz force:[13] a force parallel to the electric field strength $\mathbf{E}$, and a second component perpendicular to both the particle velocity and the magnetic flux density $\mathbf{B}$. In particle accelerators, both components provide steering and focusing capabilities, but only the electric field can be used to change the kinetic energy of the particles, i.e. to accelerate (or decelerate) them. A particle traveling a short distance dz along the z-axis through an axis-parallel electric field E_z experiences a change in kinetic energy amounting to

$$d\mathcal{W} = qE_z dz. \tag{2.39}$$

In order to deliver net energy to the passing particles through a time-harmonic resonant electromagnetic field found in RF cavities, the frequency of the resonance has to be synchronized with the beam.

2.2 Numerical Treatment of Electromagnetic Fields

Analytic solutions to Maxwell's Equations, in particular the arising eigenvalue problem of the Helmholtz equations (2.16), (2.17), as well as the Laplace equation (2.19), are not available for all but the simplest of geometries. In practice, numerical methods such as the finite difference method [85], the boundary element method [85], the finite integration technique [86, 87], or the finite element method (FEM) [85, 88] are employed to compute the electromagnetic fields.

Of these methods, FEM is the most general and most widely used. The sought-after field is approximated by a weighted sum of ansatz functions, which

[13] With the introduction of special relativity it turns out that both forces are aspects of the same phenomenon, viewed from different frames of reference that are moving with respect to each other at constant velocities [68].

are locally defined on a mesh discretizing the computational domain. For example, from the Helmholtz equation (2.16) the eigenvalue problem

$$\left(\mathbf{S} + k^2\mathbf{M}\right)\mathbf{x} = \mathbf{0} \tag{2.40}$$

emerges, where $\mathbf{S}$ and $\mathbf{M}$ are sparse matrices, k^2 is the eigenvalue and $\mathbf{x}$ the eigenvector comprising the weighting coefficients of the electric field ansatz functions. The arising sparse and large-scale systems of equations are solved using dedicated algorithms. Accurate solutions are obtained by adaptive mesh refinement, where the solution is improved locally by refining the mesh based on an error indicator, which is computed from the previous solution. More details can be found in Appendix C and Refs. [69, 85, 88], to name a few.

Throughout this thesis, the RFQ cavities were simulated using FEM made available by commercial computer-aided engineering software, namely Ansys High-Frequency Structure Simulator® (HFSS) [89, 90], CST Microwave Studio® [91], and COMSOL Multiphysics® [92, 93]. The latter was also employed to compute the electric field between the RFQ vanes in quasi-electrostatic approximation. Similarly, the coupled problem describing the thermal expansion of the RFQ cavity was solved using Ansys Mechanical® [94], CST Multiphysics Studio® [91], and COMSOL Multiphysics® [92, 93]. Appendix C presents a selection of the convergence studies conducted for the simulated structures.

The dynamics of charged particles in all but the most simple electromagnetic field distributions are computed by numerically integrating some form of the equations of motion [Eq. (2.38)]. For example, when using the well-known leapfrog scheme (see e.g. Ref. [95]) to relativistically integrate in time, momentum and position are updated iteratively. Codes employed in practice feature sophisticated, higher-order algorithms, and use time or position as the independent variable, depending on the specific application [96, 97]. For the present work, the codes Travel [98] and RF-Track [99] were used to simulate the beam in the RFQ. In both cases, a so-called field map obtained from a 3D quasi-electrostatic or RF simulation tabulated the data of the electric field acting on the particles.

2.3 The Radio-frequency Quadrupole Linac

In this section, the operation principle of the radio-frequency quadrupole accelerator (RFQ) is detailed. After an introduction of the multipole potential function, longitudinal and transverse beam dynamics are briefly reviewed. It follows a discussion of the four-vane RFQ cavity.

The RFQ channel consists of four electrodes arranged parallel to the beam axis, as shown in Fig. 2.2. A time-alternating voltage $\pm V_0/2\cos(\omega t)$ is applied to the electrodes, such that opposite electrodes have equal polarity and adjacent electrodes have opposite polarity, as indicated in Fig. 2.2 by the blue and red colors. Here, V_0 denotes the inter-electrode voltage (sometimes inter-vane voltage

or inter-rod voltage, depending on the RFQ type), the peak potential difference between two adjacent electrodes. Such an arrangement with flat electrodes produces a quadrupole electric field, which provides focusing and defocusing forces in a time-alternating manner, but no acceleration. Kapchinsky and Teplyakov proposed to modify the four electrodes by means of a sinusoidal-like modulation [11]. The modulation profiles of opposite electrodes are mirrored with respect to each other, whereas the profiles of adjacent electrodes are offset by half a period. This produces on-axis potential differences, and thus longitudinal electric field components that provide accelerating forces.

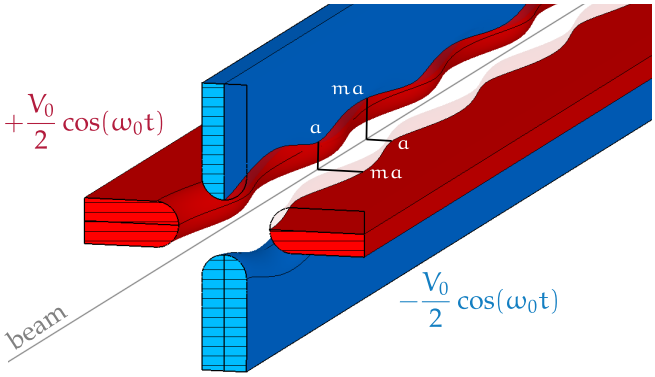

Figure 2.2: Operation principle of the radio-frequency quadrupole linac (RFQ). A time-alternating voltage is applied to four electrodes such that two adjacent electrodes have opposite polarity. In addition to strong transverse electric focusing forces, longitudinal acceleration is achieved by introducing a sinusoidal-like modulation to the electrodes. The closest and farthest distances from the beam axis are denoted as minimum aperture a and maximum aperture $m\,a$, respectively. The modulation profiles of opposite electrodes are mirrored with respect to each other, whereas the profiles of adjacent electrodes are offset by half a period.

To design RFQs and carry out beam dynamics simulations on a fast time scale, the field between the electrodes is commonly described by means of a multipole potential function, where the electric potential is expanded in terms of longitudinal and azimuthal harmonics. It is detailed in the following section.

2.3.1 Multipole Potential Function in an RFQ Cell

The electric field between the four RFQ electrodes, i.e. in the vicinity of the beam, can be described in quasi-static approximation[14] [Eq. (2.18)]. In cylindrical coordinates $\mathbf{r} = (r, \vartheta, z)$, the Laplace equation (2.19) reads

$$\nabla^2 \Phi(r,\vartheta,z) = \left(\frac{\partial^2}{\partial r^2} + \frac{1}{r}\frac{\partial}{\partial r} + \frac{1}{r^2}\frac{\partial^2}{\partial \vartheta^2} + \frac{\partial^2}{\partial z^2} \right) \Phi(r,\vartheta,z) = 0. \tag{2.41}$$

Assume that a potential of $\pm V_0/2$ is applied to the RFQ electrodes in an alternating manner. A possible solution to this boundary value problem is the general

[14] In an RFQ, the electric and magnetic fields are spatially separated, and the magnetic field vanishes in the vicinity of the beam. This becomes clear in Section 2.3.4, Fig. 2.9.

potential function based on multipole expansion, introduced by Kapchinsky and Teplyakov [1, 11] (in a slightly different notation):

$$\frac{\Phi(r,\vartheta,z)}{V_0/2} = \sum_{\nu=0}^{\infty} A_{0,\nu} \left(\frac{r}{r_0}\right)^{2\nu} \cos(2\nu\vartheta) + \sum_{\mu=1}^{\infty}\sum_{\nu=0}^{\infty} A_{\mu,\nu} \mathcal{I}_{2\nu}(\mu k r) \cos(2\nu\vartheta) \cos(\mu k z) \tag{2.42}$$

Here, μ and ν are the longitudinal and azimuthal indices, respectively, and $\mathcal{I}_n()$ denotes the modified Bessel function of the first kind and order n. Furthermore, r_0 is known as the mid-cell aperture, $k = \pi/L$ identifies the spatial wavenumber, and $A_{\mu,\nu}$ are the multipole expansion coefficients. Equation (2.42) comprises both 2D solutions with purely transverse field patterns ($\mu = 0$, first sum), as well as 3D solutions that vary along z (second sum). Because of the transverse quadrupole symmetry and longitudinal antisymmetry of the RFQ cell, the terms in Eq. (2.42) are non-zero only if $\mu + \nu$ is odd.

In order to simplify the general potential function [Eq. (2.42)] with its infinite number of terms, Kapchinsky and Teplyakov neglected all but the two lowest order terms and defined the two-term potential function

$$\frac{\Phi(r,\vartheta,z)}{V_0/2} = \mathcal{X} \left(\frac{r}{a}\right)^2 \cos(2\vartheta) + A_{1,0} \mathcal{I}_0(kr) \cos(kz) \tag{2.43}$$

where

$$\mathcal{X} = \frac{\mathcal{I}_0(ka) + \mathcal{I}_0(kma)}{m^2 \mathcal{I}_0(ka) + \mathcal{I}_0(kma)} \tag{2.44}$$

is the quadrupole focusing efficiency, and

$$A_{1,0} = \frac{m^2 - 1}{m^2 \mathcal{I}_0(ka) + \mathcal{I}_0(kma)} \tag{2.45}$$

identifies the acceleration efficiency. Both are functions of the spatial wavenumber k, the minimum aperture a and the modulation factor m (Fig. 2.2), that can be given in closed form. Note that by these conventions, the quadrupole terms are related by $A_{0,1} = (r_0/a)^2 \mathcal{X}$.

Figure 2.3 visualizes the electric field described by the two-term potential function in one cell. The top figures depict the transverse fields at the beginning, center, and end of the cell. The bottom figure shows the longitudinal and radial fields in both the horizontal (upper half) and vertical plane (lower half). Generally, the transverse electric field acting on the beam is much higher than its longitudinal component, explaining the strong focusing but limited acceleration capabilities of the RFQ.

The electrode geometry is obtained by means of Eq. (2.43) as the $\Phi = \pm V_0/2$ equipotential surfaces. Corresponding to the quadrupole field pattern, the transverse profile describes a hyperbola [Figs. 2.3, 2.4(a)]. In practice, the electrodes

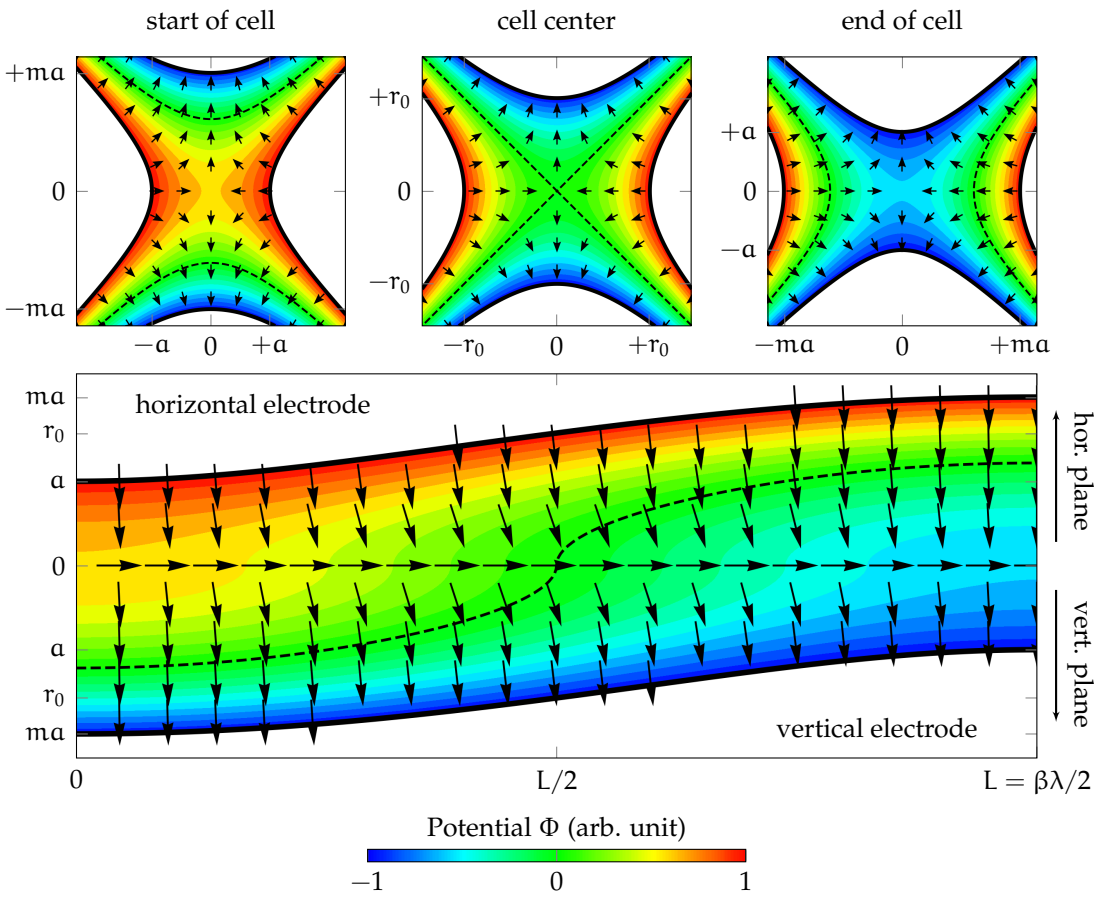

Figure 2.3: Visualization of the two-term potential function in an RFQ cell, and the corresponding shape of the electrodes (white). The top diagrams show the transverse fields at the beginning, center, and end of the cell. The bottom diagram shows the fields in the horizontal and vertical plane. Black dashed lines highlight the $\Phi = 0$ equipotential surfaces.

are modified to deviate from the hyperbolic shape in order to control the maximum surface electric field and to simplify the machining process [1]. Typically, transverse-circular electrodes with constant or varying radius of curvature ρ_t are used, while the electrode tip still follows the ideal longitudinal trajectory. Figure 2.4 shows a selection of different transverse electrode profiles. It becomes clear that the modifications of the hyperbolic shape significantly reduce the maximum surface electric field. The longitudinal profile may be altered for the same reasons, as well as to increase the acceleration efficiency. Next to the standard profile given by the two-term potential function, typical longitudinal shapes include sinusoidal and—in terms of acceleration highly efficient—trapezoidal profiles. Figure 2.5 shows a standard cell and a trapezoidal cell with identical transverse profile.

The deviation from the ideal electrode shape introduces higher-order multipole terms in Eq. (2.42), that have to be considered for the purpose of beam dynamics simulations. Commonly, the eight-term potential function [1, 100] is

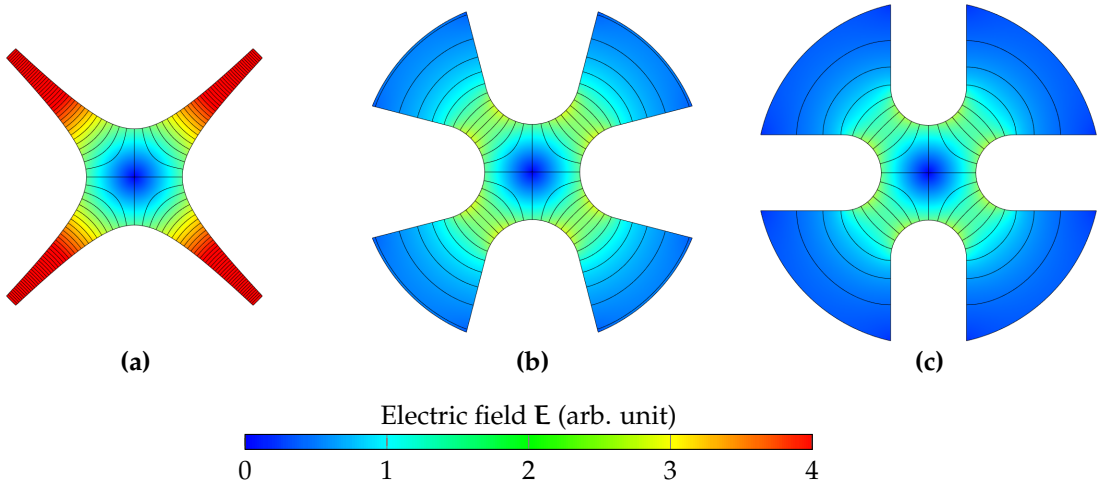

Figure 2.4: Selection of different transverse electrode shapes and their electric fields **E**: Ideal hyperbolic electrodes with perfect quadrupole field pattern but unacceptably high electric field strength (a), wedge-shaped electrodes with circular tip of radius $\rho_t = r_0$ (b), and semi-circular electrodes with $\rho_t = 0.8r_0$ and straight support vanes (c). The deviation from the ideal geometry gives rise to higher-order multipole components in the field.

used:

$$\begin{aligned}\frac{\Phi(r,\vartheta,z)}{V_0/2} = {} & A_{0,1}\left(\frac{r}{r_0}\right)^2\cos(2\vartheta) + A_{0,3}\left(\frac{r}{r_0}\right)^6\cos(6\vartheta) \\ & + A_{1,0}\mathcal{I}_0(kr)\cos(kz) + A_{3,0}\mathcal{I}_0(3kr)\cos(3kz) \\ & + [A_{1,2}\mathcal{I}_4(kr)\cos(kz) + A_{3,2}\mathcal{I}_4(3kr)\cos(3kz)]\cos(4\vartheta) \\ & + [A_{2,1}\mathcal{I}_2(2kr)\cos(2\vartheta) + A_{2,3}\mathcal{I}_6(2kr)\cos(6\vartheta)]\cos(2kz).\end{aligned} \tag{2.46}$$

The coefficients $A_{\mu,\nu}$ are functions of the geometric cell parameters, notably k, m, r_0, a, ρ_t—and others depending on the specific geometry—all of which may vary along the RFQ according to beam dynamics requirements. Generally, the functions cannot be written in closed form. Instead, the coefficients are precomputed over a range of viable cell geometries, and stored in lookup tables [100]. With the parameters given for each cell, slowly (adiabatically) varying along the RFQ, beam dynamics simulations can be carried out and field maps can be produced by means of interpolation. This approach is primarily used by PARMTEQ [1, 100–102], the most commonly used RFQ design code, but also adopted by other codes [103–106].

Mesh-based methods, see e.g. Refs. [105, 107–112], allow for a more accurate representation of the actual electrode geometry compared the potential function. With the ever-increasing availability of computational power, on-the-fly numerical computation of the electric fields during RFQ design becomes more common. This is especially useful for the more recently introduced trapezoidal electrode geometry, where the eight-term potential [Eq. (2.46)] is no longer sufficient. Several RFQs with trapezoidal electrodes have been designed by means of 3D sim-

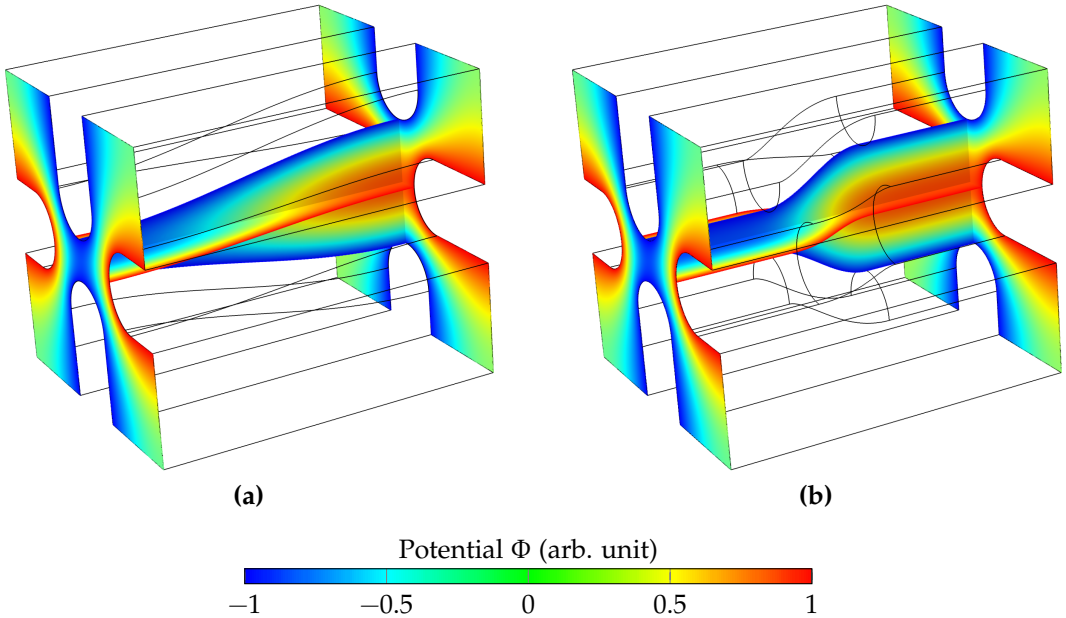

Figure 2.5: RFQ cells with different longitudinal electrode profiles and their electric potentials Φ: standard electrodes whose tips follow the two-term potential function (a), and trapezoidal electrodes with higher acceleration efficiency (b).

ulations [110, 112–117]. However, the potential function remains a useful tool, speeding up the RFQ design process by orders of magnitude. In fact, one of the contributions of this thesis is the expansion of the potential function to describe the electric fields in RFQs with trapezoidal electrode shapes.

2.3.2 Longitudinal Beam Dynamics

The following two sections provide a brief introduction to the beam dynamics of the RFQ linac. For more exhaustive explanations, the reader is referred to the relevant literature, e.g. Refs. [1, 10, 118], to name a few.

The RFQ longitudinal beam dynamics are the same as in other RF linear ion accelerators. Consider a particle that travels with constant[15] velocity β [Eq. (2.34)] through an RFQ cell at a constant radial position r. The particle arrives at the cell center when the electric field has the phase $\phi = \phi_s$. If the cell length is chosen as

$$L = \beta\lambda/2, \tag{2.47}$$

[15] In reality, the velocity of the particle changes as it is accelerated upon passing through the electric field. However, the constant-velocity approximation is accurate enough in most cases, as the increase in velocity within one cell is small. The approximation is widely used in accelerator design, as it linearizes the governing equations [1]. Similarly, the radial position is only approximately constant as well.

the particle will arrive with the same phase at the center of the next cell, and is denoted as synchronous particle. Eq. (2.47) is the synchronism condition and the phase ϕ_s of the synchronous particle is known as the synchronous phase [1, 10].

Since the potential function [Eq. (2.43)] gives a electro-quasistatic description of the RF electric field [see Eq. (2.18)], the longitudinal electric field seen by the synchronous particle is obtained as

$$E_{acc}(z) = E_z(z)\cos(\omega t + \phi_s) = \left(-\frac{\partial}{\partial z}\Phi\right)\cos\left(2\pi\frac{z}{\beta\lambda} + \phi_s\right). \tag{2.48}$$

With Eq. (2.39), the corresponding energy gain amounts to[16]

$$\Delta W = q\int_0^L E_{acc}(z)dz = \frac{\pi}{4}qV_0A_{1,0}J_0(kr)\cos\phi_s = qE_0T_{tr}LJ_0(kr)\cos\phi_s. \tag{2.49}$$

Equation (2.49) is brought into standard linac terminology of a linear accelerating channel by identifying the effective longitudinal electric field E_0T_{tr} [1, 119]:

$$E_0T_{tr} = \frac{V_0}{L}\frac{\pi}{4}A_{1,0}, \tag{2.50}$$

where

$$E_0 = \langle E_z\rangle = \frac{1}{L}\int_0^L E_z(z)dz \tag{2.51}$$

is the average longitudinal electric field and

$$T_{tr} = \frac{1}{E_0L}\int_0^L E_z(z)\sin(kz)dz \tag{2.52}$$

is the transit-time factor. In an ideal RFQ cell following the two-term potential function, $T_{tr} = \pi/4$.

With the convention that $\phi = 0$ is the phase when the electric field reaches its peak value, the longitudinal bunching and acceleration is stable if ϕ_s is negative, i.e. the synchronous particle arrives on the rising slope of the electric field (Fig. 2.6). Faster particles arrive earlier (smaller phase) and receive less energy, while later particles (larger phase) experience a higher energy and catch up, such that a harmonic motion is established around the synchronous particle, known as the synchrotron motion. The ensemble of the oscillating particles in one RF period

[16] Although Eq. (2.49) is derived from the two-term potential function [Eq. (2.43)], it equally holds for the general potential function [Eq. (2.42)] with an arbitrary number of coefficients. Because of the mutual orthogonality of the cosine functions, only the term multiplying $A_{1,0}$ is nonzero.

constitutes a bunch. In a typical RFQ, the synchronous phase starts at $\phi_s = -90°$ and slowly increases to its final value of $-30°$ to $-15°$. This is known as adiabatic bunching and ensures that an as large as possible fraction (up to $\approx 100\,\%$) of the beam is captured. However, one may chose values deviating from this recipe, for example to sacrifice transmission in favor of a more compact design—as is the case for the two RFQs discussed in this thesis.

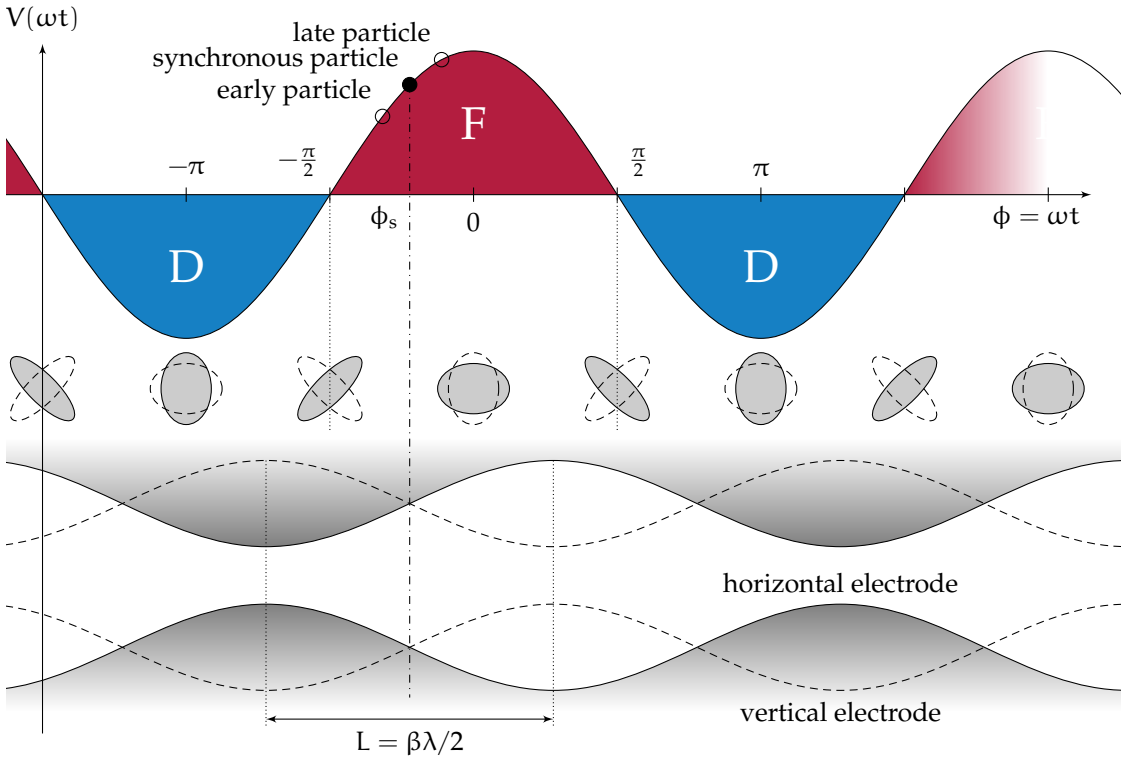

Figure 2.6: Time and space periodicity of the RFQ linac. The longitudinal dynamics correspond to those of other RF hadron linacs and are machined into the electrode geometry. The transverse focusing lattice is periodic in time, with a focusing period of the corresponding length of two cells. The figure sketches the shapes of the horizontal (solid) and vertical (dashed) beam ellipses upon passing through this focusing lattice.

2.3.3 Transverse Beam Dynamics

To adequately describe the RFQ transverse beam dynamics, the beam description by means of rms ellipses is briefly reviewed. Each particle is described by six parameters: its position along the three spatial coordinates as well as the derivatives of these positions with respect to time or space. Each of the six coordinates occur in different variants depending on the formulation [1, 10]. For example, the longitudinal motion can be described in terms of velocity, momentum, or kinetic energy. Throughout this thesis, the author uses the $(x, y, x', y', \Delta\phi, \Delta W)$ convention to describe the phase space at a specific position z along the beam axis.

Here, x and y denote the horizontal and vertical positions, and $x' = p_x/p_z$ and $y' = p_y/p_z$ the angles of the particle trajectories with respect to the beam axis, defined in terms of momenta [Eq. (2.36)]. Furthermore, $\Delta\phi = \omega\Delta t$ is the phase difference, and ΔW the kinetic energy difference with respect to the synchronous particle.

In accelerator physics it is customary to describe the combined motion of the particles in the beam by means of a projected beam ellipse. The projection onto a specific plane greatly simplifies the analysis and visualizes correlations between two of these parameters. Figure 2.7 shows the rms ellipse of the horizontal plane, here for a diverging beam. The ellipse is described by the Courant-Snyder or Twiss parameters $\tilde{\alpha}$, $\tilde{\beta}$, and $\tilde{\gamma}$, that generally depend on time or position along the beam axis. The Twiss parameters of the beam can be defined by means of its rms parameters. For instance, in the horizontal (x, x')-plane, the rms values are given by

$$\begin{aligned} \sigma_x^2 &= \Big\langle \big(x - \langle x\rangle\big)^2 \Big\rangle, \qquad \sigma_{x'}^2 = \Big\langle \big(x' - \langle x'\rangle\big)^2 \Big\rangle, \\ \sigma_{xx'}^2 &= \Big\langle \big(x - \langle x\rangle\big)\big(x' - \langle x'\rangle\big) \Big\rangle. \end{aligned} \tag{2.53}$$

The Twiss parameters are found by identifying

$$\sigma_x^2 = \tilde{\beta}\tilde{\varepsilon}, \quad \sigma_{x'}^2 = \tilde{\gamma}\tilde{\varepsilon}, \quad \text{and} \quad \sigma_{xx'}^2 = -\tilde{\alpha}\tilde{\varepsilon}, \tag{2.54}$$

where $\tilde{\beta}\tilde{\gamma} - \tilde{\alpha} = 1$. The geometric rms emittance $\tilde{\varepsilon} = \sqrt{\sigma_x^2\sigma_{x'}^2 - \sigma_{xx'}^4}$ connects Twiss parameters with physical beam sizes. One differentiates between the geometric emittance $\tilde{\varepsilon}_{xx'}$, proportional to the area occupied by the ellipse, and the normalized emittance $\varepsilon_{xx'} = \beta\gamma\tilde{\varepsilon}_{xx'}$.[17] The normalized emittance is invariant with respect to the acceleration, and a more convenient measure of beam quality in an accelerator [1]. Contrarily, the unnormalized emittance, defined in terms of the transverse momentum deviation $x' = p_x/p_z$, reduces during acceleration, because the forward momentum p_z increases while the transverse momentum remains unaffected.

The transverse focusing characteristics of the RFQ follow the alternating gradient-focusing principle used in most modern accelerators. The main difference is that the polarity of the focusing system does not vary in space—as is the case for linacs with magnetic quadrupole lattices—but instead varies in time. The instantaneous focusing strength seen by an off-axis particle oscillates harmonically with the RF frequency, as shown in Fig. 2.6 (upper row). Its amplitude depends linearly on the inter-electrode voltage and by an inverse-square law on the cell aperture. It is customary to define an effective transverse focusing

[17] Here, β and γ are the relativistic velocity and mass, respectively, which should not be confused with the Twiss parameters $\tilde{\beta}$ and $\tilde{\gamma}$.

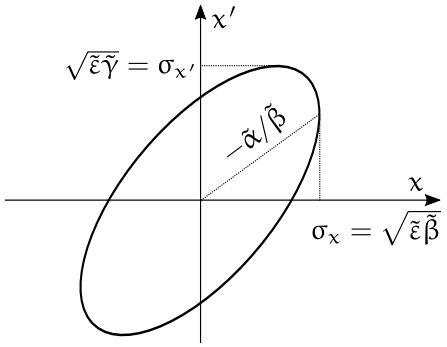

Figure 2.7: Sketch of the rms beam ellipse and its parameters, exemplary for the horizontal (x, x')-plane. Corresponding to the physical width of the beam, the maximum projection onto the x-axis is a critical parameter. Graphic adapted from Ref. [1].

strength [120]

$$\mathcal{B} = \frac{q}{m_0 c^2}\lambda^2\frac{\mathcal{X}V_0}{a^2} = \frac{q}{m_0 c^2}\lambda^2\frac{A_{0,1}V_0}{r_0^2}, \tag{2.55}$$

that takes the charge-to-mass ratio $q/(m_0c^2)$ of the accelerated particles into account. The trajectories σ_x, σ_y described by the transverse ellipses obey the Mathieu equation [121], taking the form of a slow oscillation superimposed by a flutter.

The slow oscillation of the smoothed motion depends on the averaged focusing parameters that are determined by the electrode geometry and slowly—ideally adiabatically—change along the RFQ. The associated transverse phase advance per focusing period σ_0 describes the movement of individual off-axis particles along their transverse phase-space ellipses. It is determined by the effective quadrupole focusing force and the RF-defocusing impulse of the accelerating field. For the RFQ, the (zero-current) transverse phase advance per focusing period is calculated as

$$\sigma_0^2 = \frac{\mathcal{B}^2}{8\pi^2} + \frac{\pi^2 q A_{1,0} V_0 \sin\phi_s}{2m_0 c^2 \beta^2}, \tag{2.56}$$

where $\mathcal{B}$ denotes the effective quadrupole focusing force [Eq. (2.55)]. Stable transverse motion requires that $\sigma_0^2 > 0$, i.e. that the quadrupole focusing force is stronger than the RF defocusing (and potentially space-charge forces). The quantity $\sigma_0/(2L)$ is the effective wavenumber of the slow transverse amplitude oscillation, sometimes called betatron oscillation [1].

The flutter frequency equals ω and corresponds to the alternating-gradient focusing in time. Because of the synchronism between electrode modulation and RF frequency ($L = \beta\lambda/2$), the beam is focused and defocused every two cells. Figure 2.6 (middle row) depicts the general shape of the horizontal (solid) and vertical (dashed) ellipses. The ellipses are upright ($\tilde{\alpha} = 0$) at $\phi = 0$ with maximum horizontal and minimum vertical projection, and at $\phi = \pi$ with the projections interchanged. At $\phi = \pm\pi/2$, when the electric field is zero, the ellipses are tilted, as the beam is now fully focused or defocused. The strong, velocity-independent

focusing force provided by the electric field and the short focusing period makes the RFQ the accelerator of choice for low-energy protons and ions, allowing for adiabatic bunching and high beam currents [1].

2.3.4 Four-vane RFQ Cavity Eigenmodes

The RFQ electrodes are charged periodically to $\pm V_0/2$ to produce the quadrupole field pattern shown in Figs. 2.3 and 2.9(a). The range of the oscillation frequency—tens to hundreds of megahertz—requires the electrodes to be placed in an RF cavity. Since the invention of the RFQ, various cavity types have been developed and evaluated, however, only a few types survived [1, 122, 123]. The four-vane cavity covers the high-frequency range (protons and light ions), and is the type used by the 750 MHz RFQs discussed in this thesis. Low-frequency applications (heavy ions) are dominated by the four-rod RFQ [124]. Several special structures are occasionally used, such as the ladder RFQ [125–128], the four-vane cavity with windows [129, 130], the CH-RFQ [131], or the IH-RFQ [132].

Photographs of a four-vane cavity are shown in Fig. 2.8. The electrode geometry is machined into the tip of four vanes that are placed dividing the tank into four chambers in a cloverleaf-like manner. Thus, the RFQ electrodes are referred to as vanes in the further course of this thesis. Examples of RFQs realizing the four-vane cavity are found in e.g. Refs. [34–36, 39, 72, 74, 78, 133–144], to name only a few. Recently, the HF-RFQ for medical applications has been designed, constructed and commissioned at CERN in cooperation with AVO-ADAM [18, 27, 40, 41, 43, 63], and represents the operational RFQ linac with the highest frequency to date, resonating at 750 MHz. This machine serves as the basis for the PIXE-RFQ [27, 29–31] and the Carbon-RFQ, operating at the same frequency, that are discussed in this thesis.

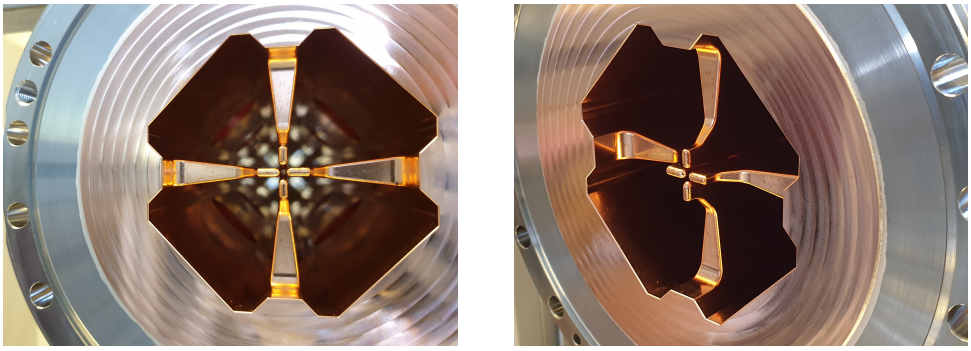

(a) **(b)**

Figure 2.8: Photographs of four-vane cavity of the PIXE-RFQ, with in a frontal view of the cross section (a) and the specially tuned (downstream) end geometry (b). Operating at 750 MHz, the width of each chamber reads approximately 4.5 cm.

In the four-vane cavity, one distinguishes two types of eigenmodes by their transverse field pattern: quadrupole modes [Figs. 2.9(a), (d)] and dipole modes

in two polarizations[18] [Figs. 2.9(b), (e) and (c), (f)], each of them occurring in an infinite number with increasing number of longitudinal field oscillations (Fig. 2.11). Quadrupole modes are also denoted as TE_{21n} modes, while dipole modes are referred to as TE_{11n}. These designations are derived from the eigenmodes of the cylindrical cavity [69], where TE indicates that the field patterns are transverse-electric. The first and second subscript identify the number of azimuthal and radial periods, respectively, whereas the last subscript n denotes the number of longitudinal half-wavelengths.

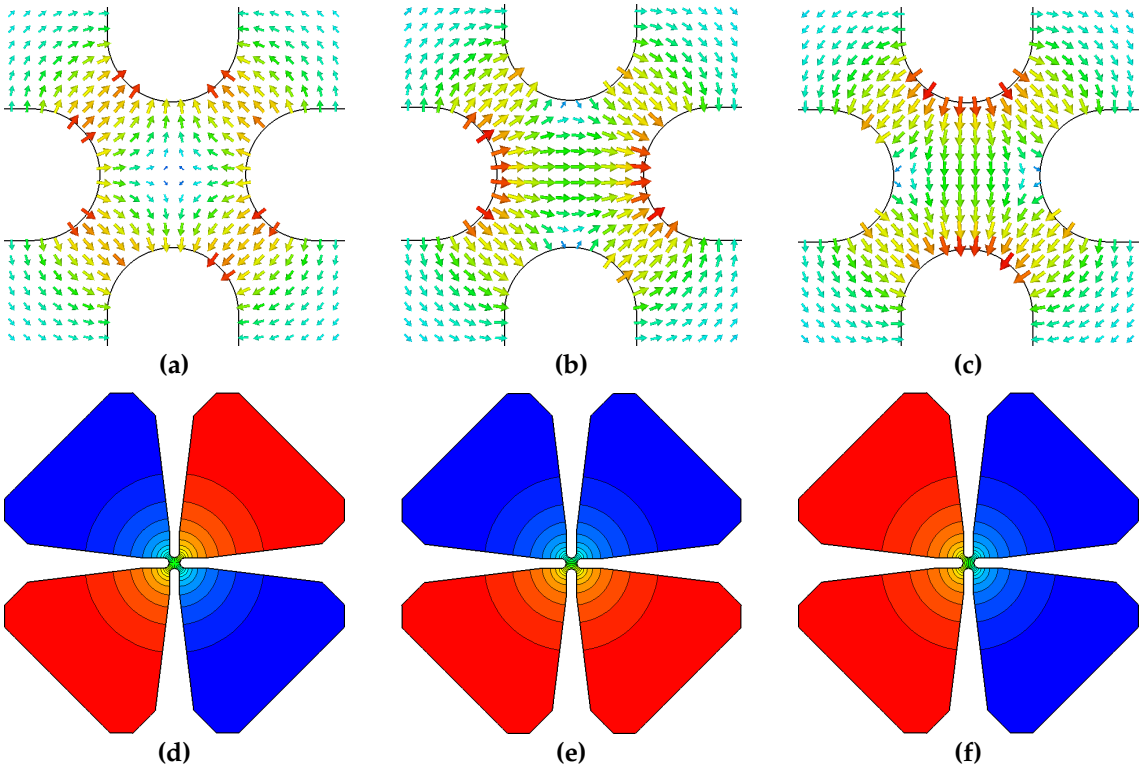

Figure 2.9: Transverse field patterns of the quadrupole (TE_{21n}) and dipole modes (TE_{11n}) of the four-vane RFQ (left to right), the latter are shown in both polarizations. The electric fields at the vane tips are shown in (a)–(c), while the corresponding magnetic fields in the RFQ cavity are depicted in (d)–(f).

The operating mode of the RFQ is the TE_{210} quadrupole mode. Because a TE_{210} field distribution cannot exist in a cylindrical cavity with short-circuited, PEC-like metallic terminations [1], special end geometries [Fig. 2.8(b)] are designed. Tuned to the desired operating frequency, they emulate an open-circuit, PMC-like boundary condition, allowing the magnetic fields to flow between the four quadrants.

[18] In a perfectly symmetric RFQ, the resonant frequencies of the two dipole polarizations are identical, and they can be decomposed into two arbitrary orthogonal field patterns, i.e. the modes are degenerated. Commonly, a vertical and horizontal mode, or two diagonal modes are defined [1]. In a real RFQ, the polarizations separate because of the asymmetry introduced by the vane modulation and geometric imperfections.

2.3.5 Four-vane Cavity Transmission Line Model

Because of the spatial separation of electric and magnetic fields of the four-vane RFQ, the cavity can be described as a transmission line [1, 36, 145–148]. Such a lumped circuit model is shown in Fig. 2.10.

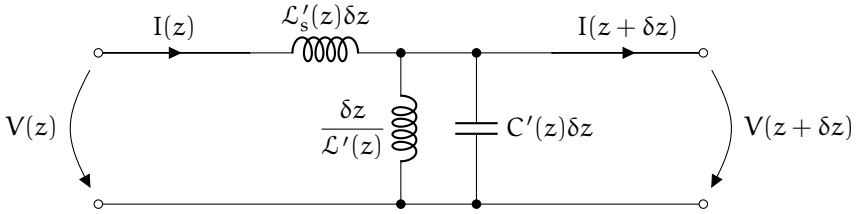

Figure 2.10: Two-wire transmission line model of a homogeneous slice with length δz of the four-vane RFQ. With the lumped circuit elements adjusted accordingly, this model is valid for both quadrupole and dipole modes.

The shunt capacitance C' (in units of F/m) models the capacitive load given by the electric field between the vane tips. With the shunt inductance $\mathcal{L}'$ (in units of H m) of the cavity it forms resonant circuits that are tuned to the frequency of the operating quadrupole mode. The series inductance $\mathcal{L}'_s$ (in units of H/m) is associated with transverse magnetic fields, i.e. longitudinal current flow along the vane tips. In a perfectly tuned constant-voltage RFQ, these currents are zero. While the capacitance is generally given by the electrode geometry from beam dynamics design, the shunt inductance $\mathcal{L}'$ representing the magnetic field in the cavity volume is chosen such that the operating mode (TE_{210}) resonates at the desired frequency:

$$\omega_0 = \frac{1}{\sqrt{\mathcal{L}'C'}}. \tag{2.57}$$

This frequency is also the quadrupole cutoff frequency of the transmission line. The shunt inductance $\mathcal{L}'$ has the same value for quadrupole and dipole modes. However, dipole modes not only see the capacitance between adjacent vanes, but also an additional capacitive load between opposite vanes. Thus, the dipole cut-off frequency is always lower than the quadrupole cutoff frequency. To represent the known dispersion curve, the value of the series inductance $\mathcal{L}'_s$ is identified by $c^2 = 1/(\mathcal{L}'_s C')$ for each type of modes [1, 147].

Figure 2.10 shows that the equivalent circuit of a homogeneous symmetric RFQ slice is that of a dispersive transmission line. In each of these slices the lumped quantities are assumed to be constant. By concatenating many such slices, one obtains a transmission line model for the entire RFQ, which can be inhomogeneous with z-dependent circuit elements. The relation between voltage and current on the line are given by the well-known telegraph equations [67], which can be transferred to the dispersive wave equation

$$\frac{\partial^2}{\partial z^2} V(z) + \left[(\omega/c)^2 - k_{co}^2(z)\right] V(z) = 0 \tag{2.58}$$

where

$$k_{co}^2(z) = \frac{\omega_{co}^2(z)}{c^2} = \frac{1}{c^2 \mathcal{L}'(z) C'(z)} \tag{2.59}$$

is the cutoff wavenumber of the respective mode, with $\omega_{co}^2(z)$ identifying the cutoff frequency. Only if the vane modulation is neglected and a constant cross section is assumed along the RFQ, $k_{co} = \text{const}$. Then the solutions to Eq. (2.58) for an RFQ of length L_{RFQ}, that fulfill the open-circuit boundary conditions $[I(0) = I(L_{RFQ}) = 0]$, are given by

$$V_n(z) = V_0 \cos k_n z. \tag{2.60}$$

With $k_n = n\pi/L_{RFQ}$, $\omega_n = c\sqrt{k_n^2 + k_{co}^2}$, and n denoting the number of longitudinal half-wavelengths, the eigenfrequencies of the four-vane cavity lie on a hyperbolic curve that is characteristic of any longitudinally uniform resonator.

Figure 2.11 shows the spectrum of an idealized four-vane cavity. Because of the dipole cutoff frequency being lower than that of the operating quadrupole mode, the possibility of degeneracy between the operating mode and higher-order dipole modes exists. The risk grows with the square of the RFQ length as the mode spectrum becomes more dense, imposing a practical limit to the length of the RFQ [149, 150]. Small spectral margins increase the sensitivity of the RFQ to construction errors, leading to field-tilt effects [1, 151]. This problem is typically addressed by locally adjusting the cavity volume—and thus its inductance—after construction, for instance by means of movable slug tuners. The spectral margin can be addressed by adding additional reactive loads to all or a certain group of eigenmodes. Proposed or implemented techniques for dipole-mode detuning include vane coupling rings, stabilizing loops, dipole stabilization rods, coupling of adjacent cavity chambers, coupling of individual RFQ cavities, asymmetric cavities, or bent vanes [1, 18, 123, 129, 147, 152–155]. Furthermore, long RFQs are commonly divided into multiple shorter and thus easier to tune RF cavities [1, 119, 150, 156].

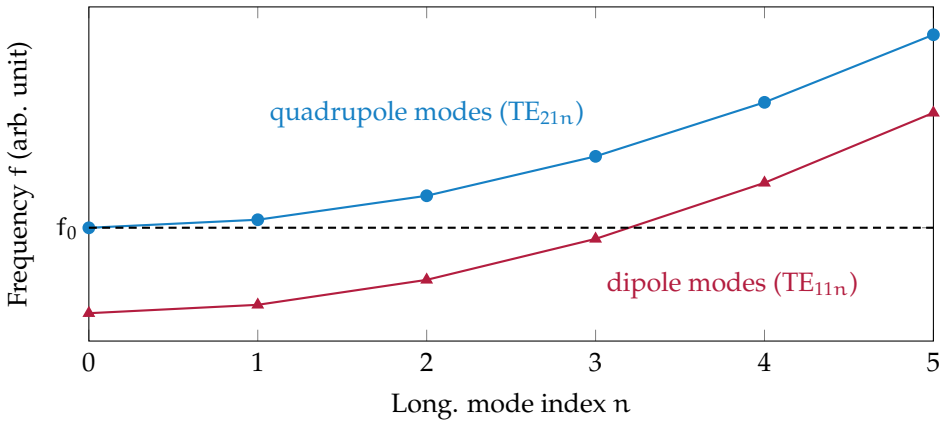

Figure 2.11: Characteristic eigenmode spectrum of an idealized four-vane RFQ. Both quadrupole and dipole modes lie on a hyperbolic curve. The spectrum becomes more dense with increasing RFQ length, posing a risk of mode degeneracy.

2.4 Field Limitations in RFQs

A major performance limit for any linac is the peak amplitude of the surface electric field E_s [1]. At sufficiently high field levels, normal-conducting copper cavities suffer sparking and RF breakdown. The detailed breakdown phenomenon is not well understood, involving mechanisms from different areas of physics, such as electromagnetism, material science, surface and plasma physics [157]. In the following, experimental data on field levels achieved in RFQs are reviewed, and the applicability of different field-limiting quantities is discussed.

2.4.1 Surface Electric Field and Kilpatrick Criterion

In the 1950s, Kilpatrick analyzed experimental data on RF breakdown in normal-conducting cavities [158], and expressed the findings in a convenient formula. As reformulated in Ref. [159], the condition for breakdown-free operation reads

$$f = 1.64\,\mathrm{MHz}\left(\frac{E_K}{\mathrm{MV/m}}\right)^2 \exp\left(-\frac{8.5\,\mathrm{MV/m}}{E_K}\right), \tag{2.61}$$

where f is the frequency and E_K is known as the Kilpatrick limit.[19] This relationship is visualized in Fig. 2.12. Already in the original paper, Kilpatrick pointed out that higher field levels may be achieved through proper surface treatment. Because of improvements in vacuum technology that no longer involves organic compounds, the Kilpatrick criterion is considered conservative by today's standards. Nevertheless, most modern accelerator designs still make use of Eq. (2.61),

[19] Equation (2.61) must be solved iteratively to obtain the Kilpatrick limit E_K for a given frequency f. An estimate is obtained using the approximate formula $E_K = 1.8\,\mathrm{MV/m} \cdot (f/\mathrm{MHz})^{0.4}$ given in Ref. [145].

however, the maximum surface electric field $E_{s,max}$ is commonly chosen in the range of 1.0 to 2.0 E_K, i.e. as the Kilpatrick limit E_K multiplied by a so-called "bravery factor" [1]. This includes the majority of RFQs operated worldwide (Fig. 2.12).

Recent research discovered that the breakdown rate is not only affected by the maximum surface electric field and the frequency, but also by the RF pulse length t_{pls}, the duty cycle d, and the pulse repetition rate f_{rep} [1, 157, 160], where $d = t_{pls} f_{rep}$. For instance, while in continuous-wave (CW) RFQs ($d \approx 100\,\%$) the electric field should generally not exceed 1.8 Kilpatrick, values significantly higher than 2.0 Kilpatrick are well achievable in accelerators with RF pulse lengths of about 1 ms or less. The scaling

$$E_{s,max} \cdot t_{pls}^{1/4} \cdot f_0^{-1/2} = \text{const.} \tag{2.62}$$

was observed in Ref. [160] for high-gradient accelerating structures limited both by high-voltage breakdown and dark current. Through experiments with high-gradient structures operating in the X-band and at 30 GHz, it was found that

$$E_{s,max} \cdot t_{pls}^{1/6} = \text{const.} \tag{2.63}$$

for a given breakdown rate and sufficiently short pulses [157, 161]. For these structures, a surface field of approximately 2.8 Kilpatrick was calculated.

2.4.2 Review of Experimental Data

In the following, the quantities introduced in Section 2.4.1 are investigated with respect to experimental data. In Table 2.1, data on maximum surface electric fields $E_{s,max}$ and RF pulse lengths t_{pls} have been collected for a selection of commissioned ($\star$) or recently designed RFQs. In the former case—in particular for the CW RFQs—the highest electric fields achieved during high-power test and the corresponding pulse lengths are given, even if they do not correspond to the design values.

Of particular importance is the HF-RFQ for proton therapy [18, 27, 40–43], which to date is the only RFQ commissioned at a frequency of 750 MHz or greater. Maximum surface electric field—and two other quantities discussed in Section 2.4.3—of the HF-RFQ were studied to obtain reference values for the designs of PIXE-RFQ and Carbon-RFQ. The two RFQs discussed in this thesis operate at the same frequency and with comparably short pulse lengths. Figure 2.14(a) shows the surface electric field E_s of the HF-RFQ on the vane tip and at the inter-module gap for the nominal inter-vane voltage of 67.6 kV/m. The electric field on the vane tip matches the design value of 50 MV/m or less along the entirety of the RFQ. This corresponds to 1.98 Kilpatrick, since for $f = 750$ MHz, $E_K = 25.3$ MV/m. During commissioning, 1.5 % higher fields were achieved [43]. The value of roughly 2 Kilpatrick falls well in line with the field levels that were achieved in other RFQs, albeit at half the RF frequency [Figs. 2.12, 2.13(b)]. The

maximum field concentrated at the inter-module gap exceeds the overall value on the vane tip by roughly 10 % because of the small edge rounding radius, a consequence of the mechanical design rather than the beam dynamics design. Nevertheless, the author does not include the gap field in the above comparison, since, with the exception of the SPIRAL2-RFQ [142], gap fields have not been published for other RFQs.

Table 2.1: Selection of RFQs and their achieved maximum surface electric fields $E_{s,max}$ and pulse lengths t_{pls}. Where experimental data is available ($\star$), the highest achieved fields and corresponding pulse lengths are given.

RFQ	exp.	f_0 (MHz)	t_{pls} (µs)	$E_{s,max}$ (MV/m)	Kilp.
UNILAC HSI [162]	$\star$	36	200	31.3	3.89
ITEP TWAC [114]		81		25.0	2.37
SPIRAL2 [142]	$\star$	88	250	18.8	1.74
Linac3 [126, 163]	$\star$	101	400	23.9	2.10
IMP CW [164]	$\star$	163	100	17.7	1.29
PKU CW [64]		163		20.4	1.50
IFMIF [165, 166]	$\star$	175	20	25.9	1.85
J-PARC RFQ II [136]	$\star$	324	25	33.8	1.89
J-PARC RFQ III [137, 138]	$\star$	324	600	33.8	1.89
J-PARC epRFQ [143]	$\star$	324	50	31.2	1.75
Ladder-RFQ (unmod.) [128]	$\star$	325	200	53.5	3.00
RRCAT ISNS [167]		325	2000	34	1.90
XiPAF [168]		325	40	32	1.79
LEDA [72, 135]	$\star$	350	500	37.6	2.04
BARC [169]	$\star$	350	1000	32.9	1.79
Linac4 [34, 39]	$\star$	352	250	36.7	1.99
TRASCO [74]	$\star$	352	400	39.8	2.18
IPHI [139, 141]	$\star$	352	400	37.2	2.02
SNS [78]	$\star$	403	1000	36	1.85
RANS-III [144]		500		31.5	1.35
HF [40, 43]	$\star$	750	20	50.7	2.00
PIXE [30, this thesis]		750	125	36.5	1.44
CERN Carbon [this thesis]		750	5	50.5	2.00

Figure 2.12 visualizes achieved $E_{s,max}$, frequency f_0, and the corresponding Kilpatrick values of the reviewed RFQs. In the plot, the line marked as 1.0 Kilpatrick corresponds to the original criterion [Eq. (2.61)]. The data highlight that by choosing the maximum field between 1 and 2 Kilpatrick (slightly less for CW mode), RFQs that are safe with respect to RF breakdown can be designed. Nevertheless, a few experiments, e.g. Refs [72, 74, 126, 128], indicate that significantly higher values are possible in short-pulsed operation. A missing pulse length dependence is thus a considerable drawback of the Kilpatrick criterion.

In an effort to find a possible correlation with the pulse length, the proportionalities observed in high-gradient accelerating structures [Eqs. (2.62) and (2.63)] are graphed in Fig. 2.13 next to the raw maximum surface electric field and the commonly used Kilpatrick criterion. The plot restricts itself to RFQs for which

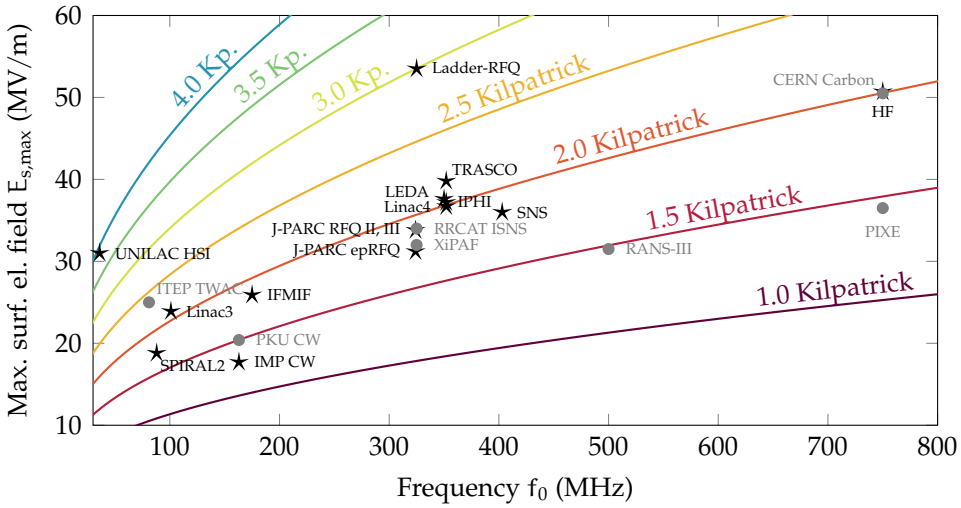

Figure 2.12: Selection of RFQs and the maximum achieved surface electric fields $E_{s,max}$ at their operating frequency f_0. A differentiation is made between design values (•) and values achieved during commissioning (⋆). The curves indicate multiples of the Kilpatrick limit [158] as functions of the RF frequency, following Eq. (2.61).

experimental data were available (⋆ in Table 2.1). An ideal quantity suitable to describe the field limit would assume approximately the same value for all RFQs—given that the experimental data were acquired at comparable points of operation with similarly or equally low breakdown rates. Aside from the Kilpatrick criterion, the quantity $E_{s,max} t_{pls}^{1/6}$ [Fig. 2.13(a), Eq. (2.63)] appears to be the most promising, as it can explain the exceedingly high field achieved in some RFQs by means of a pulse length scaling. However, its overall fluctuation is only marginally smaller than that of the raw $E_{s,max}$ [Fig. 2.13(a)]. With the above mentioned exceptions, the Kilpatrick criterion seems the most consistent, as the maximum surface field reached amounts to roughly 2 Kilpatrick. Yet it is important to note that this could just be a consequence of the design choices, for which the Kilpatrick criterion [Eq. (2.61)] was used in most cases. Then, the $E_{s,max}$ achieved during high-power tests would not necessarily be limited by sparking between the RFQ electrodes, but rather by the RF power source. Usually, the maximum peak input power the source can provide is chosen only a few ten percent higher than the design power P_0. In this case, the surface electric field cannot be increased significantly above the design value during high-power testing, since $E_{s,max} \propto \sqrt{P_0}$.

2.4.3 Other Limiting Quantities

Alongside the maximum surface electric field, other quantities incorporating also the magnetic field have been considered [157]. Two of them, RF pulsed heating and the modified Poynting vector, are presented in this section.

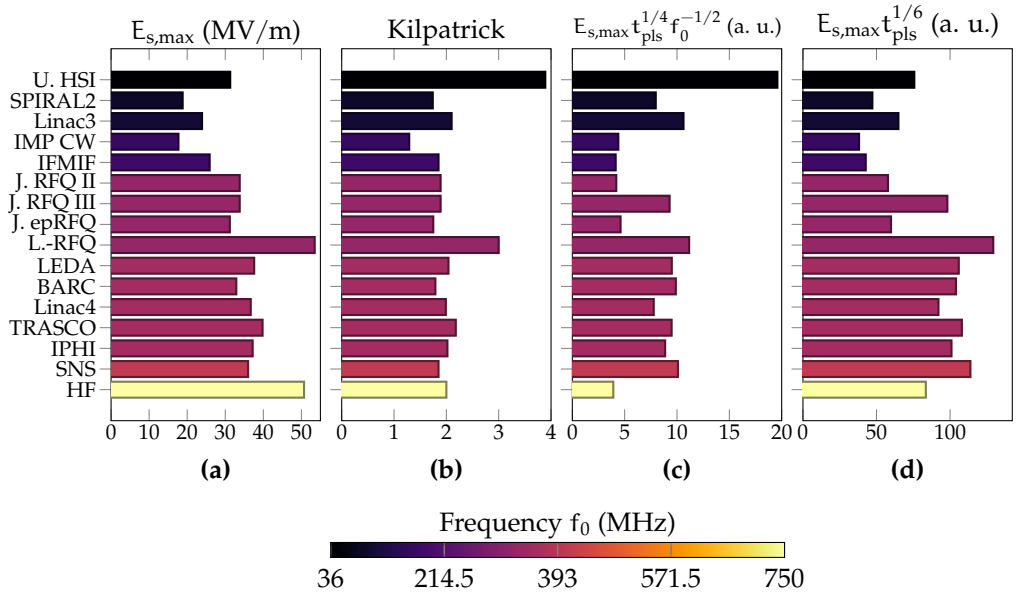

Figure 2.13: Field levels and pulse lengths achieved in a variety of operational RFQs ($\star$ in Table 2.1), plotted as four different quantities: maximum surface electric field $E_{s,max}$ (a), Kilpatrick value (b) from Eq. (2.61), as well as the quantities from Eqs. (2.62) and (2.63) in (c) and (d), respectively. The color scaling indicates the RFQ operating frequency.

RF pulsed heating means local temperature increase in the surface of metals. It originates in the thermal power deposited through Ohmic losses by the eddy currents of a pulsed RF electromagnetic field inside a cavity. If the heating occurs faster than the material has time to expand (which happens roughly at the speed of sound), considerable stress is induced in the metal surface where the currents are concentrated. Stresses higher than the material yield strength lead to cyclic fatigue and damage to the surface in terms of microscopic cracks and roughening, ultimately degrading cavity performance [170, 171]. Equaling the eddy currents in magnitude, the surface magnetic field H_t can thus be considered a performance limit for linacs alongside the surface electric field E_s. For annealed copper, the temperature rise can be estimated in one-dimensional approximation as [172]

$$\Delta T = H_t^2 \sqrt{t_{pls}}\, \Re\{Z_s(\omega)\} \cdot 1.54 \times 10^{-5}\, m^2K/W/\sqrt{s}, \tag{2.64}$$

where the last factor is derived from mass density, thermal conductivity, and specific heat capacity of the material, while Z_s is the frequency-dependent surface impedance from Eq. (2.24). The threshold temperature rise for damage caused by RF pulsed heating is usually quoted between 40 K and 110 K for annealed copper [171, 173–176], where uncertainties in the material properties are propagated to the estimate.

The highest magnetic field in a four-vane RFQ is located at the vane undercut window, shown in Fig. 2.14(c) for the HF-RFQ, since the total magnetic flux of one cavity quadrant is guided through the window. From the maximum surface

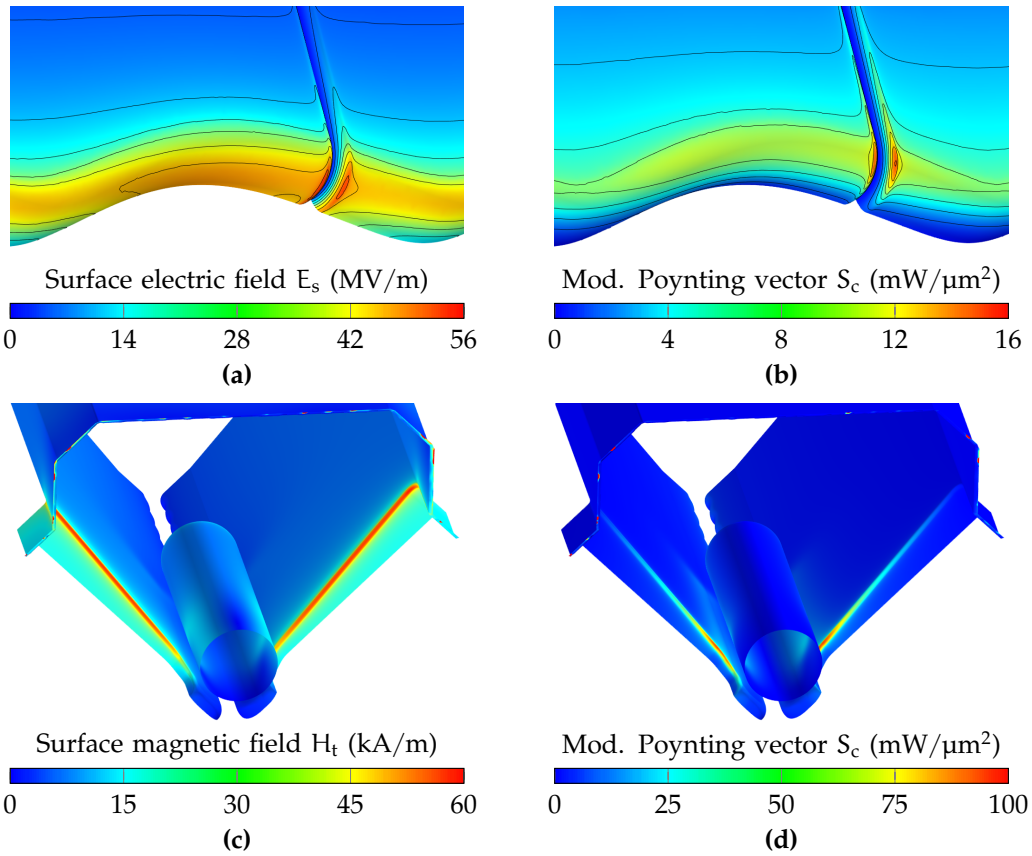

Figure 2.14: Surface electric field E_s on the vane tip and at the inter-module gap (a), surface magnetic field H_t around vane undercut window and dipole stabilization rod (c), as well as the modified poynting vector S_c in the respective locations (b), (d) of the HF-RFQ at design voltage ($V_0 = 67.6\,\mathrm{kV/m}$).

magnetic field $H_t = 60\,\mathrm{kA/m}$ and the pulse length $t_{pls} = 20\,\mu\mathrm{s}$, the local temperature rise originating in RF pulsed heating can be calculated using Eq. (2.64). With $\Delta T = 1.8\,\mathrm{K}$, the local temperature rise in the HF-RFQ is by an order of magnitude lower than the empirical limit mentioned above. While RF pulsed heating would become pertinent for RFQs operating with pulse lengths of several milliseconds, poses no relevant limitation for the RFQs discussed in this thesis.

Experiments conducted on high-gradient accelerating structures indicated that the magnetic field is also involved in the breakdown mechanism, which may be driven by local power flow. The modified Poynting vector[20] S_c was proposed in Ref. [157] in an effort to provide a local field quantity that can predict the performance of high-gradient accelerating structures. It is based on power flow balance considerations in a breakdown model where field emission currents cause local pulsed heating, and thus takes both electric and magnetic fields into

[20] Although S_c represents a scalar quantity, it is usually referred to as modified Poynting vector, being directly derived from the complex Poynting vector $\mathbf{S}$.

account. The "conventional" Poynting vector is defined as

$$\mathbf{S} = \frac{1}{2}\mathbf{E} \times \mathbf{H}^{\star} \tag{2.65}$$

in terms of the complex field phasors, giving direction and magnitude of local power flow in the electromagnetic field. The modified Poynting vector takes both active power flow (real part) and reactive power flow (imaginary part) into account, and is given by [157]

$$S_c = \left\| \Re\{\mathbf{S}\} \right\| + g_c \left\| \Im\{\mathbf{S}\} \right\|. \tag{2.66}$$

The scaling factor g_c accounts for the reactive power flow being less efficient than the active power flow at providing energy for field emission. It is a weak function of the local maximum electric field, and for most cases the assumption $g_c \approx 1/6$ is sufficient. S_c has been evaluated for a variety of high-gradient cavities structures operating in X-band and at 30 GHz, and has been used to guide the high-gradient traveling-wave structure development for the Compact Linear Collider (CLIC) project [177, 178]. For a breakdown rate for less than 1×10^{-6} breakdowns per pulse at a pulse length of $t_{pls} = 200\,\text{ns}$, S_c should not exceed $4\,\text{W}/\mu\text{m}^2$ [157, 179].

The quantity S_c has been computed for the regions of both maximum surface electric field [Fig. 2.14(b)] and maximum surface magnetic field [Fig. 2.14(d)] of the HF-RFQ. On the vane undercut edge close to the dipole stabilization rod both significant magnetic and electric field amplitudes are found. The latter originates in the short distance between the vanes, which are charged to $\pm V_0/2$ in an alternating manner, and the rod, which always has ground potential. Thus, a hot spot of the modified Poynting vector, which is proportional to the product of both fields, occurs here, with the maximum amounting to $S_c = 100\,\text{mW}/\mu\text{m}^2$. The value can be compared to the limit observed in X-band and 30 GHz experiments, which has to be scaled [157] to the HF-RFQ pulse length of 20 µs. With $S_c \propto E^2$,

$$S_c \leqslant 4\,\text{W}/\mu\text{m}^2 \cdot \left(\frac{200\,\text{ns}}{t_{pls}} \right)^{1/3}, \tag{2.67}$$

yielding a threshold of $860\,\text{mW}/\mu\text{m}^2$. The simulated S_c is nearly an order of magnitude lower than the scaled limit. This is attributed to the strong spatial separation of electric and magnetic fields in the RFQ, contrasting the high-gradient traveling wave structures for which the limit was established. Furthermore, the location of the maximum does not coincide with the typical breakdown areas in RFQs, located on the vane tips. Here, S_c merely amounts to $16\,\text{mW}/\mu\text{m}^2$.

2.4.4 Conclusion

In Section 2.4, three field-limiting quantities were investigated, the surface electric field E_s associated with the Kilpatrick limit, the surface magnetic field H_t leading

to RF pulsed heating, and the modified Poynting vector S_c. Within the context of the RFQs discussed in this thesis, operating at pulse lengths of several tens of microseconds, only the maximum surface electric field provides a meaningful limitation. The maximum surface magnetic field would only become relevant at pulse lengths of several milliseconds (and comparable field amplitudes). The modified Poynting vector S_c was proposed based on experimental data on high-gradient standing-wave and traveling-wave accelerating structures. It assumes values close to the critical limits where both strong electric and magnetic fields are present, for instance on the irises of such structures. However, in an RFQ, electric and magnetic field are spatially well-separated. The maximum S_c in the investigated four-vane RFQ (Fig. 2.14) is both by orders of magnitude lower than the critical limit, and does not coincide with typical breakdown locations. These results indicate that S_c is not a suitable quantity to estimate the high-field performance of an RFQ.

A selection of available experimental data on $E_{s,max}$ in RFQs was reviewed in an effort to find a quantity which predicts the breakdown performance in RFQs (Figs. 2.12 and 2.13). Emphasis was given on the recently commissioned HF-RFQ for proton therapy, operating at the same high frequency as the RFQs discussed in this thesis. It was found that the well-known Kilpatrick limit, which depends only on frequency, is the criterion with the most consistent values among the available data. Maximum surface fields of roughly 2 Kilpatrick are safe for RFQs operating at pulse lengths up to a few hundred microseconds. A few experiments hinted that significantly higher values might be achievable. Pulse-length dependent quantities established for high-gradient accelerating structures can potentially explain these exceptions, however, they show an overall larger scattering of values among the RFQs. Although the Kilpatrick criterion provides the overall most consistent criterion, it should be noted that this could come from the design choices. Nevertheless, in this thesis, the considerations are restricted to the pure maximum surface electric field and the Kilpatrick criterion.

3 RF Design of the PIXE-RFQ

The PIXE-RFQ [27, 29–31] was developed and built at CERN in the framework of the MACHINA project [31, 32]. The aim of MACHINA is to build the first transportable system for *in situ* PIXE ion beam analysis, allowing mobile employment in museums, restoration centers, or even in the field.

As the first of two chapters dedicated to the PIXE-RFQ, Chapter 3 covers the RF design of the compact linac operating at 750 MHz. First, a brief summary of the initial beam dynamics, RF, and mechanical design choices is given in Section 3.1. Sections 3.2 and 3.3 reconstruct the RF design process of 2D cross section, 3D cavity including dipole-mode detuning, RFQ auxiliaries, as well as power calculation and coupler design. The thermal behavior of the copper structure subject to RF losses is discussed in Section 3.4. The chapter concludes with beam dynamics studies validating the RF design in Section 3.5.

A significant portion of the content and the results presented in Chapter 3 have been previously published by the author in Refs. [29, 30]. Some of the figures shown here are taken and adapted from these papers.

3.1 General Design Choices

The PIXE-RFQ was designed and constructed with the experience gained from the Linac4-RFQ [34–39] and the HF-RFQ for proton therapy [18, 27, 28, 40–43]. Like the HF-RFQ, it operates at a frequency of 749.48 MHz, resulting in a small cavity with an exterior cross section less than 14 cm wide. The high frequency makes the four-vane cavity an obvious choice over a four-rod structure.

Innovative beam dynamics were developed using the PARMTEQ code [102] to facilitate the 20 keV to 2 MeV acceleration over just one meter [28, 40]. Low power consumption was an important optimization goal to allow for portability, such that a constant inter-vane voltage of $V_0 = 35\,\mathrm{kV}$ was chosen. The PIXE-RFQ features a very short bunching section, entering at a synchronous phase of $-30°$ (as opposed to the conventional $-90°$) which results in a comparatively low transmission of only 30 %. Also noteworthy are the small minimum aperture $a = 0.706\,\mathrm{mm}$ and the constant mid-cell aperture $r_0 = 1.439\,\mathrm{mm}$. The constant transverse vane tip radius of $\rho_t = r_0 = 1.439\,\mathrm{mm}$ significantly reduces the machining effort, as a rotating concave milling tool may be used. Furthermore,

the RF design was simplified because of the constant V_0 and r_0. Table 3.1 lists a selection of the design parameters, and Fig. 3.1 shows the variable channel parameters along the RFQ.

Table 3.1: Design parameters of the PIXE-RFQ.

Species	H^+	proton	
Input energy	$\mathcal{W}_{in}$	20	keV
Output energy	$\mathcal{W}_{out}$	2	MeV
RF frequency	f_0	749.48	MHz
Inter-vane voltage	V_0	35	kV
RFQ length	L_{RFQ}	1072.938	mm
Vane tip transverse radius	ρ_t	1.439	mm
Mid-cell aperture	r_0	1.439	mm
Minimum aperture	a	0.706	mm
Final synchronous phase	ϕ_s	-15	deg
Output beam diameter		0.5	mm
Beam transmission	$\mathcal{T}$	30	%
Peak beam current	I_b	200	nA
Repetition rate	f_{rep}	200	Hz
RF pulse length	t_{pls}	125	µs
Duty cycle	d	2.5	%
RF wall plug power		$\leqslant 6$	kVA

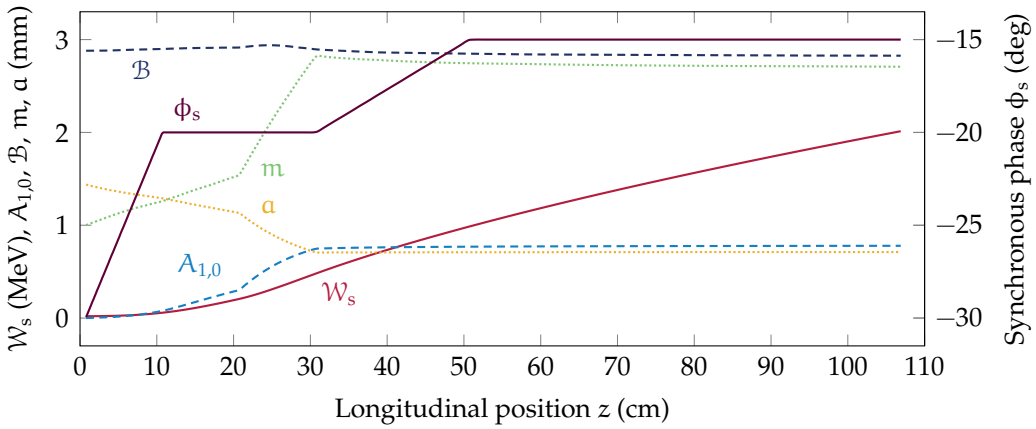

Figure 3.1: Beam dynamics design parameters of the PIXE-RFQ. Synchronous energy $\mathcal{W}_s$, synchronous phase ϕ_s, acceleration efficiency $A_{1,0}$, focusing strength $\mathcal{B}$, modulation parameter m and minimum aperture a are shown as functions of the longitudinal position z. Inter-vane voltage $V_0 = 35\,\text{kV}$, mid-cell aperture $r_0 = 1.439\,\text{mm}$, and transverse radius of curvature $\rho_t = r_0$ are held constant along the RFQ.

The PIXE-RFQ consists of two roughly half-meter long modules as well as two end plates that were each vacuum-brazed individually. It features a total of 24 ports with a diameter of 36 mm, which support the sixteen tuners, seven vacuum pumping ports, and a single input power coupler. Eight additional smaller ports were added for RF field pick-up antennas for diagnostic purposes. A CAD model and a sketch of the cross section are depicted in Fig. 3.2.

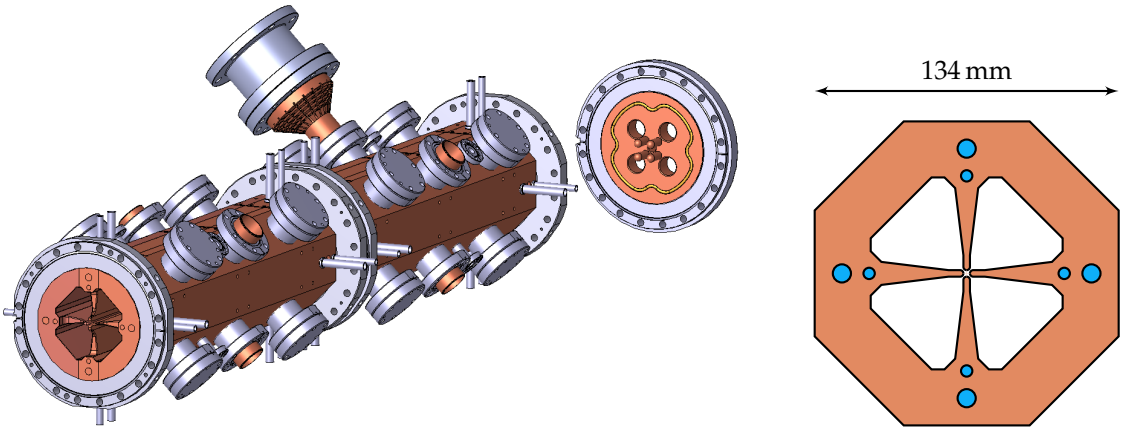

Figure 3.2: CAD model of the the PIXE-RFQ with detached end plates (a) and sketch of the cross section (b). The RFQ consists of two modules and features sixteen tuners (covered flanges), seven vacuum pumping ports (open flanges), eight slots for diagnostic pickup antennas (small flanges), and one input power coupler (top of picture). The eight water cooling channels present in each module are highlighted in blue.

3.2 RFQ Cavity and Auxiliaries

The RF design of the PIXE-RFQ was initiated with an optimization of the 2D cross section before 3D effects of the vane modulation were taken into account. To achieve the desired spectral mode placement, end shapes with dipole rods were designed. Finally, the geometries of tuners, pumping ports, and pick-up antennas were determined. The design of the input power coupler is covered in Section 3.3.

3.2.1 2D Cross Section Optimization

The goal of the two-dimensional cross section optimization was to place the resonance frequency of the operating quadrupole mode (TE_{210}) at $f_0 = 749.48\,\mathrm{MHz}$. At the same time, the power loss of this mode had to be minimized, corresponding to an as large as possible quality factor Q_0 [Eq. (2.25)]. Figure 3.3(a) shows one quadrant of the theoretical optimum cloverleaf cavity fulfilling these requirements, which is composed of three quarters of a circle and a square [1]. The radius R_c is determined by

$$\omega_0 = 2\pi f_0 = \sqrt{\frac{16}{\mu_0(4+3\pi)R_c^2 C'}}\,, \tag{3.1}$$

where C' is the capacitance per unit length between adjacent vane tips seen by the operating quadrupole mode. The intrinsic quality factor Q_0 reads, independent

of R_c,

$$Q_0 = \sqrt{\frac{8\sigma}{(4+3\pi)\omega_0 C'}}. \tag{3.2}$$

Here, $\sigma = 5.8 \times 10^7\,\mathrm{S/m}$ [67] is the conductivity of annealed copper, which constitutes the interior surface of the RFQ. For a PIXE-RFQ cell without modulation, the quadrupole capacitance reads $C' = 125\,\mathrm{pF/m}$, thus, according to these formulas, $R_c = 1.85\,\mathrm{cm}$ and $Q_0 = 7660$.

Qualitatively speaking, the smaller the cavity surface area (proportional to the surface losses) is in relation to the cavity volume (proportional to the stored energy), i.e. the more its shape resembles a circle, the higher the quality factor will be. In practice however, constructing the ideal shape shown in Fig. 3.3(a) is difficult because of the following reasons:

1. The vanes must have a finite thickness, which, for stability and cooling purposes, is significantly larger than the transverse vane tip radius.

2. The PIXE-RFQ cavity interior—except for the vane tips—should be bounded by planar surfaces alone with the aim of simplifying machining. It is particularly desirable that the equipment ports cut into the bulk copper solely intersect with a planar back surface of the cavity, forming a planar circular aperture.

3. A minimum material thickness of copper between the water-bearing cooling channels and the copper-vacuum interface is necessary to avoid degrading the vacuum by water diffusion. In the specific case, a minimum thickness of 4 mm was required [180].

Figure 3.3(b) shows the above-mentioned restrictions to the cavity shape.

In order to determine the optimum geometry for the desired resonance frequency and maximum quality factor subject to these constraints, several parametric studies were performed. Figure 3.4 shows frequency f_0 and 2D quality factor $Q_{0,2D}$ as function of the geometric parameters b_c and c_c for different values of α_c, the slope angle of the vane structure supporting the electrode tip. Reducing this angle increases the quality factor, however, a minimum thickness of the support structure is required regarding mechanical stability of the vane, heat dissipation and cooling channel placement. The finalized cross section can be seen in Figs. 3.3(b) or 3.5(b), and the corresponding 2D unloaded quality factor reads $Q_{0,2D} = 7280$. With this value, the PIXE-RFQ is in line with other four-vane RFQs [34–36, 39, 63, 72, 78, 133, 136, 147, 148, 168, 181], whose 2D quality factor amounts to approximately $2 \times 10^5 / \sqrt{f_0/\mathrm{MHz}}$. The 3D quality factor of the finalized cavity, including all auxiliaries, is typically 20 % to 30 % lower.

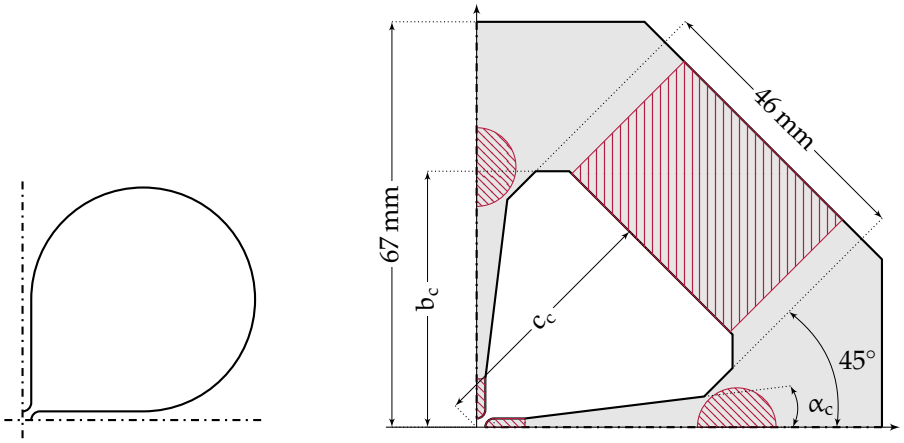

Figure 3.3: Sketch of one quadrant of the idealized RFQ cavity (a) consisting of three quarter circles and a square (adapted from Ref. [1]), and real cavity cross section of the PIXE-RFQ (b). The restrictions to the optimization highlighted in red: vane tips fixed by the beam dynamics design, at least 4 mm of bulk copper between cooling channels and vacuum domain, and a wide-enough back wall such that the port apertures intersect solely with a planar surface. After optimizing with respect to frequency and quality factor (Fig. 3.4), the parameters read $\alpha_c = 7°$, $b_c = 42.3\,\text{mm}$, $c_c = 40.862\,\text{mm}$. The sketches (a) and (b) are shown on the same scale.

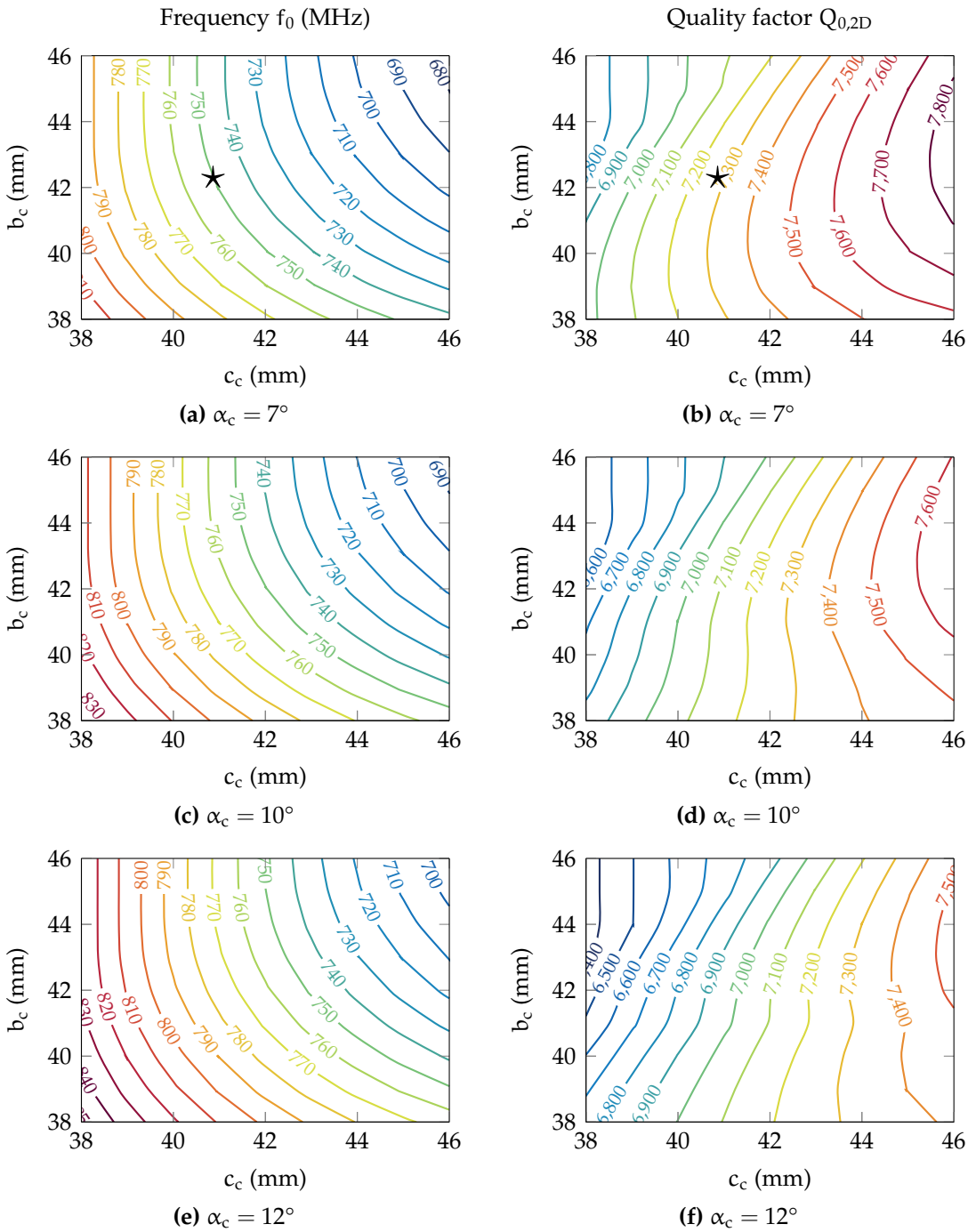

Figure 3.4: Parametric study for the PIXE-RFQ cavity cross section. For different vane angles α_c, the geometric parameters b_c and c_c are varied. The plots in the left and right columns show the quadrupole resonant frequency f_0 and 2D quality factor $Q_{0,2D}$, respectively, as functions of these parameters. A decrease of the vane angle sees a notable increase in quality factor, however, this is limited by cooling and mechanical stability considerations. The optimum parameter combination is indicated by $\star$.

3.2.2 Maximum Surface Electric Field

Figure 3.5(a) shows the field lines of the transverse electric quadrupole field between the vane tips for the unmodulated case, i.e. all four tips have a distance from the beam axis equal to the mid-cell aperture $r_0 = 1.439\,\text{mm}$. The field is plotted at $\phi = 0$ when it reaches its maximum value. From this 2D simulation, a maximum electric field amplitude of 33.4 MV/m was obtained, which agrees very well with the analytic estimate[21] of 33.1 MV/m, but is exceeded significantly when considering the actual 3D vane geometry (see below). The corresponding longitudinal component of the magnetic field in the four quadrants (a quarter RF period later) is depicted in Fig. 3.5(b). It vanishes in the vicinity of the beam.

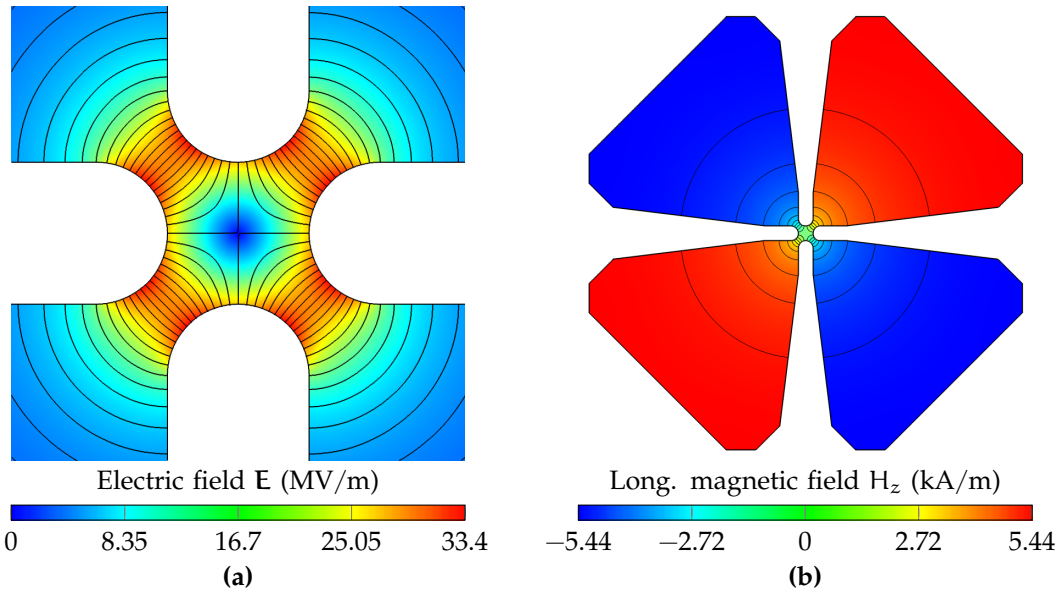

Figure 3.5: Transverse electric field lines at the equidistant vane tips of a cell without modulation (a), and longitudinal magnetic field of the 2D quadrupole mode in the RFQ cavity (b), where the lines connect points of equal amplitude. The peak values for an inter-vane voltage of $V_0 = 35\,\text{kV}$ are shown, and the maximum surface electric field amounts to 33.4 MV/m.

To accelerate particles with a nonzero longitudinal electric field component, a spatially modulated on-axis potential is required. This is achieved by varying the distances of the vane tips from the beam axis. The resulting shape deforms the electric field of the TE_{210} mode to produce an accelerating component in the longitudinal direction.

Accurate 3D simulations are necessary to study the 3D effects of the vane modulation. In particular, local surface curvatures of small radii and gaps significantly impact the local surface electric field E_s. As high fields may lead to RF breakdown by means of electron emission and sparking, the maximum field $E_{s,max}$ is an important quantity to consider, and a major performance limit

[21] The peak surface electric field between four electrodes with circular transverse profile with radius $\rho_t = r_0$ and no longitudinal modulation is given by $E_s = 1.36 \cdot V_0/r_0$ [1].

in conventional linear accelerators [1]. The surface electric field, computed using HFSS, is reported in Fig. 3.6. The overall maximum, amounting to 39.1 MV/m, occurs at the gap between the vanes of the two modules (b) because the small rounding radius. This value corresponds to 1.55 Kilpatrick [158] at the given operating frequency of 750 MHz. If this geometric feature is ignored, the maximum field occurs in the bunching section of the RFQ (c) with 36.5 MV/m (1.44 Kilpatrick). This value agrees well with the prognosis of the PARMTEQ design tool [102] at 36.9 MV/m. It is notably higher than the value solely obtained from 2D simulations [33.4 MV/m, Fig. 3.5(a)].

The maximum computed field strength of 1.55 Kilpatrick falls well below the values achieved in other RFQs without breakdown. The review of experimental data carried out in Section 2.4.2 suggests that field levels up to 2 Kilpatrick are safe choices for short-pulsed RFQs. In particular, the medical HF-RFQ was recently commissioned, featuring the same frequency, a somewhat shorter pulse length, and maximum surface electric field of 2.0 Kilpatrick [43].

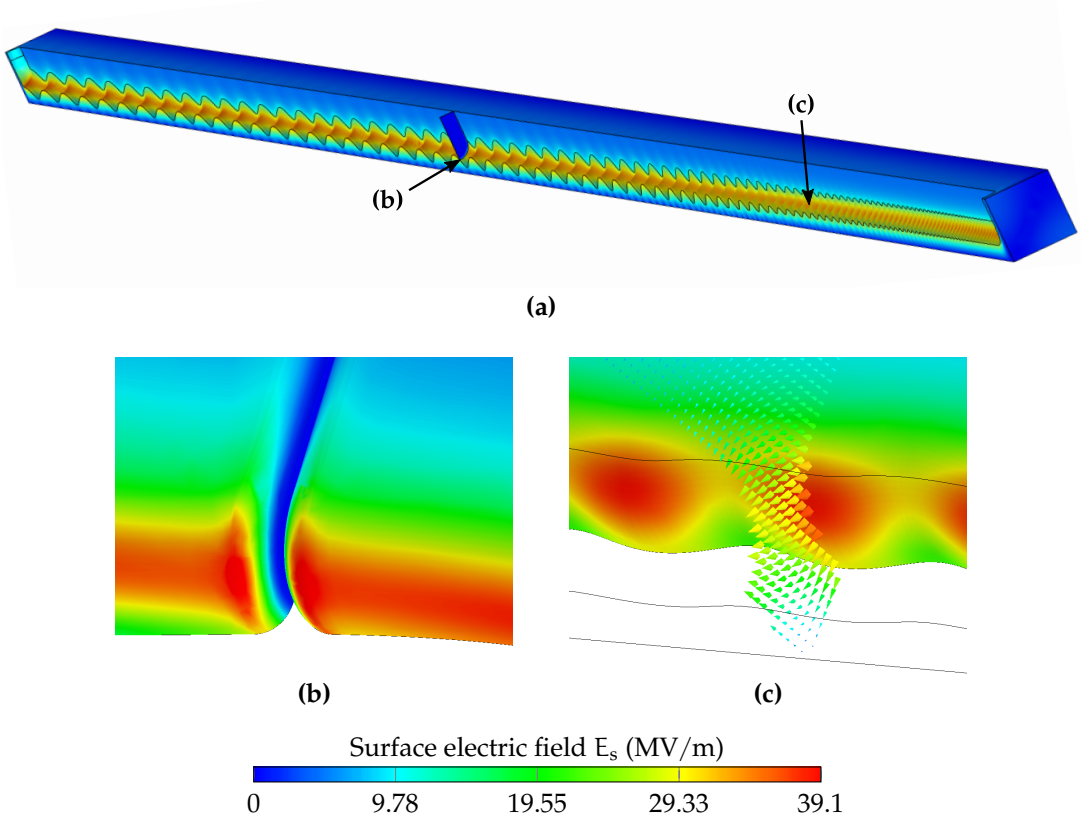

Figure 3.6: Surface electric field on the modulated vane tip (a). The overall maximum occurs at the gap between the two RFQ modules with 39.1 MV/m (b). Neglecting the gap, the maximum is located in the bunching section with 36.5 MV/m (c).

3.2.3 Capacitance and Transmission Line Model

Not only the surface electric field, but also the capacitances of the quadrupole and dipole modes between the vane tips depend on the local vane shape, and are thus z-dependent. Consequently, the RFQ has to be considered as a tapered structure.

Each RFQ cell would require a slightly different cavity shape to tune the local lumped LC circuit given by the vane capacitance and the cavity volume inductance (Fig. 2.10). Since this would be more difficult for machining, all geometric parameters of the cross section, except for the distance c_c between the cavity back wall and the beam axis, were kept constant along the entire RFQ. The optimum value of c_c for each cell was obtained by eigenmode simulation of selected individual RFQ cells, such as the one shown in Fig. 3.7(a). The topmost plot of Fig. 3.7(b) shows the interpolating curve $c_c(z)$. The quantity was then averaged over each of the two modules, such that—apart from the vane tip—only planar surfaces must be machined. The averaged parameters are given by Table 3.2.

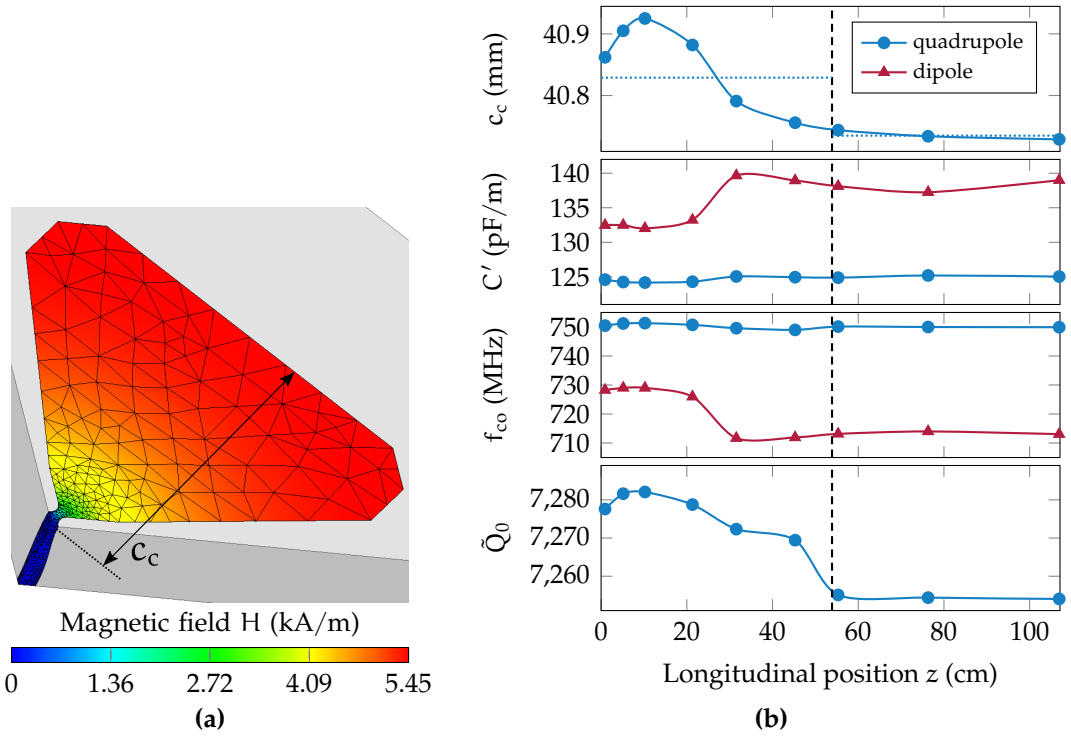

Figure 3.7: Finite element mesh and computed magnetic field H of a single RFQ cell with modulated vanes (a). The optimum cavity depth c_c is determined for a local resonance frequency of 749.48 MHz. The optimum value over the length of the RFQ is shown in (b). This parameter was averaged over each of both RFQ modules to obtain planar surfaces inside the cavity. The plot further shows the capacitance C', local cutoff frequency f_{co} and quality factor $\tilde{Q}_0$ in the thus non-optimum cavity.

For these fixed shapes, the quadrupole and dipole capacitances C' were computed for the individual cells as the ratio of stored energy to inter-vane voltage,

Table 3.2: Modulation-dependent parameters averaged over each of the two RFQ modules.

	$\langle c_c \rangle$ (mm)	$\langle \tilde{Q}_0 \rangle$	$\langle C'_{quad} \rangle$ (pF/m)	$\langle C'_{dip} \rangle$ (pF/m)
Module 1	40.829	7275	124.4	136.0
Module 2	40.735	7254	125.2	138.0
Entire RFQ	—	7264	124.8	137.0

the latter of which can be obtained by integrating the longitudinal magnetic flux density in one quadrant:

$$C' = \frac{2W_0}{LV_0^2} = \frac{\iiint_{\mathcal{V}} \mathbf{H} \cdot \mathbf{H}^\star \mathrm{d}\mathcal{V}}{L\omega \iint_{\mathcal{S}} H_z \mathrm{d}\mathcal{S}}. \tag{3.3}$$

Here, $\mathcal{V}$ denotes the four-quadrant volume of one cell, $\mathcal{S}$ the cross section of one quadrant, and L is the length of the cell. The capacitances, the local quadrupole and dipole cutoff frequencies f_{co}, and the quadrupole quality factor $\tilde{Q}_0$ are shown in Fig. 3.7(b). This information was also used to estimate the power loss of the RFQ cavity (Section 3.3.1). Effectively detuning the inductance of the local resonant circuit, the non-optimum shape results in a non-uniform voltage distribution along the RFQ and must be compensated by the tuners.

For computing spectral properties of the RFQ, it is advantageous to employ a transmission line model (TLM), as 3D simulations of the full RFQ geometry can then be avoided. Instead, only short individual segments have to be simulated to determine the TLM lumped quantities. Such models were developed in Refs. [36, 146–148], to name a few. In the following, a TLM is constructed for the PIXE-RFQ, in which the non-uniform vane capacitance $C'(z)$ is taken into account. In Section 3.2.4, the TLM is then used to determine the appropriate dipole detuning measures to achieve a desired spectrum.

Recall the dispersive wave equation introduced in Section 2.3.5:

$$\frac{\partial^2}{\partial z^2} V(z) + \underbrace{\left[(\omega/c)^2 - k_{co}^2(z)\right]}_{k(z)} V(z) = 0 \tag{2.58}$$

where

$$k_{co}(z)^2 = \frac{\omega_{co}^2(z)}{c^2} = \frac{1}{c^2 \mathcal{L}'(z) C'(z)}. \tag{2.59}$$

For an RFQ segment of thickness δz, where we assume constant circuit parameters (i.e. $k(z) = \text{const.}$ for a given frequency), the solution to Eq. (2.58) can be

written in matrix form [147]:

$$\begin{bmatrix} V(z+\delta z) \\ V'(z+\delta z) \end{bmatrix} = \underbrace{\begin{bmatrix} \cos k(z)\delta z & 1/k(z)\sin k(z)\delta z \\ -k(z)\cos k(z)\delta z & \cos k(z)\delta z \end{bmatrix}}_{\mathbf{M}_{wg}(z)} \begin{bmatrix} V(z) \\ V'(z) \end{bmatrix}, \tag{3.4}$$

where $\mathbf{M}_{wg}(z)$ describes the solution behavior in a waveguide-like RFQ slice. In this context, $V(z)$ equals the inter-vane voltage V_0 proportional to the magnetic field in the RFQ cavity, and its derivative $V'(z) = -j\omega\mathcal{L}'_s(z)I(z)$ corresponds to the longitudinal currents along the vane tips.

Neglecting the end geometry and assuming perfect open-circuit (PMC) boundaries instead, the RFQ can be modeled as an inhomogeneous waveguide by appending many such slices. In the impedance formulation, this is done by multiplying the corresponding matrices:[22]

$$\begin{bmatrix} V(z_{dn}) \\ V'(z_{dn}) \end{bmatrix} = \prod_{z=z_{up}}^{z_{dn}} \mathbf{M}_{wg}(z) \begin{bmatrix} V(z_{up}) \\ V'(z_{up}) \end{bmatrix}. \tag{3.5}$$

Here, z_{up} and z_{dn} identify the positions of upstream and downstream end, respectively.

In reality, the impact of the end geometry on the RFQ spectrum cannot be ignored. In fact, it is used to adjust the RFQ spectrum for maximum mode separation with the help of dipole rods. Thus, the ends are modeled as additional matrices [147]

$$\mathbf{M}_e = \begin{bmatrix} 1 & 0 \\ j\omega\mathcal{L}'_s Y_e & 1 \end{bmatrix} = \begin{bmatrix} 1 & 0 \\ \dfrac{1}{c^2 C'}\left(\dfrac{1}{\mathcal{L}_e} - \omega^2 C_e\right) & 1 \end{bmatrix}, \tag{3.6}$$

where $Y_e = j\omega C_e + 1/(j\omega\mathcal{L}_e)$ is the shunt admittance associated with the end geometry. The electric field between vane nose and end plate gives the end capacitance C_e. It is effectively fixed by beam dynamics constraints and surface field amplitude limits on the vane nose. The end inductance $\mathcal{L}_e$ depends on the size of the vane undercut window and was chosen such that $\omega_0 = 1/\sqrt{\mathcal{L}_e C_e}$, and consequently $Y_e \to 0$ for the operating quadrupole mode. Thus, the ends appear as perfect open-circuit boundaries to this mode. On all other modes they act as mismatched impedances that perturb frequency and field distribution. The specific values of the end shunt capacitances and inductances were determined by 3D eigenmode simulations of short end segments of length ΔL, such as the one shown in Fig. 3.10(b). As these parameters cannot be obtained directly, they are computed as the differences between total capacitance or inductance (C_{tot}, $\mathcal{L}_{tot}$) of

[22] The repeated matrix multiplication, here expressed through the Π symbol, is carried out such that matrices with increasing z-coordinate are multiplied from the left with the current partial product, i.e. $\cdots \mathbf{M}_{wg}(z_{i+1}) \cdot \mathbf{M}_{wg}(z_i) \cdot \mathbf{M}_{wg}(z_{i-1}) \cdots$.

the segment and the corresponding contribution of the regular RFQ cells:

$$C_e = C_{tot} - \left(\int_{z_{up/dn}}^{z_{up/dn} \pm \Delta L} C'(z) dz \right), \qquad \frac{1}{\mathcal{L}_e} = \frac{1}{\mathcal{L}_{tot}} - \left(\int_{z_{up/dn}}^{z_{up/dn} \pm \Delta L} \frac{dz}{\mathcal{L}'(z)} \right). \tag{3.7}$$

The thereby computed values are shown in Table 3.3 for the quadrupole and dipole transmission line as well as the upstream and downstream end, respectively.

Table 3.3: Geometric and transmission line parameters of the PIXE-RFQ ends.

		Upstream end		Downstream end		
		Quad.	Dip.	Quad.	Dip.	
Undercut size	Δz	13.952		13.213		mm
DSR length	ℓ_{DSR}	25		25		mm
Vane capacitance	C'	124.6	132.5	125.0	139.0	pF/m
End capacitance	C_e	1.263	2.655	1.265	2.354	pF
End inductance	$\mathcal{L}_e$	36.58	14.58	35.62	15.77	nH

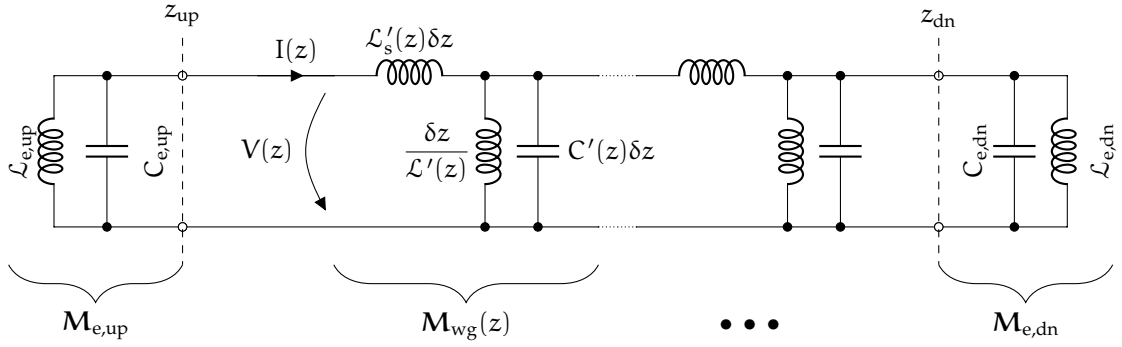

Figure 3.8: Two-wire transmission line model of the PIXE-RFQ. The chain of dispersive transmission line segments in the center takes the influence of the vane geometry into account. Additional shunt LC circuits at both ends of the line model the vane noses and undercut windows.

The complete transmission line model—one for quadrupole and dipole modes each—is shown in Fig. 3.8 and the equivalent matrix equation reads

$$\begin{bmatrix} V(L_{RFQ}) \\ V'(L_{RFQ}) \end{bmatrix} = \underbrace{\mathbf{M}_{e,dn} \left(\prod_{z=z_{up}}^{z_{dn}} \mathbf{M}_{wg}(z) \right) \mathbf{M}_{e,up}}_{\mathbf{M}_{RFQ}} \begin{bmatrix} V(0) \\ V'(0) \end{bmatrix}. \tag{3.8}$$

The frequencies of the RFQ eigenmodes can be found by (numerically) solving

$$[\mathbf{M}_{RFQ}]_{2,1} = 0, \tag{3.9}$$

i.e. by finding the frequencies for which the longitudinal current at the end of the RFQ $I(L_{RFQ}) \propto V'(L_{RFQ})$ is zero for any given nonzero voltage $V(0)$. Then, a standing wave is established and the approximate longitudinal field profile is given by $V(z)$.

3.2.4 Spectrum and Dipole Stabilization Rods

Small but unavoidable fabrication errors lead to mixing of modes of the ideal four-vane RFQ, which results in a perturbed field for the operating quadrupole mode (TE_{210}). This perturbation is proportional to $1/(\Delta f)^2$, with Δf being the frequency difference between the modes [1]. It is therefore desirable to have a maximum spectral separation between the operating mode and both lower and higher order modes. A variety of techniques for tuning parasitic dipole modes away from the operating mode have been developed, such as vane coupling rings, stabilizing loops, coupling of individual RFQ cavities, asymmetric cavities, or bent vanes [1, 123, 129, 152, 154, 155]. A common practice in modern RFQs is the use of dipole stabilization rods (DSRs) to lower the dipole mode frequencies, achieving a greater margin to the operating mode [18, 147, 153]. The end plates of the PIXE-RFQ with their DSRs are shown in Fig. 3.9.

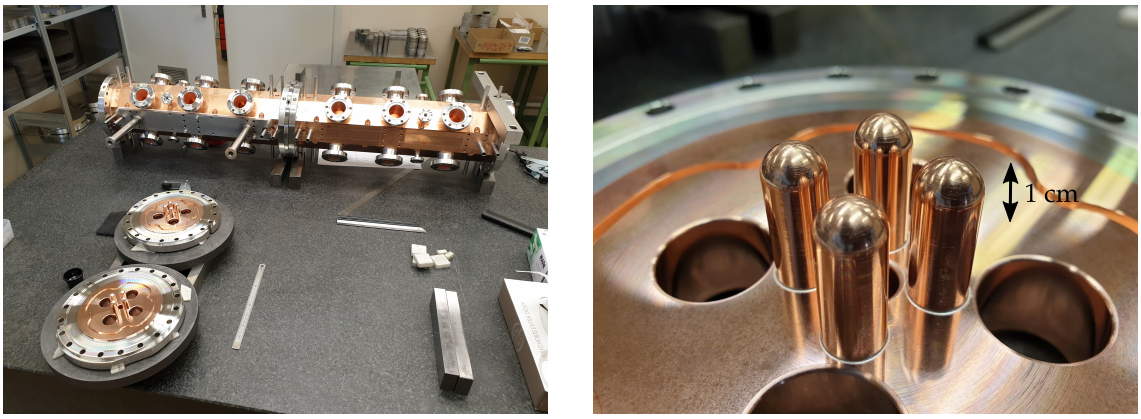

(a) **(b)**

Figure 3.9: Photograph of the PIXE-RFQ during alignment of the two modules with end plates in the foreground (a), and close-up of an end plate with dipole stabilization rods (b).

The transmission line model constructed in Section 3.2.3 was used to determine the required DSR length ℓ_{DSR} to achieve the desired spectrum. By using this model, only short end segments, depicted in Fig. 3.10, had to be simulated, while a time-consuming eigenmode computation of the full-length RFQ could be avoided. Figure 3.11(a) shows the RFQ spectrum, i.e. the frequencies of the lowest-order quadrupole and dipole modes depending on the dipole rod length ℓ_{DSR}. For each ℓ_{DSR}, the undercut size Δz was adjusted to match the operating quadrupole mode, i.e. chosen such that the end shunt admittance Y_e vanishes for the frequency of this mode. It becomes clear that the rods significantly lower

the dipole mode frequencies, while their effect on the quadrupole spectrum is practically negligible.[23]

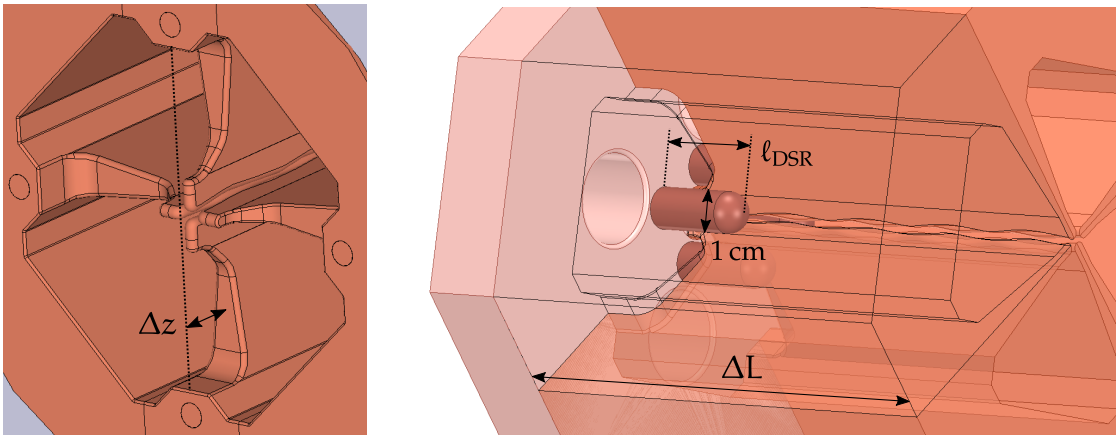

Figure 3.10: CAD model of the downstream end of the PIXE-RFQ (a) with the vane undercuts of width Δz that allow the magnetic field to close back on themselves. The end segment with termination plate and dipole stabilization rods (DSR) are shown in (b). The DSR diameter reads 1 cm, and the finalized length is $\ell_{DSR} = 2.5\,\text{cm}$.

Because of the short length of the PIXE-RFQ of only 2.5λ, the modes were initially quite well separated [Fig. 3.11(b), blue lines]. Nevertheless, the spectrum was adjusted such that a symmetric separation was obtained between the operating quadrupole mode (TE_{210}) and the next closest quadrupole mode (TE_{211}) and dipole mode (TE_{111}), respectively. A separation slightly larger than $\Delta f = \pm 12\,\text{MHz}$ was achieved by installing four DSRs with a length of 25 mm to each end plate of the RFQ. Figure 3.11(b) shows the effect of the DSRs on the PIXE-RFQ spectrum. Furthermore, it highlights the accuracy of the employed transmission line model by comparing its results to those obtained from HFSS 3D eigenmode simulations.

Figure 3.12 shows the magnetic field in the finalized geometry of the downstream end and on the DSR. The vane undercut window is the critical region for the surface current density, which is in magnitude equal to the tangential magnetic field H_t. Its maximum of 25.1 kA/m is located at the edge of the undercut [Fig. 3.12(a)]. As hinted in Section 2.4.3, this value is by nearly an order of magnitude lower than a magnetic field that would produce a critical local temperature rise ΔT via RF pulsed heating. With an RF pulse length of 125 µs, ΔT at the undercut edge amounts to merely 0.8 K [Eq. (2.64)], whereas material fatigue is expected for ΔT not lower than 40 K.

[23] The DSRs introduce a coaxial TEM-like mode between two adjacent vanes and around the rod itself, which strongly couples to the dipole modes. However, the mode is orthogonal to the quadrupole modes, to which the DSRs merely appear as perturbing objects [147].

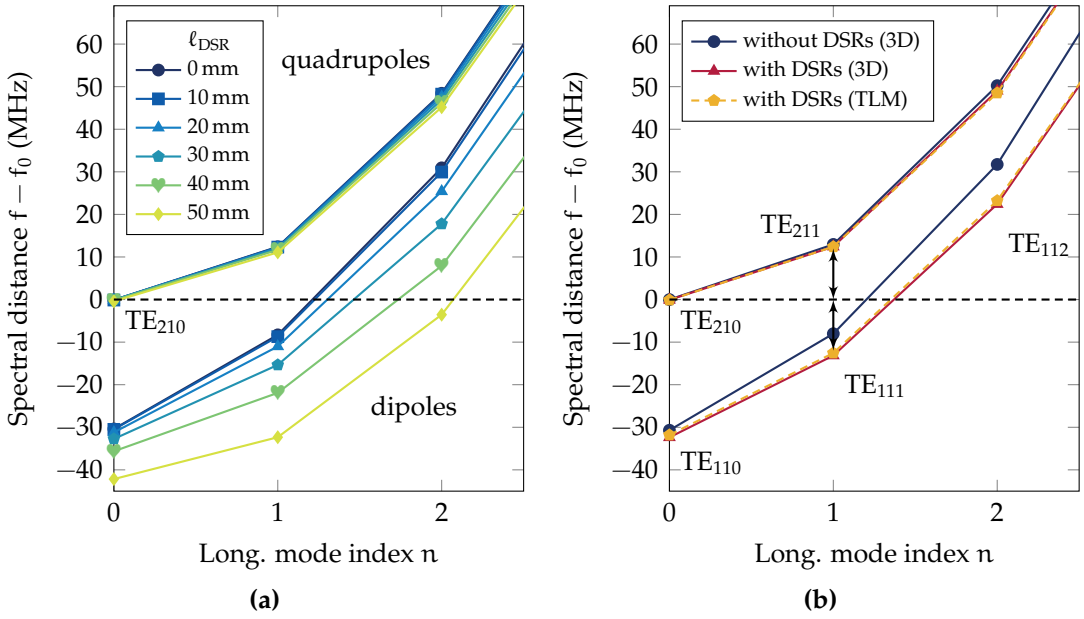

Figure 3.11: Eigenmode spectrum of the PIXE-RFQ. The results of a parametric study to find the optimum dipole rod length ℓ_{DSR} are shown in (a). An increasing length lowers the dipole frequencies, whereas the quadrupole modes are practically unaffected. The spectrum for the final chosen rod length $\ell_{DSR} = 25\,mm$ compared to the initial spectrum without DSRs is reported in (b). Very close agreement between TLM and 3D simulation results is observed, validating the circuit model shown in Fig. 3.8.

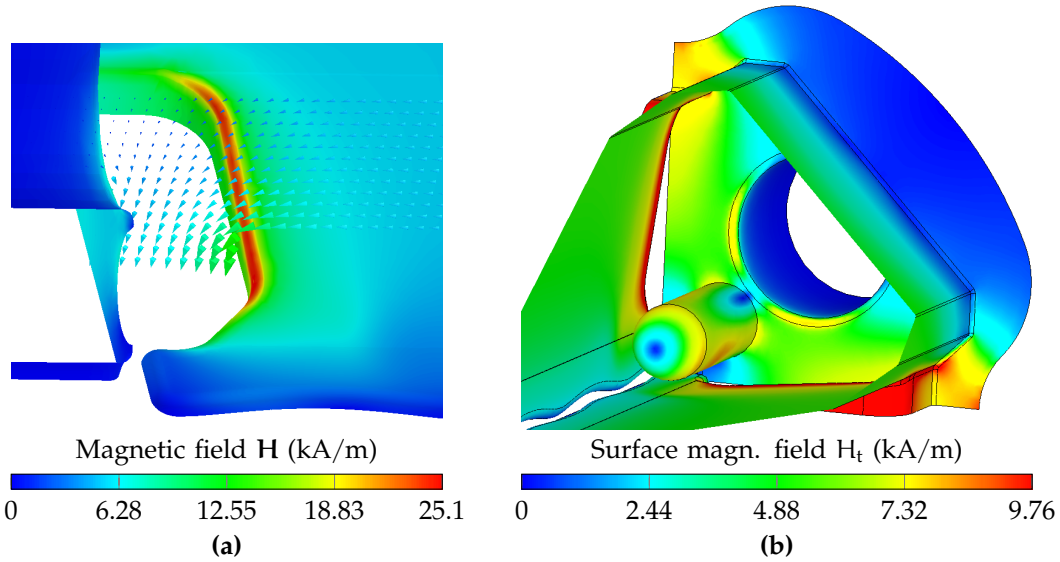

Figure 3.12: Magnetic field at the downstream end passing through the vane undercut window and magnetic field tangential to the surface, equal to the surface current density (a). The hot spot at the edge of the undercut is the maximum surface current density in the entire RFQ with 25.1 kA/m. The field at the dipole stabilization rod is depicted in (b). Note that different scales are used for better visualization.

3.2.5 Vacuum Pumping Ports and Tuners

The PIXE-RFQ features sixteen slug tuners, seven vacuum pumping ports, and one input power coupler, which are mounted to a total of 24 DN 40 flanges with an inner diameter of 36 mm. Together with the RF pickup antennas (Section 3.2.6), they constitute the RFQ auxiliaries.

Finite manufacturing and alignment tolerances of the four individually manufactured vanes lead to frequency detuning. Additionally, the asymmetries perturb the electric field distribution between the vane tips by introducing dipole components and negatively impact the beam dynamics. The purpose of the slug tuners is to deform the magnetic field distribution in the four quadrants, effectively tuning the shunt inductances. The electric field can be corrected by adjusting the tuners appropriately, since with Eq. (2.6) the inter-vane voltages are proportional to the quadrant magnetic fields. The slugs feature a conical tip to have a low impact on the quality factor while being convenient to manufacture [27]. A CAD model as well as the surface magnetic field on the tuner tip are depicted in Fig. 3.13, and a photograph of a machined tuner is shown in Fig. 3.17(a). The PIXE-RFQ tuner configuration is essentially the same as that of the HF-RFQ [27, 41, 42], taking into account that the PIXE-RFQ is only half as long. Four tuners each are installed at four longitudinal positions along the RFQ, i.e. 1.6 tuners per wavelength and quadrant. They were initially machined with an over-length of 11 mm providing a movement range of 22 mm, or ±11 mm with respect to the nominal position. This results in a combined frequency tuning range of approximately ±12 MHz. The setup as well as the tuning process itself are detailed in Chapter 4.

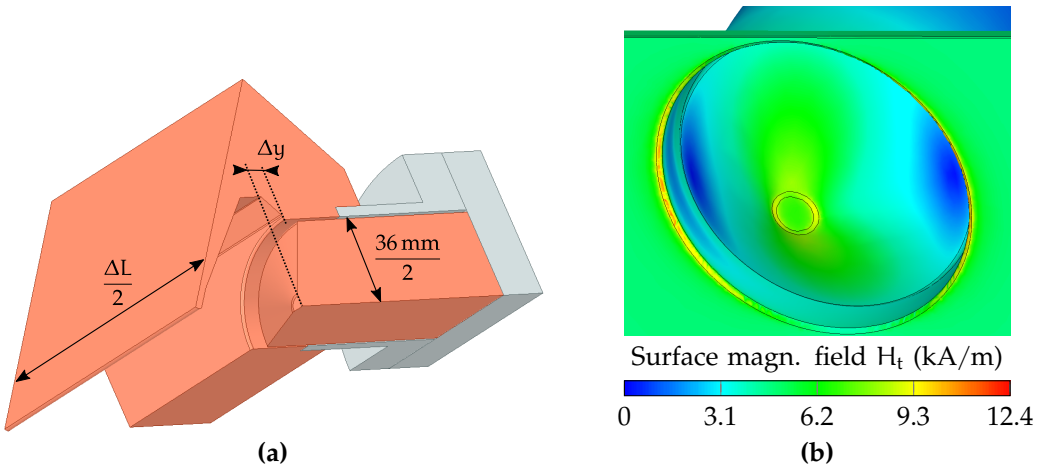

Figure 3.13: CAD model of the PIXE-RFQ slug tuner (a). The computational domain of the simulation is reduced to a segment of length ΔL and makes use of symmetry planes. The tangential magnetic field H_t, equal to the surface current density, is shown in (b) on the tip of the tuner and on the cavity surface close to the tuner aperture.

Seven turbo pumps maintain the vacuum inside the RFQ cavity. The interface between intake manifold and domain occupied by the electromagnetic field

is realized through circular copper pumping ports, whose geometry was adapted from the HF-RFQ pumping ports [27]. The inner port diameter measures 31 mm, corresponding to a cutoff frequency of 5.7 GHz, such that electromagnetic fields entering the port decay rapidly. The pumping ports were designed with a single bar across the aperture that provides a path for the surface currents, reducing the impact on the quality factor. Figure 3.14 depicts a CAD model of the vacuum pumping port and the simulated surface magnetic field, equivalent to the surface current density. A photograph of a machined pumping port is shown in Fig. 3.17(b). Four pumping ports are located in the first module, closer to the proton source and the regions of most expected particle losses. In the second module, three additional pumping ports and the input power coupler are mounted [Fig. 3.2(a)]. The coupler is discussed in detail in Section 3.3.

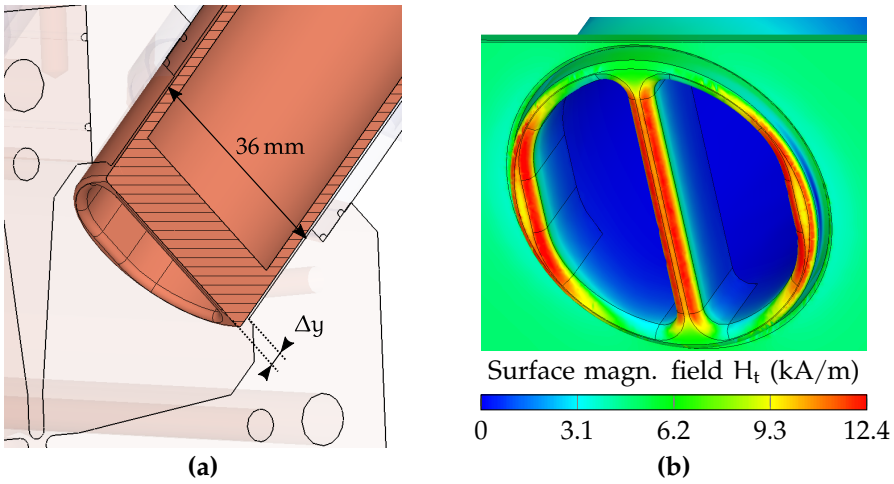

Figure 3.14: CAD model of the vacuum pumping port (a). The tangential magnetic field H_t, equal to the surface current density, around the inlet is shown in (b). It is significantly higher than that of the tuner [Fig. 3.13(b)], thus having a larger impact on the quality factor.

Nominal penetration and impact on the quality factor of both vacuum pumping ports and tuners were determined by means of 3D eigenmode simulations of short segments, such as the one shown in Fig. 3.13(a). The frequency deviation from the unperturbed cavity Δf and the quality factor Q_0^{prt} were calculated as functions of the penetration Δy into the cavity and the segment length ΔL. Figures 3.15 and 3.16 show these values for the tuner and pumping port, respectively. The nominal penetration is independent of ΔL and restores the resonant frequency to that of the unperturbed cavity. The corresponding value of Q_0^{prt} was used to estimate the power loss of the entire RFQ (Section 3.3.1).

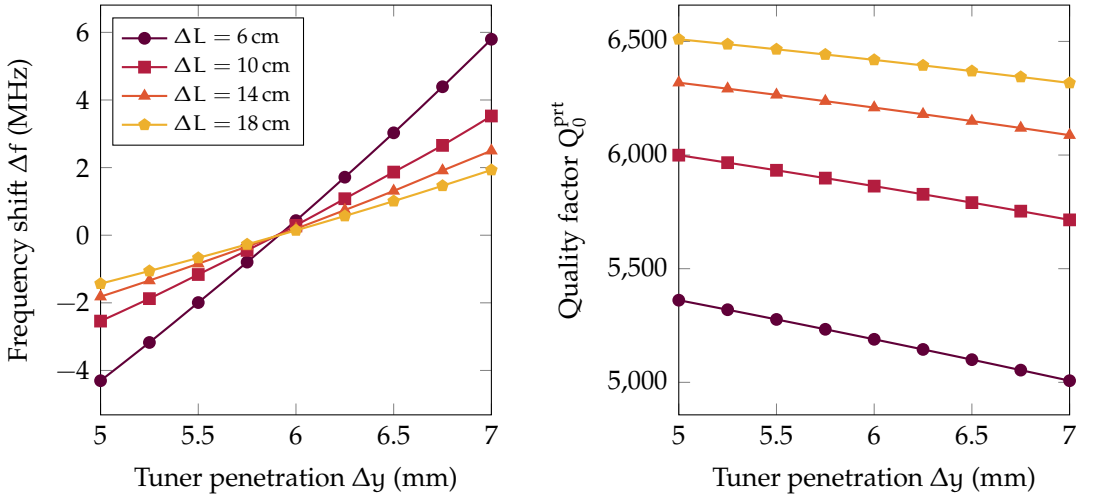

(a) **(b)**

Figure 3.15: Resonant frequency shift Δf (a) and unloaded quality factor Q_0^{prt} (b) of an RFQ segment containing a tuner as functions of the tuner penetration Δy. The simulation was performed for different segment lengths ΔL.

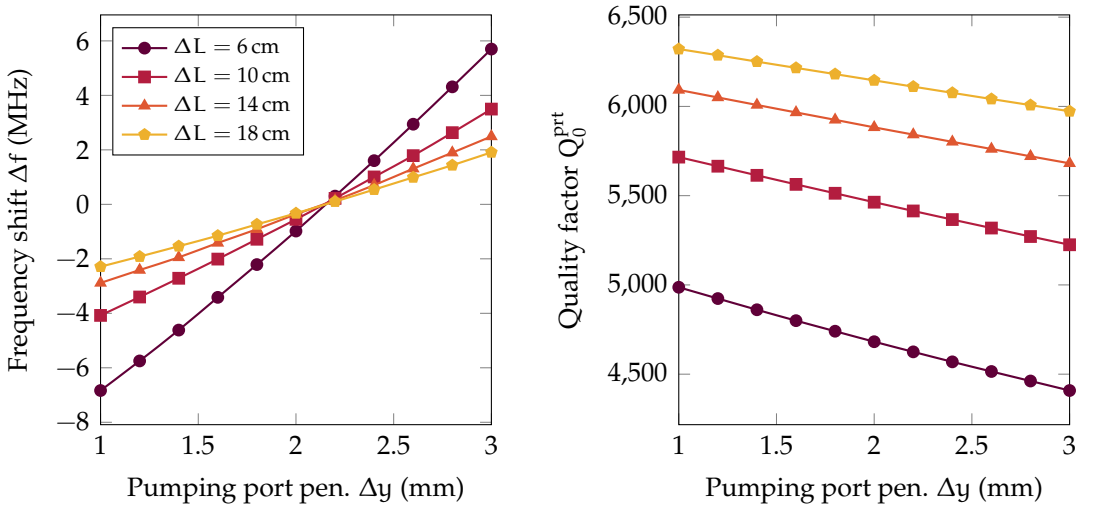

(a) **(b)**

Figure 3.16: Resonant frequency shift Δf (a) and unloaded quality factor Q_0^{prt} (b) of an RFQ segment containing a vacuum pumping port as functions of the pumping port penetration Δy. The simulation was performed for different segment lengths ΔL.

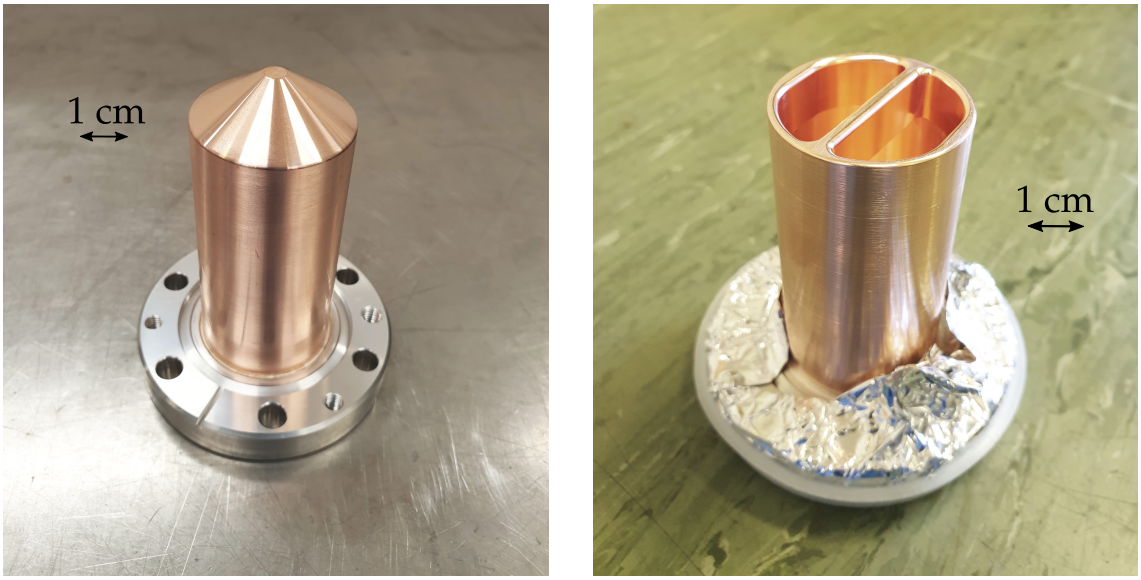

(a) (b)

Figure 3.17: Photographs of a machined tuner (a) and vacuum pumping port (b).

3.2.6 Diagnostic RF Pickup Antennas

Up to eight diagnostic RF pickup antennas are used to measure the amplitude of the magnetic field in the RFQ cavities—and thereby the inter-vane voltage—during operation. A small loop connects inner and outer conductor and weakly couples to the magnetic field [Fig. 3.18(a)]. The transition between vacuum and surrounding environment is given by a ceramic (Al_2O_3) RF window. The antennas are mounted to eight DN 16 flanges with an interior diameter of 7 mm, one per quadrant and module, which have been brazed to the RFQ modules in addition to the 24 DN 40 flanges.

The penetration of the antennas was chosen such that they are strongly undercoupled. They extract a power of merely $P_a = 1\,W$ at nominal voltage, corresponding to an external quality factor of $Q_{ex} = 3.9 \times 10^8$ for a total stored energy of $W_0 = 82.2\,mJ$ (Section 3.3.1). This value is by five orders of magnitude higher than the unloaded quality factor $Q_0 \approx 6000$ and the external quality factor of the power coupler (Section 3.3.2). Thus, the pickup antennas may be neglected in further calculations. Figure 3.18(a) shows the magnetic field around the antenna and highlights the very weak coupling. The cavity perturbation introduced by the antennas has practically no effect on the resonant frequency of the RFQ.

In Fig. 3.18(b), the transmitted power P_a is shown as a function of the antenna penetration Δy. Because of numerical errors as well as mechanical tolerances in antenna manufacturing and flange brazing,[24] a value of $P_a = 1\,W$ cannot be

[24] In fact, no antennas were manufactured specifically for the PIXE-RFQ. Instead, it uses four spare antennas that were made for the HF-RFQ, which utilizes eight of twelve originally manufactured antennas. To adjust the penetration into the cavity, the antenna flange brazed to the PIXE-RFQ was positioned further inwards, avoiding re-machining of the existing spares.

achieved with an accuracy that is sufficient for diagnostic purposes. Thus, the antennas were calibrated by means of bead-pull measurements after installation, as is discussed in Section 4.5 of the following chapter. A photograph of an RF pickup antenna is shown in Fig. 3.19.

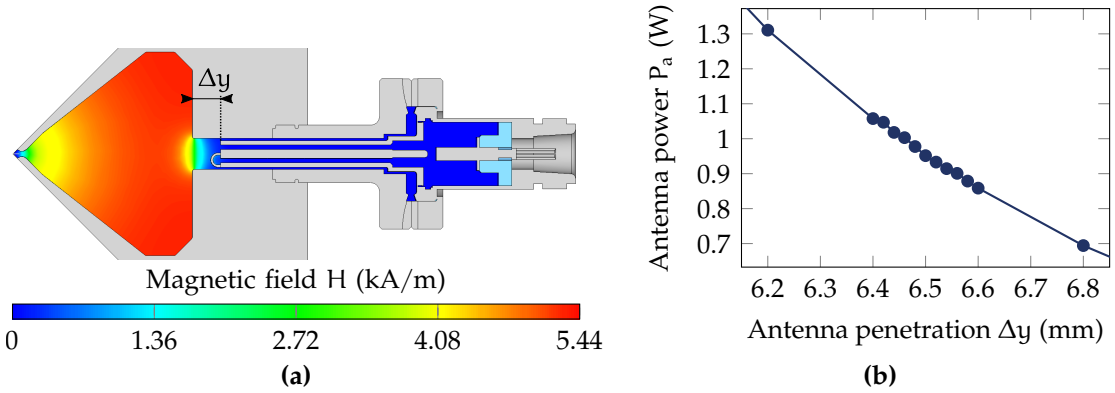

Figure 3.18: Magnetic field at the pickup antenna up to the ceramic RF window (a). The coupling is very weak since the antenna is designed for an extracted power of only 1 W. The transmitted power is shown in (b) as a function of the antenna penetration Δy.

Figure 3.19: Photograph of an RF pickup antenna.

3.3 Input Power Coupler

The PIXE-RFQ features one single input power coupler that supplies the entire cavity. It is mounted at the longitudinal center of the second module, sharing this location with three vacuum pumping ports [Fig. 3.2(a)]. Thus, four pumping ports remain in the first module in the vicinity of most expected particle losses. Before the design of the coupler itself, the RF power loss had to be determined. In Section 3.3.1, the power loss calculation by means of a semi-analytical approach, which is based on splitting the RFQ into multiple segments, is described and compared to the result of a full 3D eigenmode computation. Section 3.3.2 discusses the matching procedure and gives details on the particular coupler geometry.

3.3.1 Surface Power Loss

The total RF power P_0 dissipated on surface losses is given by the integral of the surface current density over the entire interior RFQ surface [Eqs. (2.22), (2.23)], and thus generally requires a time-consuming 3D eigenmode simulation of the entire structure. However, the longitudinal decomposition of the RFQ into segments suggests an efficient alternative that can estimate the power loss with sufficiently high accuracy. The technique is detailed in the following.

The segments of the decomposition are chosen with respect to the components that imply a deviation from the ideal 2D geometry, such as tuners and pumping ports. By individual simulation of each segment, the quality factor $Q_{0,n}$ of the n-th segment is obtained. The (quadrupole) capacitance C' changes along the accelerator because of the vane modulation, and is interpolated by computing specific isolated cells as illustrated before [Section 3.2.3, Fig. 3.7(b)]. By integrating $C'(z)$, one obtains the energy $W_{0,n}$ stored in the electromagnetic field

$$W_{0,n} = \frac{1}{2} C_n V_0^2 = \frac{V_0^2}{2} \int_{z_{0,n}}^{z_{1,n}} C'(z) dz, \tag{3.10}$$

where $z_{0,n}$ and $z_{1,n}$ denote the beginning and end of the segment, respectively, and $\Delta L_n = z_{1,n} - z_{0,n}$ is the segment length. Using Eq. (2.25) and summing up over the segments, one obtains for the total power loss

$$P_0 = \sum_n P_{0,n} = \omega_0 \frac{V_0^2}{2} \sum_n \frac{1}{Q_{0,n}} \int_{z_{0,n}}^{z_{1,n}} C'(z) dz. \tag{3.11}$$

The particular method to obtain the quality factor $Q_{0,n}$ of the nth segment varies depending on the segment type. For the input and output end, it is computed directly by the respective 3D simulation, since the vane modulation is already included here (Section 3.2.4). Otherwise it is obtained by averaging over the interpolated quality factor profile $\tilde{Q}_0(z)$ [Fig. 3.7(b)]:

$$\frac{1}{\tilde{Q}_{0,n}} = \frac{1}{\Delta L_n} \int_{z_{0,n}}^{z_{1,n}} \frac{dz}{\tilde{Q}_0(z)}. \tag{3.12}$$

Here, $\tilde{Q}_{0,n}$ solely considers the effect of the vane modulation, but not the influence of ports that may be present in this segment. For plain segments, $Q_{0,n} = \tilde{Q}_{0,n}$, while the perturbation of tuners, pumping ports or couplers[25] in the port

[25] As mentioned before, the diagnostic RF pickup antennas discussed in Section 3.2.6 can be ignored in this calculation because of their negligibly small influence.

segments is accounted for by

$$Q_{0,n} = \tilde{Q}_{0,n} \frac{Q_{0,n}^{prt}}{Q_{0,2D}}, \tag{3.13}$$

where $Q_{0,n}^{prt}$ is the quality factor of the nth segment with a port, but without vane modulation. This value is obtained from the simulations conducted in Section 3.2.5, Figs. 3.15(b) and 3.16(b). The author assumes that the relative change in quality factor caused by inserting a port into a given plain, modulation-free segment n, i.e. the ratio $Q_{0,n}^{prt}/Q_{0,2D}$, is the same as if the segment contained modulated vanes, $Q_{0,n}/\tilde{Q}_{0,n}$.

Table 3.4: RFQ segments and their parameters used for the semi-analytic power estimation.

Segment n	ΔL_n (cm)	$Q_{0,n}$	$P_{0,n}$ (kW)
Upstream end	10.02	5644	6.37
Plain (compensate overlap)	-0.08	7282	-0.04
4× tuner	6.00	5204	4.13
Plain	8.00	7279	3.94
4× pumping port	6.00	4634	4.66
Plain	8.00	7272	3.97
4× tuner	6.00	5196	4.17
Plain	19.64	7259	9.76
4× tuner	6.00	5185	4.18
Plain	8.00	7254	3.98
3× pumping port + coupler	6.00	4654	4.66
Plain	8.00	7254	3.98
4× tuner	6.00	5185	4.18
Plain (compensate overlap)	-2.21	7254	-1.10
Downstream end	11.93	5759	7.48
Total	107.30	6012	64.32

Table 3.4 shows the segments of the PIXE-RFQ and their parameters. The two plain segments with negative lengths $\Delta L_n < 0$ account for longitudinal overlaps of the upstream end with the first four tuners, and the downstream end with the last four tuners, respectively. Their negative power loss contributions compensate for the losses that would otherwise be counted twice because of the overlaps. Equation (3.11) gives 64.3 kW for a nominal voltage of $V_0 = 35$ kV, which deviates by merely 0.3 % from the result of 64.5 kW obtained from full 3D eigenmode simulation based on a CAD model.[26] The corresponding quality factors read 6012

[26]The 3D eigenmode simulation of the full RFQ is based on a CAD model generated by a mechanical engineering design tool. It assumes quarter symmetry, where the power coupler is neglected and considered as a vacuum pumping port because of the—in terms of surface losses—comparable geometry. The HFSS simulation takes several days on a workstation machine with two Intel® Xeon® E5-2650 v4 processors, 48 virtual cores at 2.2 GHz and 500 GB RAM. Furthermore, caused by the non-optimum cavity dimension, the model is detuned and the voltage varies by 10 % along the RFQ, as the tuners are fixed at their nominal position.

and 5995, respectively. Discrepancies originate from the simplifications made by the segmented model itself, numerical errors, as well as geometric details that are only considered in the CAD model. These include for instance the diagnostic antennas and the central gap between the two RFQ modules.

The power transfered from the operating mode of the cavity to the beam equals the product of effective accelerating voltage and beam current:

$$P_b = V_{acc} I_b \approx 2\,\mathrm{MV} \cdot 200\,\mathrm{nA} = 0.4\,\mathrm{W}. \tag{3.14}$$

Because of the small beam peak current of $I_b = 200\,\mathrm{nA}$, P_b is negligible compared to the surface power loss $P_0 \approx 65\,\mathrm{kW}$, and beam loading does not need to be considered. Table 3.5 summarizes important RF quantities computed in the foregoing sections.

Table 3.5: Computed RF quantities of the PIXE-RFQ.

Frequency	f_0	749.48	MHz
Inter-vane voltage	V_0	35	kV
Unloaded quality factor	Q_0	5995	
Capacitance	$\langle C' \rangle$	125.1	pF/m
Stored energy	W_0	82.2	mJ
Surface power loss	P_0	64.5	kW
Beam power	P_b	0.4	W
Maximum surf. el. field	E_s	39.1	MV/m

3.3.2 Coupler Design

The coupler geometry was adapted from the medical HF-RFQ design [18], which was shown to be able to transfer a peak power of up to 100 kW [43]. The coupling loop was enlarged and the overall penetration was adjusted to account for the different cavity shape and higher coupling strength per coupler.[27]

The specific geometric parameters were determined by means of the equivalent RLC circuit introduced in Section 2.1.3, Fig. 2.1, as well as 3D eigenmode simulations of a segment similar to those used for the previously discussed RFQ auxiliaries (Section 3.2.5). The open waveguide is modeled with the help of a perfectly matched layer absorbing boundary condition [182] in order to calculate the external quality factor Q_{ex}. Figure 3.20(a) depicts a CAD model of the simulated geometry, while a photo of the assembled coupler is shown in Fig. 3.20(b). It resembles a magnetic loop antenna that couples to the RFQ magnetic field and terminates a coaxial waveguide. The outer diameter is identical to those of the tuners and vacuum pumping ports (35 mm), simplifying possible replacements

[27] The HF-RFQ for medical applications uses four input couplers to supply a total RF power of 400 kW, or 100 kW per coupler. Initially it was considered to re-machine the PIXE-RFQ coupler from a fifth spare coupler that was constructed for the HF-RFQ. Thus, the PIXE-RFQ coupler geometry was chosen with the aim of minimizing the cost of re-cutting.

and rearrangements. The penetration Δy of the coupler into the cavity and the size $\Delta \ell$ of the loop were chosen such that the desired coupling strength β_c is achieved without perturbing the resonant frequency of the cavity. Figure 3.21 shows frequency shift Δf and coupling strength β_c as functions of Δy and $\Delta \ell$.

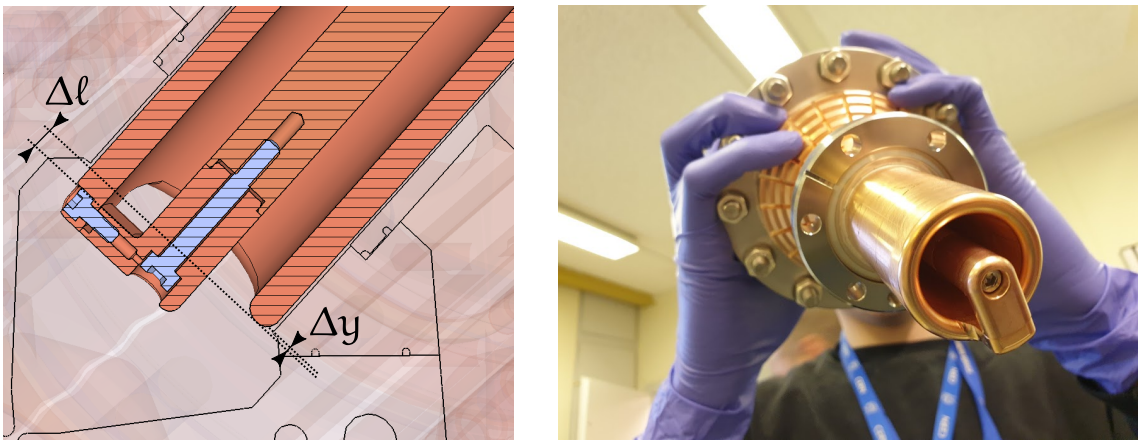

(a) **(b)**

Figure 3.20: CAD model of the PIXE-RFQ input power coupler (a). The coupler penetration Δy and the size of the loop $\Delta \ell$ were adjusted to obtain the desired coupling without perturbing the resonance frequency of the cavity. A photograph of the assembled coupler just before installation is shown in (b).

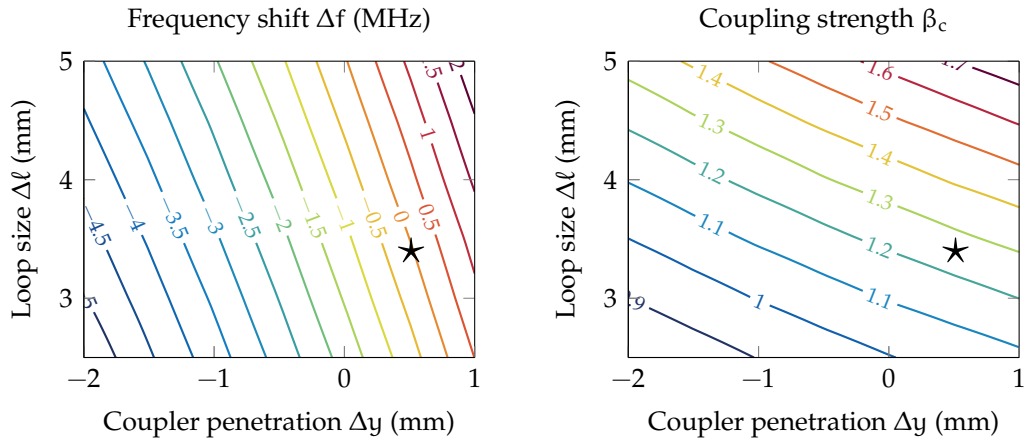

(a) **(b)**

Figure 3.21: Resonant frequency shift Δf (a) in the coupler segment and coupling strength β_c (b) as functions of the coupler penetration Δy and loop size $\Delta \ell$. The simulations were performed for a segment of length $\Delta L = 6\,\text{cm}$ with PML boundaries modeling the feeding waveguide. The optimum parameter tuple is indicated by $\star$.

Figure 3.22(a) shows a polar plot of the reflection coefficient Γ [Eq. (2.30)] describing a circle in the complex plane. The circle is located in the detuned short position, has a radius of $\beta_c/(\beta_c + 1)$, and its center is positioned on the real axis at $-1/(\beta_c + 1)$. Critical coupling is achieved if $\beta_c = 1$ and $\Delta\omega = 0$. The marks

denote operation points of d = 0 %, 1 %, and 2.5 % duty cycle, corresponding to cavity resonant frequency shifts of $\Delta f = 0$ kHz, 74.4 kHz, and 186 kHz, respectively, which occur because of heat-induced deformation of the RFQ cavity. This is discussed in more detail in Section 3.4. For the case of critical coupling ($\beta_c = 1$), input impedance Z_{in} [Eq. (2.31)], reflection coefficient Γ, as well as incident power P_+ and reflected power P_- [Eq. (2.32)] are shown in Fig. 3.22(b) as functions of the frequency shift. The black dashed lines mark the 3 dB bandwidth of the loaded resonator with a quality factor of $Q_\ell = 3000$.

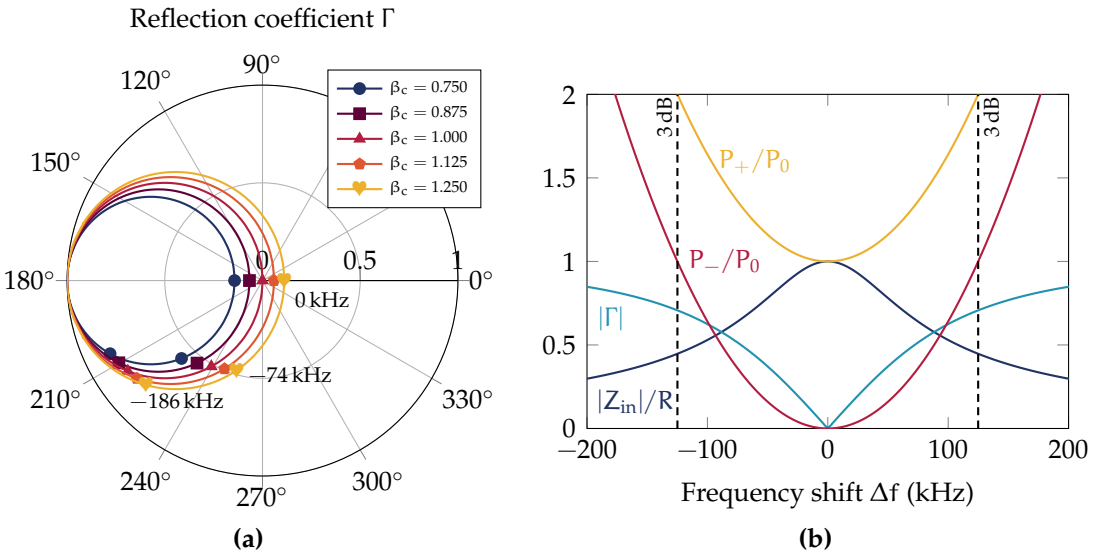

Figure 3.22: Smith chart with reflection coefficient Γ as a function of the coupling strength β_c and the offset $\Delta\omega$ between RFQ natural frequency and RF source frequency (a). The points mark frequency shifts corresponding to a heat-induced deformation at operation with 0 %, 1 %, and 2.5 % duty cycle, respectively. For the case of $\beta_c = 1$ critical coupling, the input impedance Z_{in}, reflection coefficient, as well as feed power P_+ and reflected power P_- are shown in (b) as functions of the frequency; the dashed lines mark the 3 dB bandwidth of the loaded resonator.

By design, the coupler is 25 % over-coupled ($\beta_c = 1.25$) as a safety margin accounting for deviations between simulated and the real Q_0, which is determined by means of RF measurements. The coupler is mounted to a rotatable flange to provide the possibility to adjust the coupling according to the measured Q_0, such that critical coupling is achieved after assembly. Q_{ex} can be adjusted by rotating the coupler around its axis by an angle ϑ. The coupling is proportional to the transmitted power, i.e. to the square of the voltage V induced [Eq. (2.6)] in the coupling loop:

$$V = \omega_0 \mu_0 \iint_{\mathcal{S}} \mathbf{n} \cdot \mathbf{H} \, d\mathcal{S}, \tag{3.15}$$

where $\mathbf{n}$ is the normal vector of the surface $\mathcal{S}$ enclosed by the loop. Since $\mathbf{n} \cdot \mathbf{H} \propto \cos\vartheta$, the power and thus the coupling strength are—assuming homogeneous magnetic field—proportional to $\cos^2\vartheta$. Figure 3.23 shows the coupling

strength β_c as a function for the rotation angle ϑ. The results obtained by numerical simulation resemble the analytical curve almost perfectly.

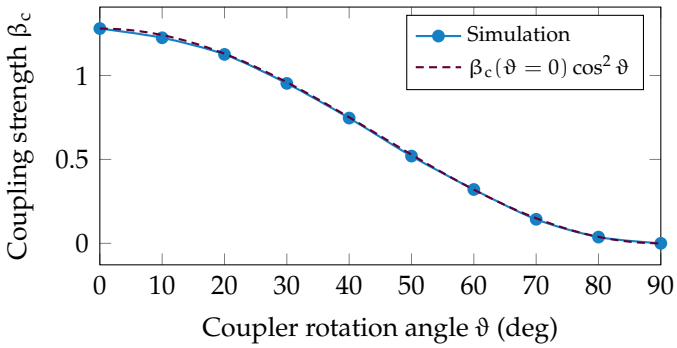

Figure 3.23: Coupling coefficient β_c as a function of coupler rotation angle ϑ. The simulation results (solid curve) confirm the analytical estimate (dashed curve).

Figures 3.24(a) and 3.24(b) show the magnetic field in the vicinity of the coupler tip and in the coaxial waveguide at an RF phase of $\phi = \pi/2$, i.e. when the magnetic field in the RFQ quadrants reaches its peak value. Maxima occur at the edges of the holes for the bolts that attach the separately machined loop piece to the inner and outer conductors. Their magnitudes reach 60 % of the maximum surface magnetic field computed for the entire RFQ (Fig. 3.12). The integrated power loss density and thus the effect on Q_0 are comparable to that of the vacuum pumping port. The RF power is supplied via a standard EIA $3^1/_8$ in coaxial waveguide[28] (50 Ω) filled with air. It is connected to the coupler by a taper and a polyether ether ketone (PEEK) RF window that separates the vacuum from air-filled domains. Figure 3.24(c) shows the electric field amplitude at the taper and the PEEK window when 65 kW are transmitted. Hotspots are located at the contact zones of the PEEK window and the coax inner conductor, as well as on the concave edge of the coupler inner conductor [Fig. 3.24(d)]. The field reaches values of 0.91 MV/m, but is by orders of magnitude lower than the maximum surface field on the RFQ vane tips (39.1 MV/m).

Figure 3.25 shows the transmission $|S_{21}|$ through PEEK window and taper as a function of the frequency. At the operating frequency, the transmission loss amounts to $|S_{21}| = -0.026$ dB.

[28]The EIA (Electronic Industries Alliance) standard RS-225 (EIA-225) [183] standardizes the inner and outer conductor dimensions of high-power RF connectors for 50 Ω.

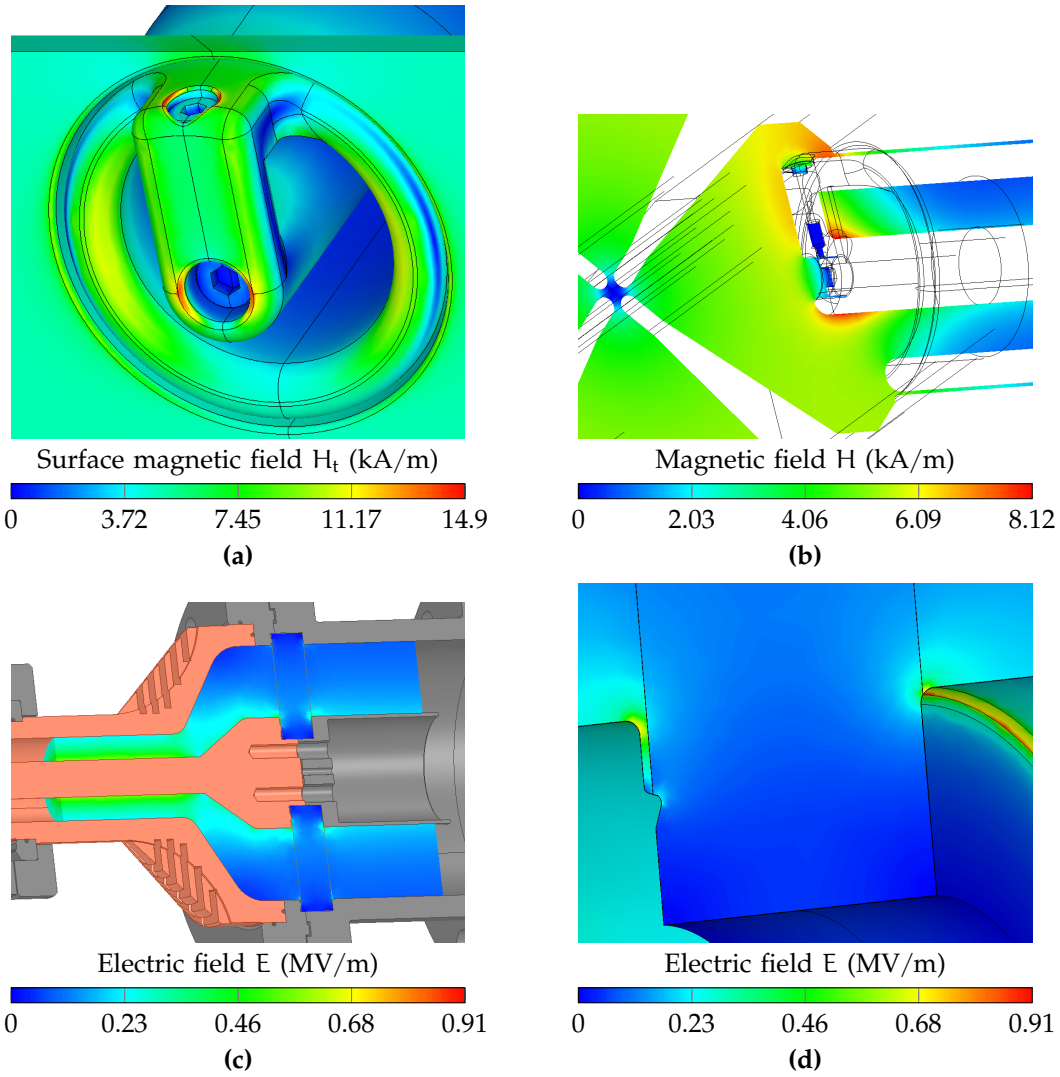

Figure 3.24: Magnetic field at the input power coupler at $\phi = \pi/2$ when the field reaches its maximum value. Hot spots are located on the edges of the bolt holes (a), while generally high currents are located on the edges of the loop and the border of the outer conductor (b). Furthermore, the electric field amplitude at the taper and PEEK window of the input power coupler, for a transmitted power of 65 kW, is depicted in (c). The maximum field of 0.91 MV/m is located at the contact of the PEEK window and the inner conductor of the coaxial waveguide (d).

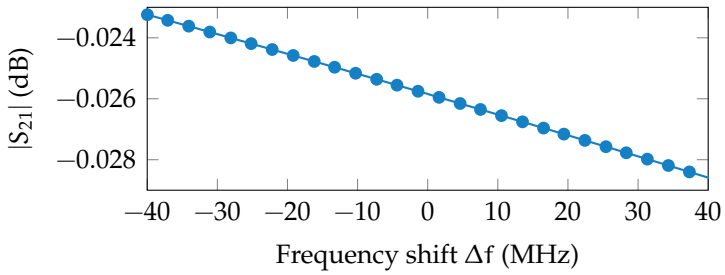

Figure 3.25: Transmission $|S_{21}|$ through PEEK window and taper of the power coupler as a function of the frequency shift Δf. At 749.48 MHz, the transmission loss amounts to -0.026 dB.

3.4 Thermal Simulations

During operation, the RF power deposited in the cavity walls acts as a heat source on the copper structure. The heat is dissipated by eight water cooling channels per module. The resulting temperature increase and gradient cause a deformation of the structure and thus a detuning of the resonant frequency. In the current section, the dependence of this effect on duty cycle, cooling water temperature, and water flow speed is presented. Additionally, the passive cooling of the RFQ auxiliaries is discussed.

The stationary equations arising from the coupled problem were solved with the help of FEM using the tools CST Multiphysics Studio® [91], Ansys Mechanical® [94] and COMSOL Multiphysics® [92]. In favor of a concise text, the author refrains from explaining the theoretical foundations, and instead refers the reader to the relevant literature, e.g. Refs. [68, 88, 92, 184, 185], to name a few.

3.4.1 Heating and Deformation of the Cavity

The average surface power loss density $\langle p_s \rangle = d p_s$, the product of duty cycle $d = t_{pls} f_{rep}$ and peak surface loss density p_s, is generated by Ohmic losses of the surface eddy currents according to Eq. (2.23). Figure 3.26(a) shows the distribution of $\langle p_s \rangle$ for the anticipated operating point. The heat is conducted through copper and steel domains (flanges), both of which need to be considered during the computation. For the simulation of the power coupler (Section 3.4.2), also the characteristics of the PEEK window had to be considered. The relevant thermal and structural properties are listed in Table 3.6.

Table 3.6: Material properties of annealed copper, stainless steel, and PEEK used in the thermal simulations.

		Copper	Steel	PEEK	
Electric permittivity	ε_r	—	—	3.3	
Electric conductivity	σ	58.0	7.0	0	MS/m
Surface impedance (750 MHz)	$\Re\{Z_s\}$	7.14	20.56	∞	mΩ
Thermal conductivity		401	65.2	0.25	W/(m K)
Coeff. of thermal expansion	α_T	16.6	13.5	60	10^{-6}/K
Mass density		8950	7870	1320	kg/m^3
Specific heat (constant pressure)		390	450	1100	J/(kg K)
Young's modulus		120	205	3.8	GPa
Poisson's ratio		0.34	0.29	0.30	

Eight water cooling channels—four each with a diameter of 5 mm and 8 mm—per module provide the corresponding heat sinks. The heat transfer coefficients h between copper structure and cooling water depend on the average water flow speed v_w. Their estimated values [184, 185] are summarized in Table 3.7. Generally, higher flow speeds increase the conductance as the flow becomes more turbulent. As the water cooling channels dissipate the bulk of the power, the

copper-to-air convection, estimated with $h = 10\,W/m^2/K$, is insignificant for the cooling of the cavity itself. However, it gains importance for the passive cooling of the input power coupler discussed in Section 3.4.2.

Table 3.7: Heat transfer coefficients of copper-water and copper-air interfaces.

h ($W/m^2/K$)	Water (1 m/s)	Water (2 m/s)	Air
⌀8 channel	3900	7310	—
⌀5 channel	3900	7500	—
Outer surface	—	—	10

Figure 3.26 shows the distributions of surface losses, temperature, deformation, and stress in 2D and 3D models for the anticipated operating point with $d = 2.5\,\%$ duty cycle, a cooling water temperature of $T_w = 22\,°C$, and an average flow speed of $v_w = 1\,m/s$. Considering only the 2D cross section, the maximum temperature occurs in the vane tip with 3.7 K above the reference temperature of 22 °C (b). This value is significantly exceeded (12.3 K above reference) when taking the 3D end shapes into account. The maximum temperature is located around the center of the end plate and the DSR, since they are only passively cooled via the flange connecting the end plate to the RFQ module (d). Furthermore, the occurrences of maximum von Mises equivalent stress (20.8 MPa) are located in the end plate (e), as it expands significantly more because of its increased temperature compared to the module. However, the stress remains significantly lower than the yield strength of annealed copper (33 MPa). Hence, the low duty cycle makes merely passive cooling of both end plates and RFQ auxiliaries acceptable, as is detailed in Section 3.4.2.

Two 2D effects dominate the frequency shift caused by the cavity deformation, as illustrated by Fig. 3.26(c): the increasing tank size raises the inductance $\mathcal{L}$ of the cavity as the back wall moves by approximately 3 µm. Caused by the temperature gradient between the vanes and the tank, the vane tips move closer towards the beam axis (0.7 µm), increasing the inter-vane capacitance C. While retracting the vanes from the beam axis, the increasing tank size only partially counters this effect. Both effects reduce the resonant frequency, since

$$\frac{\partial f}{f} = -\frac{1}{2}\left(\frac{\partial \mathcal{L}}{\mathcal{L}} + \frac{\partial C}{C}\right) \tag{3.16}$$

holds for the lumped LC circuit. The 3D deformation of the end shape affects the frequency detuning only marginally.

Within the considered parameter domain, the frequency shift is linear with respect to duty cycle and water temperature, which is demonstrated in Fig. 3.27(b). The sensitivities read $\partial f/\partial d = -74.4\,kHz/\%$ and $\partial f/\partial T_w = -13.3\,kHz/K$ for a 1 m/s water flow speed. The latter changes only slightly when doubling the water flow speed, however it would significantly increase the requirements on the chiller in the cooling circuit. Therefore, a flow speed of 1 m/s was chosen. In this

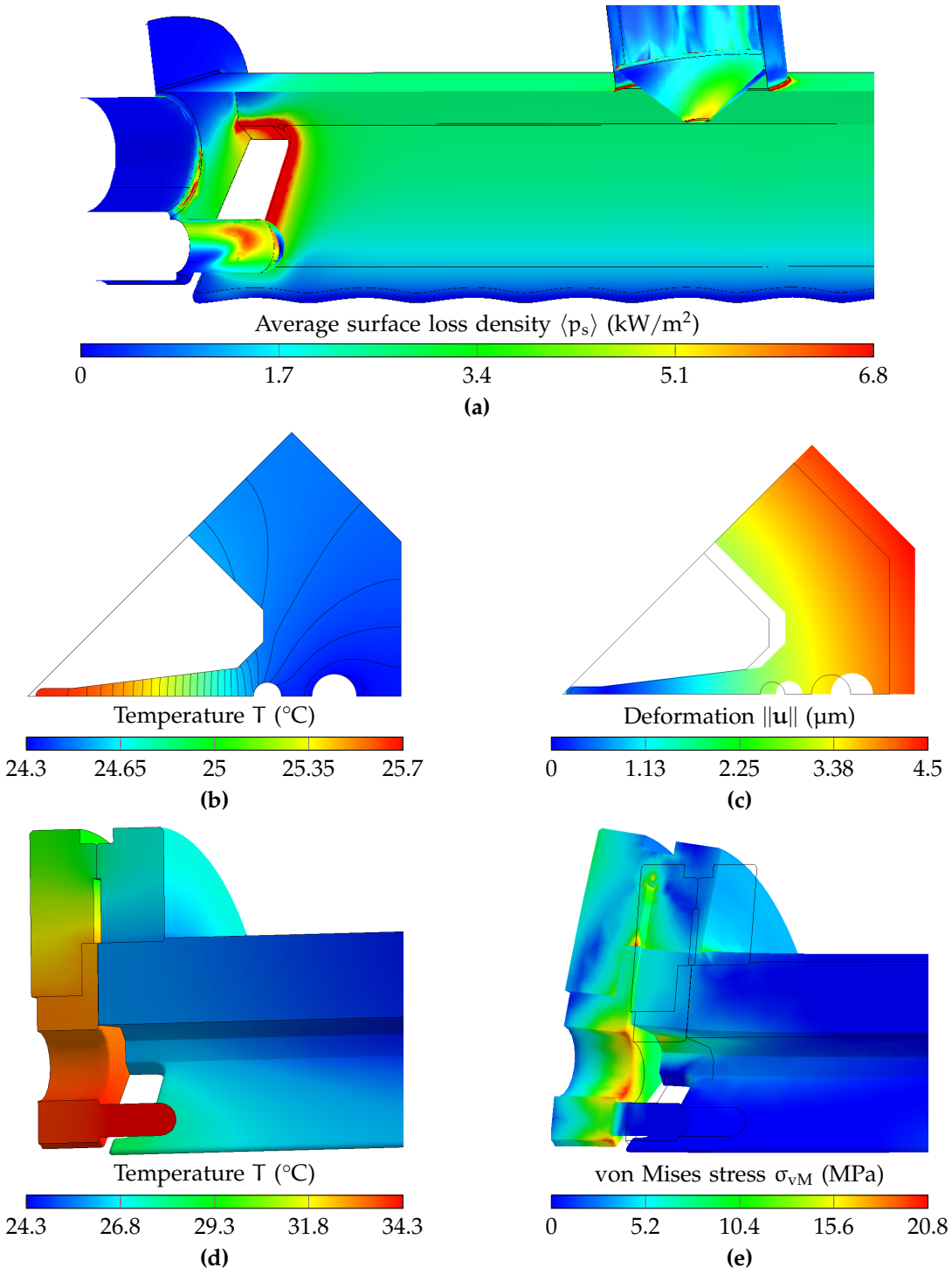

Figure 3.26: Thermal and structural simulation results for nominal operation parameters ($d = 2.5\,\%$, $T_w = 22\,°C$, $v_w = 1\,m/s$, $\star$ in Fig. 3.27). The surface loss density on the upstream end, cavity wall, and tuner tip is reported in (a), where the maximum value is cut off for visualization purposes. The resulting temperature distribution is shown in (b) and (d) for the 2D cross section and the end including a DSR. The corresponding deformation and equivalent stress are shown in (c) and (e).

configuration, the anticipated frequency shift amounts to −186 kHz for nominal operation.

With the 3 dB bandwidth of the PIXE-RFQ cavity amounting to only ±125 kHz, the frequencies of RF source and cavity have to match accurately to minimize the reflected power. Since no further accelerating structures are present, no frequency or phase stability is required at the output of the RFQ, and no frequency feedback loop in the cooling system is required. Instead, the RF power source follows the resonant frequency shift of the cavity. For the proposed range of operation of up to 5 % duty cycle, the effect of the detuning on the beam dynamics is negligible, as is demonstrated in Section 3.5.2, Fig. 3.35.

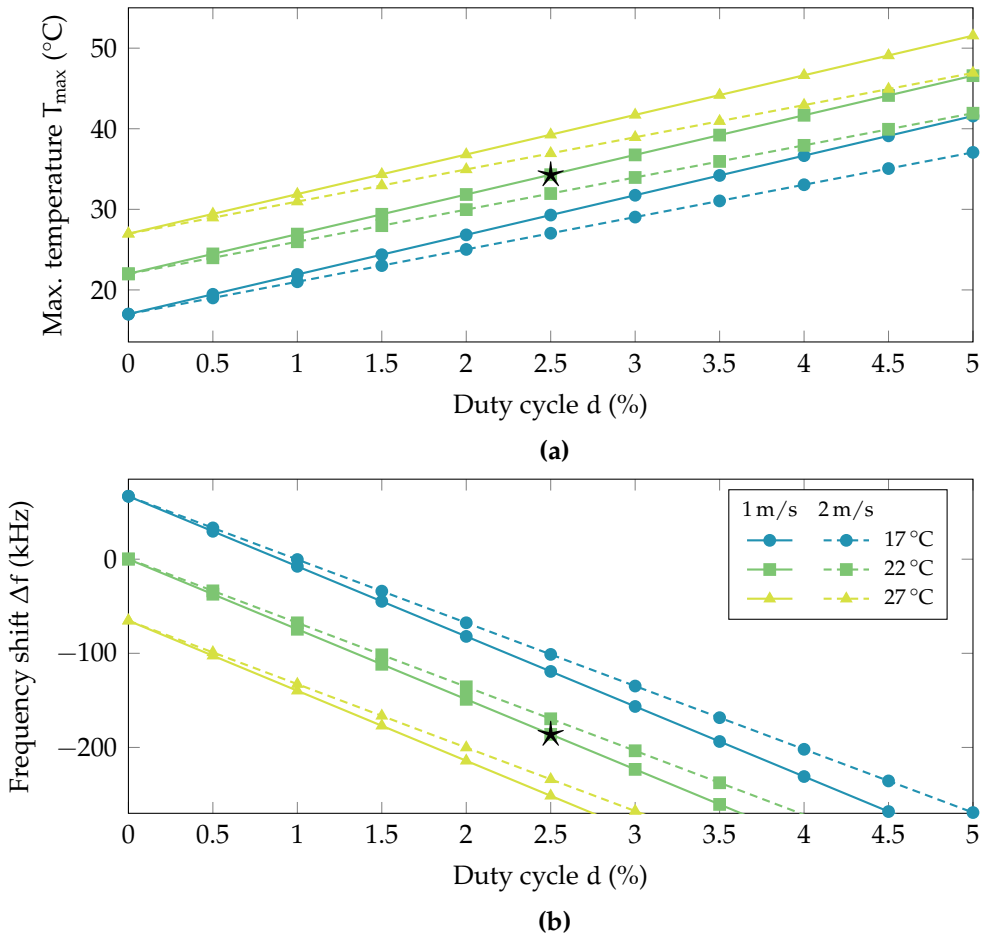

Figure 3.27: Maximum temperature T_{max} in the RFQ cavity subject to heating by RF surface losses (a), located in the dipole rod (DSR), and shift of the resonance frequency Δf of the RFQ cavity subject to heat-induced deformation (b). Both quantities are shown as functions of the duty cycle d, the average cooling water flow speed v_v, and water temperature T_w. Linear behavior is observed within the domain of RFQ operation. The effect of reducing the water flow speed is comparatively small. The nominal operation point is indicated by ⋆.

3.4.2 Passive Cooling of RFQ Auxiliaries

Neither end plates nor auxiliary RFQ components, namely tuners, vacuum pumping ports, the input power coupler, and diagnostic antennas, feature dedicated cooling circuits. Because of the low duty cycle it is sufficient to cool them passively by means of their flange connection to the RFQ cavity and air convection.

Figure 3.28 shows the temperature distributions in vacuum pumping port, tuner, and input power coupler.[29] The highest temperature of 37.9 °C (15.9 K above reference) occurs in the tip of the vacuum pumping port [Fig. 3.28(a)], since here the losses generated by a high surface current density [Fig. 3.14(b)] have to be transported by the comparatively thin walls of the pipe-like geometry of the pumping port. Figure 3.29 shows this value as a function of duty cycle for different cooling water temperatures and average flow speeds. It exceeds the hot spot of 34.3 °C determined in Section 3.4.1 for the tip of the DSR [Figs. 3.26(d), 3.27(a)]. With 35.5 °C, the maximum temperature in the inner conductor of the power coupler is slightly lower. Here, cooling fins machined into the outer conductor exterior surface aid with heat dissipation [Fig. 3.28(c)]. The temperature distribution in the tuner is less critical because of the bulk copper mass of the slug, and only reaches 31.6 °C during nominal operation [Fig. 3.28(b)].

The previously described simulation results neglect the thermal contact resistance between surfaces of same or different materials. In reality, the interfaces feature finite contact conductances h_c and act as additional thermal resistors in series to the bulk material resistances. They raise the temperature in the domains that lie opposite of the heat sinks with respect to the contact surface.

Specific numerical values of h_c are challenging to determine as they depend on many—sometimes unknown—parameters. Complementing a variety of theoretical models, the values are often determined by means of experiments and empirical models; see for instance Refs. [186–189]. Two different material interfaces occur in the thermal analysis of the PIXE-RFQ: The brazed surfaces between copper structures and attached stainless steel flanges, as well as the bolted connection between two flanges. For the brazed interfaces one can assume perfect conductance $h_c \to \infty$ in the steady-state solution, as the thermal resistances of these interfaces are negligibly small[30] compared to those of the bolted connections [190] and the cooling water channels.

The contact conductance between the bolted flange surfaces can be obtained by the theoretical Mikić model for pressed contacts [187, 191]. The simplified model shown in Fig. 3.28(a) assumes that the entire heat flux is transmitted via

[29] The heat dissipation in the diagnostic pick-up antennas is not considered because of their low transmitted power of only 1 W.

[30] The thermal contact resistance increases for low-quality brazed interfaces, or if by orders of magnitude larger heat fluxes are conducted.

the touching flange surfaces.[31] Figure 3.30 shows by the example of the vacuum pumping port the contact conductance and the resulting maximum temperature as functions of the contact pressure p_c.

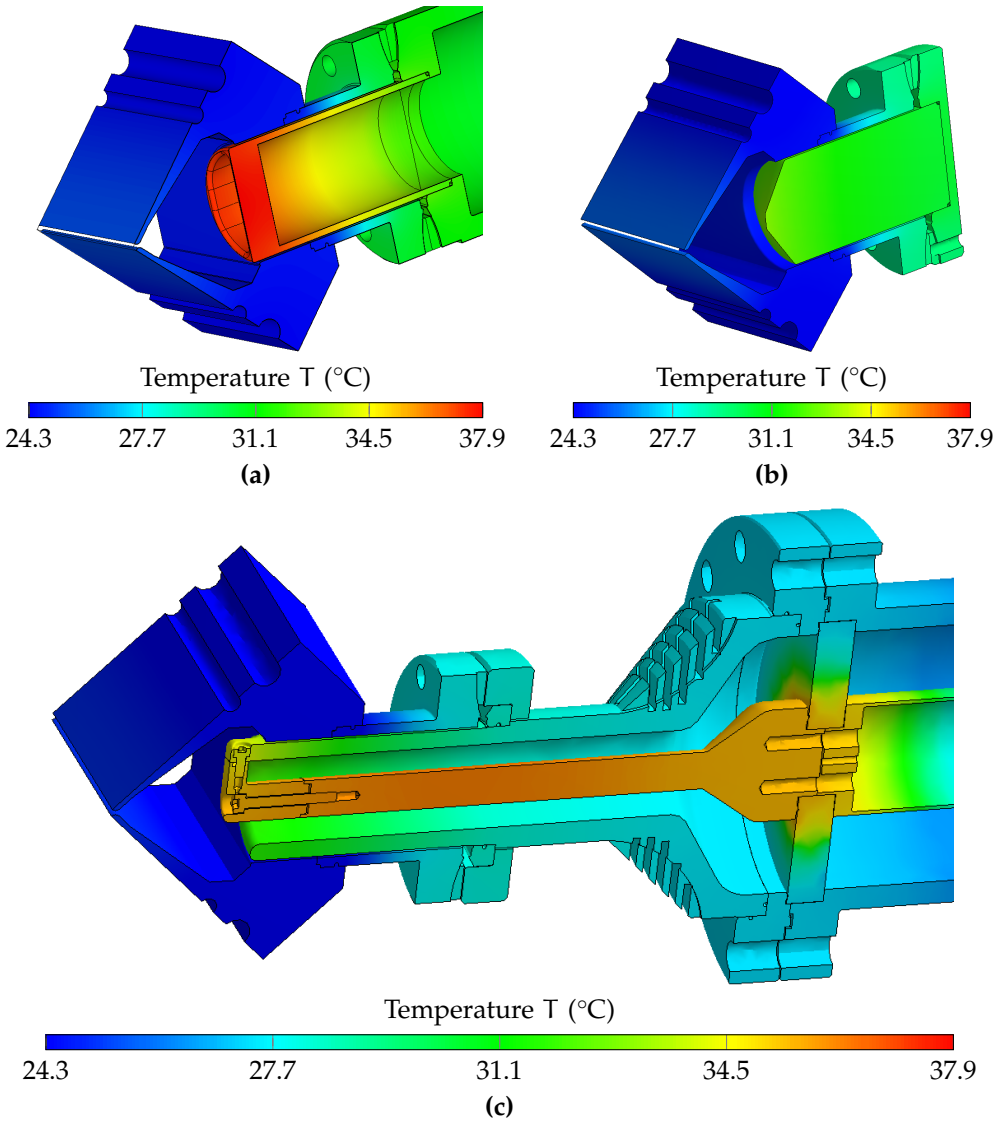

Figure 3.28: Thermal simulation results of the passively cooled RFQ auxiliaries for nominal operation parameters ($d = 2.5\,\%$, $T_w = 22\,°C$, $v_w = 1\,m/s$, $\star$ in Fig. 3.27). The highest temperature of $T = 37.9\,°C$ is found in the vacuum pumping port (a), slightly higher than the maximum in the coupler inner conductor (c), and significantly exceeding the temperature of the tuner (b). The plots use the same scale for easier comparison.

[31] With a real ConFlat flange [192], contact is not only established by the stainless steel surfaces, but also by a copper gasket that is squeezed between the knife-edges of the steel flanges. By filling surface defects in the flange, the gasket provides the actual leak-tight seal. The heat flux transmitted through gasket and clamping bolts is neglected in the simulation setup.

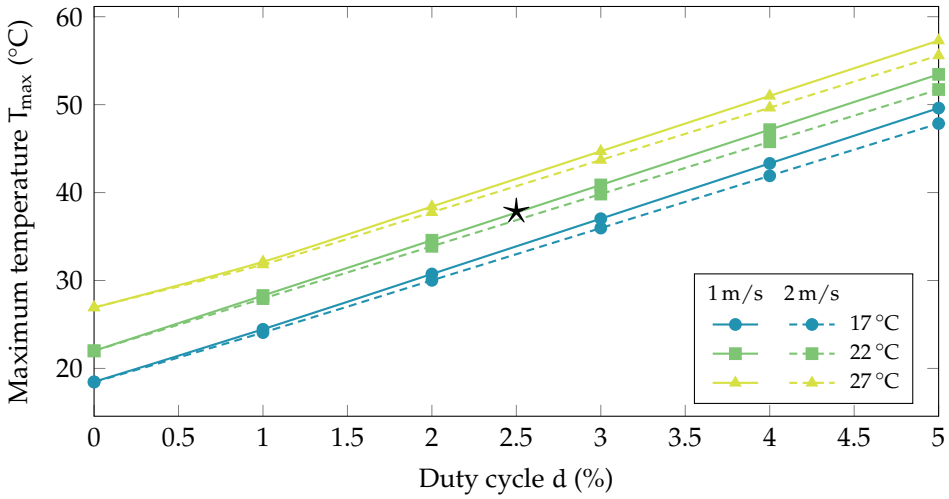

Figure 3.29: Maximum temperature T_{max} in the vacuum pumping port subject to heating by RF surface losses, shown as a function of the duty cycle d, the average cooling water flow speed v_v and temperature T_w. The nominal operation point is indicated by $\star$.

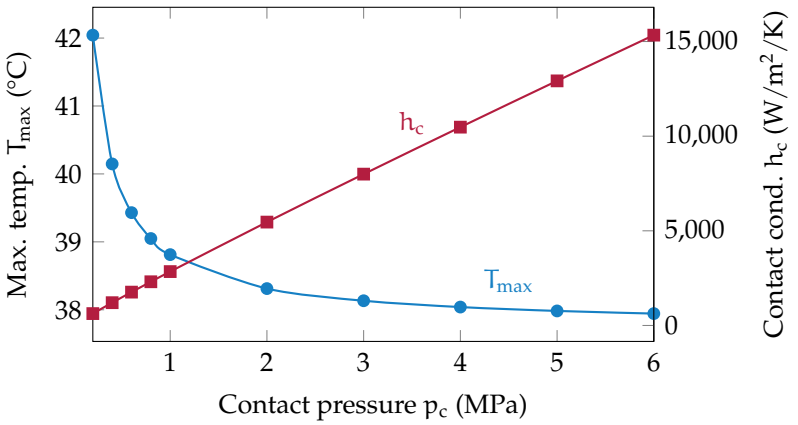

Figure 3.30: Contact heat conductance coefficient h_c and resulting maximum temperature T_{max} in the vacuum pumping port as functions of the flange contact pressure p_c. The values are given for nominal operation parameters ($d = 2.5\,\%$, $T_w = 22\,°C$, $v_w = 1\,m/s$).

3.5 Beam Dynamics Simulations

The final RF design was validated by means of beam dynamics simulations, where a distribution of macroparticles was tracked through the electromagnetic field. First, in order to estimate the reliability of the simulations, a comparison was drawn between four distinct models used to describe the RFQ beam dynamics. The effect of deviations of inter-vane voltage and frequency on the beam were evaluated. Lastly, the acceptance of the PIXE-RFQ and its lost particles were investigated.

Each particle in the beam experiences the Lorentz force [Eq. (2.38)] by the external electromagnetic field provided by the RFQ electrodes. As the magnetic field practically vanishes in the vicinity of the beam, only forces caused by the electric field need to be considered. The particles are also subject to collective effects which arise from the interaction of the particles with each other. At low velocities $\beta \ll 1$, space charge forces caused by Coulomb interaction between the particles, as well as image charges on the RFQ electrodes, have defocusing effects on the beam [1, 106, 193]. In the case of the PIXE-RFQ, however, these forces are negligibly small because of the low beam current of only 200 nA at the output plane. They can be safely ignored, greatly simplifying the simulation.

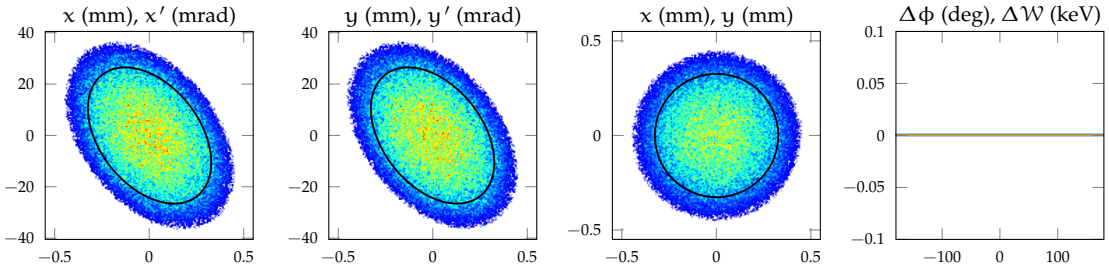

Figure 3.31: Phase space with 10^5 macroparticles at the input matching plane of the PIXE-RFQ. Approximately 30 % of the continuous input beam are captured and accelerated. The depicted input distribution is assumed during design and the following beam dynamics simulations.

Figure 3.31 shows phase space projections of the unbunched input beam, as it is expected from the proton source and low energy beam transport (LEBT) before the RFQ. In the plots, the ellipse corresponding to the geometric 4-rms emittance $4\tilde{\varepsilon}$ is indicated as a black line. According to the Lapostolle convention [1, 194], the 4-rms emittance contains approximately 90 % of a Gaussian beam.

3.5.1 Model Comparison

Figure 3.32 shows the phase space projections at the output matching plane if the unbunched beam shown in Fig. 3.31 is applied at the input matching plane, computed based on four distinct models.

The first row, Fig. 3.32(a), depicts the result of PARMTEQ [102], the tool used to design the PIXE-RFQ in terms of beam dynamics. It relies on an analytic po-

tential representation using the eight lowest-order terms of the RFQ multipole expansion [eight-term potential function, Eq. (2.46)], which is valid for the electric field between the vane tips. The expansion coefficients were obtained from lookup tables that have been precomputed for different vane geometries [100].

The coefficients can also serve to generate a (quasi-static) field map for other tracking tools: The distribution shown in Fig. 3.32(b) was obtained when tracking through the eight-term potential field map using Travel [98]. Virtually identical results were produced by TraceWin [195] or RF-Track [99] with the same field map. They show minimal differences compared the PARMTEQ results for the transverse planes. For the longitudinal plane (right-most plots), the phase spaces feature a near-identical shape, however, the average energy and phase are slightly offset. Furthermore, the transmission $\mathcal{T}$, defined as the fraction of particles that are captured, accelerated and reach the output plane, is lower (29.3 % compared to 32.4 %).

From the initial design, a 3D CAD model of the vane tips was generated based on the longitudinal vane profile. Figures 3.32(c) and (d) show the phase spaces after tracking through field maps of a quasi-electrostatic simulation performed with COMSOL Multiphysics® [92], and a full RF simulation of the entire RFQ cavity with Ansys HFSS® [89], respectively.[32]

Table 3.8 summarizes important phase space parameters of the four discussed models: particle transmission, final energy and rms energy spread, the final synchronous phase, and the normalized emittances in the horizontal, vertical, and longitudinal planes. For the HFSS field map, the transmission amounts to 29.0 %. The corresponding final average energy is $\mathcal{W}_{\text{out}} = 2.028\,\text{MeV}$ and the final synchronous phase reads $\phi_s = -13.4°$.

Table 3.8: PIXE-RFQ output phase space parameters for the different field models.

		P.TEQ	8-term	COMSOL	HFSS	
Transmission	$\mathcal{T}$	32.44	29.34	29.93	29.02	%
Energy	$\mathcal{W}_{\text{out}}$	2.015	2.027	2.028	2.028	MeV
Rms energy spread	$\sigma_{\mathcal{W}}$	4.0	3.7	3.5	3.3	keV
Sync. phase	ϕ_s	-14.7	-17.2	-12.8	-13.4	deg
Hori. rms emit. (norm.)	$\varepsilon_{xx'}$	0.0170	0.0169	0.0165	0.0166	π mm mrad
Vert. rms emit. (norm.)	$\varepsilon_{yy'}$	0.0173	0.0169	0.0170	0.0169	π mm mrad
Long. rms emit. (norm.)	$\varepsilon_{\phi\mathcal{W}}$	0.0088	0.0086	0.0089	0.0124	π deg MeV

The observed differences between the models may partially be explained by the different algorithms used by the codes Travel and PARMTEQ, particularly their particle loss models. While Travel is a general purpose tracking tool using field maps, PARMTEQ is tailored to the characteristics of RFQ and makes

[32] As a result of an eigenmode simulation, the HFSS field map is initially of arbitrary magnitude. Furthermore, because of the non-uniform capacitance profile [Fig. 3.7(b)] and consequent detuning of the RFQ cavity, the inter-vane voltage of the HFSS model is non-uniform as well. The field map was scaled by a longitudinally-dependent factor such that $V_0 = 35\,\text{kV} = \text{const.}$ along the RFQ, corresponding to a perfectly tuned cavity.

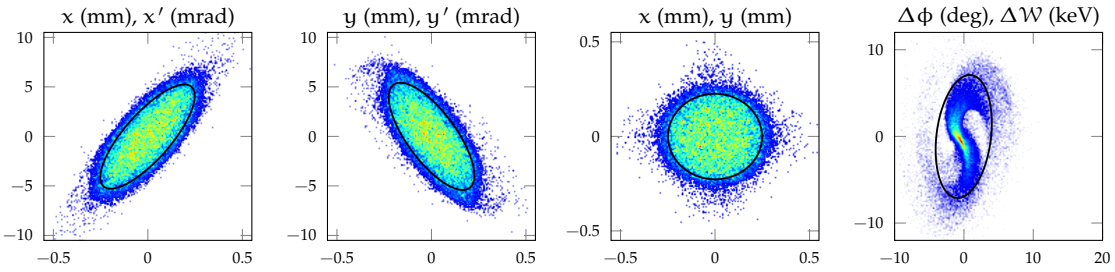

(a) PARMTEQ (analytic, quasi-static)

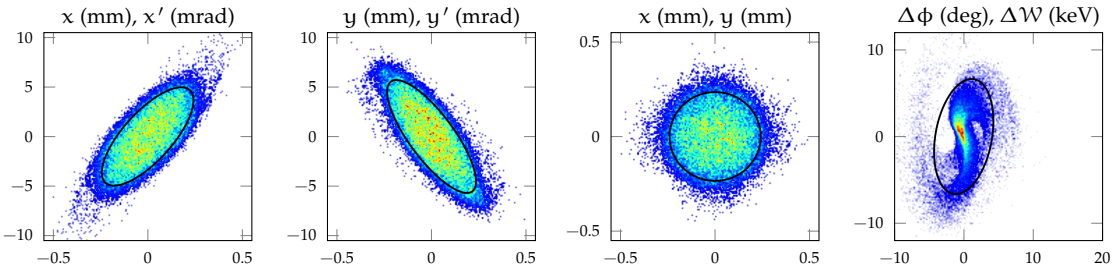

(b) Travel, 8-term potential field map (analytic, quasi-static)

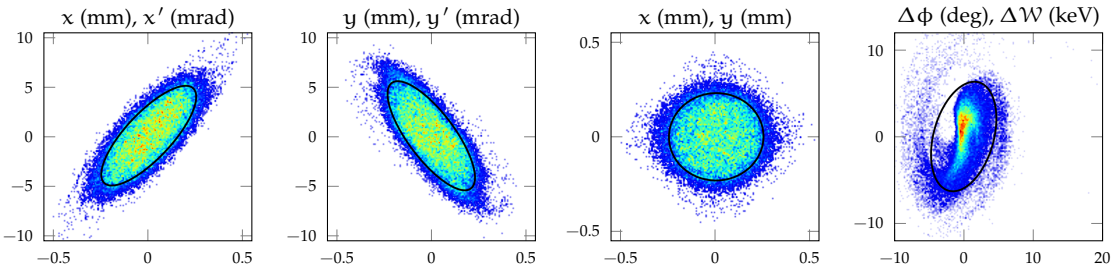

(c) Travel, COMSOL field map (FEM, quasi-static)

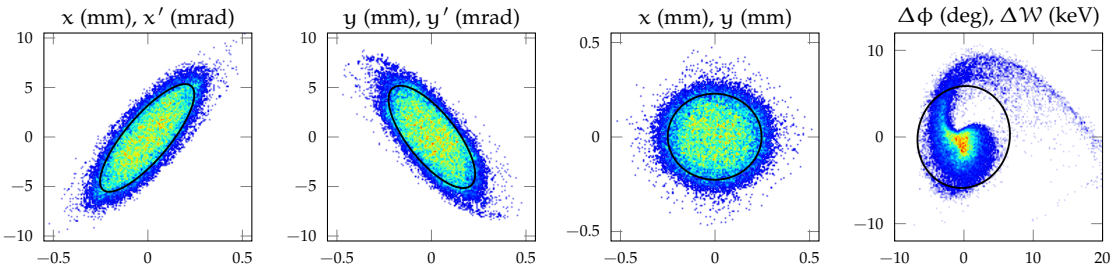

(d) Travel, HFSS field map (FEM, RF)

Figure 3.32: Side-by-side comparison of the PIXE-RFQ output phase spaces simulated with four different models: Design phase space obtained from the PARMTEQ tool chain (a). The result of tracking through a generated 8-term potential field map with the same multipole coefficients as in (a) using Travel is shown in (b). The tracking results of COMSOL and HFSS field maps that were obtained from numerical simulation of the actual 3D vane geometry are visualized in (c) and (d).

certain simplifications. Specifically, in Figs. 3.32(a) and (b), a circular aperture is assumed, while with the FEM-based field maps (c) and (d) a particle collision with the actual 3D vane geometry is simulated. For more details, the reader is referred to the documentations of the respective tracking tools [98, 99, 102, 195]. Disadvantageous for the FEM simulations (c) and (d) is the numerical noise produced by their finite element meshes. Careful meshing is required to obtain an accurate solution for the electric field between the vane tips free of artifacts, while the field representation used for the cases (a) and (b) is smooth by definition.

Instead of the phase spaces, one may also examine the coefficients of the eight-term potential function [Eq. (2.46)] to validate the RF field. Figure 3.33 shows the eight coefficients[33] extracted from the HFSS field map as functions of the longitudinal cell position (solid lines; see Appendix B.2 for details on the extraction). The respective values obtained from PARMTEQ [102] serve as references (dotted lines). Of special interest are the quadrupole focusing strength $A_{0,1}$ and the acceleration efficiency $A_{1,0}$. For these terms, the agreement is very good with an error less than 1 %. A possible explanation for the nevertheless noticeable differences in phase space (Fig. 3.32) is the tapering of the vane tips, which is required to obtain a smooth continuous surface between two consecutive RFQ cells. In the eight-term potential function representation, the tapering is approximated by defining the coefficients $A_{\mu,\nu}$ as piecewise linear functions, whose support points are located at the end of each cell [1]. Another error source is the numerical noise of the HFSS mesh, particularly visible in the first 10 cm for the $A_{3,0}$ component. The gap between the two RFQ modules (shown in Fig. 3.6(b)) is observed to have a particular effect on the multipole components with quadrupole field patterns, and is visible as a small dent in the respective $A_{0,1}$ and $A_{2,1}$ lines.

As a final note, it is emphasized that the differences shown in Fig. 3.32 and Table 3.8 amount to merely a few percent, such that while they are clearly visible in simulation, they will likely not be measurable in the real RFQ setup. Thus, the discrepancies between the design tools are generally negligible for practical purposes.

[33] The higher-order terms are multiplied by their accompanying modified Bessel function $\mathcal{I}_{2\nu}(\mu k r_0)$. This scaling not only helps with visualization, but also allows to compare their contribution to the overall field to that of the quadrupole component $A_{0,1}$ [100].

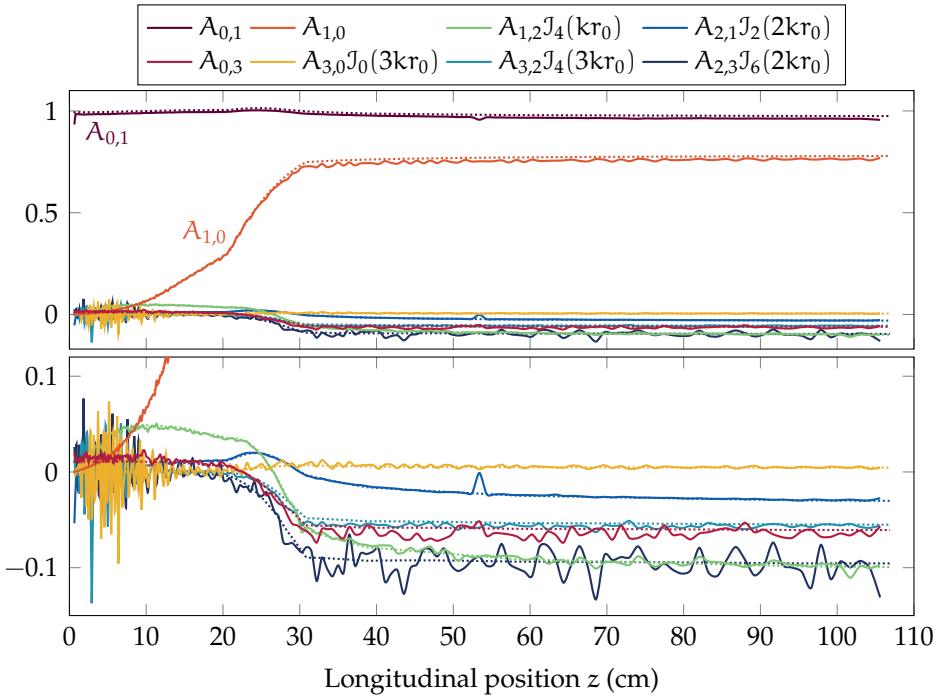

Figure 3.33: Comparison between the eight multipole expansion coefficients computed from the HFSS electric field (solid) and their design values (dotted) for each RFQ cell. The bottom plot enlarges a region of the upper graphic to enhance the visualization of the higher order terms.

3.5.2 Effect of Inter-vane Voltage and RF Frequency

Figure 3.34 shows the transmission $\mathcal{T}$, final energy $\mathcal{W}$, and final synchronous phase ϕ_s as functions of the inter-vane voltage V_0. The shape of the curves for V_0 smaller than the design value (35 kV) originates in the bunching section, i.e. the first few centimeters of the PIXE-RFQ. A minimum voltage is required to form the bucket and capture the particles from the unbunched input beam. The differences between the four models described above are also visible here. For both models that rely on the eight-term potential function, the threshold voltage is located at roughly 33.7 kV, while the value reads approximately 34.4 kV for the HFSS field. In the stable region ($V_0 \geqslant 35$ kV), a weak linear dependence of transmission and synchronous phase on V_0 is observed. The final energy—fixed by the vane geometry with cell length $\beta\lambda/2$—saturates at the design value, while ϕ_s reduces with increasing voltage, as the particles receive more energy in a cell and arrive earlier at the center of the next cell. The smaller synchronous phase increases the size of the RF bucket and thus the capturing capabilities of the RFQ, giving rise to higher transmission values. Here, a near-perfect agreement between tracking results of the three field map-based models is observed, while a—likely not measurable—difference of few percent remains with respect to the PARMTEQ results, confirming the observations made in Section 3.5.1.

A second parametric analysis was conducted to study the influence of the RF frequency on the beam dynamics. This is of special interest in conjunction with

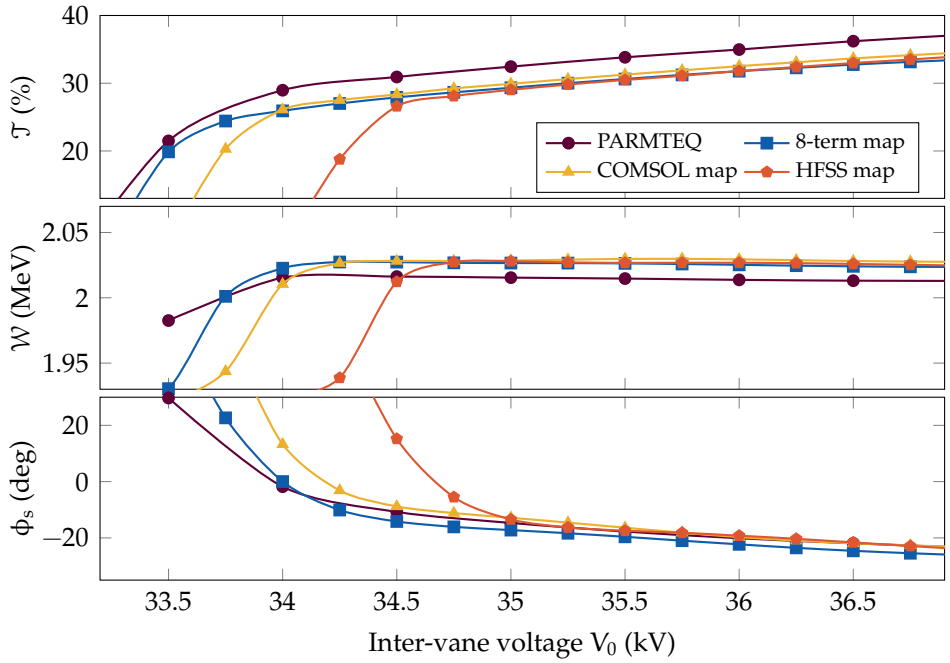

Figure 3.34: Transmission $\mathcal{T}$, final energy $\mathcal{W}$, and final synchronous phase ϕ_s as functions of the inter-vane voltage V_0 for the four investigated field models: tracking by the PARMTEQ code, as well as tracking by Travel through an 8-term potential field map and through FEM field maps produced from COMSOL and HFSS models.

the thermal simulations performed in Section 3.4.1: Figure 3.35 demonstrates that the dependences of transmission and final energy on the frequency are approximately linear. An increase in frequency means the particles arrive later at the center of each cell, and thus closer to the crest ($\phi = 0$) of the electric field oscillation. This results in a decrease of the longitudinal phase acceptance, lowering the transmission, and in an increase of the integral electric field seen by the particle, increasing the final energy.

The effect of a heat-induced detuning of $-186\,\mathrm{kHz}$ corresponding to 2.5 % duty cycle is negligibly small. This validates the particular operation principle of the PIXE-RFQ: Instead of tuning the cavity by means of the cooling system to compensate heating and maintain a constant resonance frequency—as would be necessary if more RF accelerating structures were present downstream of the RFQ—the frequency shift is accepted and the RF source follows the cavity to minimize power losses through reflection in the coupler.

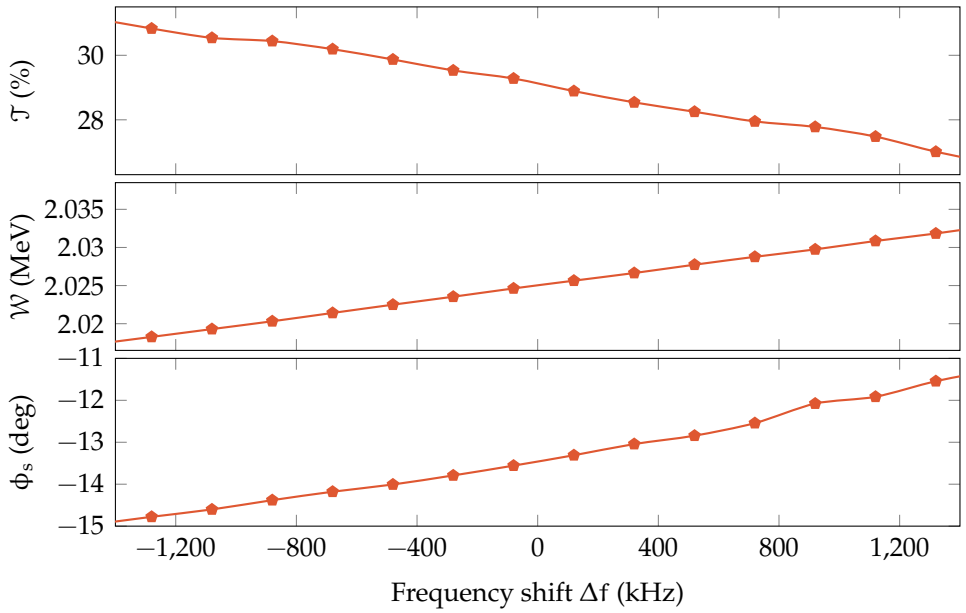

Figure 3.35: Transmission $\mathcal{T}$, final energy $\mathcal{W}$, and final synchronous phase ϕ_s as functions of the offset Δf from the design RF frequency of 749.48 MHz. The magnitude of the frequency shift caused by the heat-induced deformation of the cavity is expected to be less than 200 kHz.

3.5.3 Beam Envelope, Acceptance, and Lost Particles

The PIXE-RFQ features an innovate beam dynamics design (Fig. 3.1), that sacrifices transmission in favor of a short length and minimized power consumption [27, 31, 40]. To quantify particle losses, one distinguishes between longitudinal losses, when particles leave the stable area bounded by the longitudinal separatrix but still reach the end of the accelerator at a lower energy, and transverse losses, when they collide with the RFQ electrodes. As by design 70 % of the input beam are lost, it is important to verify that the lost particles do not collide with the electrodes at high energies. High-energy particles hitting the vane tip could induce radioactivity by neutron activation, posing a safety risk and decreasing performance by eroding the RFQ electrodes.

Figure 3.36(a) shows the longitudinal acceptance of the PIXE-RFQ with its typical golf club shape. At nominal input energy (20 keV), approximately 30 % of the particles are accepted. The code RF-Track [99] allows for computing individual particle collisions with the real 3D electrode geometry. Using this feature it was confirmed that most of the lost particles are lost longitudinally and stay confined by the RFQ focusing system, progressing to the output matching plane without being accelerated. The transverse losses amount to less than 0.5 % and approximately occur at injection energy. Figure 3.36(b) shows the kinetic energy spectrum of the lost particles.

In Fig. 3.37 the evolution of the beam along the RFQ, simulated using RF-Track [99], is shown in terms of the Twiss parameters $\tilde{\alpha}$ and $\tilde{\beta}$. Additionally, the rms beam envelopes σ_x and σ_y for the horizontal and vertical planes, respectively,

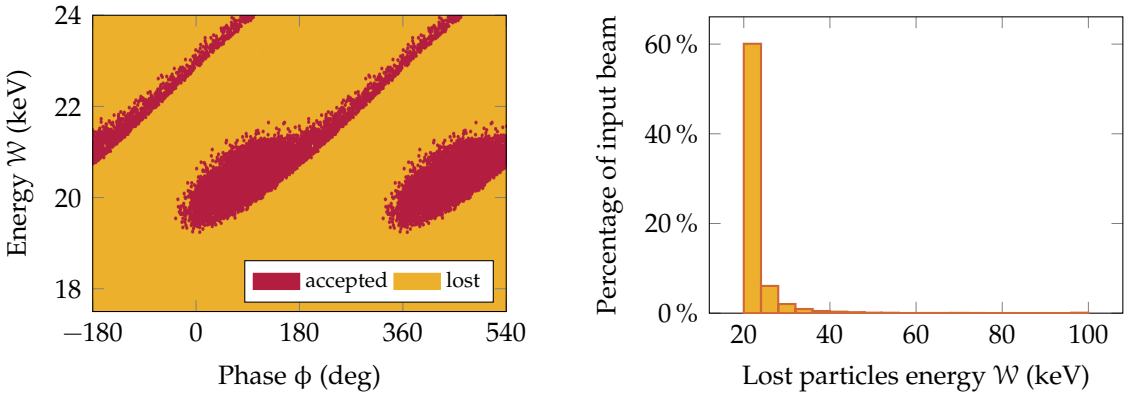

Figure 3.36: Acceptance and lost particles of the PIXE-RFQ. The longitudinal acceptance with its typical golf club shape is depicted in (a) over the span of two RF cycles. The energy spectrum of the lost particles is reported in (b). Virtually all losses occur at an energy less than 100 keV. The overwhelming majority drifts to the end of the RFQ without being accelerated, while the particles colliding with the vane amount to less than 0.5 %. These collisions furthermore occur only at injection energy or slightly above.

are depicted. From the trajectories obeying the Mathieu equation [121], both the slow oscillation at betatron frequency, and the fast flutter at RF frequency are clearly visible. The plot of the rms envelopes verifies that the beam is significantly smaller than the minimum aperture $a = 0.7$ mm at all times.

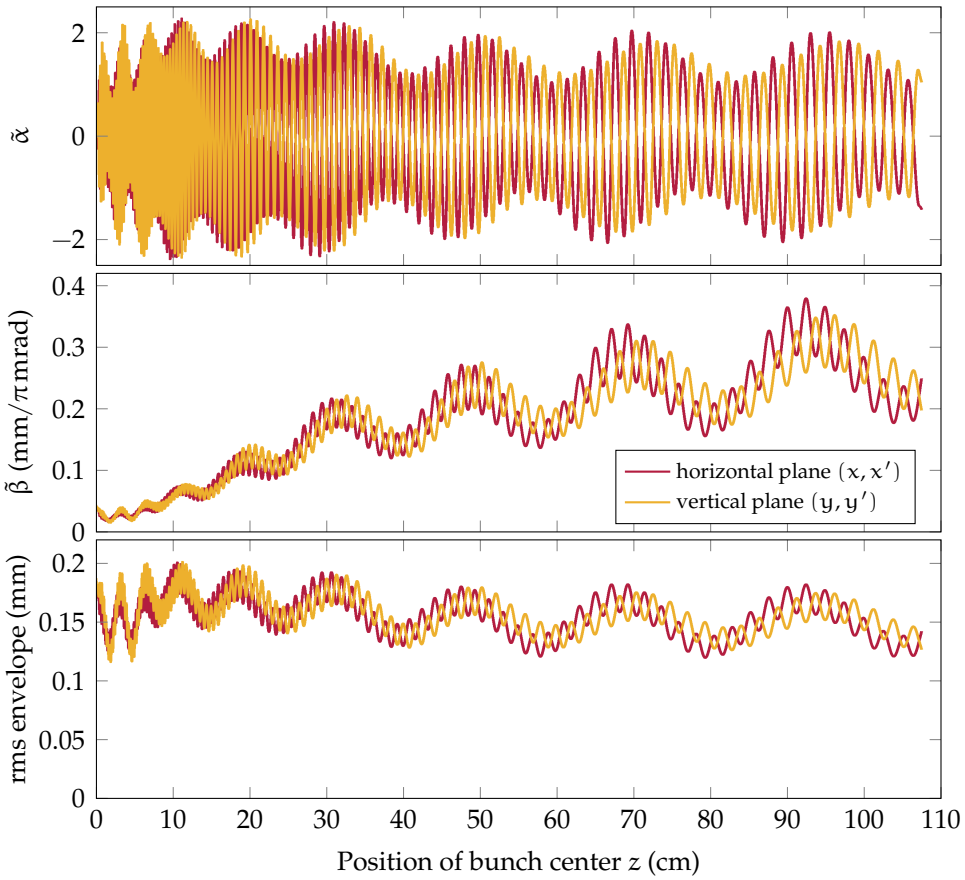

Figure 3.37: Beam evolution along the PIXE-RFQ. The Twiss parameters $\tilde{\alpha}$, $\tilde{\beta}$, and the rms beam envelope are shown as functions of the bunch center longitudinal position z for both transverse planes. The envelope is smaller than the minimum aperture at all times. The high-frequency oscillations correspond to the alternating focusing lattice acting on the beam.

3.6 Conclusion

The compact, transportable PIXE-RFQ linac, operating at 750 MHz, will provide 2 MeV protons for PIXE-analysis over a length of just one meter. Starting from the vane-tip geometry given by the beam dynamics design, Chapter 3 discusses the complete RF design process of the PIXE-RFQ. Inspiration was drawn from the HF-RFQ operating at the same frequency. Geometric dimensions arising from the design studies were provided for the construction of both RFQ cavity and auxiliaries. The design was validated by means of thermo-mechanical and beam dynamics simulations.

The RF design studies were initiated with an optimization of the 2D cross section for desired resonance frequency and minimum power loss, where geometric restrictions such as vane shape and thickness, cooling channel placement, and simplicity of construction were considered. Then, the 3D effects of the vane modulation—maximum surface electric field and inhomogeneous capacitance profile—were taken into account. It was confirmed that the maximum

surface electric field is significantly lower than that achieved in existing RFQs operating and the same and at lower frequencies. A transmission line model was constructed to facilitate the calculation of spectral properties. The accuracy of this model could be confirmed by means of 3D eigenmode computation. It was used to determine the shape of the RFQ ends. With the help of dipole-mode detuning rods, a frequency separation larger than 12 MHz was achieved between the operating mode and the next-closest parasitic modes. Furthermore, the geometries of vacuum pumping ports, tuners, and diagnostic RF pickup antennas were determined.

Based on previously determined capacitance profile and quality factors obtained for the auxiliaries, a segmented model was used to calculate the total RF power loss of the RFQ. This approach proved to be highly accurate, providing a result deviating from the 3D eigenmode computation by less than 1 %. The total RF power loss amounts to 65 kW, corresponding to an unloaded quality factor of 6000. A single magnetic-loop input power coupler was then designed to supply the RF power. The coupler features an over-coupling margin of 25 %, which can be fine-tuned by means of a rotatable flange. Furthermore, matching conditions, transmission loss through RF window, and maximum field amplitudes in the coupler were determined.

The thermo-mechanical behavior of the RFQ subject to RF power loss was studied to anticipate the resulting temperature distribution and deformation. Because of the low duty cycle, neither maximum temperature, deformation, nor stress reach critical values. It was confirmed that an exclusively passive cooling of end plates and RFQ auxiliaries is sufficient for nominal operation. Furthermore, the frequency shift originating in the cavity deformation was calculated for different duty cycles, cooling water temperatures, and flow speeds. The choice of a cost-efficient cooling system, running at constant water temperature and flow speed—without frequency feedback—was validated. The resonance frequency thus decreases linearly with the duty cycle, reaching $\Delta f \approx -190\,\mathrm{kHz}$ for the nominal operating point at 2.5 % duty cycle. In order to minimize the power reflected from the RFQ cavity, the RF power source has follow this shift.

Finally, the RFQ beam dynamics were simulated to validate the RF design. Four distinct combinations of particle tracking tools and field models were used: The output phase spaces obtained from the RFQ design tool PARMTEQ, a multipole potential function field map, an electrostatic field map, and an RF field map were compared. Generally very good agreement was observed, whereas differences of a few percent—likely too small to be measured—persisted, for which possible explanations were discussed. Then, the phase space parameters were studied as functions of the inter-vane voltage and the RF frequency. The studies confirmed that the frequency shift caused by the heat-induced deformation is acceptable for beam operation. Lastly, the beam envelopes, the longitudinal acceptance, and the energy spectrum of the lost particles were computed. As the PIXE-RFQ—by design—captures and accelerates only 30 % of the input beam, it was verified that all particle losses occur at or close to injection energy, avoid-

ing copper activation and vane deterioration. The overwhelming majority of the particles drifts to the end of the RFQ without being accelerated, while the particle collisions with the vane amount to less than 0.5 %, all of which occur at low energy.

In the following chapter, low-power RF measurements conducted on (parts of) the PIXE-RFQ during and after construction are presented. Furthermore, the field and frequency tuning of the RFQ cavity is discussed.

4 RF Measurements and Tuning of the PIXE-RFQ

In any four-vane RFQ, field tuning plays an important role in order to achieve the desired transverse and longitudinal field distribution. Manufacturing imperfections and misalignments, but also certain design choices like the piecewise-constant cross section, lead to perturbations of the capacitance and inductance distribution. Consequently, the ideal quadrupole field of the operating TE_{210} mode is perturbed. The perturbation must be corrected by means of bead-pull measurements and movable piston tuners.

In this chapter, the RF measurements and tuning procedure of the PIXE-RFQ are presented. First, Section 4.1 discusses prerequisites to the measurements. Section 4.2 reports measurements that where carried out during construction of the RFQ on its two modules and the input coupler. In Section 4.3, the RFQ tuning procedure is presented, the improved tuning algorithm is explained, and the corrections of field and frequency over the tuning steps are reported. Finally, quality factor measurements and pickup antenna calibration are discussed in Sections 4.4 and 4.5, respectively.

4.1 Prerequisites

This section provides the reader with contextual information regarding the measurements, listing the utilized devices before briefly reviewing frequency correction with respect to temperature and medium, as well as the principle of bead-pull measurements. Lastly, the tuning goals are formulated.

4.1.1 Experimental Setup

Unless stated otherwise, all measurements were carried out by means a Keysight E5061B vector network analyzer (VNA) with a frequency range of 100 kHz to 3 GHz [196]. It features two Type-N sockets, each of which was connected to a rugged phase-stable Keysight 12 ft (3.7 m) RF cable with a characteristic line impedance of 50 Ω. The VNA was calibrated with the help of a Keysight

85032F Type-N 50 Ω mechanical calibration kit [197], where the calibration planes were located at the connectors between RFQ and RF cables.

The temperature, which is critical for frequency correction (see following section), was recorded by means of Hanna Instruments HI98509 Checktemp® 1 thermometers [198]. The digital thermometers feature a scale resolution of 0.1 K and an accuracy of ±0.2 K.

4.1.2 Frequency Correction

Most of the measurements presented in Chapter 4 were conducted under air since the bead-pull measurement setup denies evacuating the RFQ cavity. Furthermore, the ambient temperature was not controlled and deviated significantly from the RFQ design reference temperature of 22 °C. The measured frequency was therefore affected by two main aspects:

1. thermal expansion (or contraction) of the RFQ cavity, as its bulk temperature slowly follows the ambient temperature, and
2. the compared to vacuum larger relative perimittivity ε_r of air.

The (partial) correction of both influences during measurement data processing is discussed in the following.

The thermal behavior of the cavity during low-level RF measurements is dominated by the ambient temperature, which changes during the day because of e.g. sun exposure and people present in the room. If the copper bulk temperature increases (decreases), the measured frequency will be smaller (larger) because of thermal expansion. The frequency shift is inversely proportional to the wavelength, which in turn is in first-order approximation proportional to the linear strain. Hence

$$\frac{\Delta f}{f} = -\alpha_T \Delta T = -\frac{\Delta \lambda}{\lambda}, \tag{4.1}$$

where $\alpha_T = 1.66 \times 10^{-5}/\mathrm{K}$ is the linear thermal expansion coefficient of the copper cavity, and ΔT is the difference between measured and reference temperature. The corrected frequency f is thus obtained from the measured value f_{meas} as

$$f = \frac{f_{meas}}{1 - \alpha_T \Delta T}. \tag{4.2}$$

The second major effect originates in the fact that the measurements were carried out under air. Because of interactions between electromagnetic fields and material atoms, the speed of light is by a factor of $\sqrt{\varepsilon_r \mu_r}$ slower in any medium than the speed of light in vacuum c [68]. For air one assumes $\mu_r = 1$ and $\varepsilon_r = 1.00058986$ [199] at standard temperature and pressure (STP). Then, the frequency is corrected as follows:

$$f = f_{meas} \cdot \frac{\sqrt{\varepsilon_r}}{1 - \alpha_T \Delta T}. \tag{4.3}$$

That being said, a major source of uncertainty is the dependence of ε_r on the humidity. The relative permittivity of air can be determined as function of humidity from the empirical equation [200]

$$\varepsilon_r = 1 + \frac{211}{T} \cdot \left(p_{air} + \frac{48 \cdot p_{vap}(T)}{T} \cdot RH \right) \cdot 10^{-6}, \tag{4.4}$$

where T denotes the absolute temperature in K, RH the relative humidity in %, p_{air} the air pressure in units of mmHg, and p_{vap} the saturation vapor pressure of moist air in mmHg. The vapor pressure is obtained from the empirical Buck equation [201, 202]:

$$p_{vap} = 4.584 \cdot \exp\left[\left(18.678 - \frac{T}{234.5} \right) \cdot \left(\frac{T}{257.14 + T} \right) \right], \tag{4.5}$$

where T is the temperature in °C. Figure 4.1 shows the permittivity of air estimated using Eqs. (4.4) and (4.5) and the resulting frequency shift as functions of RH.

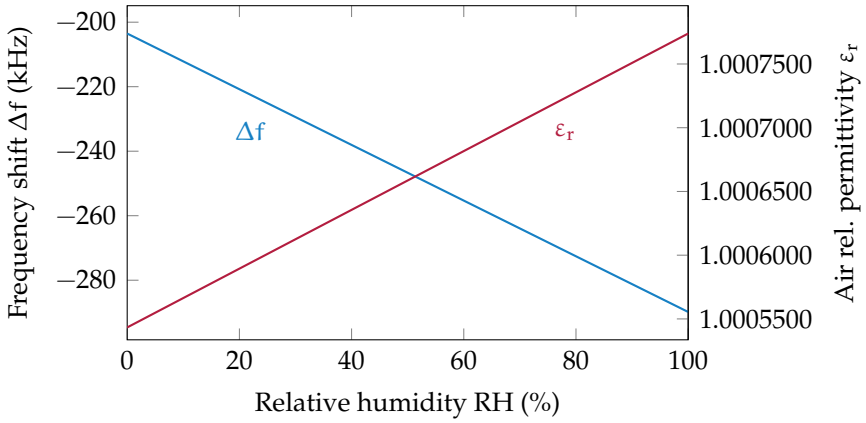

Figure 4.1: Difference Δf between frequency under air and frequency under vacuum, as well as relative permittivity of air ε_r as functions of the relative humidity RH.

4.1.3 Bead-pull Field Measurement

Maier and Slater [84] introduced the principle of utilizing Slater's cavity perturbation theorem (Section 2.1.4) to measure field amplitudes in an RF cavity. A small metallic[34] object—commonly referred to as bead—is introduced into the cavity, perturbing the fields by effectively removing a small volume $\Delta\mathcal{V}$ from the

[34]The bead-pull measurement technique was later generalized to use not only conducting, but also beads with arbitrary material properties [203]. Today both metallic and dielectric beads are used depending on the specific application, most importantly if the region of interest is dominated by the magnetic or the electric field.

resonator. With Eq. (2.33), this can be observed as a change in resonance frequency of the cavity, proportional to the squared field amplitudes $\mu_0 H^2 - \varepsilon_0 E^2$ at the location of the bead. A schematic representation of a bead-pull cavity measurement is shown in Fig. 4.2.

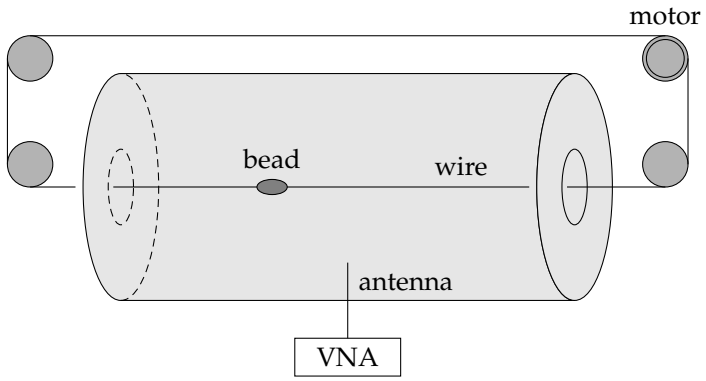

Figure 4.2: Principle of the bead-pull setup used to measure the field amplitude in an RF cavity. In the case of the PIXE-RFQ, the bead traversed all four quadrants subsequently on a single wire, was guided using a system of return and alignment pulleys, increasing the efficiency of the procedure.

In RFQs it is not feasible to insert a bead in the region of high electric fields between the vane tips, because the the size of the perturbing object must be by orders of magnitude smaller than the field region of interest. In fact, the minimum aperture, i.e. the radius of the largest coaxial cylinder that could be inserted, amounts to merely 0.7 mm in the PIXE-RFQ. Therefore, the bead is introduced into the magnetic field region of the cavity instead, making use of relation

$$V_0 = \omega \mu_0 \iint_S H_z \mathrm{d}S \tag{4.6}$$

that emerges from Faraday's law [Eq. (2.6)]. Assuming that $H = H_z$ at the position of the bead is proportional to the integral over the entire quadrant, the inter-vane voltage can be determined—and tuned—by measuring the magnetic field magnitude H in the four quadrants alone.

Depending on the specific setup, either the reflection (S_{11}) or transmission scattering parameter (S_{21}) may be measured, the latter requiring at least two antennas. The measurements of the proton HF-RFQ, featuring four couplers in total, were carried out measuring the transmission from one power coupler to another [42]. The PIXE-RFQ features only one single power coupler; hence, the bead-pull measurements presented in the following were performed using S_{11} [identical to Γ from Eq. (2.30)] only.

For bead-pull measurements it is generally impractical to measure the frequency shift directly to a sufficient accuracy. Instead, the frequency of the exciting wave is fixed to ω_0, the cavity resonant frequency in absence of the bead. The phase ϕ of the measured scattering parameter is observed as the bead is introduced into the cavity. As $\phi(\Delta\omega)$ is approximately linear for small $\Delta\omega$, one takes

advantage of the steep slope in the curve around the resonance frequency ω_0:

$$\Delta\phi \propto \Delta\omega \propto H^2 \propto V_0^2. \tag{4.7}$$

A higher signal-to-noice ratio (SNR) is achieved compared to measuring the shift of the maximum or minimum of the measured scattering parameter. This proved especially useful for the single module measurements, where the VNA was coupled to the RFQ by means of a small custom loop antenna instead of the power coupler, and the reflection was large by the strong under-coupling alone.

For the PIXE-RFQ, the same bead-pull bench and pulley system as for the HF-RFQ for proton therapy [41, 42, 63] was used, which in turn was adapted from the Linac4-RFQ tuning setup [37, 38]. The bead was threaded on a fishing wire with a diameter of 0.3 mm that was tensioned using a spring. The size of the perturbing bead must be chosen small enough, such that the frequency shift stays within the linear regime of the $\phi(\Delta\omega)$-curve, but large enough, such that an acceptable SNR is achieved. The measurements of the HF-RFQ for medical applications revealed a 7 mm $\times$ 4 mm aluminum bead [Fig. 4.3(a)] as an appropriate compromise for an RFQ of this frequency and quality factor [63]. While the PIXE-RFQ features the same frequency and a comparable quality factor, its length and thus its volume are approximately halved compared to the medical HF-RFQ. Therefore, the same aluminum bead introduces roughly double the frequency shift when inserted into the PIXE-RFQ. However, the shift still remains well within the linear regime [Fig. 4.3(b)].

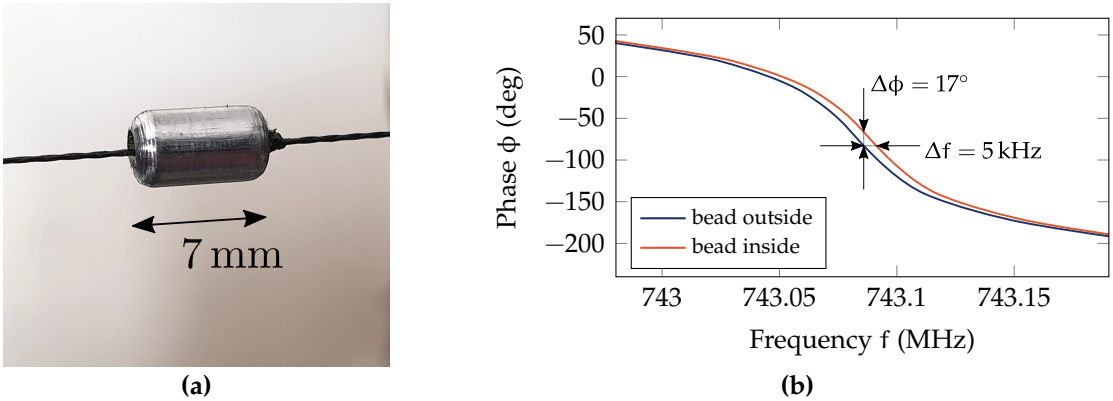

(a) **(b)**

Figure 4.3: Photograph of the metallic bead used for perturbation measurements of the PIXE-RFQ (a). The shift of the resonant frequency and the corresponding phase shift when the bead is inserted into the cavity are indicated in (b).

The raw phase data are shown in Fig. 4.4(a) with the example of a single module measurement. Note that the phase decreases as the bead is introduced into the cavity, because the measurement antenna is strongly under-coupled. Contrarily, Fig. 4.3(b) illustrates the phase shift of the full assembly, were the reflection at the input power coupler was measured. Since the coupler represents an over-

coupled antenna, the phase shift is positive. That being said, for the bead-pull measurements only the magnitude of the phase shift is of interest.

From the raw phase measurements of the four quadrants, the quadrupole and dipole components are extracted by means of a few data processing steps that are illustrated in Fig. 4.4: First,[35] the signals are vertically aligned (b) using the average of the first few tens of samples that correspond to bead positions just before entering or after exiting the RFQ cavity, where $H \approx 0$. A difference of up to a few percent of the maximum phase shift (depending on bead movement and VNA sweep time) between the average of the first and last few tens of samples, i.e. between the input and output of the RFQ, can be observed. It changes randomly from one measurement to the next and is thus different for the four quadrants. This phase drift originates in the VNA itself, and is corrected by means of linear interpolation (c). To reduce the noise, the data are smoothed (d) using a Savitzky-Golay filter [204, 205]. This allows for using single signal samples for longitudinal alignment: Although the setup features light sensors for detecting the traversing bead, the longitudinal alignment (e) was performed in software using the intersections of the rising and falling slopes with the third-maximum line. This method also compensated for any constant wire slippage between the quadrant measurements. By observing the positions of the local minima in the curves originating from the auxiliary ports, the alignment can be validated and any potential irregular wire slippage can be detected and compensated for. With $\Delta\phi \propto H^2$, the relative amplitudes of the magnetic field arise by taking the square root[36] and assigning the proper sign to account for the the alternating field orientation of the TE_{210} quadrupole mode in the four quadrants (f):

$$a_1 = +\sqrt{\Delta\phi_1}, \quad a_2 = -\sqrt{\Delta\phi_2}, \quad a_3 = +\sqrt{\Delta\phi_3}, \quad a_4 = -\sqrt{\Delta\phi_4}. \tag{4.8}$$

The field flatness of the TE_{210} mode can then be quantified by three field components: one quadrupole component Q and two dipole components D^S and D^T of orthogonal polarization, that are defined following Ref. [1]:

$$\begin{aligned} Q &= \frac{1}{4}\left(a_1 - a_2 + a_3 - a_4\right), \\ D^S &= \frac{1}{2}\left(a_1 - a_3\right), \qquad\qquad D^T = \frac{1}{2}\left(a_2 - a_4\right). \end{aligned} \tag{4.9}$$

[35] In fact, because of the particular bead-pull measurement system—one single wire running through all four quadrants using a set of pulleys—the direction of the signal, i.e. the horizontal orientation, alternates from one quadrant to the next. As this is trivial to correct, it is not further discussed. Furthermore, if the VNA can measure with a sufficient number of sampling points, it is possible to take the data of all four quadrants subsequently in a single measurement. Then, the four quadrant measurements are separated with the help of an edge-detection algorithm.

[36] While in theory always $\Delta\phi > 0$, negative values can occur because of measurement noise. The square root is therefore taken as $\mathrm{sgn}(\Delta\phi) \cdot \sqrt{|\Delta\phi|}$ under preservation of the sign. Here, $\mathrm{sgn}(\cdot)$ denotes the signum function [71].

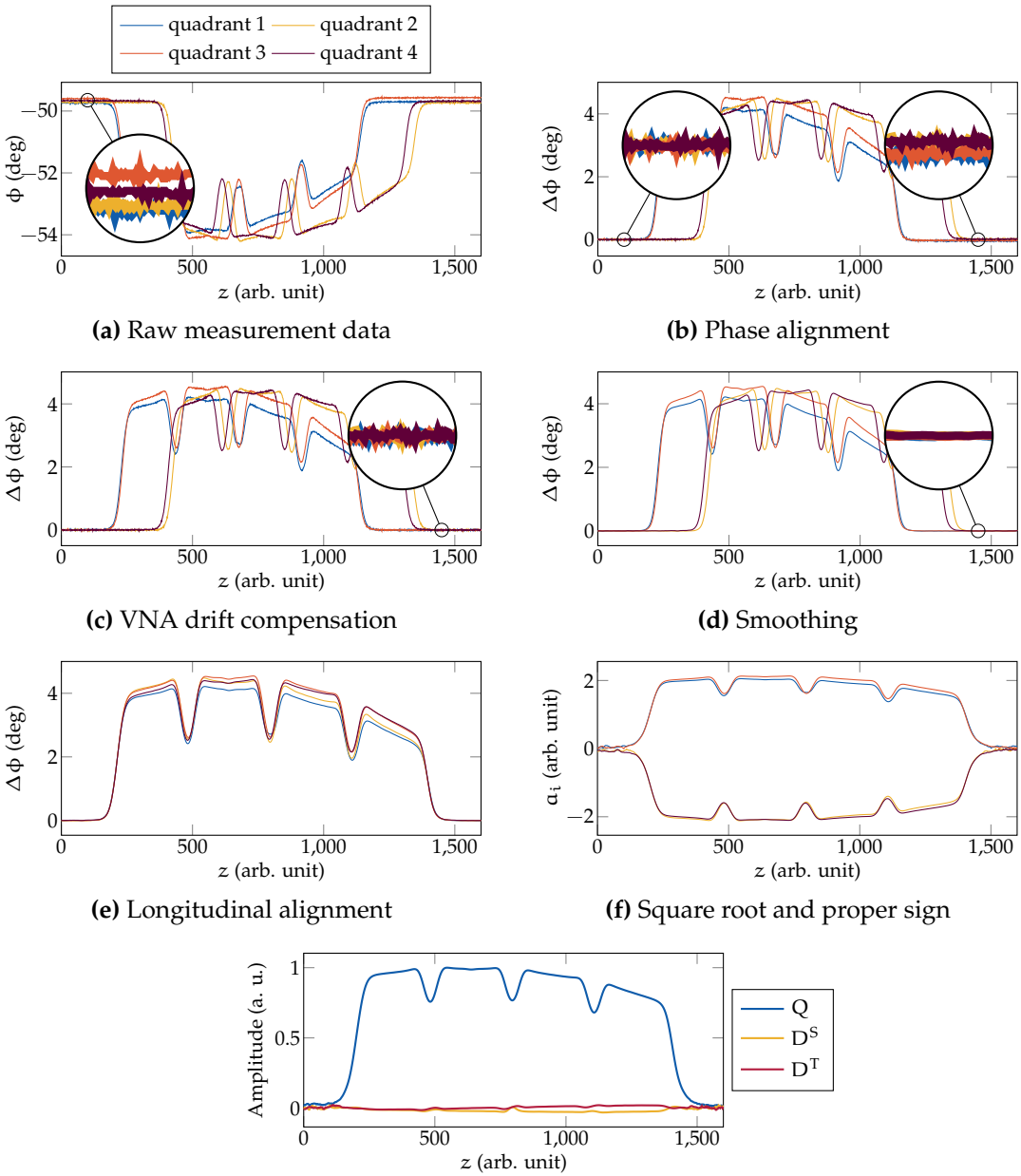

(a) Raw measurement data

(b) Phase alignment

(c) VNA drift compensation

(d) Smoothing

(e) Longitudinal alignment

(f) Square root and proper sign

(g) Quadrupole and dipole components

Figure 4.4: Processing steps of the bead-pull data of the four quadrants obtained from the VNA phase measurement. The raw data (a) are first vertically aligned (b) using the average of the first few samples. The phase drift of the VNA is linearly corrected by also considering the last few samples (c). The data are smoothed using a Savitzky-Golay filter (d) and then longitudinally aligned by their rising and falling slopes (e). By taking the square root, assigning the proper sign (f), the quadrupole and dipole components (g) are obtained according to Eq. (4.9). The illustration is inspired by Ref. [63].

4.1.4 Tuning Goals

In the case of the PIXE-RFQ, the inter-vane voltage $V_0 = 35\,\mathrm{kV}$ is designed to be constant, corresponding to a magnetic field that is flat along the RFQ and in magnitude equal in all four quadrants. Thus, the goal of the tuning process can be defined as $Q = 100\,\%$ and $D^S = D^T = 0$ at all sampling points. Errors of $\pm 2\,\%$ with respect to the average quadrupole component are acceptable in each of the three field components from a beam dynamics point of view. These tolerances equal the tuning requirements of the medical HF-RFQ [42].

A peculiarity of the PIXE-RFQ is that it represents a stand-alone machine. No RF structures which would require frequency and phase stability are installed downstream of the RFQ. Thus, frequency accuracy does not represent a critical requirement. As explained in Section 3.4, a frequency shift is in fact foreseen by design during nominal operation in order to maintain a constant cooling water temperature. Deviations from the design resonant frequency as much as few MHz are acceptable for the beam dynamics (see Section 3.5.2). Notwithstanding the above, the frequency was tuned to match the design value: 749.480 MHz under vacuum at 22 °C with an error smaller than $\pm 60\,\mathrm{kHz}$. This tolerance emerges from the water temperature range of a typical RF cavity cooling system: commonly the water temperature can be varied by $\pm 5\,\mathrm{K}$ around the nominal value. The corresponding sensitivity of the PIXE-RFQ resonant frequency amounts to $-13.3\,\mathrm{kHz/K}$, as determined in Section 3.4.1.

The precision of the digital thermometers used to measure the RFQ cavity temperature amounts to $\pm 0.2\,\mathrm{K}$. With Eq. (4.2) and the RFQ operating frequency, this translates to a frequency uncertainty of $\pm 2.6\,\mathrm{kHz}$. This error is by an order of magnitude smaller than the error introduced by humidity uncertainty, which is discussed the following.

The influence of the relative humidity RH on the frequency can be removed either by measuring RH and calculating the corresponding ε_r, or by flooding the cavity with a dry gas. The latter represents a standard procedure for RF cavity measurements. Commonly, dry nitrogen (N_2) is used as a flooding gas, as has been done during for the final tuning steps of the medical HF-RFQ [42]. However, since there are no strict requirements for frequency accuracy in the PIXE-RFQ, it was decided to accept the uncertainty in RH and work with the STP value of $\varepsilon_r = 1.00058986$. An uncertainty in relative humidity of $\pm 30\,\%$ translates to an error in frequency of approximately $\pm 30\,\mathrm{kHz}$, since $\partial f/\partial \mathrm{RH} \approx -1\,\mathrm{kHz/\%}$ (Fig. 4.1). Additional—however smaller—errors originate in pressure and temperature dependence of the relative permittivity [206]. Thus, it was expected that the PIXE-RFQ could be tuned under air to an accuracy of approximately $\pm 30\,\mathrm{kHz}$ when measuring only the cavity temperature. If phase and frequency stability would be required, this error would still lie well within the $\pm 5\,\mathrm{K}$ tuning range of a typical water cooling system.

In all following statements and spectrum diagrams, the frequency is exclusively reported in terms of the corrected value (the value under vacuum at 22 °C). The raw measured value was scaled using Eq. (4.2) or Eq. (4.3), where applicable.

4.2 Validation Measurements of RFQ Components

The construction of the PIXE-RFQ and its auxiliaries was accompanied by RF measurements to validate the respective status and quality of the manufacturing. Notably, the input power coupler—the most critical auxiliary—and the individual RFQ modules where measured independently. The results are briefly reported in the following two sections.

4.2.1 Coupler Head-on Measurement

Two couplers were manufactured for the PIXE-RFQ: one is mounted to the RFQ and the other is kept as a spare. To assess the coupler construction quality and confirm agreement with the RF simulations before installing the coupler in the RFQ, both couplers where mounted facing each other in a purpose-built aluminum tube [Fig. 4.5(a)]. The transmission S_{21} was measured[37] from one EIA $3^1/_8$ in coaxial connector to the other as a function of the frequency f. The couplers were rotated around their common axis by different angles ϑ, where $\vartheta = 0$ identifies the case where both coupling loops are closest to each other in a mirror-symmetrical arrangement.

The measurement data are reported in Fig. 4.6 in comparison to RF simulation results. A nearly perfect agreement is observed for the high-transmission cases of $\vartheta = 0°$ and 180°, where the coupling loops and their electromagnetic fields are parallel or anti-parallel, confirming the quality of the coupler construction. A slightly larger error of roughly 1 dB can be observed for the case of $\vartheta = 90°$, where the fields are virtually orthogonal and the transmission nearly vanishes.[38] A small bump at roughly 795 MHz was observed, which is attributed to a resonance effect originating in repeated reflections caused by the imperfect measurement setup.

[37] The coupler head-on measurements were carried out by means of a Copper Mountain® TR1300/1 vector network analyzer [207].

[38] Because of 3D effects there will always be some residual transmission at every angle.

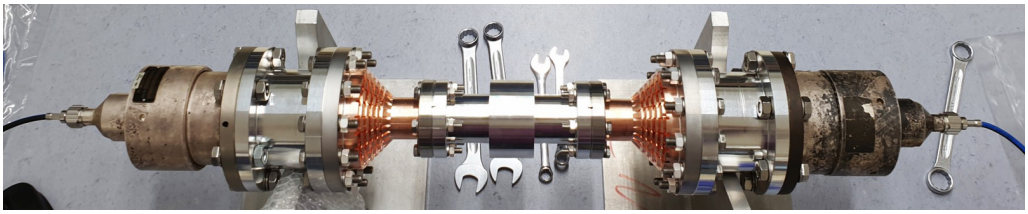

(a)

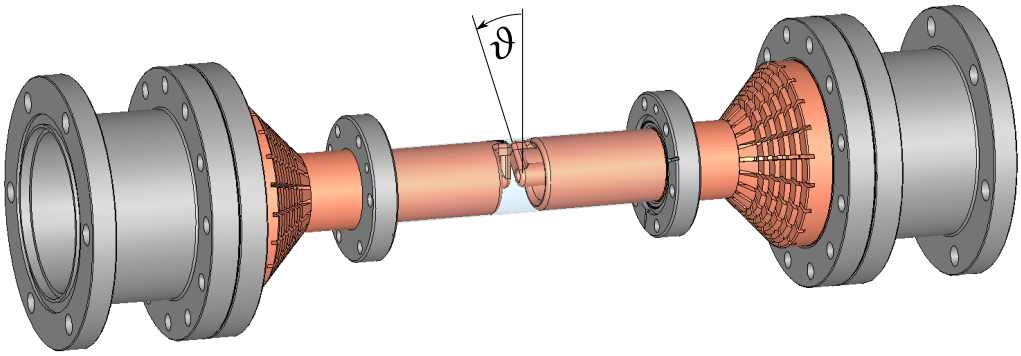

(b)

Figure 4.5: Photograph (a) and simulation CAD model (b) of the coupler head-on measurement. The angle ϑ indicates the rotation of the couplers against each other, where $\vartheta = 0$ refers to the mirror-symmetrical arrangement.

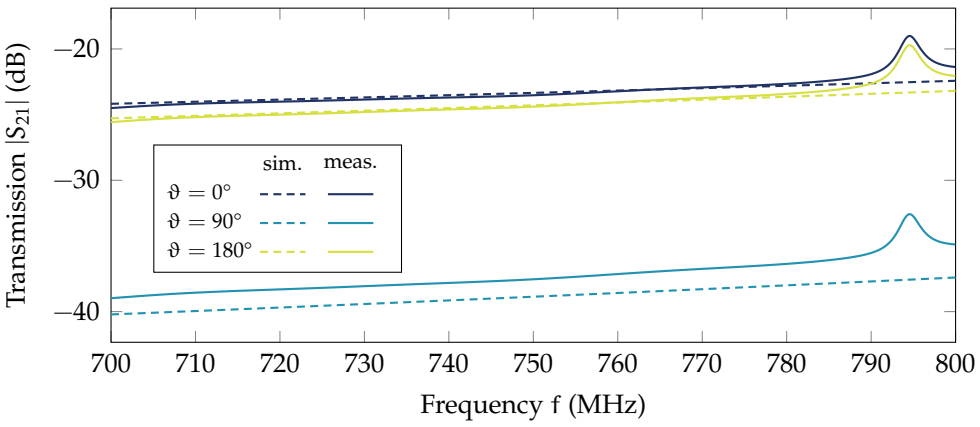

Figure 4.6: Transmission coefficient $|S_{21}|$ from one coupler to the other during head-on measurement for different coupler angles ϑ as a function of the frequency f. Data obtained from measurement (solid lines) and from simulation (dashed lines) are compared. The bumps at approximately 795 MHz likely originate in a resonance effect caused by imperfections of the measurement setup.

4.2.2 Bead-pull Measurements of Single RFQ Modules

Both mechanical modules of the PIXE-RFQ (in the following denoted as module 1 and 2) were measured individually by means of the bead-pull technique. The purpose of these measurements was to ascertain the manufacturing quality of the modules, and to determine if it would be necessary to use the pumping ports as "emergency" tuning features in addition to the piston tuners. By comparing both resonant frequency and field distribution to the simulation, it was assessed that no special measures were required, as very close agreement was observed between measurement and simulation.

Figure 4.7(a) shows module 1 mounted to the RF test bench for the single module measurement. No auxiliaries were installed and all ports were closed by simple aluminum flange covers. In the absence of the coupler or RF pickup antennas, a small makeshift antenna crafted from simple copper wire [Fig. 4.7(b)] was mounted to one of the ports. The antenna was strongly under-coupled, however, a phase shift of 4° was observed upon introducing the bead into the cavity. With an SNR of roughly 45 dB this was considered as sufficient. As no end plates were present, the upstream and downstream ends of the module were terminated by aluminum extension tubes in order to obtain well-defined boundary conditions that can be reproduced in a 3D eigenmode simulation.

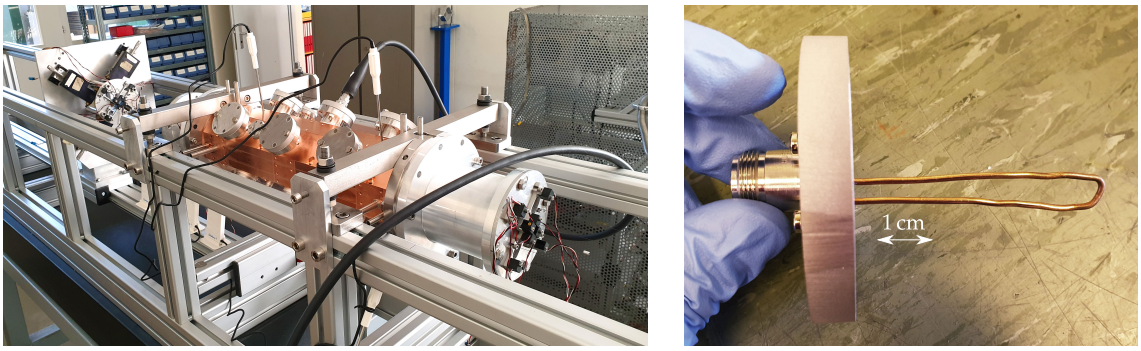

(a) (b)

Figure 4.7: Photograph of the first module of the PIXE-RFQ mounted on the bead-pull support frame for single module measurements (a). Two aluminum extension tubes were attached to the ends to obtain a well-defined boundary, avoiding stray fields. One of the two plates with return and alignment pulleys is visible on the left. The RF connection and the sensors used to measure the cavity temperature are also shown. The makeshift antenna used for single module measurements is shown in (b).

Figures 4.8(a) and (b) show the measured spectra of the individual modules with attached extension tubes. For both modules the TE_{210} frequencies are roughly 6 MHz lower than the RFQ design frequency of 749.48 MHz. The obvious reason is given by the absence of any auxiliaries and the metallic extension tubes, which—resembling a geometry that is completely different from the end plate or neighboring module—act as mismatched loads on the operating mode. The measured TE_{210} frequencies deviate from the values obtained from an appro-

priate simulation model by 150 kHz for module 1 and 600 kHz for module 2. The deviations in the dipole mode frequencies are smaller than 1 MHz.

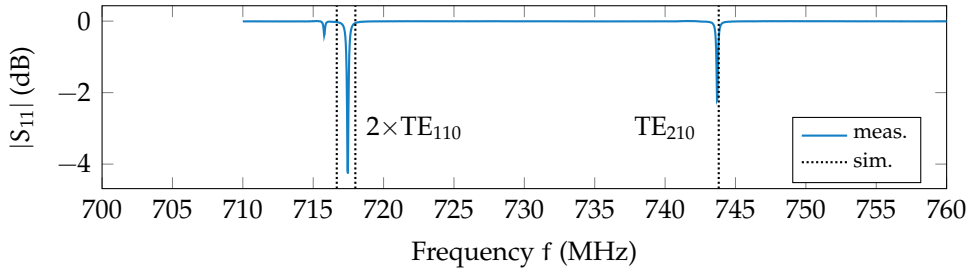

(a) Module 1

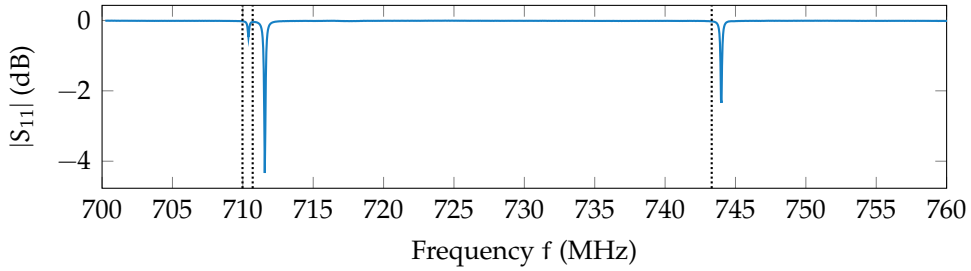

(b) Module 2

Figure 4.8: Measured spectra of the individual RFQ modules in terms of the reflection coefficient. In order to obtain a defined boundary, aluminum tubes were mounted to both ends of the modules, and all flanges were covered by aluminum plates [Fig. 4.7(a)]. The small measurement antenna was mounted to one of the flanges intended for a vacuum pumping port. Because of this asymmetric arrangement, it coupled to one of the dipole modes much stronger than to the other.

In terms of field amplitudes, a near-perfect agreement between measured and simulated quadrupole component Q was observed with an error less than 1 % of the average quadrupole amplitude (Fig. 4.9). The measured dipole components D^S, D^T, which vanish in the simulation, reach amplitudes of up to ±4 %. Larger deviations should be expected for the full assembly, as the alignment between the two modules can be carried out with only finite accuracy.

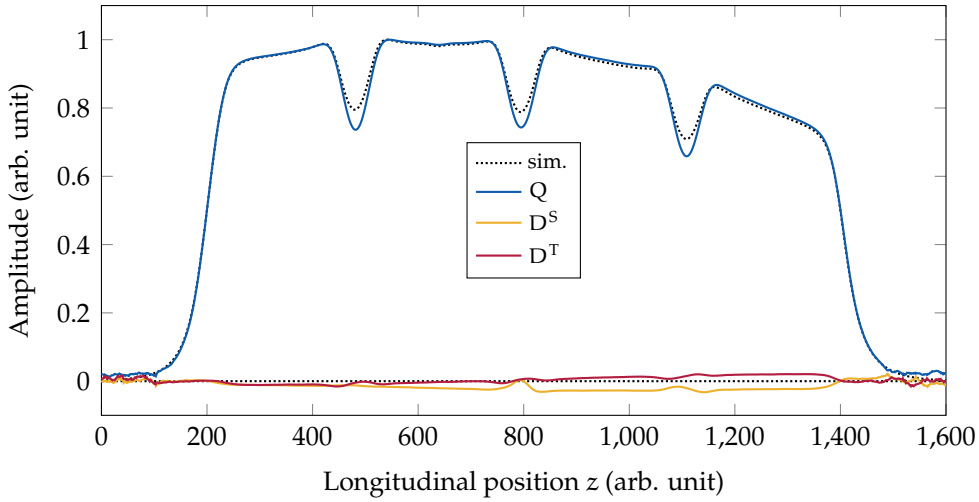

(a) Module 1

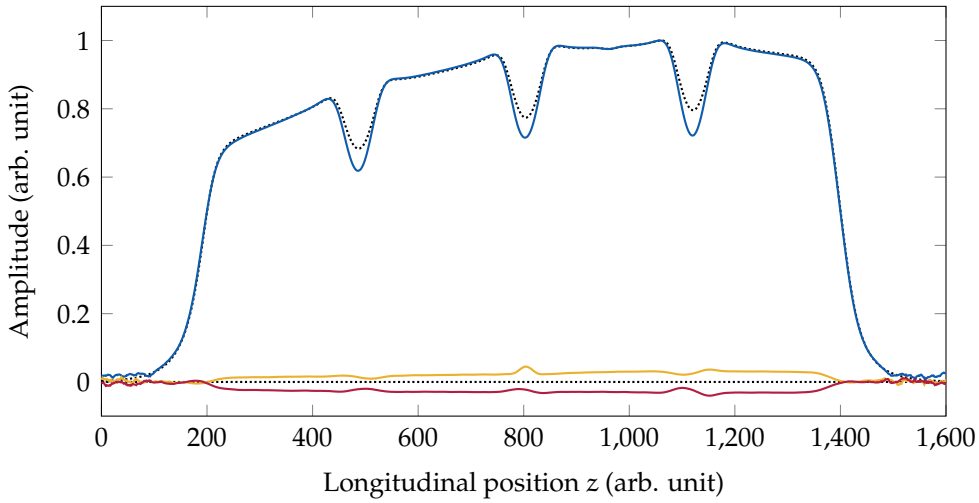

(b) Module 2

Figure 4.9: Measured quadrupole Q and dipole field components D^S, D^T of the individual RFQ modules in comparison to the simulation (dotted lines).

4.3 Tuning

A local variation in the longitudinal capacitance or inductance profile leads to a local variation in cutoff frequency f_{co}, and thus in longitudinal nonuniform voltage of the TE_{210} operating mode. The voltage perturbation amounts to [139]

$$\frac{\delta V}{V} = \pi^2 \left(\frac{L_{RFQ}}{\lambda}\right)^2 \cdot \frac{\delta f_{co}}{f_{co}} = -\frac{\pi^2}{2} \left(\frac{L_{RFQ}}{\lambda}\right)^2 \cdot \left(\frac{\delta C'}{C'} + \frac{\delta \mathcal{L}'}{\mathcal{L}'}\right). \tag{4.10}$$

The variation in capacitance C' can be compensated by a local adjustment of the cavity inductance $\mathcal{L}'$ by means of piston tuners that are inserted into the cavity with a certain penetration depth (see also Section 3.2.5).

4.3.1 Tuning Setup and Tooling

The PIXE-RFQ features sixteen piston tuners in the form of copper slugs with a conical tip [Fig. 4.10(d)]. Four tuners each are mounted at four positions along the RFQ. Their designations are shown in Fig. 4.11.

The tuners were initially machined with an over-length of 11 mm with respect to the nominal dimension. The nominal length is given by the nominal tuner penetration into a perfect cavity while mounted flush in the so-called flange-to-flange position. The over-length allows for a mechanical tuning range of ± 11 mm. A final length for each tuner was determined by iterative tuner adjustments and bead-pull measurements. The tooling, originally developed for the HF-RFQ [42, 63], is shown in Figs. 4.10(b) and (c). During the tuning, the slugs were mounted on a threaded, spring-loaded piston, allowing for adjustment of the tuner penetration into the RFQ. The piston was mounted in a guidance tube fixed to the RFQ flange, which offered accurate transverse positioning with respect to the flange axis. A scale with 10 µm graduation was used to adjust the tuner position. The penetration was confirmed by means of a caliper before the tooling was removed after the final tuning step. Then, the tuners were remachined to their final lengths and installed flange-to-flange with copper gaskets.

During the tuning procedure, the frequency and bead-pull measurements were carried out as described in Sections 4.1.2 and 4.1.3, respectively, while measuring the reflection $\Gamma = S_{11}$ at the input power coupler. The field quality was assessed by measuring the quadrupole and dipole components of the TE_{210} eigenmode, Q, D^S, and D^T [Eq. (4.9)] at discrete points. Each sampling point corresponds to an interval of the continuous field profile over which the data were averaged to further reduce measurement noise. The averaging windows are visualized in Fig. 4.12.

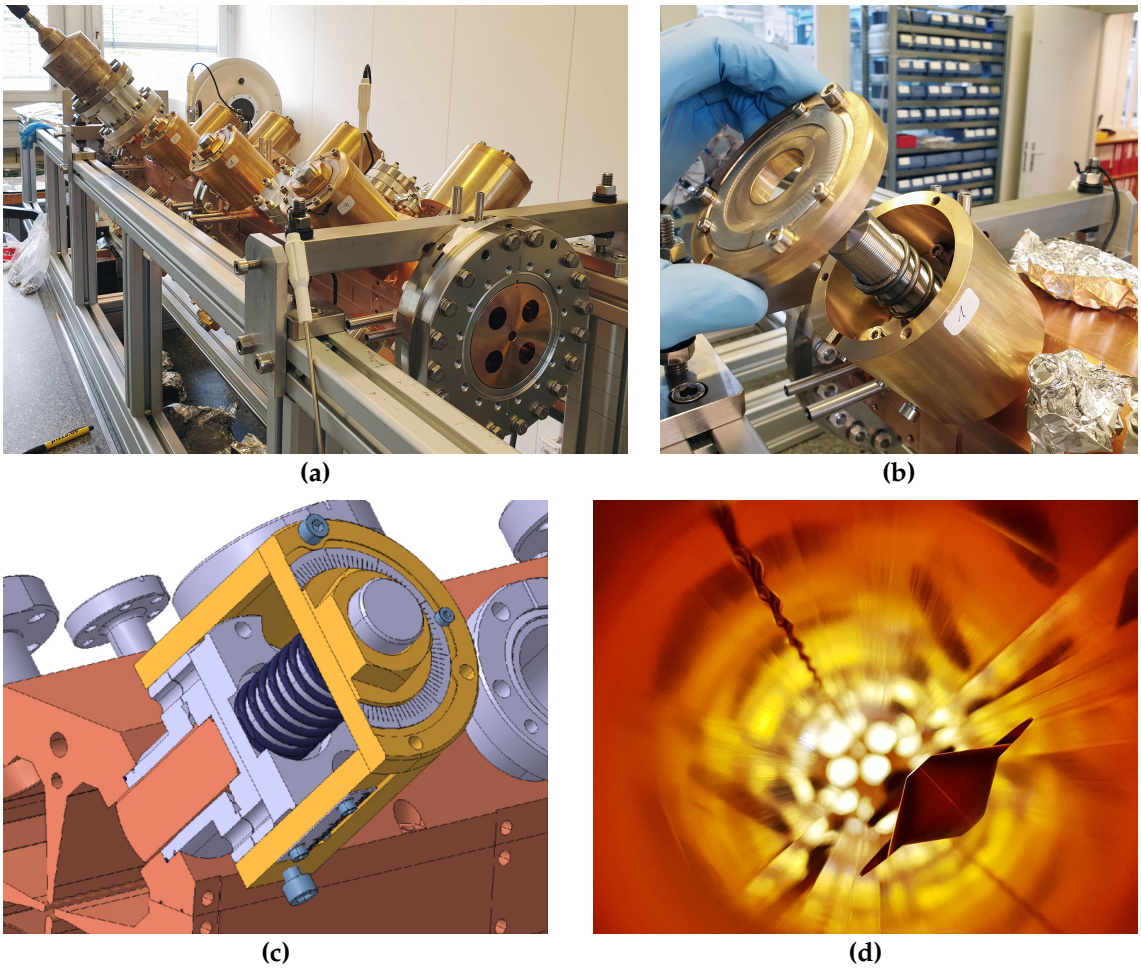

Figure 4.10: Photograph of the PIXE-RFQ tuning setup with tuners mounted in their guidance tubes (a). A closeup of the tuner tooling during assembly is shown in (b). A CAD model of the tuner tooling is shown in (c); note that the depicted shape does not represent the final design with conical tip. The tip of the tuner inside the cavity seen from one of the bead-pull holes is depicted in (d). Figure (c) was taken from Ref. [42] with courtesy of B. Koubek.

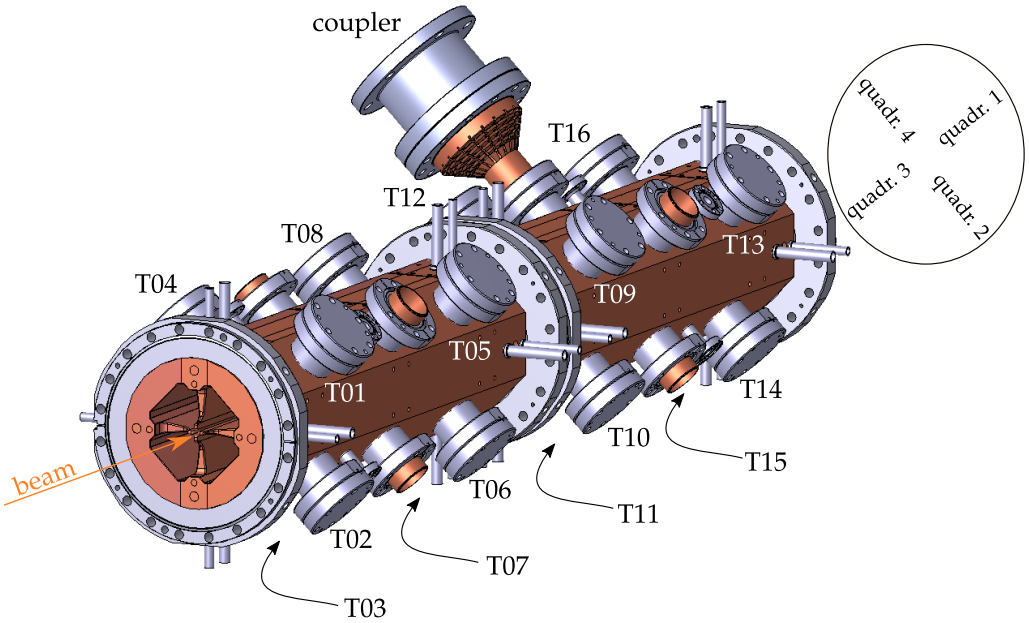

Figure 4.11: Labeling of the PIXE-RFQ quadrants and tuners. The arrows indicate the labels of hidden tuners in quadrant 3.

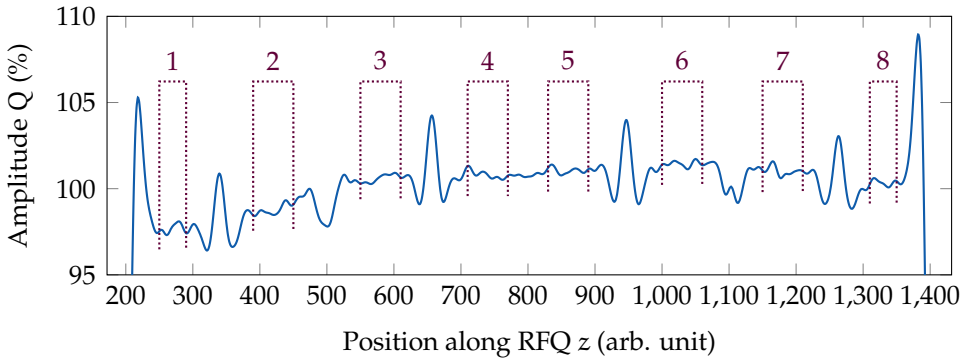

Figure 4.12: Example of a measurement of the quadrupole component before tuning. The brackets visualize the windows over which the measurement is averaged to obtain the value at the indicated discrete sampling points.

4.3.2 Reliability Measurements

Before the actual tuning process it was important to estimate the measurement error by means of repeated reliability measurements. The author differentiates between two distinct concepts:

1. Repeatability, which refers to the error observed between various bead-pull measurements carried out over several hours, without any changes to the RFQ itself—in particular no tuner movements.

2. Reproducibility, which means the error introduced by tuner movements and mechanical hysteresis effects.

The accuracy arising from these two aspects poses the ultimate limit for the accuracy that can be achieved during tuning.

To assess the measurement repeatability, bead-pull measurements of a single quadrant were carried out ten times on the same day without moving any tuners (Fig. 4.13). Errors observed between the measurements comprise systematic errors related to the change of ambient parameters such as temperature and humidity. These errors are expected to be negligible for field measurements, as e.g. the length changes of the RFQ subject to thermal expansions are by several orders of magnitude smaller than what could be resolved by bead-pull measurement. A significantly larger error source is random noise introduced by wire vibration and slippage, as well as by the VNA itself in the form of thermal noise, quantization noise, and nonlinear phase drift. Figure 4.13 shows that the deviation between the repeated measurements is larger than 0.5 % for one quadrant. Because the dipole components are defined as the difference between two quadrants [Eq. (4.9)], such an error would limit the tuning accuracy with respect to these components to more than 1 % by the bead-pull measurement alone. It was observed that this error increases when measurements over several days are considered (Fig. 4.14).

Therefore, a study was carried out on how the error would reduce if the measurements were averaged over several repetitions. Based on the original data (thirteen four-quadrant measurements spread over several days), all possible combinations of three, six, or ten measurements were formed. The average of each combination was calculated, generating new artificial sets of measurements. The resulting error at each sampling point was then calculated as

$$\begin{aligned} \delta Q &= \max |Q - \langle Q \rangle| , \\ \delta D^S &= \max \left| D^S - \left\langle D^S \right\rangle \right| , \\ \delta D^T &= \max \left| D^T - \left\langle D^T \right\rangle \right| , \end{aligned} \tag{4.11}$$

where $\langle \cdot \rangle$ indicates averaging over all thirteen available measurements at one sampling point. The results are summarized in Fig. 4.14, given as a percentage of the quadrupole component ($\langle Q \rangle = 100\,\%$). Averaging over three measurements

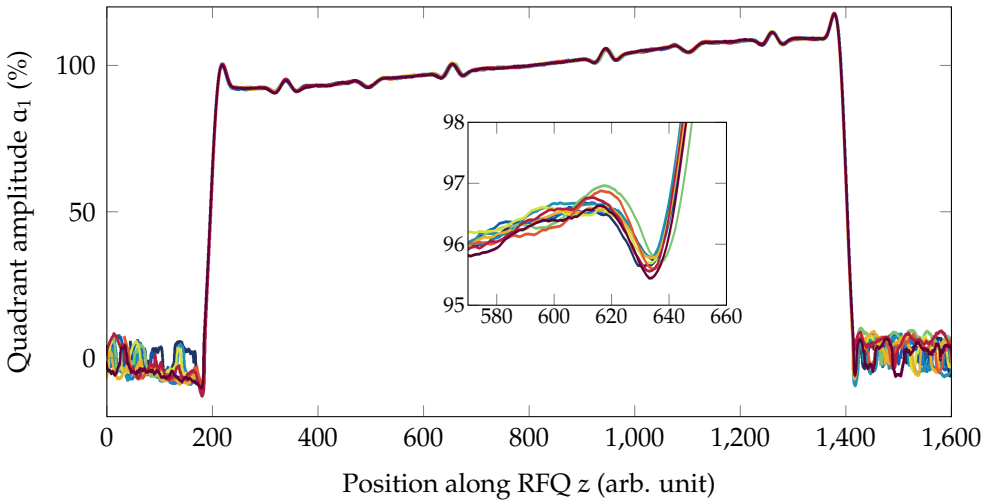

Figure 4.13: Ten measurements of quadrant 1 carried out over the course of one day without any tuner movement. The observed error of approximately 0.5 % results solely in wire vibration and slippage as well as VNA noise.

guarantees a dipole measurement error lower than 0.5 % and a quadrupole error of 0.2 % or better, which lies well within the tuning requirements. Especially for sampling points with large spread, the measurement error of the quadrupole component could be reduced by nearly a factor of two. With respect to the considerable effort for carrying out these measurements, it was decided to repeat all tuning-related bead-pull measurements—sixteen measurements for the response matrix and then one for each tuning step—three times and take the mean value at each sampling point.

A second study was performed in order to assess the measurement reproducibility, i.e. errors that originate from tuner movements. Several tuners were moved starting from 0 mm (nominal position) to 3 mm, 6 mm, and back to nominal, after which the sequence was repeated. As an example, the results for tuner 4 are shown in Fig. 4.15 (without any averaging). The error observed in this study is virtually the same as the one observed during the repeatability test (Figs. 4.13 and 4.14). Thus, the overall error is dominated by the measurement itself, while mechanical hysteresis plays only a subordinate role.

From Fig. 4.15, an estimate of the influence of a single tuner on the field distribution could be obtained. An insertion by 3 mm reduces the quadrupole component by roughly 3 % in the vicinity of the tuner, and changes one of the dipole components by roughly 6 %. Particularly in the bottom plot at $z \approx 700$ it becomes clear that the relationship is indeed nonlinear. The influence of a tuner increases with its insertion depth. Finally, it is interesting to note that one tuner has a strong influence on the D^T component, but almost none on D^S—as one would expect because of the dipole component definitions, each incorporating two opposite quadrants [Eq. (4.9)].

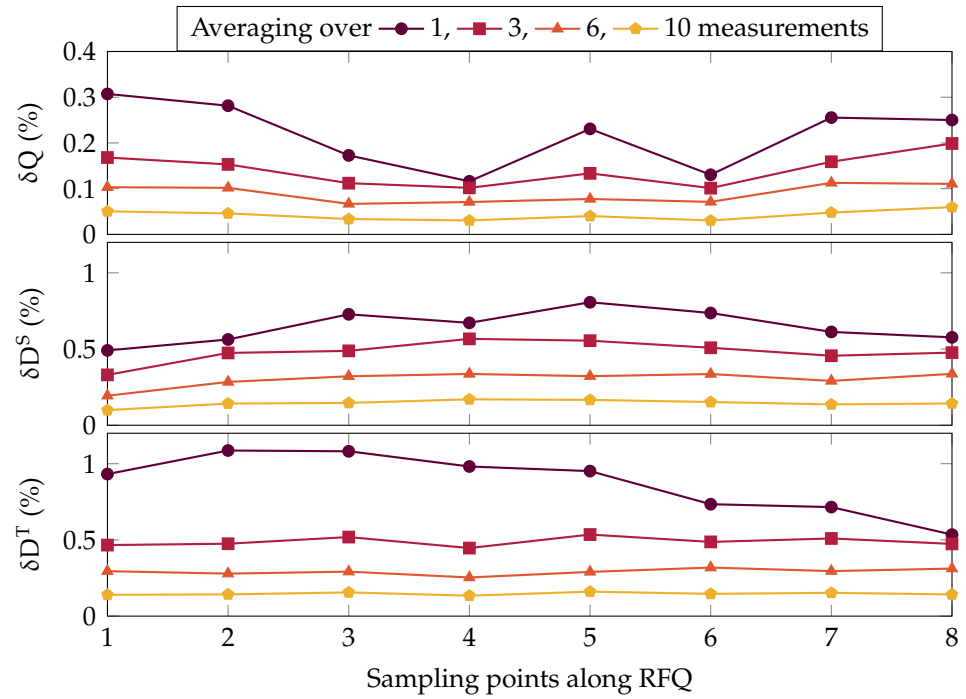

Figure 4.14: Reduction of error in quadrupole component (δQ) and dipole components (δD^S, δD^T) when averaging over three, six, and ten measurements, compared to no averaging (one measurement). The source data was obtained from thirteen measurements carried out over several days.

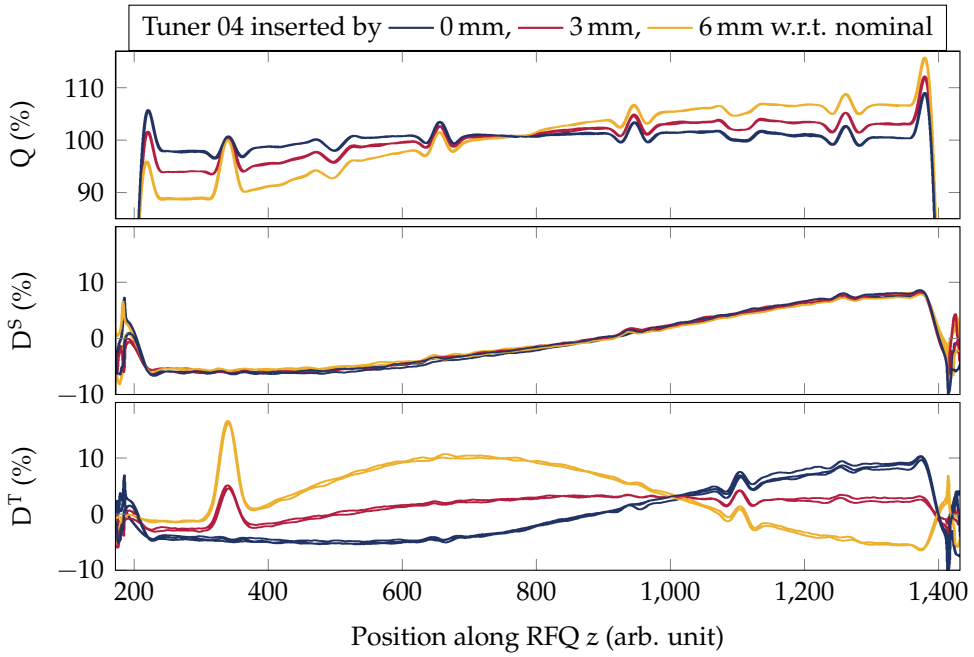

Figure 4.15: Reproducibility of the field components after movement of tuner 4 (exemplary). The tuner was repeatedly inserted by 0 mm (nominal position), 3 mm, 6 mm, and retracted again. No mechanical hysteresis effects stronger than the measurement noise were observed.

4.3.3 Augmented Tuning Algorithm

The PIXE-RFQ was tuned with an improved version of the tuning algorithm developed by Koubek, which was used for the tuning of the proton therapy HF-RFQ [42]. Based on a tuning scheme described in Ref. [1], the first-order responses of selected field sampling points to individual movements of the tuners are collected in a response matrix $\mathbf{R}$. Koubek proposed the singular value decomposition (SVD) to carry out the necessary inversion of the rectangular and potentially ill-conditioned matrix. This way, repetitive matrix measurements could be avoided. For the PIXE-RFQ, $\mathbf{R}$ was augmented by the author of the present thesis to also include the frequency responses, such that field and frequency can be tuned at the same time. In the following, the algorithm proposed by Koubek is reviewed, and the augmented variant is derived.

In Ref. [42], Koubek defined (in a slightly different notation)

$$\boldsymbol{x}_{\text{cur}} = \begin{bmatrix} Q_1 & \cdots & Q_n & D_1^S & \cdots & D_n^S & D_1^T & \cdots & D_n^T \end{bmatrix}^T \in \mathbb{R}^{3n} \tag{4.12}$$

as the vector of quadrupole and dipole field amplitudes Q_i, D_i^S, and D_i^T currently measured in the RFQ at the discrete field sampling points $i = 1, \ldots, n$. The corresponding target values are summarized in the vector

$$\boldsymbol{x}_{\text{trg}} = \begin{bmatrix} Q_{\text{trg},1} & \cdots & Q_{\text{trg},n} & D_{\text{trg},1}^S & \cdots & D_{\text{trg},n}^S & D_{\text{trg},1}^T & \cdots & D_{\text{trg},n}^T \end{bmatrix}^T \in \mathbb{R}^{3n}. \tag{4.13}$$

Similarly, the current tuner positions t_j and target tuner positions $t_{\text{trg},j}$, $j = 1, \ldots, m$ are collected in

$$\mathbf{t}_{\text{cur}} = \begin{bmatrix} t_1 \\ \vdots \\ t_m \end{bmatrix} \in \mathbb{R}^m, \quad \mathbf{t}_{\text{trg}} = \begin{bmatrix} t_{\text{trg},1} \\ \vdots \\ t_{\text{trg},m} \end{bmatrix} \in \mathbb{R}^m. \tag{4.14}$$

By moving each tuner individually by some distance while leaving all other tuners in nominal position, the response matrix $\mathbf{R} = \partial \boldsymbol{x}_{\text{cur}} / \partial \mathbf{t}_{\text{cur}} \in \mathbb{R}^{3n \times m}$ is obtained. Each matrix entry quantifies the effect of one tuner on Q, D^S, or D^T at one sampling point in first-order approximation. Matrix $\mathbf{R}$ can be interpreted as the Jacobian of the field amplitudes with respect to the tuner positions. In a perfectly tuned RFQ—with constant inter-vane voltage—the quadrupole component equals unity ($Q_{\text{trg},i} = 1$) whereas the dipole components vanish ($D_{\text{trg},i}^S = D_{\text{trg},i}^T = 0$) at all sampling points. Thus, the arising system of equations

reads

$$\underbrace{\begin{bmatrix} 1-Q_1 \\ \vdots \\ 1-Q_n \\ 0-D_1^S \\ \vdots \\ 0-D_n^S \\ 0-D_1^T \\ \vdots \\ 0-D_n^T \end{bmatrix}}_{\substack{\mathbf{x}_{trg}-\mathbf{x}_{cur} \\ =\Delta\mathbf{x}}} = \underbrace{\begin{bmatrix} \frac{\partial Q_1}{\partial t_1} & \frac{\partial Q_1}{\partial t_2} & \cdots & \frac{\partial Q_1}{\partial t_m} \\ \vdots & \ddots & \ddots & \vdots \\ \frac{\partial Q_n}{\partial t_1} & \frac{\partial Q_n}{\partial t_2} & \cdots & \frac{\partial Q_n}{\partial t_m} \\ \frac{\partial D_1^S}{\partial t_1} & \frac{\partial D_1^S}{\partial t_2} & \cdots & \frac{\partial D_1^S}{\partial t_m} \\ \vdots & \ddots & \ddots & \vdots \\ \frac{\partial D_n^S}{\partial t_1} & \frac{\partial D_n^S}{\partial t_2} & \cdots & \frac{\partial D_n^S}{\partial t_m} \\ \frac{\partial D_1^T}{\partial t_1} & \frac{\partial D_1^T}{\partial t_2} & \cdots & \frac{\partial D_1^T}{\partial t_m} \\ \vdots & \ddots & \ddots & \vdots \\ \frac{\partial D_n^T}{\partial t_1} & \frac{\partial D_n^T}{\partial t_2} & \cdots & \frac{\partial D_n^T}{\partial t_m} \end{bmatrix}}_{\mathbf{R}} \underbrace{\begin{bmatrix} t_{trg,1}-t_1 \\ \vdots \\ t_{trg,m}-t_m \end{bmatrix}}_{\substack{\mathbf{t}_{trg}-\mathbf{t}_{cur} \\ =\Delta\mathbf{t}}}. \tag{4.15}$$

The new tuner positions required to correct the field distortion are obtained as

$$\mathbf{t}_{trg} = \mathbf{t}_{cur} + \Delta\mathbf{t} = \mathbf{t}_{cur} + \mathbf{R}^{\dagger}\Delta\mathbf{x}, \tag{4.16}$$

where $\mathbf{R}^{\dagger}$ identifies the pseudo-inverse of $\mathbf{R}$.

This thesis proposes to augment the previously presented system of equations to include also the frequency. The measured frequency is introduced as a dimensionless quantity $\bar{f} = w_f f$, such that it can be combined with the likewise dimensionless measured field amplitudes Q_i, D_i^S, D_i^T by appending it to $\mathbf{x}_{cur}$. Analogously, the target frequency $\bar{f}_{trg} = w_f f_{trg}$ is appended to $\mathbf{x}_{trg}$. The normalizing weight w_f (in units of 1/Hz) can be used to control the influence of the frequency compared to the field amplitudes. More precisely, w_f determines the contribution of the frequency deviation $f_{trg} - f$ to the residual norm $\|\Delta\mathbf{x} - \mathbf{R}\Delta\mathbf{t}\|$, which is minimized when solving the overdetermined system of equations [Eq. (4.15)] by means of the least-squares method. Larger w_f translate to higher importance. The frequency is incorporated by appending a new row to $\mathbf{R}$:

$$[\mathbf{R}]_{3n+1} = \frac{\partial \bar{f}}{\partial \mathbf{t}_{cur}} = \begin{bmatrix} \frac{\partial \bar{f}}{\partial t_1} & \cdots & \frac{\partial \bar{f}}{\partial t_m} \end{bmatrix}. \tag{4.17}$$

The algorithm presented in Ref. [63] forces the normalized quadrupole component to equal unity, $Q_{trg,1} = \cdots = Q_{trg,n} = 1$, which might not lead to an optimum solution when including the frequency. Instead, the more relaxed condition

$$Q_{trg,1} = \cdots = Q_{trg,n} = \hat{Q}_{trg} \tag{4.18}$$

is used, which only requires all quadrupole component samples to be equal to an unknown value $\hat{Q}_{trg}$. This value does not necessarily equal unity, but will be

close. The system (4.15) becomes

$$\begin{bmatrix} \hat{Q}_{trg} - Q_1 \\ \vdots \\ \hat{Q}_{trg} - Q_n \\ 0 - D_1^S \\ \vdots \\ 0 - D_n^S \\ 0 - D_1^T \\ \vdots \\ 0 - D_n^T \\ \bar{f}_{trg} - \bar{f} \end{bmatrix} = \begin{bmatrix} \frac{\partial Q_1}{\partial t_1} & \frac{\partial Q_1}{\partial t_2} & \cdots & \frac{\partial Q_1}{\partial t_m} \\ \vdots & \ddots & \ddots & \vdots \\ \frac{\partial Q_n}{\partial t_1} & \frac{\partial Q_n}{\partial t_2} & \cdots & \frac{\partial Q_n}{\partial t_m} \\ \frac{\partial D_1^S}{\partial t_1} & \frac{\partial D_1^S}{\partial t_2} & \cdots & \frac{\partial D_1^S}{\partial t_m} \\ \vdots & \ddots & \ddots & \vdots \\ \frac{\partial D_n^S}{\partial t_1} & \frac{\partial D_n^S}{\partial t_2} & \cdots & \frac{\partial D_n^S}{\partial t_m} \\ \frac{\partial D_1^T}{\partial t_1} & \frac{\partial D_1^T}{\partial t_2} & \cdots & \frac{\partial D_1^T}{\partial t_m} \\ \vdots & \ddots & \ddots & \vdots \\ \frac{\partial D_n^T}{\partial t_1} & \frac{\partial D_n^T}{\partial t_2} & \cdots & \frac{\partial D_n^T}{\partial t_m} \\ \frac{\partial \bar{f}}{\partial t_1} & \frac{\partial \bar{f}}{\partial t_2} & \cdots & \frac{\partial \bar{f}}{\partial t_m} \end{bmatrix} \begin{bmatrix} t_{trg,1} - t_1 \\ \vdots \\ t_{trg,m} - t_m \end{bmatrix}. \tag{4.19}$$

As an unknown quantity, $\hat{Q}_{trg}$ must be brought the right-hand side and appended to $\Delta\mathbf{t}$, the solution vector containing the unknown tuner corrections. This is accomplished by normalizing the tuner positions similarly to the frequency by means of a weight w_t, i.e. replacing the t_i by $\bar{t}_i = w_t t_i$, and the $t_{trg,i}$ by $\bar{t}_{trg,i} = w_t t_{trg,i}$.[39] The response matrix $\mathbf{R}$ is augmented with a corresponding new column, and the final system of equations

$$\underbrace{\begin{bmatrix} -Q_1 \\ \vdots \\ -Q_n \\ -D_1^S \\ \vdots \\ -D_n^S \\ -D_1^T \\ \vdots \\ -D_n^T \\ \Delta\bar{f} \end{bmatrix}}_{\Delta\mathbf{x}} = \underbrace{\begin{bmatrix} \frac{\partial Q_1}{\partial \bar{t}_1} & \frac{\partial Q_1}{\partial \bar{t}_2} & \cdots & \frac{\partial Q_1}{\partial \bar{t}_m} & -1 \\ \vdots & \ddots & \ddots & \vdots & \vdots \\ \frac{\partial Q_n}{\partial \bar{t}_1} & \frac{\partial Q_n}{\partial \bar{t}_2} & \cdots & \frac{\partial Q_n}{\partial \bar{t}_m} & -1 \\ \frac{\partial D_1^S}{\partial \bar{t}_1} & \frac{\partial D_1^S}{\partial \bar{t}_2} & \cdots & \frac{\partial D_1^S}{\partial \bar{t}_m} & 0 \\ \vdots & \ddots & \ddots & \vdots & \vdots \\ \frac{\partial D_n^S}{\partial \bar{t}_1} & \frac{\partial D_n^S}{\partial \bar{t}_2} & \cdots & \frac{\partial D_n^S}{\partial \bar{t}_m} & 0 \\ \frac{\partial D_1^T}{\partial \bar{t}_1} & \frac{\partial D_1^T}{\partial \bar{t}_2} & \cdots & \frac{\partial D_1^T}{\partial \bar{t}_m} & 0 \\ \vdots & \ddots & \ddots & \vdots & \vdots \\ \frac{\partial D_n^T}{\partial \bar{t}_1} & \frac{\partial D_n^T}{\partial \bar{t}_2} & \cdots & \frac{\partial D_n^T}{\partial \bar{t}_m} & 0 \\ \frac{\partial \bar{f}}{\partial \bar{t}_1} & \frac{\partial \bar{f}}{\partial \bar{t}_2} & \cdots & \frac{\partial \bar{f}}{\partial \bar{t}_m} & 0 \end{bmatrix}}_{\mathbf{R}} \underbrace{\begin{bmatrix} \bar{t}_{trg,1} - \bar{t}_1 \\ \vdots \\ \bar{t}_{trg,m} - \bar{t}_m \\ \hat{Q}_{trg} \end{bmatrix}}_{\Delta\mathbf{t}}, \tag{4.20}$$

emerges, where $\Delta\bar{f} = \bar{f}_{trg} - \bar{f} = w_f \Delta f$, and all quantities are dimensionless. Vector $\mathbf{x} \in \mathbb{R}^{3n+1}$ now contains the measured field components, as well as the (normal-

[39] The particular choice of the normalization constants w_f and w_t is explained further below.

ized) current frequency $\bar{f}$ and target frequency $\bar{f}_{trg}$. Matrix $\mathbf{R} \in \mathbb{R}^{(3n+1)\times(m+1)}$ holds the linearized field and frequency responses to individual tuner movements. The solution vector $\Delta\mathbf{t} \in \mathbb{R}^{m+1}$ contains the unknown tuner adjustments, which, added to the current tuner settings $t_1, \ldots, t_m$ give the new tuner positions $t_{trg,1}, \ldots, t_{trg,m}$ required to correct field and frequency.

To obtain the new tuner setting, the system $\Delta\mathbf{x} = \mathbf{R}\Delta\mathbf{t}$ [Eq. (4.20)] must be solved. One possible solution is given by

$$\Delta\mathbf{t} = \mathbf{R}^{\dagger}\Delta\mathbf{x}, \tag{4.21}$$

where $\mathbf{R}^{\dagger} = (\mathbf{R}^{T}\mathbf{R})^{-1}\mathbf{R}$ denotes the Moore-Penrose inverse [71] (pseudo-inverse) of the generally nonsquare matrix $\mathbf{R}$. In Ref. [42], Koubek pointed out that $\mathbf{R}$ is potentially ill-conditioned and proposed to use a special method based on singular value decomposition (SVD) [71] to compute the inverse. This method also accounts for the fact the relationship between field amplitude (or frequency) and tuner position is actually not linear, but is only approximated as such by the algorithm. In the following, the approach is described.

To simplify the notation, one identifies $N = 3n + 1$ and $M = m + 1$ for the system dimensions corresponding to a setup with n longitudinal field sampling points and m tuners. The SVD of $\mathbf{R} \in \mathbb{R}^{N\times M}$ is given by

$$\mathbf{R} = \mathbf{U}\mathbf{\Sigma}\mathbf{V}^{T}, \tag{4.22}$$

where $\mathbf{U} \in \mathbb{R}^{N\times N}$ and $\mathbf{V} \in \mathbb{R}^{M\times M}$ are orthonormal matrices. $\mathbf{\Sigma}$ is a rectangular diagonal matrix

$$\mathbf{\Sigma} = \begin{bmatrix} \sigma_1 & & \\ & \ddots & \\ & & \sigma_M \\ & & \end{bmatrix} \in \mathbb{R}^{N\times M}, \tag{4.23}$$

whose diagonal entries $\sigma_1, \ldots, \sigma_M$ are the singular values of $\mathbf{R}$ in descending order. Note that $M \leqslant N$ is an essential requirement of this tuning algorithm, i.e. the number of tuners must not exceed three times the number of field sampling points, such that the system is not underdetermined. This can always be achieved by increasing the number of sampling points. The Moore-Penrose inverse of $\mathbf{R}$ can then be constructed as

$$\mathbf{R}^{\dagger} = \mathbf{V}\mathbf{\Sigma}^{\dagger}\mathbf{U}^{T}, \tag{4.24}$$

where $\mathbf{\Sigma}^{\dagger}$ is obtained simply by inverting each diagonal entry σ_i of $\mathbf{\Sigma}$ and transposing the result:

$$\mathbf{\Sigma}^{\dagger} = \begin{bmatrix} 1/\sigma_1 & & \\ & \ddots & \\ & & 1/\sigma_M \\ & & \end{bmatrix} \in \mathbb{R}^{M\times N}. \tag{4.25}$$

For ill-conditioned, (almost) singular $\mathbf{R}$, the smaller singular values σ_i are (almost) zero, and their reciprocals $1/\sigma_i$ approach infinity. With Eq. (4.21) this may lead to invalid solutions, i.e. tuner adjustments that lie outside of the physical tuner movement range. In Ref. [63], Koubek proposed to circumvent this problem by consecutively setting the largest $1/\sigma_i$ entries of $\mathbf{\Sigma}^\dagger$ to zero. One defines

$$\mathbf{\Sigma}_k^\dagger = \begin{bmatrix} 1/\sigma_1 & & & & & & \\ & \ddots & & & & & \\ & & 1/\sigma_{M-k} & & & & \\ & & & 0 & & & \\ & & & & \ddots & & \\ & & & & & 0 & \end{bmatrix} \tag{4.26}$$

as the matrix $\mathbf{\Sigma}^\dagger$ where the k largest entries have been set to zero, with $k = 0, \ldots, (M-1)$. Note that $\mathbf{\Sigma}_0^\dagger = \mathbf{\Sigma}^\dagger$ is the initial Moore-Penrose inverse, whereas the case of $k = M$ would lead to $\mathbf{R}^\dagger = \mathbf{0}$ and no tuner movements at all. The matrices give M possibly useful solutions

$$\Delta \mathbf{t}_k = \mathbf{V} \mathbf{\Sigma}_k^\dagger \mathbf{U}^T \Delta \mathbf{x} \tag{4.27}$$

to achieve a flat quadrupole field and the desired resonant frequency. Naturally, solutions $\Delta \mathbf{t}_k$ with tuner adjustments outside the physical movement range must be immediately discarded. The remaining solutions are checked by computing the prediction $\tilde{\mathbf{x}}_{trg,k}$ for corrected field and frequency using the original response matrix:

$$\tilde{\mathbf{x}}_{trg,k} = \mathbf{x}_{cur} + \mathbf{R} \Delta \mathbf{t}_k. \tag{4.28}$$

The tuner movement for the current tuning step is chosen as that $\Delta \mathbf{t}_k$ whose corresponding $\tilde{\mathbf{x}}_{trg,k}$ best fulfills the requirements: a quadrupole component as flat as possible, and dipole components as well as frequency deviations as close to zero as possible.

After applying the tuner adjustment, the field and frequency are measured again and a new vector $\mathbf{x}_{cur}$ emerges. The process is repeated until the measured field components match the requirements to a desired accuracy [1, 42]. The response matrix $\mathbf{R}$ is obtained by measuring the sensitivity of each field sampling point and frequency to the individual movement of each tuner, starting from the nominal tuner setting at the beginning of the tuning process. As $\mathbf{R}$ contains only first-order derivatives (analogous to the Jacobian matrix), it linearizes the measured sensitivities and assumes that they are constant over the entire tuning range. However, with the example of the HF-RFQ, Koubek [63] showed that it is sufficient to use only the initial $\mathbf{R}$, and to choose a different solution [Eq. (4.27)], i.e., a different value for k, for each tuning iteration. In this way, remeasuring the response matrix $\mathbf{R}$ during each tuning iteration is avoided—a procedure that for m tuners requires m bead-pull measurements.

This technique was adopted for the tuning of the PIXE-RFQ, which, featuring only half the length of the HF-RFQ, has a larger spatial separation and is thus generally easier to tune. The tuning steps of the PIXE-RFQ are reported in the following section.

4.3.4 Tuning Steps

The tuning algorithm requires determining the entries of the response matrix $\mathbf{R}$ from Eq. (4.20) by means of bead-pull measurements. Each matrix column is obtained by inserting or retracting the corresponding tuner by a certain length, while all other tuners remain in nominal position. Since the matrix measurement gives only a first-order approximation (secant) of the real nonlinear response, the individual tuner movements should resemble the anticipated corrective movement as close as possible. From Fig. 4.15 it can be seen that a movement of approximately 3 mm affects the dipole components at a level similar to the dipole component error. Therefore, the derivatives in matrix $\mathbf{R}$ were approximated as the difference quotients where $\Delta t_j = 3\,\mathrm{mm}$, i.e. each tuner was retracted by 3 mm. Naturally, the weight used to normalize the tuner adjustment was chosen as $w_t = (3\,\mathrm{mm})^{-1}$.

In Fig. 4.16, a visual representation of the response matrix—except for the last row and last column—is shown. Each entry represents one derivative that is given as the denormalized value in units of %/mm. From the plot it can clearly be seen that all four tuners at the same longitudinal position (e.g. tuners 1 to 4) have approximately the same effect on the quadrupole component, where tuners located at the extremities of the RFQ can induce slightly stronger field tilts than those near the center. Each tuner has a strong effect on the dipole component whose definition [Eq. (4.9)] comprises the quadrant in which the tuner is located, while the other dipole component is hardly influenced at all. Two tuners located opposite of each other (e.g. tuners 1 and 3, or 2 and 4, see Fig. 4.11) have opposite effects on the respective dipole component. The frequency—representing a quantity proportional to the integral field energy—is affected by each tuner with roughly the same sensitivity of $-50\,\mathrm{kHz/mm}$ (Fig. 4.17). The individual deviations are attributed to the longitudinally and transversely inhomogeneous capacitance and inductance distributions caused by vane modulation, misalignments, and design choices, which in fact motivate the RFQ tuning.

In each tuning step, the frequency was enforced to equal the nominal frequency of 749.480 MHz to an accuracy ensuring that no significant frequency error would be introduced by the tuning algorithm itself. This was accomplished by choosing the corresponding normalization weight w_f such that the predicted frequency obtained from $\tilde{\mathbf{x}}_{\mathrm{trg},k}$ [Eq. (4.28)] matched the desired frequency with an error of 0.1 kHz or better, while still keeping the weight as small as possible. In this case, $w_f = (10^4\,\mathrm{Hz})^{-1}$.

As explained in Section 4.3.3, the inversion of $\mathbf{R}$ by means of SVD allows for constructing M possible solutions $\Delta\mathbf{t}_k$ [Eq. (4.27)] for the corrective tuner move-

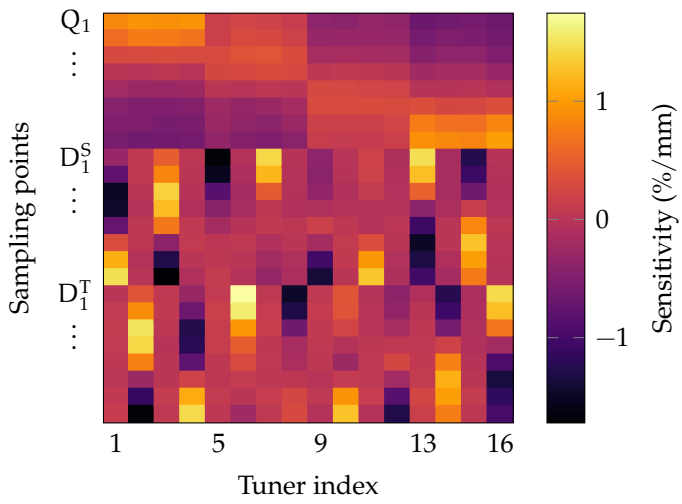

Figure 4.16: Visual representation of the response matrix **R**, except for the last row reserved for the frequency and the last column, i.e. as it appears in Eq. (4.15). Each entry represents the sensitivity of the Q (upper third), D^S (middle third), or D^T component (lower third) at one sampling point with respect to the tuner movement. Because of their definition [Eq. (4.9)], each tuner has a strong effect on one dipole component and almost none on the other. The denormalized derivative is given in units of %/mm.

ment in each tuning step. With Eq. (4.28), the possible solutions yield M predictions $\tilde{\mathbf{x}}_{\mathrm{trg},k}$ of the field distribution after the tuning step, that are shown in Fig. 4.18(a) with the example given by the first tuning step. The corresponding amplitude errors are reported in Fig. 4.18(b). As expected, solutions with lower k (less eliminated singular values) on the left side of Fig. 4.18(b) generally deliver better corrections than those on the far right. In Refs. [42, 63], Koubek reported that—with the original version of the algorithm given by Eq. (4.15)—many of the possible solutions with small k (i.e. less discarded singular values) yielded tuner adjustments that are outside the physical tuner movement range of the HF-RFQ. In the present case this could not be confirmed; all $k = 1, \ldots, M-1$ solutions

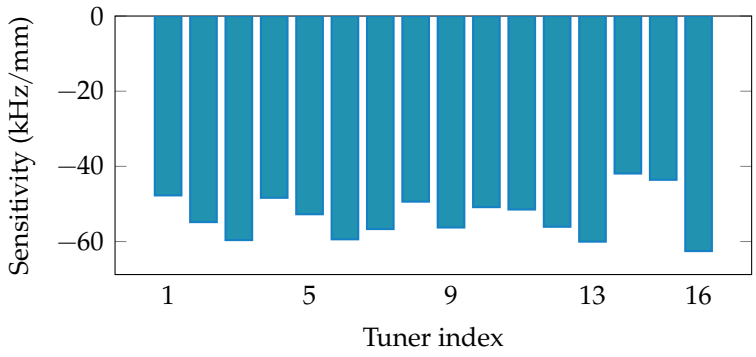

Figure 4.17: Response of the TE_{210} eigenfrequency to the movement of each tuner, i.e. the last row of **R**. The denormalized derivative is given in units of kHz/mm. A negative derivative means that the frequency is lowered when the tuner is retracted, as the total cavity inductance is increased.

provide physically possible tuner movements. This is attributed to two the fact that the augmented version of the algorithm [Eq. (4.20)] also includes the frequency, which would strongly disagree with the desired value for unphysically large tuner movements and thus acts in a dampening manner. Furthermore, the response matrix of the HF-RFQ measured in Refs. [42, 63] is more affected by measurement noise, as no averaging was performed. Nevertheless, it is still advantageous to make use of the truncated SVD for the improved algorithm and select a solution "by eye," as solution k does not strictly provide a better correction than solution $k+1$.

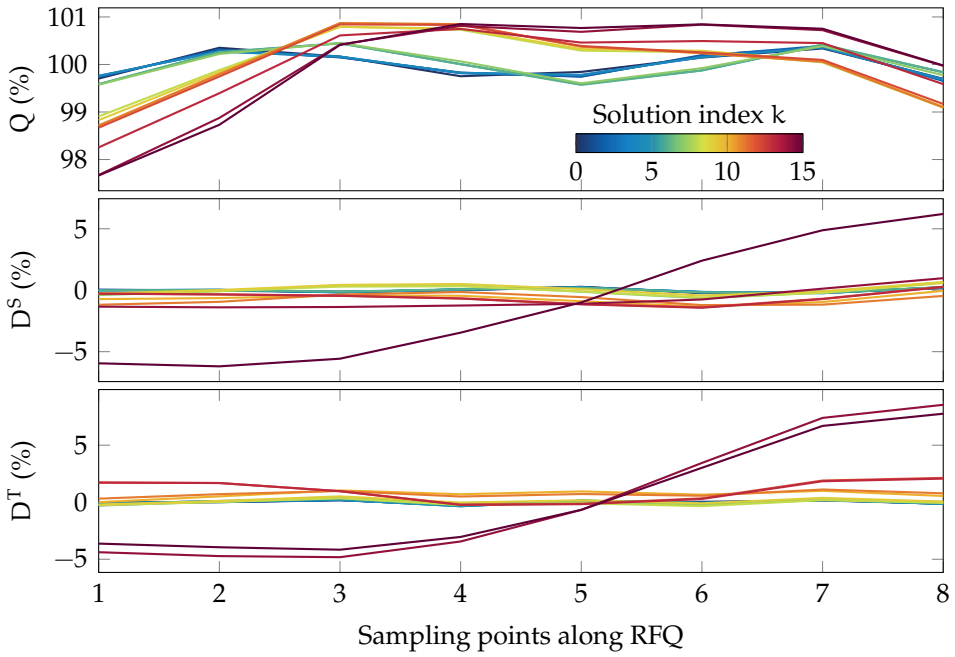

(a)

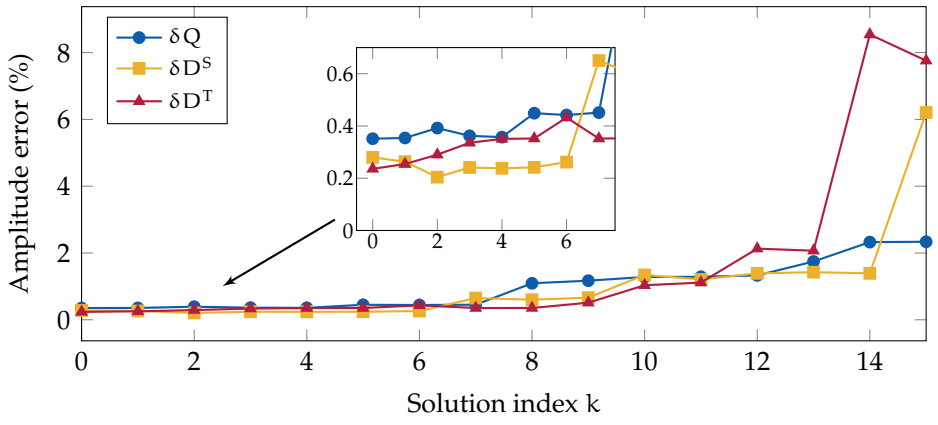

(b)

Figure 4.18: Predicted field components (a) after applying the tuner adjustments yielded during the first tuning step by discarding the smallest k singular values from the response matrix. The corresponding quadrupole and dipole component errors are reported in (b).

With the augmented tuning algorithm described above, the PIXE-RFQ was tuned with only two tuning steps after initial measurement of the response matrix **R**. For the first step, solution $k = 1$ was chosen as the option that provides very small errors for all three components while equally correcting both dipole components ($\delta D^S \approx \delta D^T$). The corresponding field prediction is shown in Fig. 4.19 (red dashed line). After applying the tuner adjustments, the field and frequency were measured again. The frequency error improved from 624 kHz to 46 kHz (Fig. 4.20). Regarding the fields, a significant deviation between field prediction and measurement (red solid line) was observed, in particular for the D^S component, where an error of nearly $\pm 3\,\%$ remained. Aside from measurement noise, the reason is found in the nonlinear relation between field and tuner position, that is represented in the response matrix only by linear secant approximation. Thus, a second tuning step with the same response matrix was carried out, however, this time solution $k = 3$ was selected. Predicted and measured field components after the second tuning step are reported in Fig. 4.19 (yellow dashed and solid lines, respectively). The D^S component could be suppressed to an error of 1.3 % with respect to the quadrupole component, and the frequency error was improved to merely 1.5 kHz. This error is of the same order of magnitude as the error arising from the thermometer precision (± 2.6 kHz). The second tuning step already saw a slight worsening of the D^T component. This indicates that an accuracy limit given either by the overall noise level or by the approximating nature of the response matrix was reached. As the errors in frequency and field after the second tuning step fulfilled the requirements listed in Section 4.1.4, and a third iteration delivered no satisfying predictions, it was decided to stop the tuning procedure after two steps.

The final tuner positions are reported in Fig. 4.21. Note that on average the tuners were retracted (positive t_j), since the initial measured frequency was too high such that the total cavity inductance had to be increased. All adjustments are considerably smaller than the maximum foreseen movement range of ± 11 mm. Since all tuners were initially manufactured with an over-length of 11 mm to provide the movement range, the length to be removed during remachining amounts to $11\,\text{mm} + t_j$. The final t_j were determined both from the scale on the tuner tooling [Fig. 4.10(b)], which was used during the tuning process itself, and from an additional measurement using a caliper. The error between these two measurements amounted to up to 60 µm, likely originating in a small inclination of the tuner within its guidance tube. The average of both values was used for the remachining.

Following remachining, a bead-pull measurement was carried out with the tuners fixed to the corresponding flanges as a mean of validation, after which they were installed with vacuum gaskets and a final bead-pull measurement was performed. The results of these measurements are shown in Fig. 4.22(a) in comparison to the initial field and the field after the second tuning step in terms of discrete sampling points. The corresponding errors are summarized in Table 4.1. A small deviation, larger than the measurement noise, was observed between

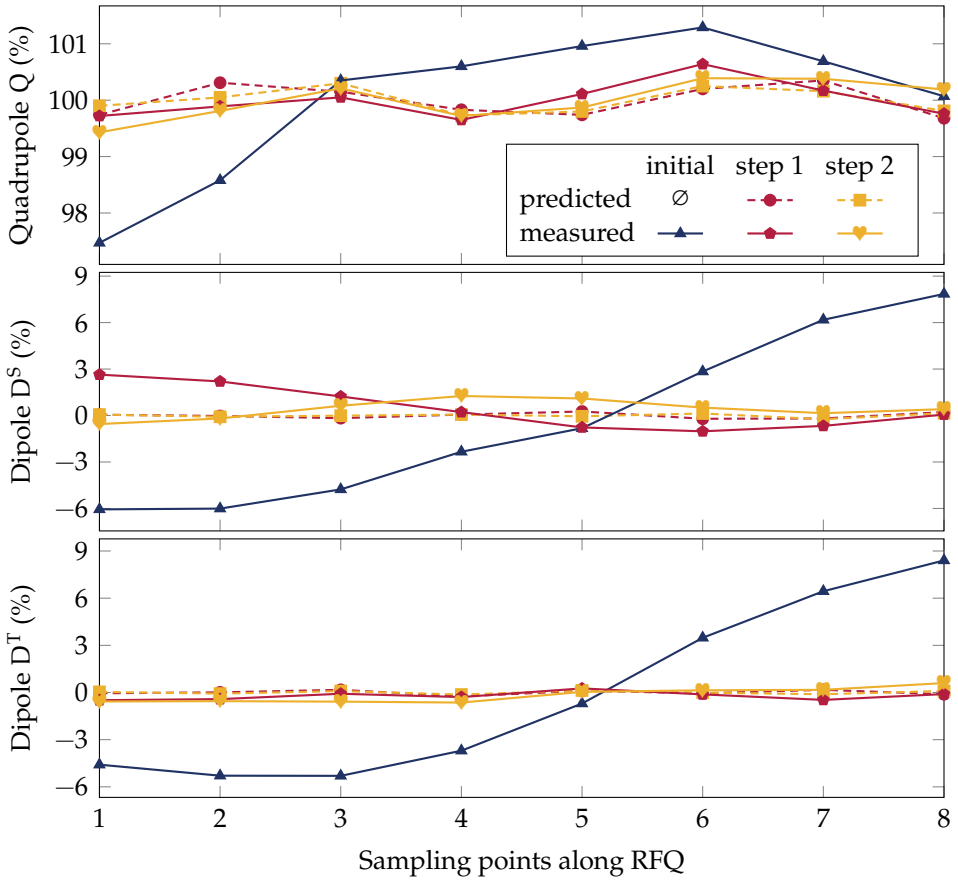

Figure 4.19: Quadrupole and dipole field components for nominal tuner position (initial) and after the first and second tuning step. Dashed lines indicate the field as predicted by Eq. (4.28), while solid lines report the actually measured field. After the second and final tuning step, the errors read as follows: $\delta Q = \pm 0.6\,\%$, $\delta D^S = \pm 1.3\,\%$, and $\delta D^T = \pm 0.6\,\%$.

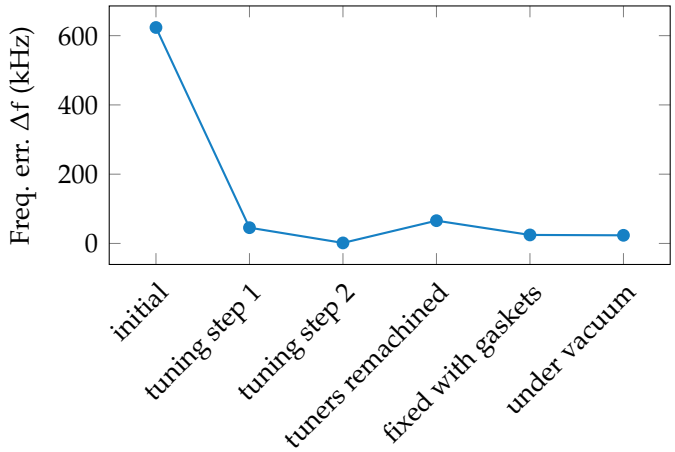

Figure 4.20: Frequency of the TE_{210} operating mode for nominal tuner position (initial), after the first and second tuning step, and after remachining. The last two steps correspond to measurements of the final configuration (tuners fixed with vacuum gaskets), conducted under air and vacuum. The final frequency error amounts to $\Delta f = 23.5\,\text{kHz}$, measured under vacuum.

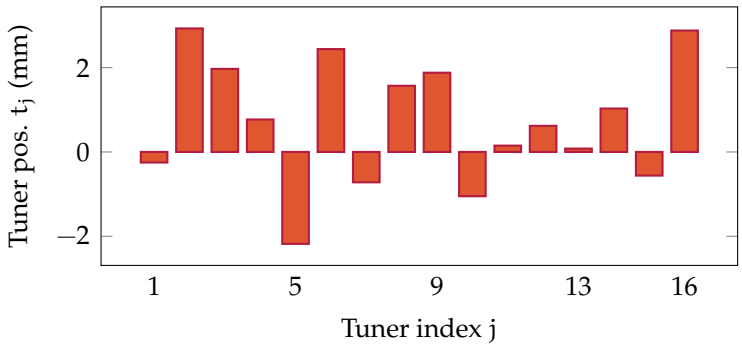

Figure 4.21: Tuner positions after the final tuning step. A positive (negative) value indicates that the tuner was retracted (inserted) with respect to the nominal position.

the field after the second tuning step, when the tuners were still mounted in the tooling, and the field after they were remachined and fixed. This deviation likely originates in the finite accuracy of length measurement and material cutting. Figure 4.22(b) reports the field distributions of the initial and final setup (without sampling).

The final frequency measured under vacuum was 23.5 kHz above the target value. This error was achieved measuring under air without the use of dry nitrogen, solely correcting with measured temperature and the STP value for air permittivity. It can be explained by the fact that the response matrix and thus the initial frequency were measured on a rainy day with high humidity (RH $\approx$ 100 %), while the tuning steps were performed under sunny weather. It is likely that with the use of a hygrometer the remaining error could have been significantly reduced by correcting for the measured humidity according to Fig. 4.1. However, even without accounting for humidity, the final frequency error is by more than a factor of two smaller than the tuning range given by a typical water cooling system ($\pm$60 kHz).

Table 4.1: Errors in field components and frequency during tuning and subsequent measurements in chronological order.

Step	δQ (%)	δD^S (%)	δD^T (%)	Δf (kHz)
Initial	2.5	7.9	8.4	623.6
Tuning step 1	0.6	2.6	0.5	45.5
Tuning step 2	0.6	1.3	0.6	1.5
Tuners remachined	0.3	1.0	0.9	65.7
Tuners fixed with gaskets	0.3	0.9	0.9	24.5
Under vacuum	—	—	—	23.5

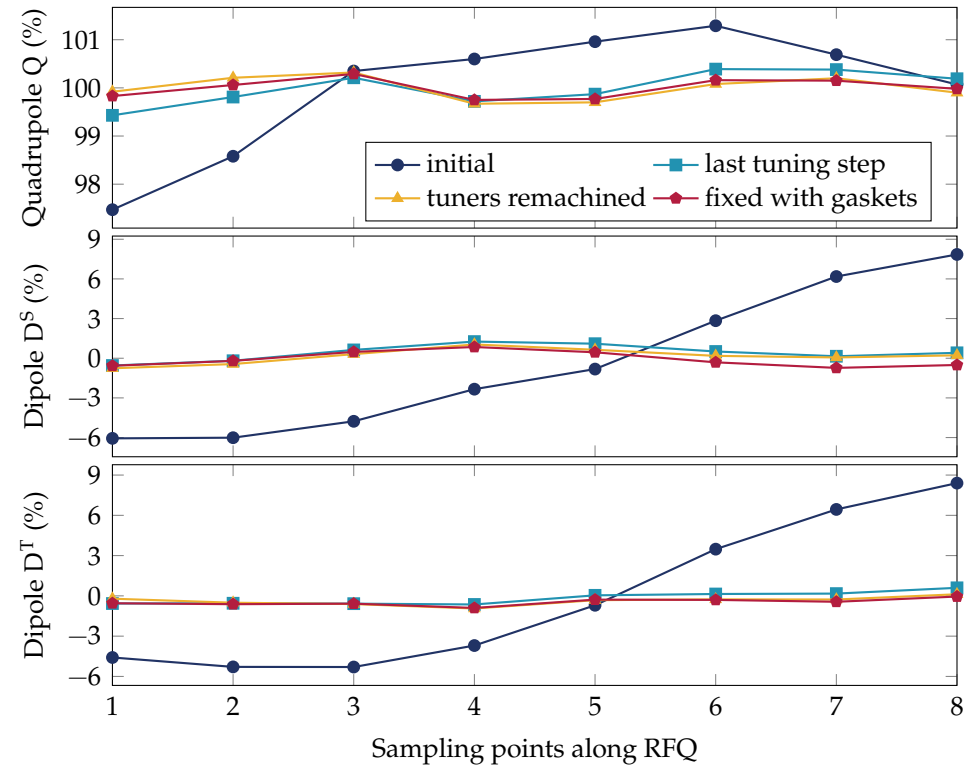

(a)

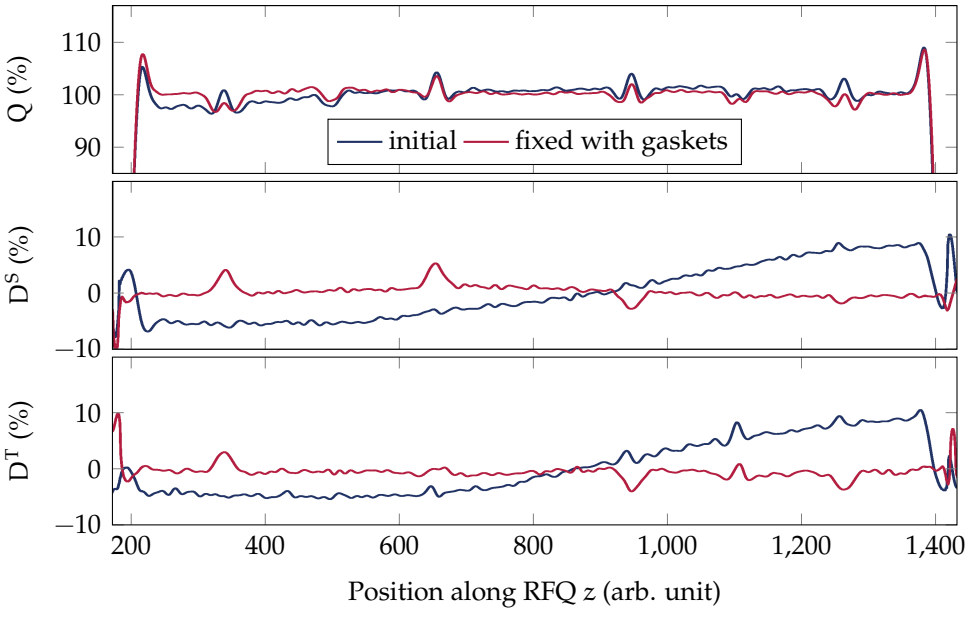

(b)

Figure 4.22: Measured field components before tuning, after tuning, with remachined tuners, and for the final installation of the tuners with gaskets (a). The field distributions of the initial and final setup (without sampling) are reported in (b).

4.4 Quality Factor Measurement

After tuning, the quality factors of the RFQ were measured. Aside from further validating the design, these measurements provide information on the input power reflection originating in potential over-coupling or under-coupling.

The raw measurement data are the real and imaginary parts of reflection coefficient $\Gamma = S_{11}$, measured in a bandwidth of 1 MHz symmetrically around the resonant frequency of the TE_{210} operating mode. The reflection coefficient describes in very good approximation a circle in the complex plane, from which the four parameters—unloaded, external, and loaded quality factor, as well as coupling coefficient—can be extracted. The results obtained by two distinct extraction methods are compared to each other and to the simulation results in the following sections.

4.4.1 Three-point Method

The first technique [66, 208], called three-point method, extracts the quality factors by means of three bandwidths, which are obtained from the intersection of the Γ circle with specific auxiliary circles in the complex plane (Fig. 4.23).

In a virtual plane between coupler and cavity, the circle is located in the so-called detuned-short position, denoted as Γ_{ds}. Both $\Gamma_{ds}(\Delta\omega \to \pm\infty) = -1$, the detuned reflection, and $\Gamma_{ds}(\Delta\omega = 0)$, the reflection coefficient of the loaded resonator, are placed on the real axis. Since the plane of VNA calibration is offset by a certain length from the coupling plane, the circle is rotated around the origin by some angle $\Delta\phi$. For the three-point method, the circle has to be rotated back into the detuned-short position, i.e.

$$\Gamma_{ds} = \Gamma e^{-j\Delta\phi}, \tag{4.29}$$

where Γ is the reflection coefficient measured in the calibration plane.

From Γ_{ds} the three quality factors and the coupling coefficient can be determined by identifying three associated bandwidths [66, 208]:

$$\begin{aligned}
Q_0 &= \frac{\omega_0}{|\omega_1 - \omega_2|} \qquad \text{where} \qquad \Re\left\{\bar{Y}(\omega_{1,2})\right\} = \pm\Im\left\{\bar{Y}(\omega_{1,2})\right\}, \\
Q_{ex} &= \frac{\omega_0}{|\omega_3 - \omega_4|} \qquad \text{where} \qquad \left|\Im\left\{\bar{Y}(\omega_{3,4})\right\}\right| = 1, \\
Q_\ell &= \frac{\omega_0}{|\omega_5 - \omega_6|} \qquad \text{where} \qquad |\Im\{\Gamma_{ds}(\omega_{5,6})\}| = \max.
\end{aligned} \tag{4.30}$$

Here,

$$\bar{Y} = \frac{1 - \Gamma_{ds}}{1 + \Gamma_{ds}} \tag{4.31}$$

denotes the normalized admittance. Notably, the unloaded quality factor Q_0 corresponds to the bandwidth between the points where the angle of the admittance (or impedance) amounts to $\pm 45°$. The three-point method with its auxiliary circles is visualized by the Smith chart shown in Fig. 4.23.

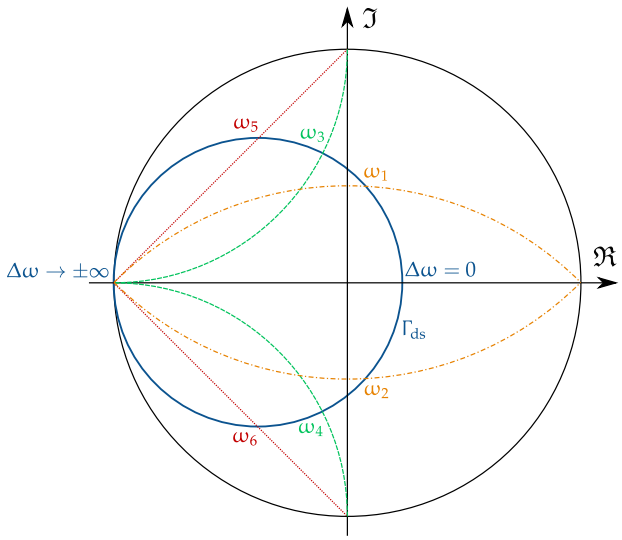

Figure 4.23: Smith chart illustrating the three-point method for determining Q_0, Q_{ex}, and Q_ℓ from the measurement of the reflection coefficient Γ_{ds} in the detuned-short position. The complex plane of the reflection coefficient is shown. The colored lines are the auxiliary circles corresponding to the conditions described in Eq. (4.30).

As a mean of error estimation, each quality factor can be calculated both from the corresponding bandwidth and from the other two quality factors using

$$\frac{1}{Q_\ell} = \frac{1}{Q_0} + \frac{1}{Q_{ex}}. \tag{2.28}$$

Similarly, the coupling coefficient β_c can be obtained from either combination of two quality factors:

$$\beta_c = \frac{Q_0}{Q_{ex}} = \frac{Q_0}{Q_\ell} - 1 = \frac{1}{Q_{ex}/Q_\ell - 1}. \tag{4.32}$$

From the rotated reflection coefficient Γ_{ds} measured on the RFQ where the tuners were fixed with gaskets, the quality factors and coupling coefficient listed in the left column of Table 4.2 were obtained. The errors between the values obtained through the different ways as described above amount to up to 10 %, which is rather high and likely unphysical.

The reason is found in the fact that the circle described by Γ_{ds} is actually not located in the ideal detuned-short position, i.e. $\Gamma_{ds}(\Delta\omega \to \pm\infty) > -1$. This can be corrected by assuming a single additional reflection $\Gamma_1 \in \mathbb{R}$ that shifts the ideal

Table 4.2: Quality factors measured using the three-point method from the solely rotated circle Γ_{ds} and the corrected circle Γ'_{ds} in the ideal detuned-short position.

		only rotated Γ_{ds}		corrected Γ'_{ds}	
Unloaded quality factor	Q_0	6089	±155	6002	±6
External quality factor	Q_{ex}	5082	±108	5101	±4
Loaded quality factor	Q_ℓ	2737	±31	2756	±2
Coupling coefficient	β_c	1.20	±0.06	1.18	±0.01

circle in the detuned-short position Γ'_{ds} along the real axis towards the origin:

$$\Gamma_{ds} = \Gamma_1 + \Gamma'_{ds}. \tag{4.33}$$

The reflection Γ_1 corresponds to a small mismatch roughly located in the transition between the Type-N connector and the EIA $3^1/_8$ in coaxial waveguide close to the calibration plane. This is consistent with the fact that the VNA was calibrated for the Type-N connector on the RFQ-side end of the RF cable (see Section 4.1.1). Therefore, no correction was made for possible reflections in the Type-N-to-coax transition. Empirically, it was determined that $\Gamma_1 \approx 0.012 = -38\,\mathrm{dB}$. From the corrected reflection $\Gamma'_{ds} = \Gamma_{ds} - 0.012$ the much more consistent values shown in the right column of Table 4.2 could be obtained. They agree with the results delivered by the circle-fitting method (see following two sections) to an error of 0.2 %, which is on the accuracy level of this kind of measurement.

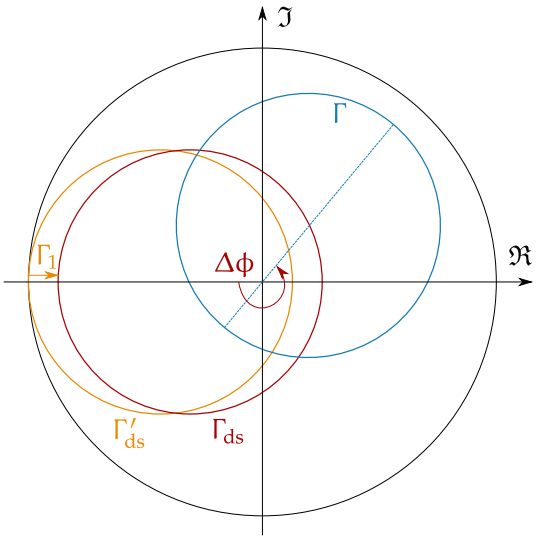

Figure 4.24: Rotation and shift of the measured reflection coefficient Γ to fulfill the requirements of the three-point method. First, the circle is rotated such that its center and the points corresponding to $\Delta\omega = 0$ and $\Delta\omega \to \pm\infty$ lie on the real axis (Γ_{ds}). Then, it is shifted along the real axis such that $\Gamma'_{ds}(\Delta\omega \to \pm\infty) = -1$. (No actual measurement data are shown, but rather the principle is visualized. The shift Γ_1 is exaggerated.)

4.4.2 Circle-fitting Method

A more accurate method emerges from fitting an ideal circle to the curve described by the reflection coefficient Γ in the complex plane [209–212]. The fitting parameters are determined by solving an overdetermined system of equations by means of the least-squares method. Because of the implicit averaging, errors originating in the small imperfections of the circle described by Γ and the influence of measurement noise can be removed to a great extent. Furthermore, this method does not require that $|\Gamma_{ds}(\Delta\omega \to \pm\infty)| = 1$, and a correction as described above for the three-point method is thus not necessary.

The technique is based on the Möbius transformation

$$\Gamma = \frac{b_1\bar{\omega} + b_2}{b_3\bar{\omega} + 1}, \tag{4.34}$$

which describes a circle in the complex plane characterized by the complex parameters b_1, b_2, and b_3. Here,

$$\bar{\omega} = 2\left(\frac{\omega}{\omega_0} - 1\right) \tag{4.35}$$

denotes the frequency normalized to ω_0, the resonant frequency of the loaded resonator. When the measurement frequency is far from the operating frequency, i.e. for $\bar{\omega} \to \pm\infty$, $\Gamma \to b_1/b_3$, the detuned reflection coefficient, which does not necessarily equal unity. On the other hand, $\bar{\omega} = 0$ delivers $\Gamma(\Delta\omega = 0) = b_2$ as the reflection coefficient of the loaded resonator. The diameter D of the circle equals the distance between these two,

$$D = \left|\frac{b_1}{b_3} - b_2\right|, \tag{4.36}$$

and the coupling coefficient can be determined as [210]

$$\beta_c = \frac{1}{2/D - 1}. \tag{4.37}$$

Furthermore,

$$Q_\ell = \Im\{b_3\}, \tag{4.38}$$

from which the two remaining quality factors can be calculated:

$$Q_0 = Q_\ell(1 + \beta_c), \qquad Q_{ex} = Q_\ell\left(1 + \frac{1}{\beta_c}\right). \tag{4.39}$$

The VNA measures the reflection coefficient $\Gamma(\omega_i)$ at N discrete frequencies ω_i. Thus, Eq. (4.34) can be written in matrix form:

$$\underbrace{\begin{bmatrix}\Gamma(\omega_1)\\ \vdots \\ \Gamma(\omega_N)\end{bmatrix}}_{\boldsymbol{\Gamma} \in \mathbb{C}^N} = \underbrace{\begin{bmatrix}\bar{\omega}_1 & 1 & -\bar{\omega}_1\Gamma(\omega_1)\\ \vdots & \vdots & \vdots \\ \bar{\omega}_N & 1 & -\bar{\omega}_N\Gamma(\omega_N)\end{bmatrix}}_{\mathbf{K} \in \mathbb{C}^{N\times 3}} \underbrace{\begin{bmatrix}b_1\\ b_2\\ b_3\end{bmatrix}}_{\mathbf{b} \in \mathbb{C}^3}. \tag{4.40}$$

This is a heavily overdetermined system of equations, in which each row represents one measurement point. The curve described by the reflection coefficient Γ is not a perfect circle—deviations become stronger with increasing distance from ω_0. Furthermore, an equidistant frequency sampling implies a lower density of measurement points around the critical ω_0. Therefore, a weighting matrix $\boldsymbol{W}$ is introduced, which diminishes the significance of measurement points measurement points further away from ω_0:

$$w_i = 1 - |\Gamma(\omega_i)|^2, \qquad \boldsymbol{W} = \operatorname{diag}\begin{bmatrix} w_1 & \cdots & w_N \end{bmatrix} \in \mathbb{R}^{N\times N}. \tag{4.41}$$

Then, the three fitting parameters are obtained as

$$\mathbf{b} = (\boldsymbol{W}\mathbf{K})^{\dagger}\, \boldsymbol{W}\boldsymbol{\Gamma}. \tag{4.42}$$

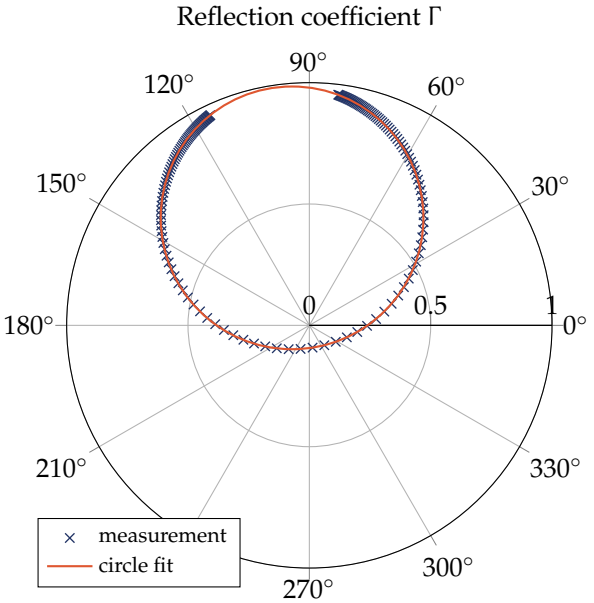

Figure 4.25: Polar plot of the reflection coefficient Γ measured over a span of 1 MHz and the fitted circle. Only every tenth measurement point is shown for clarity.

4.4.3 Measurement Results

In Table 4.3, the quality factors and coupling coefficients calculated from the measurement data using both three-point and circle-fitting method are compared to each other and to the design values. Very close agreement between the two methods can be observed: the difference in Q_0 amounts to roughly 0.5 %, and the measured Q_0 agrees with the design value to the same accuracy. This indicates not only the reliability of the full 3D FEM simulation and the segmented model for power loss calculation (Section 3.3.1), but also the manufacturing quality of the RFQ.

Table 4.3: Quality factors measured using the corrected three-point method and circle-fitting method compared to the design values.

		Three-point	Circle fit	Design value
Unloaded quality factor	Q_0	6002	6018	5995
External quality factor	Q_{ex}	5101	5099	4796
Loaded quality factor	Q_ℓ	2756	2760	2664
Coupling coefficient	β_c	1.18	1.18	1.25

A larger deviation of 6 % was observed between measured external quality factor Q_{ex} and the corresponding design value. This translates to a comparable error in β_c and an error of 3 % in Q_ℓ. The errors could be introduced when manufacturing the physical coupler and mounting it to the RFQ, caused mainly by imperfect machining, brazing, and alignment. For instance, a 6 % error in β_c could correspond to a mechanical error of 300 µm in the coupling loop size [see Fig. 3.21(b)]. Such a deviation cannot be excluded, since the coupler represents a complex geometry composed of multipole components assembled by means of bolts. Contrarily, the simulation models generally yield errors in Q_{ex} which are by an order of magnitude smaller.

The discrepancy shows that it is important to design the coupler with an over-coupling margin of a few ten percent. Although the PIXE-RFQ coupler features a rotatable flange that allows for fine-tuning the coupling coefficient after measuring the actual quality factors, it was decided not to take advantage and accept a coupling coefficient of $\beta_c = 1.18$, i.e. an over-coupling of 18 %. With Eq. (2.30), this translates to a reflection coefficient of $\Gamma = 0.083 = -22\,\mathrm{dB}$. If the RFQ cavity consumes $P_0 = 65.0\,\mathrm{kW}$ of peak power in terms of surface losses, an input power of $P_+ \approx 65.5\,\mathrm{kW}$ is required, and $P_- \approx 0.5\,\mathrm{kW}$, i.e. roughly 0.7 % of the input power are reflected back towards the generator [Eq. (2.32)]. These values are well acceptable for operation.

All measurements reported in Sections 4.4 and 4.5 were conducted under vacuum (approximately 10^{-6} mbar). An interesting observation was made in that the measured coupling increased by approximately 2 % (from $\beta_c = 1.16$ to 1.18) when the RFQ cavity was evacuated. A possible explanation is found in the structure of the power coupler shown in e.g. Fig. 3.28(c): The inner conductor is only sup-

ported by the coupling loop and the PEEK RF window. Subjected to the pressure difference between vacuum and exterior atmosphere, the PEEK window could deform and push inwards the inner conductor. This would slightly increase the effective area of the coupling loop, resulting in a larger coupling coefficient [179].

4.5 Pickup Antenna Calibration

The PIXE-RFQ features four diagnostic RF field pickup antennas that are used to measure the field amplitude during operation (see also Section 3.2.6). They are in fact spares that were originally manufactured for the medical HF-RFQ. While one antenna would be sufficient to assess the overall field amplitude, four antennas have been installed to have operational spares, which also allows for recording the field flatness during operation by comparing the measurements of multiple antennas to each other. The distortions may originate in RFQ manipulations and transport as well as long term operation in different conditions. The antennas have been arranged in such a way that both longitudinal and transverse field distortions can be measured despite the limited number of antennas (Fig. 4.26).

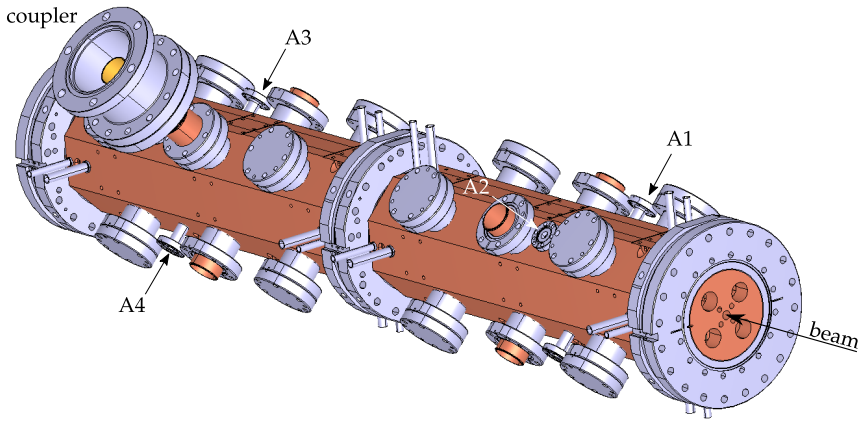

Figure 4.26: Labeling of the PIXE-RFQ diagnostic RF pickup antennas.

The penetration of the antennas into the cavity was chosen such that they extract a power of $P_a = 1\,W$ at nominal operation, corresponding to an external quality factor of 3.9×10^8. Because of finite manufacturing accuracy—all four antennas are minimally different, and so are the distances between antenna flanges and beam axis—the antennas must be calibrated by means of RF measurements. In this setup, the transmission coefficient $S_{21}^{C\to Ai}$ between power coupler and ith antenna was measured. Assuming an input power through the coupler of $P_+ = 65.5\,kW$ (Section 4.4), a transmission of $|S_{21}^{C\to Ai}| = -48.16\,dB$ at the TE_{210} resonance corresponds to the design antenna power.

Figure 4.27 shows the magnitude of $S_{21}^{C\to A3}$ as a function of frequency, measured between coupler and antenna 3 on the tuned RFQ. The PIXE-RFQ eigenmodes appear as peaks at frequencies where the cavity can accept input power

and transmit it to the pickup antenna. Note that the two dipole polarizations (TE_{11n} appearing twice for each n) separate in frequency because of slight asymmetries in the RFQ. It is interesting to note that the TE_{112} and TE_{212} modes are barely visible in the measured spectrum. Since their longitudinal field distributions vanish at the location of the coupler, they are barely excited in this configuration. Lastly, a large discrepancy between measurement and simulation (dotted lines) was observed for some higher-order modes. This is attributed to the fact that the tuners where adjusted such that the measured frequency of the TE_{210} operating mode agrees with the simulation, which in turn already assumes a perfectly tuned cavity. The effect of the tuners on higher-order modes varies depending on how strong the magnetic field amplitude of the mode is at the location of the particular tuner. Thus, the tuners can severely perturb the higher-order mode frequencies.

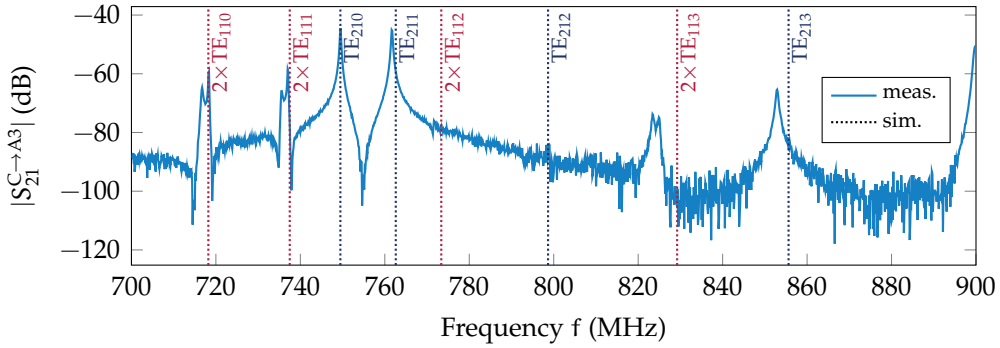

Figure 4.27: Magnitude of the transmission coefficient $S_{21}^{C\to A3}$ measured between input power coupler and pickup antenna 3. The PIXE-RFQ eigenmodes clearly appear as maxima. For comparison, the eigenfrequencies obtained from FEM simulation of the nominal RFQ design are shown as dotted lines.

The antennas were calibrated by means of measurements such as the one shown in Fig. 4.27 at the TE_{210} resonance after the RFQ was tuned, and the field flatness reported in Table 4.1 and Fig. 4.22 was established. Table 4.4 lists the transmission coefficients $|S_{21}^{C\to Ai}|$ measured between power coupler and ith antenna. The second column shows the corresponding power $P_{a,i}$ extracted by the antenna under nominal operation conditions, i.e. with the coupling coefficient measured in Section 4.4:

$$P_{a,i} = P_+ \cdot \left|S_{21}^{C\to Ai}\right|^2 \tag{4.43}$$

where $P_+ = 65.5\,\mathrm{kW}$. In the third column of Table 4.4, the powers are listed as relative quantities normalized to the power of antenna 1, independent of the absolute field amplitude:

$$\bar{P}_{a,i}^{C\to A} = \frac{P_{a,i}}{P_{a,1}} = \left(\frac{\left|S_{21}^{C\to Ai}\right|}{\left|S_{21}^{C\to A1}\right|}\right)^2 \tag{4.44}$$

These values can be used to estimate a possible field tilt in the RFQ: For instance, if the field amplitude at the location of an antenna decreased to 90 % of the nominal level, the antenna power would decrease by the square law to 81 %.

Table 4.4: Calibration data of the diagnostic RF pickup antennas, i.e. antenna powers corresponding to a flat field distribution in the RFQ, obtained by means of the measured transmission coefficient $S_{21}^{C\to Ai}$ between coupler and antenna.

	coupler-antenna $\lvert S_{21}^{C\to Ai}\rvert$	abs. power $P_{a,i}$	rel. power $\bar{P}_{a,i}^{C\to A}$
Antenna 1	−46.55 dB	1.438 W	1.000
Antenna 2	−45.82 dB	1.702 W	1.184
Antenna 3	−44.71 dB	2.200 W	1.530
Antenna 4	−46.89 dB	1.331 W	0.925
Design values	−48.16 dB	1.00 W	—

In some situations it may be desirable to diagnose a possible field tilt with a deactivated, but still connected RF power source. The only measurement access would then be provided by the four pickup antennas, but not by the power coupler. Therefore, also the transmission between each pair of antennas—six pairs emerge from four antennas—was measured while the coupler was terminated with a 50 Ω load.[40] The measured coefficients are reported in Table 4.5. Because the very weak coupling of the antennas now affects each measurement twice, the signal is considerably weaker compared to the coupler-to-antenna measurement. The transmission from the antenna-to-antenna measurement amounts to roughly −90 dB over a noise level of ≈ −100 dB (Fig. 4.27). From the six transmission coefficients, the four relative powers (of which in fact only three are unknown because the powers are normalized to antenna 1) can be calculated as follows: Assume that each antenna-to-antenna measurement $S_{21}^{Aj\to Ai}$ is affected by two contributions that decrease the transmission: the coupling from the ith antenna to the cavity (s_i) and the coupling from the cavity to the jth antenna (s_j):

$$\left|S_{21}^{Aj\to Ai}\right| = s_j \cdot s_i \tag{4.45}$$

[40] The transmission coefficients would increase by roughly $Q_0/Q_\ell \approx 3.3\,\mathrm{dB}$ if the 50 Ω termination was removed from the coupler. In that case, active power would only be lost on the cavity walls (Q_0), whereas the contribution by the coupler terminated by an open circuit would be purely reactive. Since all transmission coefficients would change by the same amount, the relative antenna powers remain unaffected.

Expressed in units of dB, multiplication turns into summation. Thus, the six Eqs. (4.45) may be condensed in the linear system

$$\underbrace{\begin{bmatrix} 1 & 1 & & \\ 1 & & 1 & \\ 1 & & & 1 \\ & 1 & 1 & \\ & 1 & & 1 \\ & & 1 & 1 \end{bmatrix}}_{\mathbf{K}} \underbrace{\begin{bmatrix} s_1 \\ s_2 \\ s_3 \\ s_4 \end{bmatrix}}_{\mathbf{s}} = \underbrace{\begin{bmatrix} \left|S_{21}^{A1\to A2}\right| \\ \left|S_{21}^{A1\to A3}\right| \\ \left|S_{21}^{A1\to A4}\right| \\ \left|S_{21}^{A2\to A3}\right| \\ \left|S_{21}^{A2\to A4}\right| \\ \left|S_{21}^{A3\to A4}\right| \end{bmatrix}}_{\mathbf{b}}, \tag{4.46}$$

which is solved by means of the least-squares method as $\mathbf{s} = \mathbf{K}^{\dagger}\mathbf{b}$. From $\mathbf{s}$, the relative antenna powers arise as

$$\bar{P}_{a,i}^{A\to A} = (s_i/s_1)^2 . \tag{4.47}$$

They are listed in Table 4.6 in comparison to the relative powers $\bar{P}_{a,i}^{C\to A}$ that were obtained from the coupler-to-antenna measurement (Table 4.4). An agreement up to a error of 1 % is observed, which can be attributed to the high noise level and very weak coupling in the antenna-to-antenna measurement. The small error indicates that the field flatness in the RFQ can be determined with sufficient accuracy from the antenna-to-antenna measurements alone, while leaving the switched-off RF generator connected.

Table 4.5: Measured transmission coefficients $S_{21}^{Aj\to Ai}$ between each pair of antennas with the coupler terminated by a 50 Ω load.

$\lvert S_{21}^{Aj\to Ai}\rvert$ (dB)	Ant. 1	Ant. 2	Ant. 3	Ant. 4
Antenna 1	—			
Antenna 2	-89.75	—		
Antenna 3	-88.68	-87.91	—	
Antenna 4	-90.78	-90.17	-88.89	—

Table 4.6: Calibration data of the diagnostic RF pickup antennas, i.e. relative antenna powers corresponding to a flat field distribution in the RFQ, obtained by means of the measured transmission coefficients $S_{21}^{Aj\to Ai}$ between ith and jth antenna.

	coupler-antenna rel. power $\bar{P}_{a,i}^{C\to A}$	antenna-antenna rel. power $\bar{P}_{a,i}^{A\to A}$
Antenna 1	1.000	1.000
Antenna 2	1.184	1.172
Antenna 3	1.530	1.536
Antenna 4	0.925	0.931

4.6 Conclusion

In Chapter 4, a set of low-power RF measurements and the tuning procedure of the PIXE-RFQ are reported. The first section reviews the frequency correction for measurements carried out under air and with varying temperature, and discusses the influences of air humidity. The principle of field amplitude measurement with the help of a perturbing object, the so-called bead-pull measurement, is also presented. The processing steps necessary to obtain the field components from the data recorded by the vector network analyzer are detailed.

During the construction of the PIXE-RFQ, validating RF measurements on the RFQ components were carried out. The two manufactured couplers—of which only one is mounted to the RFQ and the other is kept as a spare—were measured facing each other in a so-called head-on measurement. The transmission coefficient was recorded for different rotation angles and showed very small deviation from the simulation results, validating the quality of both constructed couplers.

The PIXE-RFQ consists of two mechanical modules. For both modules, bead-pull measurements were performed to confirm that no severe errors occured during machining and brazing. The field showed a near-perfect agreement with the simulation, whereas the frequency error was equal or smaller than 600 kHz in both cases. As only small deviations were observed, well within the capabilities of the tuning system, it was decided not to use the vacuum pumping ports as additional tuning features.

The main part of this chapter is dedicated to the RFQ tuning procedure. Longitudinal and transverse variations of the inter-vane capacitance and inductance, originating in both design as well as machining and alignment errors, perturb the electric field of the TE_{210} operating mode. This was compensated for by means of sixteen movable piston tuners. The goal of the tuning was an as flat as possible quadrupole field component and vanishing dipole components. Furthermore, the operating mode frequency had to be tuned to the design frequency of 749.480 MHz under vacuum at 22 °C.

Reliability measurements were carried out before the actual tuning procedure in order to assess the accuracy limit given by bead-pull measurement and tuner tooling. The bead-pull measurement error could be improved to 0.5 % by performing each measurement thrice. No significant mechanical hysteresis effect was observed.

To compute the tuner adjustment, the algorithm used to tune the medical proton HF-RFQ [42] was augmented such that frequency and field could be tuned at the same time. The results suggest that the inclusion of the frequency and corresponding weights also leads to a more stable convergence of the tuning iterations. After measuring the response matrix, recording the sensitivity of field and frequency with respect to individual tuner movement, the RFQ was tuned in only two tuning steps. The response matrix was inverted using the singular value decomposition. With the tuners initially in nominal position, quadrupole

and dipole field errors of 2.5 %, 7.9 %, and 8.4 % (two polarizations), respectively, were measured, while the frequency error amounted to 623 kHz. After the tuning, the field errors in all three components amounted to $\approx$ 1 % or better with respect the mean quadrupole component and a frequency error of 1.5 kHz was measured.

Subsequently, the tuners were recut to their final lengths and the PIXE-RFQ was evacuated. The measurement under vacuum revealed a remaining frequency error of approximately 23.5 kHz, which can be explained with the measurement uncertainty with respect to air humidity: The RFQ frequency was tuned under air instead of e.g. dry nitrogen and no humidity data were recorded, which could have been used to correct the measurement. The error of 23.5 kHz lies well within the $\pm$60 kHz tuning range given by a water temperature range of $\pm$5 K, and is in any case acceptable since no RF accelerating structures are located downstream of the RFQ.

With the RFQ under vacuum, the three quality factors (unloaded, external, and loaded) as well as the coupling coefficient β_c were measured. Two techniques for extracting the values from the circle described by the reflection coefficient were compared: the three-point method and the circle-fitting method. A correction was implemented into the former, which significantly improved the results in the presence of a small reflection in the waveguide adapter. Excellent agreement with an error smaller than 0.4 % was observed for the unloaded quality factor Q_0. The external quality factor Q_{ex} was measured to be 6 % higher than the design value. The discrepancy could be attributed to a coupler mechanical manufacturing error of roughly 300 µm. The larger Q_{ex} corresponds to a measured coupling coefficient of 1.18 compared to a design value of 1.25. The measured over-coupling of 18 % requires an extra 0.5 kW (0.7 %) of RF peak input power that is reflected by the RFQ. Thus, it was decided to not make use of the possibility of rotating the coupler to closer approach critical coupling.

Lastly, the four diagnostic RF pickup antennas were calibrated with the now tuned field distribution. They allow for assessing field level and potential field tilts without bead-pull measurements, such that the RFQ can remain closed and evacuated. The transmission between input coupler and antenna, as well as between all combinations of antennas was measured. At nominal field amplitude (peak RF power loss $P_0 = 65$ kW), each antenna extracts a peak power between 1.3 and 2.2 W, which shows close agreement with the design value of 1 W.

With the low-power RF measurements completed in July 2020, the PIXE-RFQ is now scheduled for high-power RF measurements, conditioning, as well as beam commissioning. The RFQ is expected to commence operation towards the end of the year 2020.

5 Development of the Carbon-RFQ for Hadron Therapy

One of the most recent proposals for a particle cancer therapy accelerator is the "bent linac" for carbon ions conceived in Ref. [52]. A key goal of the study was to improve the linac footprint such that it would better fit into a hospital facility without affecting the treatment beam properties. In the low energy section of the machine, the Carbon-RFQ represents the first RF accelerating structure. The RFQ has the critical role of shaping the carbon ion beam and prepare it for injection into the following accelerating structures.

The Carbon-RFQ in its entirety was developed in a joint effort between V. Bencini and the author of the present thesis. Bencini conceived general design parameters and the beam dynamics design of the initial standard-vane RFQ. This design was modified to feature trapezoidal vanes to increase acceleration efficiency. The author of the thesis proposed the sixteen-term potential function as a mean of semi-analytically describing the field of the trapezoidal vanes, allowing for rapid channel design. The Carbon-RFQ had to be split into two separate RF cavities to ensure a stable field distribution. The length of each of the two fully decoupled cavities was used as a free parameter for dipole-mode detuning, such that other dedicated detuning techniques were not necessary. This novel technique was conceptually proposed in Ref. [30] by the author and has now been implemented for the first time. Two quadrupole vane extensions were used to rematch the beam across the inter-cavity drift. Beam dynamics design, sixteen-term potential function, and beam rematching over the cavity drift were validated by means of particle tracking simulations that were carried out jointly between Bencini and the author.

The Chapter is structured as follows: Section 5.1 summarizes the general RFQ parameters and the initial design. In Section 5.2, the modified design with trapezoidal vanes is described, and the sixteen-term potential function is introduced. Particle tracking simulation results are reported in Section 5.3. The RF design is discussed in Sections 5.4 and 5.5, were the former details the splitting into two cavities and the latter covers the remaining aspects.

Large parts of this chapter have been previously published in Ref. [62]. Most of the figures shown here were taken and adapted from this paper.

5.1 General Design Choices

The characteristic parameters of the Carbon-RFQ design were determined subject to a variety of constraints. The key choices made by Bencini [52, 62] for the initial iteration of the RFQ are presented in the following.

First, the $^{12}C^{6+}$-ion beam energy at the entrance of the RFQ was defined by the maximum accelerating voltage of 30 kV that the LEBT can sustain [61]. Since the charge-to-mass ratio of the fully stripped carbon ion amounts to 1/2, this results in an input beam energy of 15 keV/u.

The frequency of 750 MHz of the Carbon-RFQ was chosen to be a subharmonic of the bent linac frequency (3 GHz) in order to allow for longitudinal beam injection. This frequency was also selected for the HF-RFQ for proton therapy and the PIXE-RFQ.[41] It represents a compromise between structure length, power consumption, beam acceptance, and machinability [28, 40].

The minimum vane aperture a and the inter-vane voltage V_0 are restricted by the maximum surface electric field $E_{s,max}$ that can be sustained by the vanes without RF breakdown. The Carbon-RFQ was designed aiming at maximum surface field of 50.6 MV/m, corresponding to 2.0 Kilpatrick [158]. Recently, the proton HF-RFQ was successfully commissioned [43], which features the same frequency and maximum surface electric field as well as a similar pulse length. Furthermore, the review of experimental data carried out in Section 2.4.2 suggests that 2.0 Kilpatrick [158] is a safe choice for these parameters. Generally, reducing the aperture results in an increased maximum surface field $E_{s,max}$. At the same time, $E_{s,max}$ can be reduced by decreasing the inter-vane voltage. Aperture and vane voltage were chosen as a best compromise between power consumption ($P_0 \propto V_0^2$) and acceptance, which decreases with a, keeping the maximum surface field below the threshold [52, 62].

The choice of a particular vane shape depends on a wide range of parameters that determine the beam dynamics in the RFQ. The main driver in the definition of modulation m, minimum aperture a, and synchronous phase ϕ_s along the structure is the kind of application the RFQ is tailored to. In Refs. [52, 62], Bencini considered both a high-transmission RFQ and a compact variant, both of which were designed using the PARMTEQ codes [102]. The high-transmission version would feature the conventional scheme proposed by Los Alamos National Laboratory [120], including long shaper and gentle buncher sections. The slow variation of the RFQ parameters necessary for adiabatic bunching results in a very high transmission ($\mathcal{T} \approx 99\,\%$) at the expense of increased structure length and power consumption. Bencini pointed out that such a high transmission is not necessary to meet the requirements of carbon ion therapy: The usual treatment dose per

[41] In fact, the frequency of the HF-RFQ (and also the PIXE-RFQ) amounts to 749.48 MHz, a subharmonic of the LIGHT S-band cavities operating at 2997.92 MHz [27, 57].

Table 5.1: General design parameters of the Carbon-RFQ.

Species	$^{12}C^{6+}$	carbon ion	
Input energy	$\mathcal{W}_{in}$	15	keV/u
Output energy	$\mathcal{W}_{out}$	5	MeV/u
Transmission	$\mathcal{T}$	50	%
RF frequency	f_0	750.00	MHz
Inter-vane voltage	V_0	50	kV
Input beam current	I_b	0.19	mA
Input trn. emit. (90 % norm.)	$\varepsilon_{xx'}$	0.02	π mm mrad
Mid-cell aperture	r_0	1.411	mm
Minimum aperture	a	0.67	mm
Final synchronous phase	ϕ_s	-20	deg
Transverse curvature radius	ρ_t	1.27	mm
Repetition rate	f_{rep}	200	Hz
RF pulse length	t_{pls}	5	µs
Duty cycle	d	0.1	%

unit mass and time amounts to 2 Gy/min,[42] which corresponds to 4×10^5 carbon ions per pulse at a repetition rate of $f_{rep} = 200$ Hz. Contrarily, it is anticipated to extract 10^9 ions per pulse from the TwinEBIS source [60], much higher than common treatment requirements. If an RFQ transmission of only 50 % is considered, the ion rate at the end of the RFQ would be 5×10^8 ions/pulse, still three orders of magnitude higher than required. As a consequence, Bencini proposed a compact RFQ with greatly shortened shaper and gentle buncher, reducing overall structure length and power consumption. Comparable to the HF-RFQ and PIXE-RFQ [28], the particle beam enters the RFQ with a larger synchronous phase ($-50°$), resulting in a smaller initial RF bucket, such that half of the injected particles are lost at injection energy. This bears the additional advantage of a smaller phase-energy emittance at the end of the RFQ, allowing for lossless bunch-to-bucket injection into the 3 GHz structure downstream of the RFQ.

The output energy was selected as 5 MeV/u [52] with respect to the accelerating structure to come downstream of the RFQ: a 3 GHz SCDTL (Side-Coupled Drift-Tube Linac). An SCDTL operating at this frequency and accepting 5 MeV protons [213] has already been machined and demonstrated to work for the LIGHT prototype linac for proton therapy [58]. Thus, it was decided that the RFQ performs the acceleration up to 5 MeV/u. The general design parameters of the Carbon-RFQ are summarized in Table 5.1.

[42] The energy deposited per unit mass of matter by ionizing radiation is commonly measured in gray (Gy). One gray corresponds to one joule of energy absorbed by one kilogram of irradiated matter, i.e. 1 Gy = 1 J/kg.

5.2 Design with Trapezoidal Vanes

The initial Carbon-RFQ iteration was designed by Bencini (Section 5.1, Refs. [52, 62]) using the PARMTEQ codes. It features vanes whose longitudinal profile is directly derived from the two-term potential function [Eq. (2.43), Fig. 2.5(a)], which are denoted as standard vanes in the following. It was then decided to modify the standard-vane design by introducing trapezoidal vanes [Fig. 2.5(b)].

RFQs with electrodes following a trapezoidal profile have been constructed from the very beginning: In fact, the first RFQ built at the Institute for High Energy Physics in Protvino, USSR in 1971 temporarily featured rods with a piecewise linear profile [112]. Some modern designs can be found in Refs. [110, 112–117], to name a few. Trapezoidal electrodes provide increased acceleration efficiency allowing for shorter—and thus less power-consuming—RFQ designs. Contrarily to RFQs with standard and sinusoidal electrodes, the electric fields of trapezoidal-electrode RFQs cannot be described by the well-known eight-term potential function [Eq. (2.46)] to suffiient accuracy. Thus, a novel method was developed, extending said function up to sixteen higher-order multipole terms.

In the following, the specific geometry of the Carbon-RFQ trapezoidal electrode, its acceleration efficiency, and surface electric field are reviewed (Section 5.2.1). Section 5.2.2 introduces the sixteen-term potential function, and the design algorithm is reported in Section 5.2.3. Finally, Section 5.2.4 compares standard-vane and trapezoidal-vane RFQ, and estimates gains in terms of length and power consumption.

5.2.1 Geometry of the Trapezoidal Vane

The tip of a trapezoidal electrode (vane or rod) consists of two straight parts that are connected by an—ideally smooth—curve. For the Carbon-RFQ trapezoidal vanes, the connecting curve is given by a sinusoidal function, providing a smooth longitudinal cell profile with a continuous first-order derivative. While other transitions may be used,[43] the trapezoidal cell geometry proposed in Ref. [112] was adopted. From here on, the sinusoidal junction is denoted as the accelerating gap with length g. Furthermore, let r_0 identify the mid-cell aperture, a the minimum aperture, m the modulation factor, and L the cell length (Fig. 5.1). In the coordinate system whose origin is located on the beam axis at the cell en-

[43] Different curves may be chosen to connect the two straight parts of the trapezoidal cell profile. In fact, the very first RFQ featured rods with step-like and piecewise linear profile [112]. However, in the sense of controlling the maximum surface electric field, a smooth surface is desirable, and the piecewise defined profile should be continuous in the first-order derivative at least. The authors of Ref. [64] proposed the use of a curve derived from the two-term potential function [Eq. (2.43)], implying a relation between mid-cell aperture r_0, minimum aperture a, and modulation factor m given as $r_0 = a\mathcal{X}^{-1/2}$ [1], with $\mathcal{X}$ from Eq. (2.44). This trapezoidal cell type is less efficient in acceleration, but provides a more homogeneous capacitance profile along the RFQ.

trance, the longitudinal profile of the x-electrode follows the piecewise defined curve

$$x(z) = \begin{cases} a & \text{for } 0 \leqslant z \leqslant \frac{L-g}{2} \\ r_0 \left(1 + \frac{m-1}{m+1} \sin\left[\frac{\pi}{g}\left(z - \frac{L}{2}\right)\right]\right) & \text{for } \frac{L-g}{2} \leqslant z \leqslant \frac{L+g}{2}\,, \\ ma & \text{for } \frac{L+g}{2} \leqslant z \leqslant L \end{cases} \tag{5.1}$$

where $a = 2r_0/(m+1)$. The profile of the y-electrode is mirrored with respect to the cell center. Note that for $g = L$, Eq. (5.1) just delivers the profile of a sinusoidal cell. The 3D geometry of the four-vane Carbon-RFQ trapezoidal cell with flat semicircular vanes is shown in Fig. 5.1. It is obtained by sweeping the transverse electrode profile, a semi-circle with constant radius $\rho_t = 0.9r_0$, along the longitudinal trajectory.

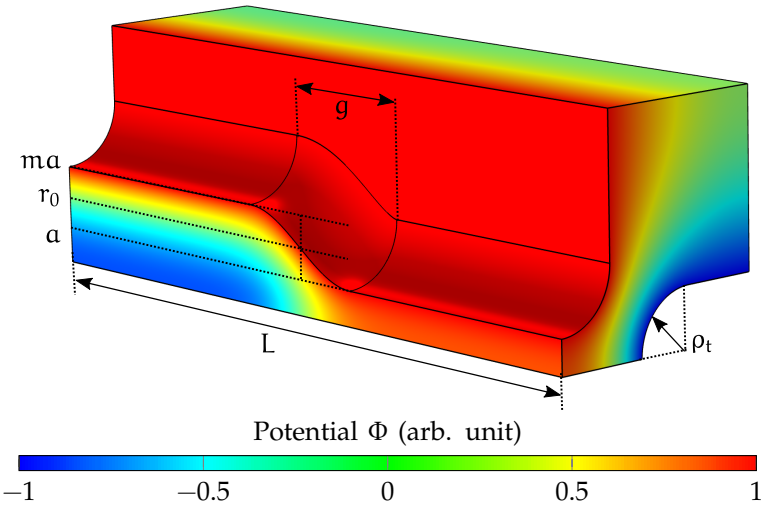

Figure 5.1: Exemplary trapezoidal cell of the Carbon-RFQ and simulated electric potential shown for the vacuum domain in quarter-symmetry. In terms of the potential function, four of the shown parameters form the degrees of freedom of the cell: length L/r_0, modulation m, accelerating gap length g/L, and transverse radius of curvature ρ_t/r_0 (constant in the Carbon-RFQ).

To gain an initial understanding of the potential improvement in acceleration efficiency, the dependence of relevant quantities on the accelerating gap length g was studied: Figure 5.2(a) shows the longitudinal electric field E_z along the beam axis of a trapezoidal cell for varying ratios g/L between accelerating gap length and cell length. While the spatial average of the longitudinal electric field E_0 [Eq. (2.51)] stays virtually constant, the transit-time factor T_{tr} of the synchronous particle [Eq. (2.52)] is significantly higher. For an ideal two-term potential cell, $T_{tr} = \pi/4 \approx 0.786$ [1]. While for purely sinusoidal cells ($g/L = 1$) the transit-time factor is already increased, it can be raised to $T_{tr} = 0.988$ by decreasing the gap length within the cell parameter space of the Carbon-RFQ. This value is only 1.2 % below the theoretical limit of $T_{tr} = 1$. With Eq. (2.50), the increase in the quantity T_{tr} is equivalent to an increase in acceleration efficiency $A_{1,0}$. Generally, the increased acceleration comes at the expense of a

reduced quadrupole term $A_{0,1}$ [or with Eq. (2.55) in effective focusing force $\mathcal{B}$]. This is also the case for sinusoidal cells when increasing the modulation m, but not for two-term potential cells, which—by definition—provide a near-constant quadrupole term $A_{0,1} \approx 1$. Figure 5.2(a) visualizes the above-mentioned quantities as functions of g/L, computed for a cell with $m = 2.7$, $L = 10.5r_0$, and $\rho_t = 0.9r_0$.

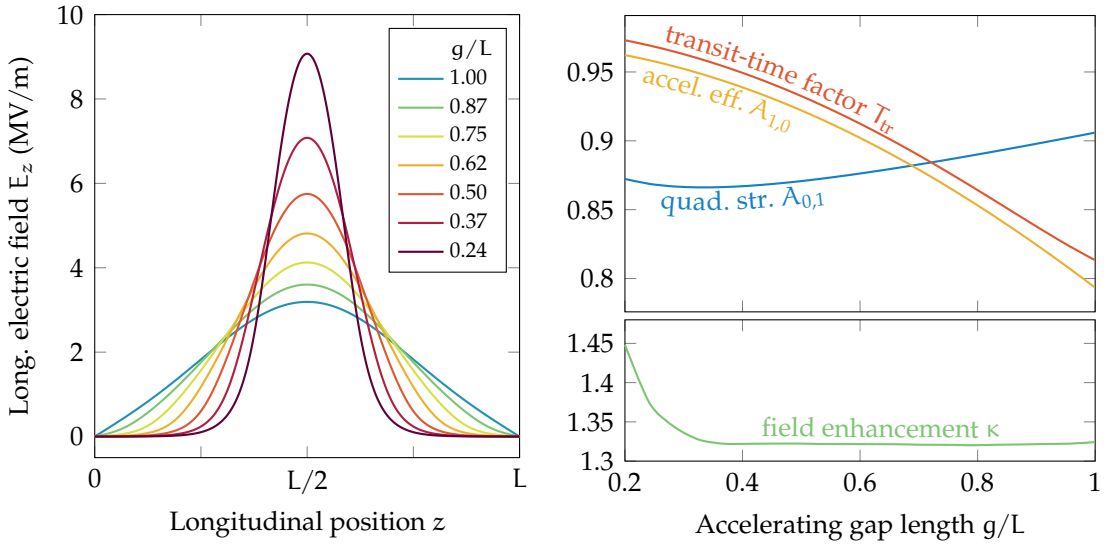

Figure 5.2: Longitudinal electric field E_z along the beam axis ($r = 0$) of a trapezoidal cell as a function of z for different gap to cell length ratios g/L (a). Reducing the gap length g concentrates the longitudinal field component in the center of the cell while increasing its peak value, resulting in a higher acceleration efficiency at the expense of focusing strength. Fig. (b) shows the quadrupole focusing term $A_{0,1}$, acceleration efficiency $A_{1,0}$, transit-time factor T_{tr}, and field enhancement $\kappa = E_{s,max}/(V_0/r_0)$ as functions of g/L. The values were computed for a trapezoidal cell with $m = 2.7$, $L = 10.5r_0$, and $\rho_t = 0.9r_0$.

Another important figure of merit is the maximum surface electric field $E_{s,max}$, posing one of the major performance limits for any linear accelerator [1]. The lower plot of Fig. 5.2(b) depicts $E_{s,max}$ as a function of g/L. As is common in RFQ nomenclature [100], the maximum field is normalized to inter-vane voltage V_0 and mid-cell aperture r_0, expressed as the field enhancement [1]

$$\kappa = \frac{E_s}{V_0/r_0}. \tag{5.2}$$

Figure 5.3 visualizes the surface electric field as the accelerating gap is decreased: the maximum value increases, and its location changes from a wide-spread area in concave region of the electrode surface (a) to a more concentrated hot spot in the convex region (d). Although the increased field enhancement poses a performance limit to accelerating cells located towards the end of an RFQ—such as the one studied here—the value is surpassed by the short cells found in the gentle

buncher during the modulation ramp-up. In terms of maximum surface field, the bottleneck thus remains in the upstream stages of the RFQ. More detail on this observation is given in Sections 5.2.2 and 5.2.3.

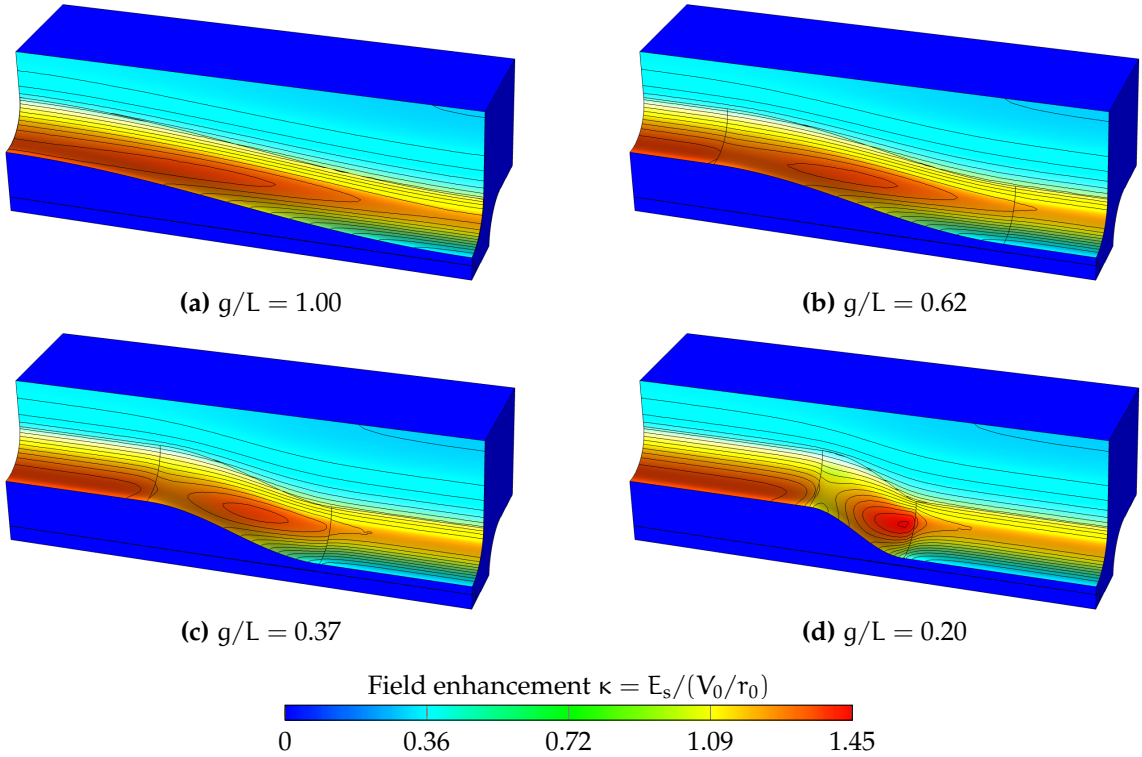

Figure 5.3: Distribution of the surface electric field E_s in a trapezoidal RFQ cell, shown for four different ratios between accelerating gap length g and cell length L. With decreasing gap length, the maximum field increases (b), and its location changes from a wide-spread area in concave region of the electrode surface (a) to a more localized hot spot in the convex region (d). The surface field is expressed as the field enhancement κ in units of V_0/r_0.

5.2.2 The Sixteen-term Potential Function

The fields of trapezoidal electrodes (be it vanes or rods) cannot be sufficiently described by the two-term potential function [Eq. (2.43)] or eight-term potential function [Eq. (2.46)] used by the majority of the available RFQ design tools [1, 100–104], PARMTEQ [102] being the most commonly used code. Previously, trapezoidal-vane RFQs were designed by employing 3D simulation code to solve the Laplace equation (usually FEM or finite differences), taking the electrode geometry directly into account [110, 112–117]. While this procedure delivers highly accurate results, it is also time-consuming, as for each parameter change new simulations have to be performed. To design the Carbon-RFQ channel, a novel technique was devised: the well-known eight-term potential function was augmented by both longitudinal and 3D higher-order terms, accounting for the particular field pattern of the trapezoidal electrode. A comparable approach has

recently been published in Ref. [64], however, no off-axis fields were considered there.

Figure 5.4 shows the approximation of the simulated on-axis electric field E_z by the multipole potential function. Here, the limitations of the eight-term potential function become clear.[44] By adding the longitudinal coefficients $A_{5,0}$, $A_{7,0}$, $A_{9,0}$, and $A_{11,0}$, the on-axis approximation error falls below 1 % of the peak field. Additionally, the four coefficients $A_{4,1}$, $A_{6,1}$, $A_{4,3}$, and $A_{6,3}$ are included in order to describe possible distortions of the transverse quadrupole field. Figure 5.5 shows the field approximation error between the sixteen-term potential function Φ_{16} and the potential Φ_{FEM} obtained from FEM simulation for a long cell with short accelerating gap ($g/L = 0.2$). This geometry is particularly difficult to approximate with the multipole expansion. Within the minimum aperture, the field approximation error does not exceed 4 %, while in the domain that is seen by the largest portion of the beam it is smaller than 2 %. The approximation was validated by means of particle tracking simulations, which are presented in Section 5.3.

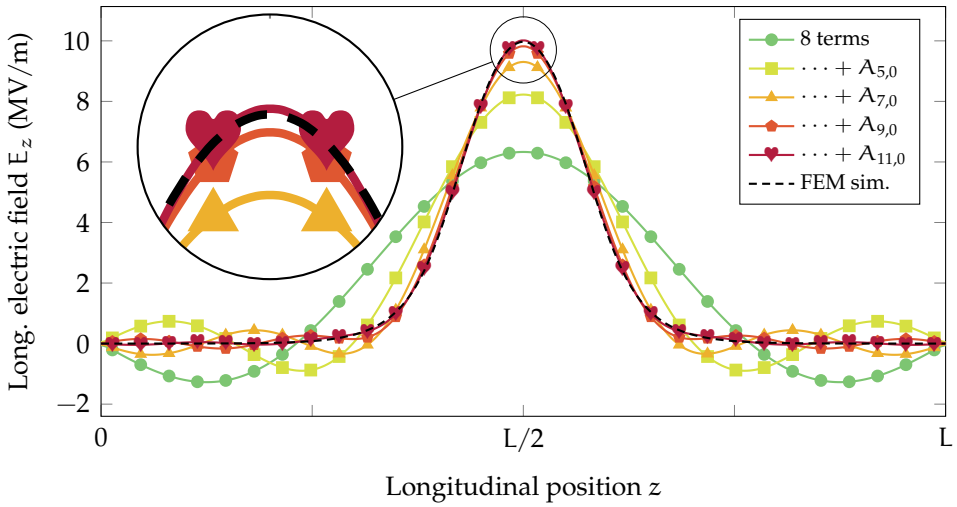

Figure 5.4: Approximation of the simulated electric field (black dashed line) on the beam axis of a trapezoidal cell by the multipole potential function. The conventional eight-term potential gives only a poor approximation. By consecutively adding four longitudinal terms up to $A_{11,0}$, the approximation is improved to an error below 1 % of the peak field. The full sixteen-term potential features an additional four terms $A_{\mu,\nu}$ with $\nu > 0$, which do not contribute to the on-axis field, but are important to simulate transverse beam dynamics.

[44] In fact, the only contributing coefficients of the eight-term potential [Eq. (2.46)] to the on-axis field are $A_{1,0}$ and $A_{3,0}$. The remaining coefficients multiply basis functions proportional to the terms $r^{2\nu}$ or $\mathcal{I}_{2\nu}(\mu k r)$ with $\nu > 0$, that vanish for $r = 0$.

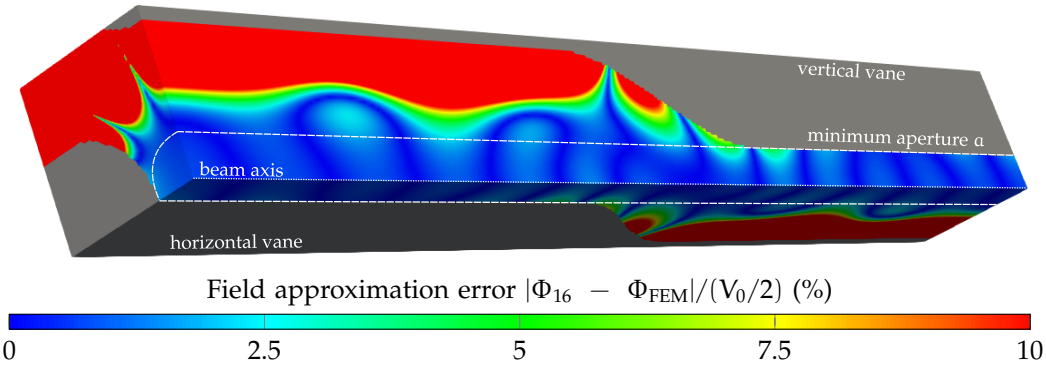

Figure 5.5: Field approximation error between the sixteen-term potential function Φ_{16} and the simulated potential Φ_{FEM} normalized to $V_0/2$. The error is shown for a long cell with very short accelerating gap length $g/L = 0.2$. Within the minimum aperture, the error stays below 4 %.

The full sixteen-term potential function reads

$$\begin{aligned}\frac{\Phi_{16}(r,\vartheta,z)}{V_0/2} = {} & A_{0,1}\left(\frac{r}{r_0}\right)^2\cos(2\vartheta) && + A_{0,3}\left(\frac{r}{r_0}\right)^6\cos(6\vartheta)\\ & + A_{1,0}I_0(kr)\cos(kz) && + A_{3,0}I_0(3kr)\cos(3kz)\\ & + A_{5,0}I_0(5kr)\cos(5kz) && + A_{7,0}I_0(7kr)\cos(7kz)\\ & + A_{9,0}I_0(9kr)\cos(9kz) && + A_{11,0}I_0(11kr)\cos(11kz)\\ & + A_{1,2}I_4(kr)\cos(4\vartheta)\cos(kz) && + A_{3,2}I_4(3kr)\cos(4\vartheta)\cos(3kz)\\ & + A_{2,1}I_2(2kr)\cos(2\vartheta)\cos(2kz) && + A_{2,3}I_6(2kr)\cos(6\vartheta)\cos(2kz)\\ & + A_{4,1}I_2(4kr)\cos(2\vartheta)\cos(4kz) && + A_{4,3}I_6(4kr)\cos(6\vartheta)\cos(4kz)\\ & + A_{6,1}I_2(6kr)\cos(2\vartheta)\cos(6kz) && + A_{6,3}I_6(6kr)\cos(6\vartheta)\cos(6kz).\end{aligned} \tag{5.3}$$

In Fig. 5.6, the sixteen coefficients are shown for the trapezoidal cell from Fig. 5.2 as functions of the normalized accelerating gap length g/L. The values are multiplied by their accompanying modified Bessel function, such that the contributions of individual terms to the total field may be estimated. The plot highlights the significance of the newly introduced terms for cells where g/L is small, in particular the longitudinal terms $A_{5,0}$, $A_{7,0}$, and the mixed term $A_{4,1}$, whose contributions read 10 % to 20 % of that of the basic components $A_{0,1}$ and $A_{1,0}$.

The multipole coefficients $A_{\mu,\nu}$, together with the maximum surface electric field (or field enhancement), were precomputed[45] and stored in a lookup table for a discrete number of cells in the parameter space of interest. This approach was adopted from the PARMTEQ RFQ codes from Los Alamos National Laboratory [100, 102], which also use lookup tables. The coefficients for a specific cell geometry can then be obtained by multidimensional linear interpolation. The trape-

[45]The coefficients were computed from single-cell models using the electrostatic solver in COMSOL Multiphysics® [93]. Information on the accuracy of this computation can be found in Appendix C.2.

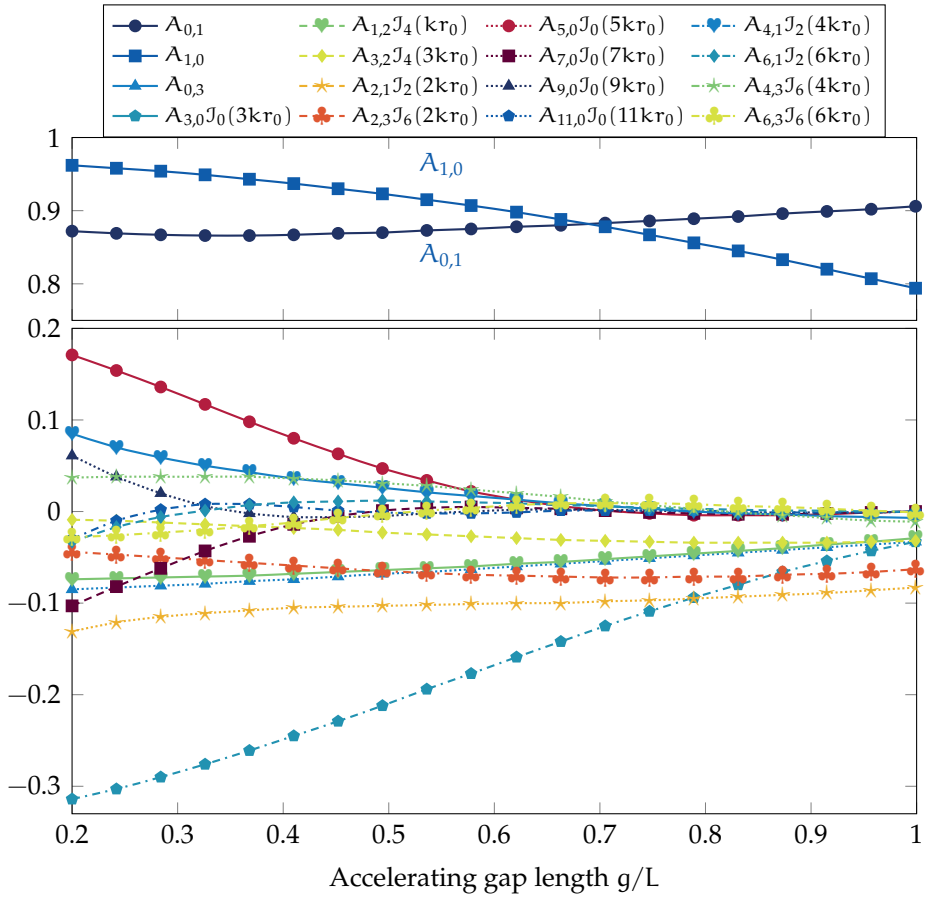

Figure 5.6: Multipole coefficients of the sixteen-term potential function multiplied by their accompanying modified Bessel function, shown as functions of the normalized accelerating gap length g/L. The plot highlights the increasing significance of both newly introduced longitudinal and mixed terms, in particular $A_{5,0}$, $A_{7,0}$, and $A_{4,1}$, whose contributions amount to 10 % to 20 % of that of the basic components $A_{0,1}$ and $A_{1,0}$ for small g/L.

zoidal cell of a four-vane RFQ with transverse semi-circular vane tips (Fig. 5.1) is described by six independent parameters: cell length L, modulation m, accelerating gap length g, transverse radius of curvature ρ_t, mid-cell aperture r_0, and inter-vane voltage V_0, all of which may vary along the RFQ. For the computation of the potential field and its coefficients, however, V_0 merely appears as a scalar factor.[46] Furthermore, the mid-cell aperture r_0 can be eliminated by replacing the length quantities by their dimensionless counterparts L/r_0, g/L, and ρ_t/r_0. This way, counting m, only four geometric parameters need to be swept to generate the lookup table.

In the particular case of the Carbon-RFQ, the transverse curvature radius $\rho_t/r_0 = 0.9$ is held constant along the channel (as are mid-cell aperture

[46]For the computation of the lookup table, V_0 can be considered as constant over one cell. When a 3D field map is generated, it is interpolated linearly from one cell to the next, where the interpolation support points are located at the end of the cells. The same holds for the multipole coefficients $A_{\mu,\nu}$.

$r_0 = 1.411\,\mathrm{mm}$ and inter-vane voltage $V_0 = 50\,\mathrm{kV}$). To create the lookup table, the remaining three free parameters are swept over the ranges $0.75 \leqslant L/r_0 \leqslant 20$, $0.15 \leqslant g/L \leqslant 1$, and $1 \leqslant m \leqslant 3.2$. A limit to the parameter space is given by the longitudinal radius of curvature ρ_ℓ:

$$\rho_{\ell,\min} \leqslant \rho_\ell = \frac{g^2}{\pi^2 r_0}\left(\frac{m+1}{m-1}\right) \tag{5.4}$$

The theoretical lower limit is given by the transverse radius of curvature, $\rho_{\ell,\min} = \rho_t = 0.9 r_0$, which must be smaller than the longitudinal radius of curvature in order to construct a physically possible geometry. In practice however, $\rho_{\ell,\min}$ is limited by the radius of the cutter tool used to machine the RFQ vanes. As a result, the cuboid spanned by the parameter ranges is incomplete starting from the corner corresponding to short cells with short accelerating gaps and large modulations, violating Eq. (5.4). In total, 2280 different cell geometries were precomputed using the FEM Laplace equation solver[47] of COMSOL Multiphysics® [93].

Figure 5.7 shows a selection of the multipoles over the parameter space. Most important for the design of the channel are the quadrupole strength (a) and the acceleration efficiency (b). The plots highlight that decreasing g/L has in first approximation the same effect as increasing m—enhanced acceleration at the expense of focusing strength. This equivalence can also be seen from the plots (c) and (d), showing high-order longitudinal components. Furthermore, by the example of $A_{5,0}$ (d), the importance of the newly introduced higher-order terms for cells with $g/L \ll 1$ is highlighted. The coefficient $A_{2,1}$ (e), which acts as a quadrupole-like force on the beam and thus is sometimes considered significant [100], is affected by the gap length g/L only marginally.

Finally, Fig. 5.7(f) shows the field enhancement [Eq. (5.2)] as a function of the free parameters. Here it becomes clear that—for a constant voltage V_0 and mid-cell aperture r_0—one should expect the maximum surface field in the short cells in the bunching section at the beginning of the RFQ. A decrease in g/L raises the field only slightly. This was confirmed during the RF design (Section 5.5.2, Fig. 5.26). One can take advantage of this fact by designing an RFQ with nonuniform V_0 and r_0, for example by increasing the field amplitude and thus efficiency in the higher-energy regions of the RFQ, evenly distributing the maximum surface field strength. While this technique is occasionally used in RFQs featuring standard or sinusoidal electrodes [72, 106, 111, 143, 168], it seems particularly useful for trapezoidal-electrode RFQs with their highly efficient accelerator sections. However, the Carbon-RFQ is implemented with constant voltage, mid-cell aperture, and transverse radius for simplified RF design and construction.

[47] To obtain accurate results in particular for the maximum surface field, FEM with a very fine mesh and continuous third-order Lagrange ansatz functions is used. Details on the numerical convergence of this simulation are given in Appendix C.2.

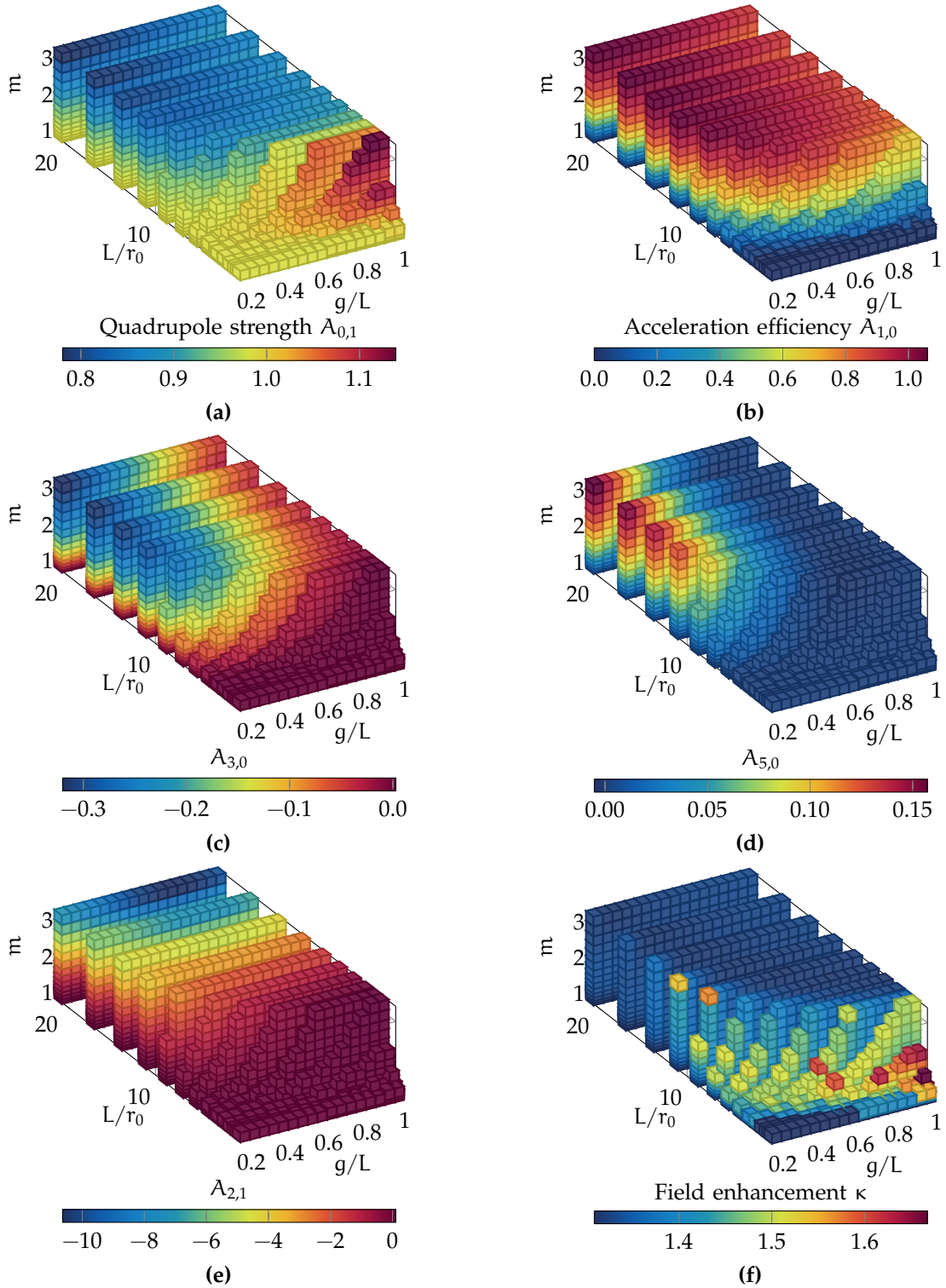

Figure 5.7: Computed multipole coefficients and field enhancement as functions of cell length L/r_0, modulation m, and gap length g/L over the parameter space available to the Carbon-RFQ cells, where $\rho_t/r_0 = 0.9$. Six exemplary entries of the lookup table are shown. Note that the multipoles $A_{\mu,\nu}$ are depicted without normalization and should thus not be compared to each other in terms of raw numbers. In (f) it becomes clear that the maximum surface field occurs in short cells with high modulation, a common bottleneck in the bunching section of the RFQ.

5.2.3 Channel Design

The Carbon-RFQ with trapezoidal vanes was designed using a simple cell-by-cell algorithm respecting the linac synchronism condition [1]: The cell length is given by

$$L = \frac{\langle\beta\rangle\lambda}{2}, \quad \langle\beta\rangle = \frac{\beta_{in} + \beta_{out}}{2}, \tag{5.5}$$

where β_{in} and β_{out} denote the velocity of the synchronous particle at cell entrance and cell exit, respectively. It is chosen such that the synchronous particle traverses the cell in half an RF period with an average velocity $\langle\beta\rangle$, assuming that the per-cell change in velocity is small. Equation (2.49) gives the synchronous energy gain upon traversing the cell:

$$\mathcal{W}_{out} = \mathcal{W}_{in} + \frac{\pi}{4} q V_0 A_{1,0}\left(\frac{L}{r_0}, \frac{g}{L}, m\right)\cos\phi_s. \tag{5.6}$$

The trapezoidal-vane RFQ is a modification of the initial design proposed by Bencini [52, 62] that is reviewed in Section 5.1. From this design, the same synchronous phase $\phi_s(z)$ and modulation[48] $m(z)$ provided the algorithm input.[49] With r_0 and V_0 constant, and $k = \pi/L$, the remaining free parameter was the accelerating gap length g. Optimizing the RFQ for maximum acceleration efficiency, g was chosen as small as possible while maintaining a minimum longitudinal curvature radius of $\rho_{\ell,min} = 2\,\mathrm{mm}$. With Eq. (5.4), g is given by

$$g = \min\left(L\,,\ \pi\sqrt{\rho_{\ell,min} r_0 \frac{m-1}{m+1}}\right), \tag{5.7}$$

as g/L must not exceed unity. Equations (5.5), (5.6), and (5.7) form a nonlinear system that is easily solved iteratively, converging within a few iterations. The determined output energy $\mathcal{W}_{out}$ was then used as input energy $\mathcal{W}_{in}$ for the subsequent cell. The procedure was repeated until the desired output energy (in this case $5\,\mathrm{MeV/u}$) was reached.

Emphasis is placed on the fact that the acceleration efficiency $A_{1,0}$ in Eq. (5.6) is obtained by multidimensional linear interpolation from the precomputed lookup table [Fig. 5.7(b)] for a given cell geometry, avoiding repetitive electrostatic simulation. Using this technique, the vane design required merely a few seconds. Furthermore, an electro-quasistatic field map can be produced rapidly based on

[48] The modulation m was scaled such that with the different cell geometry the same minimum aperture a and mid-cell aperture r_0 are achieved. This is detailed further below.

[49] Instead, one could have given ϕ_s and m parameters as functions of e.g. β. Alternatively, for high-current and high-transmission RFQs in particular, the required modulation would be obtained from the equations of adiabatic bunching, which connect synchronous phase, energy, and acceleration efficiency in order to keep the physical bunch length constant [1, 112]. Advanced algorithms have been proposed for beam-based design, actively altering the focusing strength to minimize space charge-induced emittance growth [106, 137, 143].

the sixteen-term potential function, which allows for particle tracking in a tool of choice to validate the design (Section 5.3).

Figure 5.8 shows the beam dynamics parameters of the finalized Carbon-RFQ channel with trapezoidal vanes. (Instead of the quadrupole term $A_{0,1}$, the effective focusing force $\mathcal{B}$ [Eq. (2.55)] is plotted.)

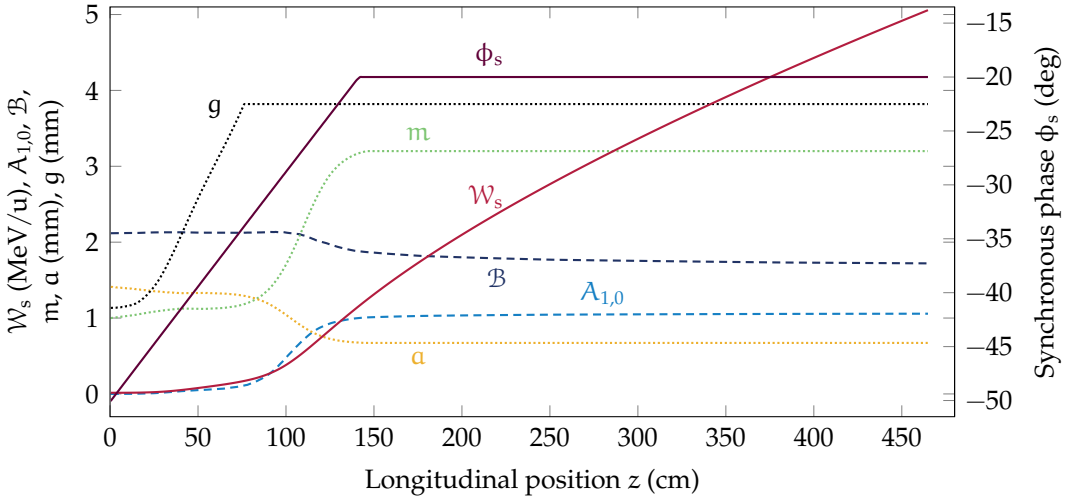

Figure 5.8: Channel parameters of the Carbon-RFQ with trapezoidal vanes. Synchronous energy W_s, synchronous phase ϕ_s, acceleration efficiency $A_{1,0}$, focusing strength $\mathcal{B}$, modulation parameter m and minimum aperture a are shown as functions of the longitudinal position z. Inter-vane voltage $V_0 = 50\,\text{kV}$, mid-cell aperture $r_0 = 1.411\,\text{mm}$, and transverse curvature radius $\rho_t = 0.9 r_0 = 1.2699\,\text{mm}$ are held constant along the RFQ.

5.2.4 Design Analysis

In the following, design parameters of the initial standard-vane and the trapezoidal-vane RFQ are compared. CAD models and computed electric potential of both standard vanes and trapezoidal vanes are depicted in Fig. 5.9. The steeper potential gradient located in the accelerating gap of the trapezoidal vanes is clearly visible.

The most relevant quantities are reported in Fig. 5.10. Additionally, the parameters of a purely sinusoidal design are shown. This channel was generated using the same algorithm described in Section 5.2.3, with the restriction $g = L$ accounting for the fact that the sinusoidal cell is a special case of the trapezoidal cell with sinusoidal step. Contrasting the three designs allows for assessing which differences solely originate in changing from two-term potential cells to sinusoidal cells, and which differences come from introducing the straight vane parts to the sinusoidal cell, i.e. choosing $g/L < 1$.

It is important to note that the modulation m of trapezoidal and sinusoidal vanes is higher than that of the standard vane. The reason comes from the definition of the geometrical parameters of the RFQ cell. For the first two cases, the mid-

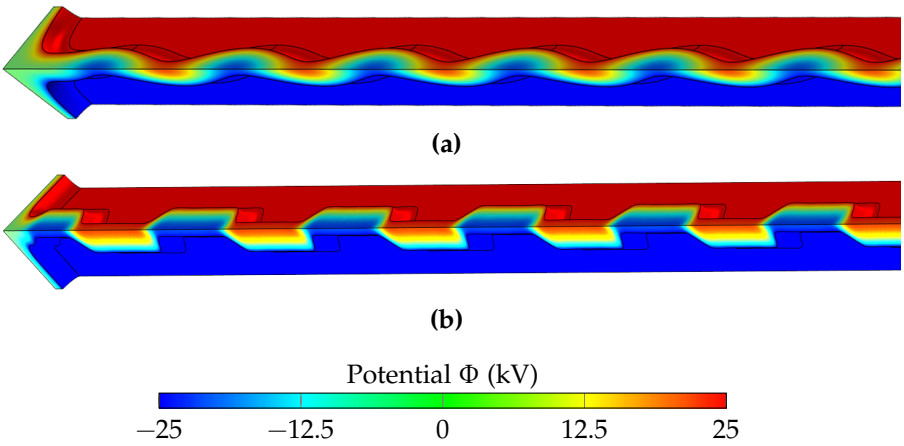

Figure 5.9: Vacuum CAD models and computed electric potential Φ of the Carbon-RFQ vanes: standard design (a) and trapezoidal design (b).

cell aperture amounts to $r_0 = a(m+1)/2$, while for standard vanes, which originate directly from the two-term potential function, it is given as $r_0 = a\mathcal{X}^{-1/2}$ [1], with $\mathcal{X}$ from Eq. (2.44). Therefore, in order to keep r_0 and the minimum aperture a equal to the original design, m had to be increased,[50] leading to the difference visible in Fig. 5.10.

The larger modulation creates a larger on-axis potential drop, directing more electric field in longitudinal direction, thereby increasing acceleration efficiency $A_{1,0}$ (Fig. 5.10, middle right plot). Consequently, choosing sinusoidal over standard vanes already leads to a shorter RFQ. This is only amplified by reducing the accelerating gap length, such that the trapezoidal vanes allow for reaching the final energy with a shorter and less power-consuming cavity. The increased acceleration efficiency comes at the expense of focusing strength $\mathcal{B}$ in the accelerator section of the RFQ where the modulation is maximum. The consequence is a non-negligible, however acceptable reduction in transverse phase advance [Eq. (2.56)]. Lastly, one observes that the trapezoidal geometry changes the distribution of the maximum surface electric field $E_{s,max}$ on the vanes. The surface field tends to be lower for trapezoidal than for standard vanes despite the smaller longitudinal curvature radius, particularly in the accelerating section of the RFQ, as anticipated from the lookup table [Section 5.2.2, Fig. 5.7(f)].

The increased acceleration efficiency of the trapezoidal-vane design reduces the length of the RFQ vanes from 5.8 m to 4.6 m by 20 %. This yields considerable advantages regarding a number of quantities linked to the RF design, which are presented in Table 5.2. Since the surface power loss is approximately proportional to the RFQ length, the RF peak power consumption is reduced by the same ratio from 600 kW to 480 kW. (This value comes indeed very close to the number obtained from RF simulations, which are discussed in Section 5.5.3.) Furthermore,

[50] As an alternative, one could have used a "squeezed" standard cell profile as the step function between the two straight parts of the trapezoidal cell. In this case, r_0 would also equal $a\mathcal{X}^{-1/2}$ for the trapezoidal cell. This approach has been adopted in Ref. [64].

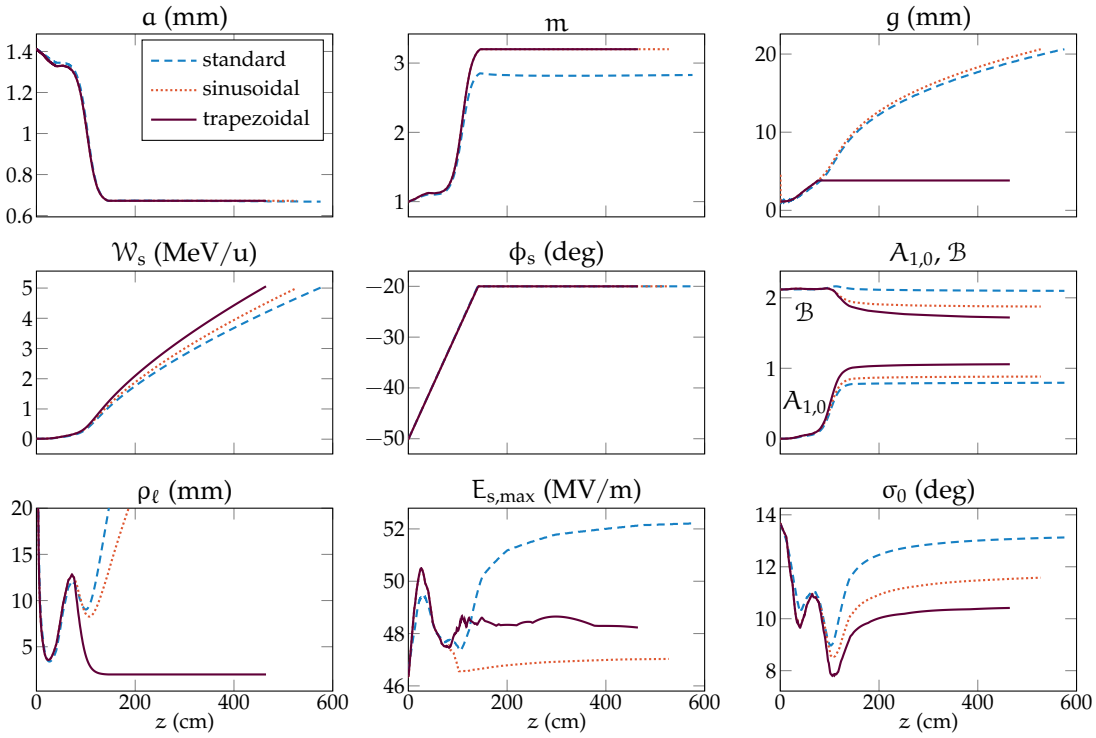

Figure 5.10: Comparison of the Carbon-RFQ channel parameters between the initial standard-vane (two-term potential) design, the final trapezoidal design, and a design employing purely sinusoidal vanes. Geometric and beam-related quantities are shown as functions of the position z, while inter-vane voltage $V_0 = 50\,\mathrm{kV}$, mid-cell aperture $r_0 = 1.411\,\mathrm{mm}$, and transverse curvature $\rho_t = 0.9 r_0$ are constant and equal in all designs. In the trapezoidal and sinusoidal designs the final modulation m is chosen higher, such that the same minimum aperture a is achieved. While the gap length g represents a free parameter for the trapezoidal design, it is equal to the cell length $L = \beta\lambda/2$ in the other designs.

the standard-vane RFQ would have a length of 15λ, far too long to be realized as a single four-vane RF cavity without compromising field stability. As the limit is generally considered to be around five to six wavelengths, the standard-vane RFQ would need to be split into three RF cavities, each requiring specialized end geometry and their own power couplers. Contrarily, the trapezoidal-vane RFQ can be implemented with two RF cavities only, as is demonstrated in Sections 5.4 and 5.5. Lastly, with view to possible industrialization, the length of individual mechanical modules should not exceed 50 cm to 60 cm [180]. A lower number of mechanical modules considerably decreases the manufacturing cost, requires less vacuum seals, and makes the RFQ less prone to misalignment errors.

Table 5.2: Comparison of key quantities of the standard-vane and trapezoidal-vane Carbon-RFQ designs. The parameters of the former were taken from Ref. [52], or estimated based on this reference.

	Standard	Trapez.		
Vane length	5.8	4.6	m	(−20 %)
Overall length (norm.)	15λ	12λ		
Number of RF cavities	3	2		
Number of RF couplers	12	8		
Number of mech. modules	$\geqslant 10$	8		
RF peak power	600	480	kW	(−20 %)

5.3 Particle Tracking Results

The beam dynamics design was validated by means of particle tracking simulations. The expected continuous output beam of the LEBT downstream of the TwinEBIS source is shown in Fig. 5.11. It is the result of simulations carried out in Refs. [52, 61] and provides the input particle distribution for the Carbon-RFQ.

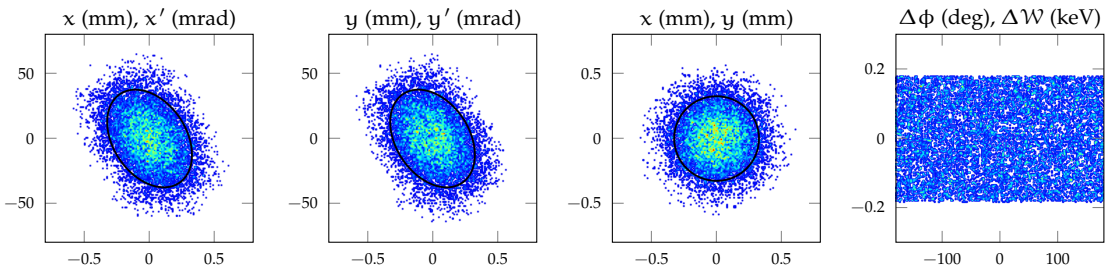

Figure 5.11: Phase space projections of the continuous Carbon-RFQ input beam, as it is expected from the LEBT after the TwinEBIS source [52, 61].

For both standard and trapezoidal design, particle tracking was performed both through a semi-analytic field map generated from the multipole potential function—comprising eight terms for the standard vanes and sixteen terms for the trapezoidal vanes—as well as through the field obtained from a quasi-electrostatic FEM simulation of the 3D vane geometry. The tracking was performed using two different tracking codes, Travel [98] and RF-Track [99], to cross-check the results. As for the PIXE-RFQ beam dynamics studies (Section 3.5), neither space charge nor image charge forces are of practical relevance because of the low beam current.

At first, the results obtained for the two different field models of the trapezoidal-vane RFQ are compared (Section 5.3.1). This allows for validating the field approximation provided by the sixteen-term potential function, which has been used for the design. In Section 5.3.2, the standard-vane RFQ is compared to the trapezoidal-vane RFQ.

5.3.1 Validation of the Sixteen-term Potential Function

Both for the standard-vane and the trapezoidal-vane RFQ, two field maps were used: The first one was built using the eight-term or sixteen-term potential function, respectively, the latter being defined in Section 5.2.2. In this map, the physical vane geometry is not included and the aperture is approximated by a circle with radius r_0 along the entire RFQ. The second map is the result of an FEM electrostatic simulation performed with COMSOL Multiphysics® [93].

In Table 5.3 and Fig. 5.12, the beam distributions resulting from the tracking of 10^4 macroparticles into the four maps are compared. Noticeable for both designs is that the transmission was slightly lower when the FEM map was used instead of the potential map. This can be explained by the different aperture definitions in the two cases. From the two left columns of Fig. 5.12 it can be seen that for the FEM map tracking, the halos—the low-density distribution of particles around the beam core—of the transverse phase spaces are less spread, and the beam is defined by a sharper border (b), (d), when compared the phase spaces obtained from the potential function field maps (a), (c). In the latter case, the transverse acceptance is defined by the circular aperture with radius r_0, which is slightly bigger than the one defined by the physical vane geometry. This approximation allows for propagating the more exterior particles of the distribution that would otherwise be scraped by the physical vane. The FEM field map on the other hand takes the physical vane geometry into account.[51] Despite these observations it is noted that the core of the beam is not affected. Differences in the transverse plane are in the order of 1 % and the corresponding rms emittances show very close agreement.

Table 5.3: Carbon-RFQ output phase space parameters for standard and trapezoidal vanes, each simulated by means of the multipole potential function and an FEM field map.

		Standard vanes		Trapezoidal vanes		
		8-term	FEM	16-term	FEM	
Transmission	$\mathcal{T}$	45.96	44.99	48.82	48.31	%
Energy	$\mathcal{W}_{out}$	5.021	5.018	5.015	5.014	MeV/u
Synchronous phase	ϕ_s	-19.7	-20.1	-19.5	-19.1	deg
Hor. norm. rms emit.	$\varepsilon_{xx'}$	0.0218	0.0197	0.0183	0.0184	π mm mrad
Vert. norm. rms emit.	$\varepsilon_{yy'}$	0.0214	0.0202	0.0178	0.0181	π mm mrad
Long. norm. rms emit.	$\varepsilon_{\phi\mathcal{W}}$	0.1353	0.1264	0.1045	0.1448	π deg MeV

In the longitudinal plane [Figs. 5.12(c), (d), right-most diagrams], larger discrepancies are found between the potential function field map and the FEM field

[51] In the 3D Cartesian field map exported from an FEM simulation tool, points that are located inside the metal conductor, i.e. outside the vacuum simulation domain, are assigned a not-a-number (NaN) value. This is recognized by e.g. the tracking code RF-Track [99], which marks particles encountering a NaN value as lost. For codes that do not implement this functionality, Travel [98] for instance, the NaN values can be replaced by large radial fields (≈ 100 GV/m) that kick particles out of the field map. However, this approach distorts the recorded kinetic energy of the lost particles.

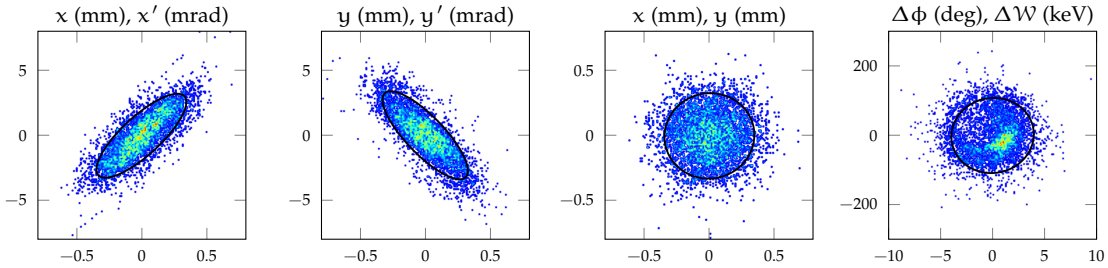

(a) Standard vanes, 8-term potential field map

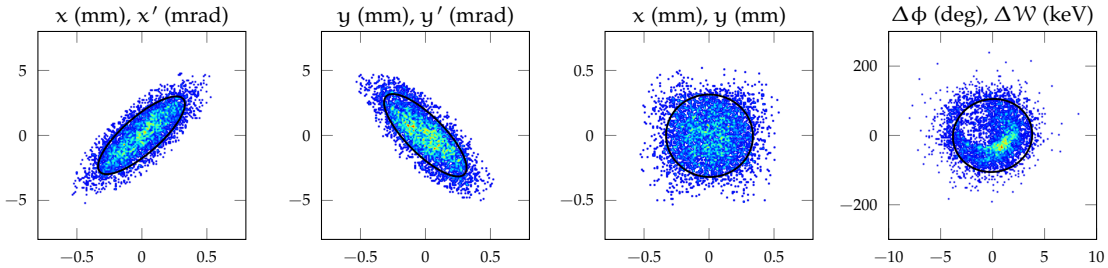

(b) Standard vanes, FEM field map

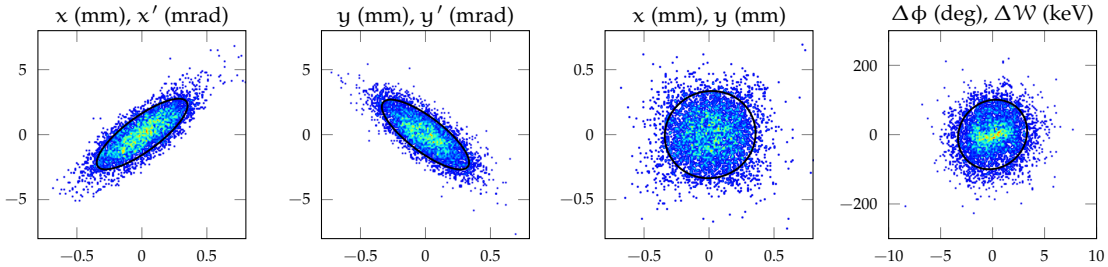

(c) Trapezoidal vanes, 16-term potential field map

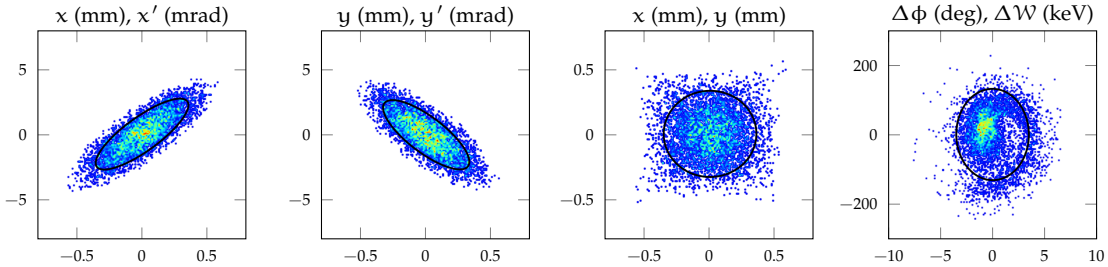

(d) Trapezoidal vanes, FEM field map

Figure 5.12: Comparison of the output phase spaces of the standard (a), (b) and trapezoidal vane design (c), (d) of the Carbon-RFQ. For each design, the simulation results from tracking through both the multipole potential function field map and the FEM field map are shown.

map. This is attributed to the approximation error between the sixteen-term potential function and the more realistic FEM field map, as hinted in Section 5.2.2. Since the main difference between trapezoidal and standard vanes is the longitudinal profile—which motivates the introduction of the sixteen-term potential function in the first place—the discrepancies in the longitudinal plane are expected to be larger than in the transverse plane. Additional deviations could originate in the cell-to-cell tapering of the vane profile, which must be implemented to obtain a smooth electrode surface, but is only approximately considered by the potential function field map. The output particle distributions differ slightly in shape and thus in rms emittance, however, the average final energy and final synchronous phase are nearly identical. This is also observed for the standard-vane RFQ (a), (b), however the effect is significantly more pronounced for the trapezoidal vanes, where the difference between potential and FEM map is larger. Nevertheless, the discrepancies are acceptable for the RFQ vane design phase. For all four simulations shown in Fig. 5.12 (right-most column), the longitudinal phase spaces lie well within the acceptance of the SCDTL downstream of the RFQ [52]. Thus, the sixteen-term potential function represents a highly useful tool for rapidly designing the trapezoidal-vane RFQ.

5.3.2 Comparison of Standard-vane and Trapezoidal-vane RFQ

After the introduction of the trapezoidal vanes to the initial Carbon-RFQ design, it was important to verify that this modification does not significantly compromise output beam quality and accelerator performance. Therefore, beam envelopes and distributions of lost particles of both standard-vane and trapezoidal-vane designs were studied using the same field models.

Figure 5.13 shows the rms beam envelopes σ_x, σ_y [see Eq. (2.53)] of standard-vane and trapezoidal-vane RFQ. The corresponding output phase spaces are reported in Figs. 5.12(b) and (d). As expected, the beam envelopes evolve nearly identical over the first 90 cm of the RFQ, which comprise the shaper and beginning of the buncher. After this length, the influence of the trapezoidal vanes comes into play, sacrificing focusing strength ($\mathcal{B}$ in Figs. 5.8, 5.10) in favor of acceleration efficiency. Consequently, the transverse phase advance σ_0 [Eq. (2.56)] is reduced, and the period of the slow oscillation increases. No increase in the oscillation amplitude was observed, as the parameter $\mathcal{B}$ still varies smoothly along the trapezoidal-vane RFQ—albeit with a steeper and larger drop during modulation ramp-up compared to the standard-vane design.

As mentioned in Section 5.1, one of the key beam dynamics design choices of the Carbon-RFQ—be it with standard or trapezoidal vanes—is that all the losses occur at injection energy, preventing activation issues. The particle tracking in the FEM maps allows for recording the actual losses on the vanes. The results are summarized in Fig. 5.14, where the percentage of lost particles is plotted as a function of the particle energy for both designs. It is noticed that the majority of the losses is concentrated in the first histogram bin, which corresponds to the

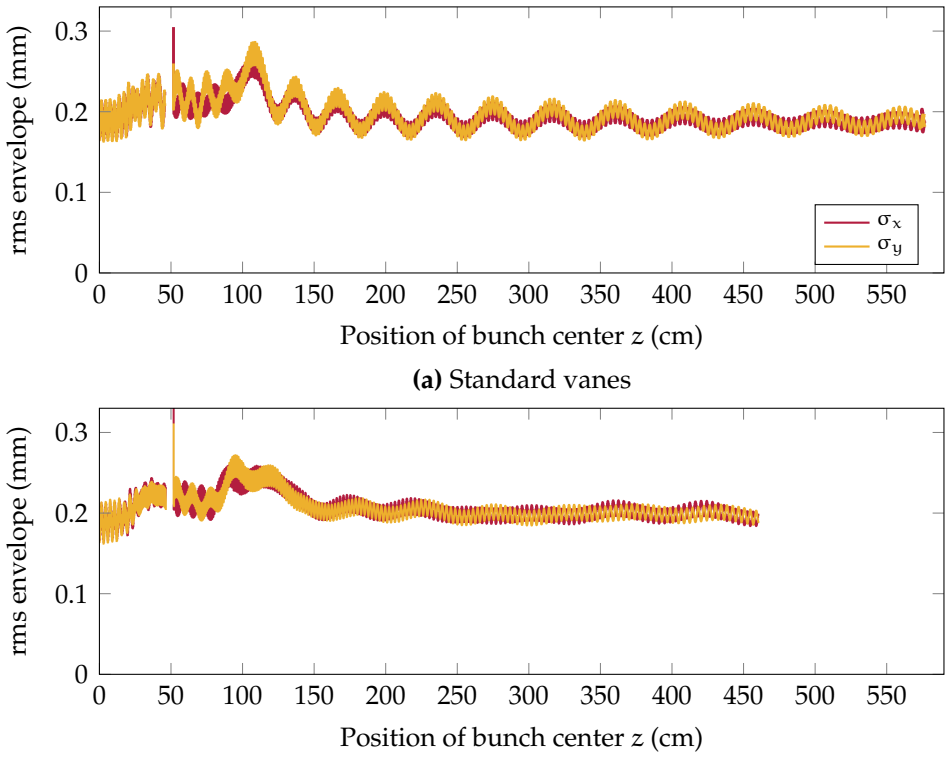

(a) Standard vanes

(b) Trapezoidal vanes

Figure 5.13: Rms beam envelopes computed for the standard (a) and trapezoidal vane design (b). The discontinuies at $z = 50\,\text{cm}$ are nonphysical artifacts originating in discarding macroparticles, which are not captured in the RF bucket, from the simulation.

injection energy. The small fraction lost at higher energies does not give reason for concern, since both the duty cycle ($d = 0.1\,\%$) and the peak input beam current ($I_b = 0.19\,\text{mA}$) are very low. Furthermore, these losses are spread-out along the RFQ and do not accumulate in a specific location.

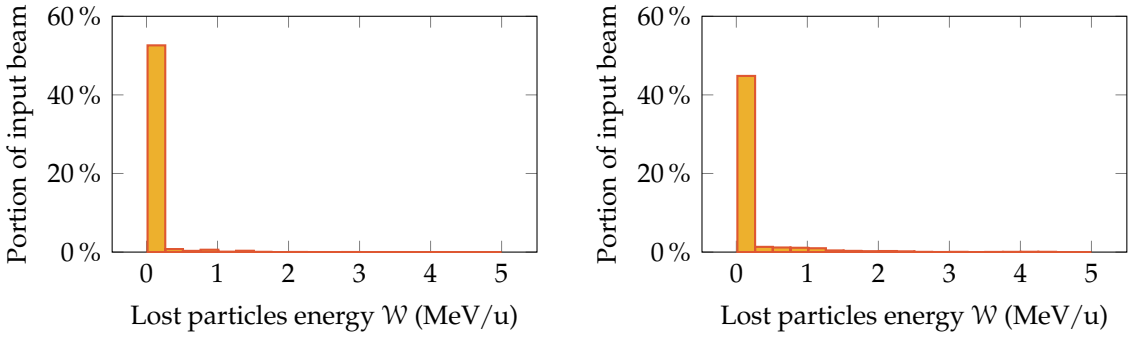

(a) Standard vanes

(b) Trapezoidal vanes

Figure 5.14: Energy distribution of the particles lost during the tracking carried out with RF-Track [99] through the FEM field maps of both standard-vane (a) and trapezoidal-vane RFQ (b).

5.4 Splitting into Two Cavities

As hinted at the end of Section 5.2, the length of the Carbon-RFQ required it to be split into two cavities. The sensitivity of an RFQ to tuning errors can be derived from the waveguide model and is proportional to $(L_{RFQ}/\lambda)^2$ [149, 150]. A length of $L_{RFQ} = 5 \ldots 6\lambda$ is generally considered as the limit for four-vane RFQ cavities that are tuned using only piston tuners [42, 119, 156]. In longer cavities, parasitic higher-order quadrupole and dipole modes are placed too close to the operating mode (TE_{210}), such that the field distribution of this mode becomes unstable without further measures.

Long four-vane RFQs are commonly divided into multiple shorter RF cavities that feature greater spectral distances between modes and are thus easier to tune. Generally, the splitting can be accomplished in several ways, however, two main variants may be identified [156]:

1. The "resonant-coupling" approach [214], where a long RFQ is divided into multiple smaller segments that are coupled by means of so-called coupling cells[52] at the respective segment ends. No dedicated beam dynamics design is required as the gaps introduced to the vane are significantly smaller than $\beta\lambda/2$; the divided structure still appears as one RFQ to the beam. Likewise, only one RF power source is needed. The resonant-coupling approach was first implemented for the 8 m long LEDA-RFQ [72], and has since been realized for several later RFQs (see e.g. Refs. [74, 146, 166, 215]).

2. The splitting of one RFQ into two decoupled RF cavities, sometimes referred to as "tandem-RFQ" approach [156]. It has been chosen in e.g. Refs. [216–219], to name a few. In this method, the RFQ is divided into two practically independent RF cavities, only sharing the vacuum domain. Each RFQ cavity has its own power source and may be tuned, commissioned, and maintained separately. Furthermore, field amplitude and phase may be adjusted independently. The length of the inter-cavity gap amounts to a few RFQ cell lengths, such that the time-periodic focusing lattice of the RFQ is interrupted. Thus, careful beam rematching between the two RFQs is required, either by modifying the vanes themselves, or by introducing a medium-energy beam transport comprising a set of quadrupole magnets in between [156].

The Carbon-RFQ features a length of 4.7 m, corresponding to approximately 12λ. Based on the experience gained with the 750 MHz proton HF-RFQ, which has been successfully tuned at a length of 2 m (5λ) in 2017 [42], it was decided to divide the Carbon-RFQ into two roughly 2.4 m (6λ) long segments. As several (eight) independent RF power sources are planned to be used for feeding the

[52] Here, the term "cell" does not refer to an RFQ cell in the sense of a half-period of the vane modulation, but rather to the RF design concept.

RFQ, the second of the two splitting approaches described above was chosen. The two RFQ cavities are from hereon referred to as RFQ1 and RFQ2.

The lengths of both cavities were used as a parameter for dipole-mode detuning, which is described in Section 5.4.1. Section 5.4.2 shows that the two cavities are indeed sufficiently decoupled, even though they are connected by the bead-pull holes. The rematching across the inter-cavity gap was carried out by Bencini and the author in close collaboration [62], and was accomplished by modifying the vane geometry, which is discussed in Section 5.4.3. The remaining aspects of RF design are covered afterwards in Section 5.5.

5.4.1 Dipole-mode Detuning by Length Adjustment

The splitting into two independent RF cavities offered the opportunity to detune the parasitic dipole modes in both segments solely by means of length adjustment. This technique was previously proposed by the author in Ref. [30], and a conceptual study on the example of the much shorter PIXE-RFQ was carried out. It was implemented for the first time for the RF design of the Carbon-RFQ. The technique reduces manufacturing cost and power consumption by avoiding any dedicated geometric features for dipole-mode detuning.

A transmission-line model (TLM, see Sections 2.3.5 and 3.2.3 for details) was used to approximate the spectra of RFQ1 and RFQ2 in order to rapidly estimate their required lengths. The goal was to maximize the spectral distance between the operating TE_{210} mode and the closest dipole modes. The length of RFQ1 was determined by the specific location of the plane of splitting. The plane may be placed at the end of any accelerating cell, which is succeeded by a short vane extension required for the rematching. The remaining accelerating cells then give a preliminary length for RFQ2. Figure 5.15 shows how the frequencies of the eigenmodes of RFQ1 change depending on the position of the splitting plane. For the TE_{114} mode—the higher of the two most critical dipole modes—the sensitivity reads approximately 0.6 MHz/cell, or 0.4 MHz/cm with the length of cell 597 taken as reference. Thus, the placement of dipole modes can be precisely controlled by varying the overall RFQ length in steps of the cell length, or $\beta\lambda/2$, where β is the synchronous particle velocity at the plane of splitting.

The Carbon-RFQ was divided such that similar lengths, and thus similar RF and mechanical designs arose for both cavities. This positions the TE_{210} operating mode of RFQ1 between dipole modes TE_{113} and TE_{114} [Fig. 5.16(a)]. The preliminary length of RFQ2 did not result in a satisfying spectrum, as the dipole modes TE_{114} and TE_{115} were placed asymmetrically around the TE_{210} mode. Thus, the length of RFQ2 was artificially increased by a few additional accelerating cells to achieve a symmetric mode arrangement [Fig. 5.16(b)].

In order to verify the spectral properties, 3D eigenmode simulations of both RFQ cavities were performed in CST Microwave Studio® [91] (full-length models with quarter-symmetry). On the 3D model created after the TLM-based length calculation it was noticed that the dipole mode frequencies were slightly lower

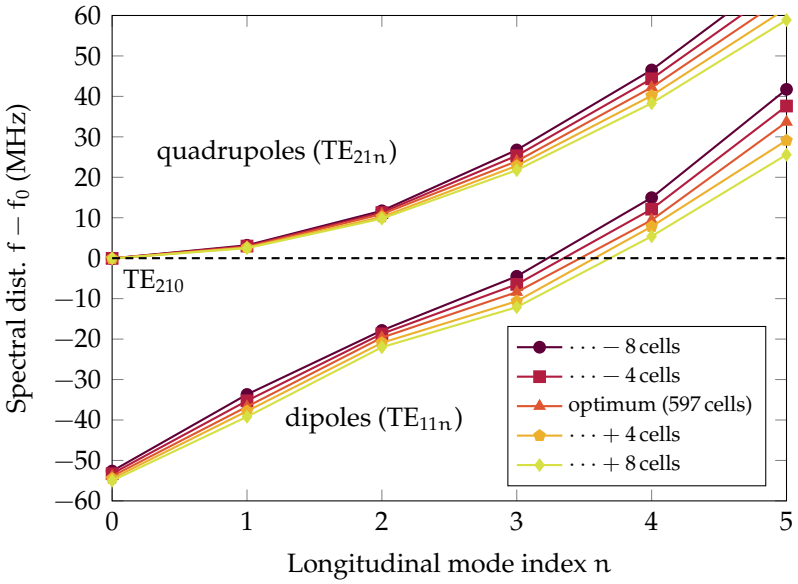

Figure 5.15: Sensitivity of the eigenmode spectrum of RFQ1 with respect to its length, which is given as the number of accelerating cells. The plot shows how both quadrupole and dipole mode frequencies shift when four or eight accelerating cells are added or removed, where the optimum spectrum corresponding to 597 cells [Fig. 5.16(a)] serves as reference. For the TE_{114} mode, the sensitivity reads 0.6 MHz/cell ≈ 0.4 MHz/cm.

than those calculated from the TLM. The differences between TLM and 3D model in the dipole modes closest to the TE_{210} mode amount to approximately 1 MHz for RFQ1 and 2 MHz to 3 MHz for RFQ2. While the relative error in frequency is less than 0.5 %, it translates to an error in length equivalent to roughly two RFQ cells for each of the cavities. Thus, the RFQ lengths and 3D models were adjusted in a second iteration.

Figure 5.16 shows the spectra of the finalized RFQ1 (a) and RFQ2 (b) cavities. Both 3D simulation and TLM results of the second iteration are reported. The spectral margins between TE_{210} mode and the closest dipole modes approximately read ±8 MHz for RFQ1, which features 597 accelerating cells over a length of 235 cm. In RFQ2, ±11 MHz mode separation was obtained by appending two additional accelerating cells. This slightly increased its output energy from 5.02 MeV/u to 5.06 MeV/u and its length to 233 cm (129 cells). The spectral distance to the closest higher-order quadrupole mode (distance between TE_{210} and TE_{211}) amounts to 2.7 MHz in both cavities. The spectral margins achieved for the two Carbon-RFQ cavities, solely adjusting their length, are comparable to those achieved in the PIXE-RFQ with dipole rods—considering that the latter is less than half as long as either of the Carbon-RFQ cavities.

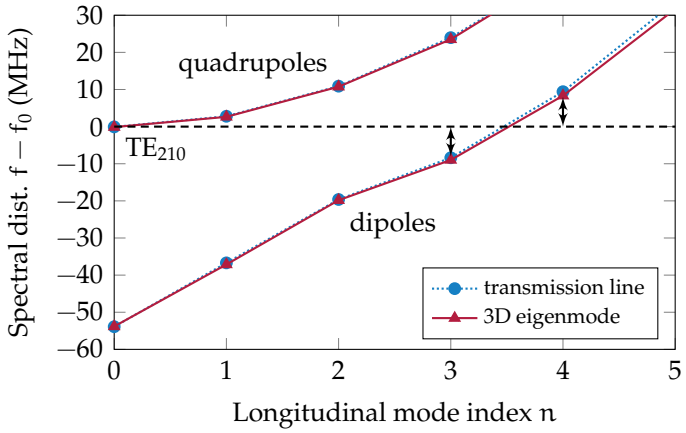

(a) RFQ1

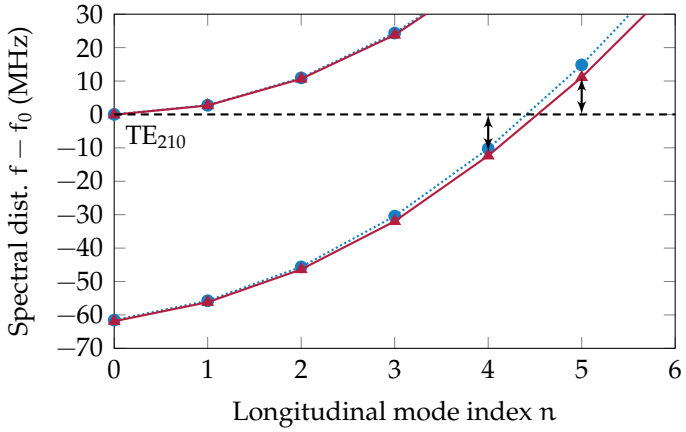

(b) RFQ2

Figure 5.16: Eigenmode spectra of the two cavities RFQ1 (a) and RFQ2 (b) after dipole detuning using the RFQ length. The spectrum of RFQ1 was adjusted by choosing an appropriate splitting position, while the spectrum of RFQ2 was tuned by appending two additional accelerating cells. The spectral margins between the TE_{210} operating mode and the closest dipole modes approximately read ± 8 MHz in RFQ1 and ± 11 MHz in RFQ2.

5.4.2 Decoupling of RFQ Cavities

In order to tune and potentially even commission RFQ1 and RFQ2 separately, both cavities require their own end plates, each featuring four bead-pull holes with a diameter of 24 mm. For each of the face-to-face mounted end plates between the cavities, a minimum thickness of approximately 2 cm is required. This value arises from mechanical considerations regarding manufacturing, stability, and cooling [180]. In this section it is shown that the combined thickness of ≈ 4 cm is sufficient to decouple the operating modes of both cavities, i.e. that the field coupling through the bead-pull holes[53] in the adjacent end plates is negligibly small.

Consider only one eigenmode, the TE_{210} operating mode with identical frequencies f_0 in each RFQ cavity. In a structure composed of two resonators, which are in this case coupled through the bead-pull holes, two orthogonal modes can be excited: the zero-mode with a lower frequency $f_{PMC} < f_0$, where the fields on both sides of the coupling plane are in phase, and the π-mode with a higher frequency $f_{PEC} > f_0$, where the fields have opposite signs (phase difference of 180°) [1]. The relation $f_{PEC} f_{PMC} = f_0^2$ holds [220]. The two cases correspond to PMC or PEC boundary conditions at the coupling plane, respectively. The coupling, in linac terminology denoted as inter-cell coupling strength [1], is proportional to the bandwidth $f_{PEC} - f_{PMC}$ normalized to f_0. For zero coupling, both frequencies equal f_0 and the bandwidth vanishes.

The bandwidth can be obtained from an eigenmode simulation of a short end segment of the RFQ of length ΔL, where either the PEC or PMC boundary condition [see Eqs. (2.20), (2.21)] is applied to the face of the bead-pull hole, delivering the respective frequencies. Figure 5.17 visualizes the magnetic field H in the end segment, shown here with an end plate thickness of $d_e = 2$ cm for the PMC case in logarithmic scale.

In order to obtain a quantity suitable for comparison, an effective quality factor can be associated with the bandwidth:

$$\text{Effective coupling Q factor} = \frac{f_0}{f_{PEC} - f_{PMC}} \cdot \frac{L_{RFQ}}{\Delta L} = 5.3 \times 10^6, \tag{5.8}$$

where the term $L_{RFQ}/\Delta L$ accounts for the fact that only a short segment was simulated; it scales the effective Q to the length of the RFQ cavity. As shown in Fig. 5.18, the effective coupling Q increases exponentially with the end plate thickness d_e (linear on the logarithmic scale of the graph). For $d_e = 20$ mm and $\Delta L = 7.8$ cm, the bandwidth amounts to $f_{PEC} - f_{PMC} = 4.3$ kHz, and the scaled Q associated with the inter-cavity coupling reads 5.3×10^6. This value is more than three orders of magnitude higher than the loaded quality factor $Q_\ell < 3000$ (see Section 5.5.3). The ratio confirms that a combined thickness of 2×20 mm indeed

[53] In theory the fields also couple through the beam pipe, however, this contribution is marginal compared to the bead-pull hole coupling, as virtually no magnetic fields are present on the beam axis.

decouples the modes of RFQ1 and RFQ2 sufficiently with the given bead-pull hole size, and no additional shielding is required.

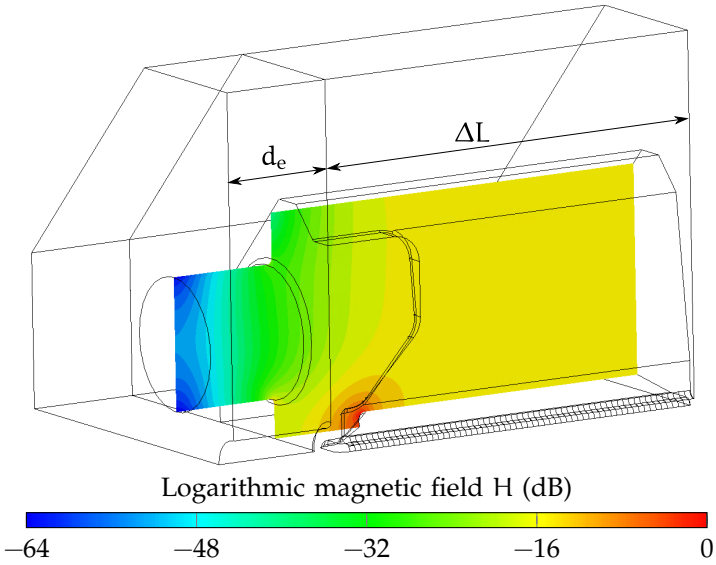

Figure 5.17: RF simulation of a Carbon-RFQ end segment of length ΔL. With this simulation it was confirmed that an end plate thickness of $d_e = 20\,\text{mm}$, i.e. a total drift length of 40 mm is sufficient to decouple the two RFQ cavities. The magnetic field is plotted in logarithmic scaling, showing that the field entering into the bead-pull hole decays rapidly.

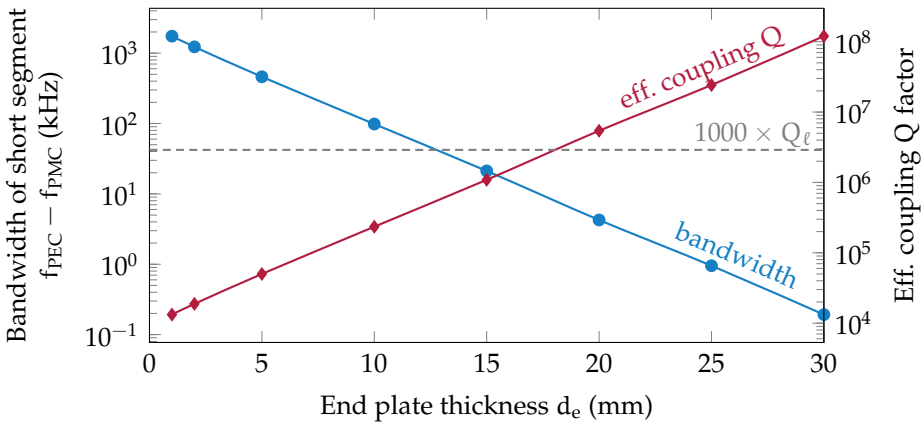

Figure 5.18: Bandwidth $f_{PEC} - f_{PMC}$, i.e. frequency difference between zero-mode and π-mode of the coupled RFQ cavities, and associated effective quality factor Q as functions of the end plate thickness d_e. A thickness of 20 mm, i.e. an inter-cavity drift space of 40 mm, is sufficient to decouple the cavities with a margin three orders of magnitude larger than the loaded quality factor Q_ℓ (also shown on the plot).

5.4.3 Beam Rematching across the Drift

The drift length of 40 mm between RFQ1 and RFQ2 corresponds to almost three RFQ cells ($1.35\beta\lambda$) for the synchronous energy of 2.56 MeV/u at the end of the last accelerating cell of RFQ1. The drift breaks the periodicity of the time-dependent focusing lattice provided by the RF electric quadrupole field. Without any corrections, i.e., ending RFQ1 with a fringe field region (FF) directly after the last accelerating cell, and entering RFQ2 via a radial matcher (RM) [1, 221], the beam would be mismatched in RFQ2 (Fig. 5.21). The reason is found in input and output particle distributions of an RFQ: The beam typically enters an RFQ while converging in both transverse planes (Twiss parameter $\tilde{\alpha} > 0$), which is accomplished in the LEBT by means of cylindrically symmetric electric lens arrays or solenoid magnets. Contrarily, at the RFQ exit the beam converges in one plane ($\tilde{\alpha} > 0$) and diverges in the other ($\tilde{\alpha} < 0$). A such severe mismatch would result in strong transverse oscillations, phase space filamentation, emittance growth, and particle losses at high energies (Fig. 5.21, dotted lines).

In Ref. [222], Crandall introduced the RFQ transition cell (TC) to smoothly connect an acceleration cell with high modulation ($m > 1$) to a zero-modulation cell ($m = 1$), which from hereon we refer to as quadrupole cell (QC). While the transition cell is commonly used to remove uncertainty in the output energy of an RFQ [1], Crandall pointed out its applicability to divide one long RFQ into two shorter ones. By choosing the length of the quadrupole cell (QC1) after the transition cell, the designer can control the output transverse phase space ellipses at the end of RFQ1. As a trade-off between the two contradicting beam behaviors described in the previous paragraph, the length of QC1 can be chosen such that the beam is neither converging nor diverging, i.e. $\tilde{\alpha} = 0$ in both planes, corresponding to upright phase space ellipses. RFQ2 then starts with an RM much shorter than $\beta\lambda/2$, followed by another quadrupole cell (QC2), followed by a transition cell from $m = 1$ to the previous high modulation, followed by the first accelerating cell of RFQ2 [222]. QC2 restores the transverse particle distributions such that the beam is again converging in one and diverging in the other plane. Figure 5.19 shows an electrostatic field map of the described lattice computed in COMSOL Multiphysics® [93].

It is interesting to note that, as RFQ1 and RFQ2 are independent cavities, the offset $\Delta\phi$ between their RF phases can a priori be chosen arbitrarily. In theory however, the offset is fixed by the longitudinal synchronism requirements: $\Delta\phi = \Delta z/(\beta\lambda)$, where Δz is the distance between the end of the last accelerating cell of RFQ1 and the start of the first accelerating cell in RFQ2. Nevertheless, in practice one could determine the optimum phase offset by observing the beam at the exit of RFQ2. Likewise, the field amplitudes in both RFQs could be altered to achieve an output beam of possibly higher quality, since the real RFQ cavities will inevitably be subject to imperfections and misalignments.

Choosing $\Delta\phi$ and the field amplitudes according to the design values, the two degrees of freedom for performing the rematching are the lengths of the two

quadrupole cells, L_{QC1} and L_{QC2}. As an analytic estimate, consider entering the drift with upright transverse ellipses ($\tilde{\alpha} = 0$) as described above. In an ideal RFQ, the beam will be in this configuration at $\phi = 0, \pm 180°$, when the electric field is maximum. The phase at the end of the last accelerating cell of RFQ1 is $\phi_s + 90°$. The required RF phase advance between this point and the end of QC1, where one wants $\phi = 180°$, thus reads $90° - \phi_s$. The corresponding length is (with good approximation) divided between the transition cell of length L_{TC} and the quadrupole cell of length L_{QC1}. Both feature a focusing strength $\mathcal{B}(m = 1) = 2.12$ that is significantly stronger than the $\mathcal{B}(\text{at cut}) = 1.77$ of the surrounding accelerating cells, which feature high modulation (Fig. 5.8). This is taken into account by introducing the ratio of the focusing strengths as a constant factor, neglecting the harmonic time-dependence of the focusing. The approximate length of QC1 is thus given by

$$L_{QC1} + L_{TC} \approx \beta\lambda \left(\frac{1}{4} - \frac{\phi_s}{360°}\right) \left(\frac{\mathcal{B}(\text{at cut})}{\mathcal{B}(m = 1)}\right). \tag{5.9}$$

By similar reasoning, one obtains

$$L_{QC2} + L_{TC} \approx \beta\lambda \left(\frac{1}{4} + \frac{\phi_s}{360°}\right) \left(\frac{\mathcal{B}(\text{at cut})}{\mathcal{B}(m = 1)}\right) \tag{5.10}$$

for the RFQ2 entrance quadrupole cell (QC2). These formulas ignore the focusing effect of the short fringe field region and radial matcher at the end of the vanes.

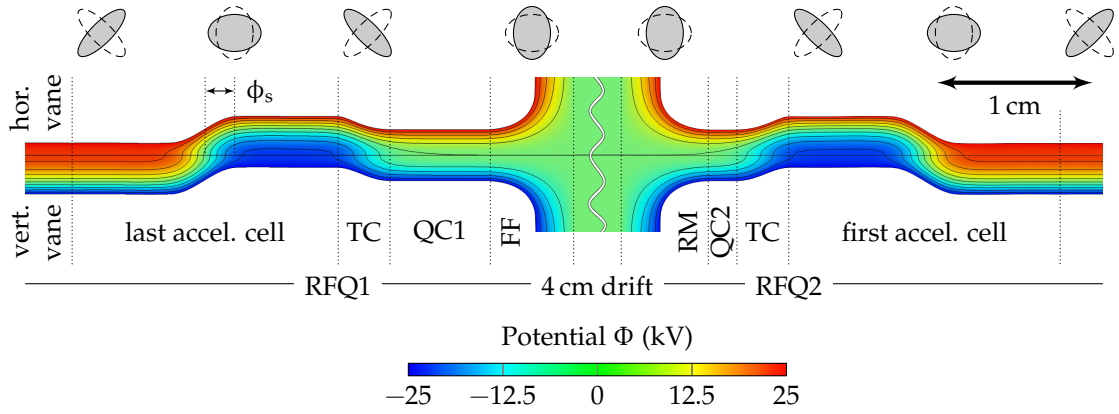

Figure 5.19: FEM field map of the vanes at the exit of RFQ1 and the entrance of RFQ2. The horizontal plane is shown in the upper half, and the vertical plane is shown in the lower half of the plot. The vanes were modified to rematch the beam from the last accelerating cell of RFQ1 over the 4 cm drift to the first accelerating cell of RFQ2. After the transition cells (TC), the vanes are extended by the quadrupole cells QC1 and QC2. The lengths of the quadrupole cells were chosen such that the beam enters the drift with approximately upright transverse ellipses, minimizing the transverse envelope oscillation in RFQ2. At the top, the qualitative transverse transverse ellipses are shown. Note that in an accelerating cell, the ellipse positions are offset with respect to the cell center by the synchronous phase ϕ_s, explaining the asymmetry between QC1 an QC2.

Because of these approximations, the final values for L_{QC1} and L_{QC2} were determined through numerical optimization by means of semi-analytic field maps generated from the sixteen-term potential function (Section 5.2.2) and the particle tracking code RF-Track [99]. As small as possible maximum transverse rms beam envelopes in RFQ2, i.e. after the drift, were selected as the optimization goal:

$$\sigma_{x,max} = \max_{z \in RFQ2} \sigma_x(z), \quad \sigma_{y,max} = \max_{z \in RFQ2} \sigma_y(z) \tag{5.11}$$

Figure 5.20 shows a parametric scan of these quantities as functions of the quadrupole cell lengths L_{QC1} and L_{QC2}. Minimizing the expression

$$\sigma_{x,max} + \sigma_{y,max} + |\sigma_{x,max} - \sigma_{y,max}| \tag{5.12}$$

delivered the numerical optimum. It differs from the analytic estimate by less than 1 mm $\approx 0.03\beta\lambda$. The plots highlight that the two individual minima for each transverse envelope are offset against each other, corresponding to solutions in which the beam would oscillate stronger in one transverse plane than in the other. The chosen optimum is a compromise between the two. In Expression (5.12), the third summand ensures that the beam is as symmetric as possible.

Figure 5.21 shows the beam envelopes in both Carbon-RFQ cavities before and after the rematch. The dotted lines show that, without any corrections, the transverse oscillations in RFQ2 ($z > 235$ cm) would be unacceptably strong, leading to large beam losses. With the optimum determined above, the envelope beating of the original design [Fig. 5.13(b)] was almost completely recovered such that high-energy particle losses are avoided.

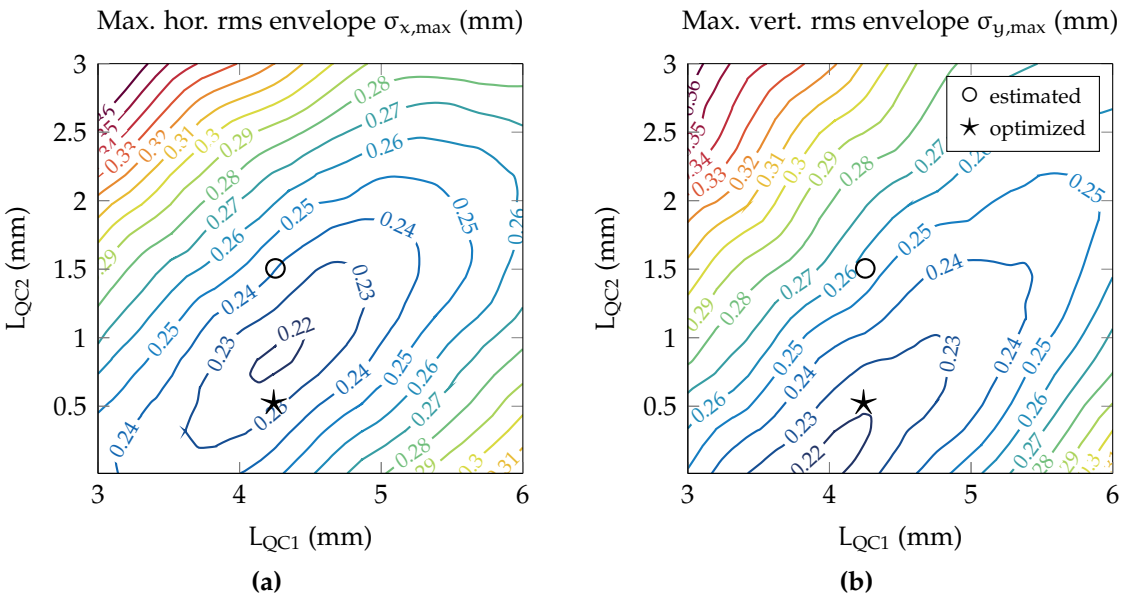

Figure 5.20: Parametric scan of the maximum transverse envelopes $\sigma_{x,max}$ (a) and $\sigma_{y,max}$ (b) as functions of the lengths of the quadrupole cells L_{QC1} and L_{QC2}. The numerically determined optimum parameters ($\star$) shows good agreement with the analytic estimate ($\circ$) obtained from Eqs. (5.9) and (5.10).

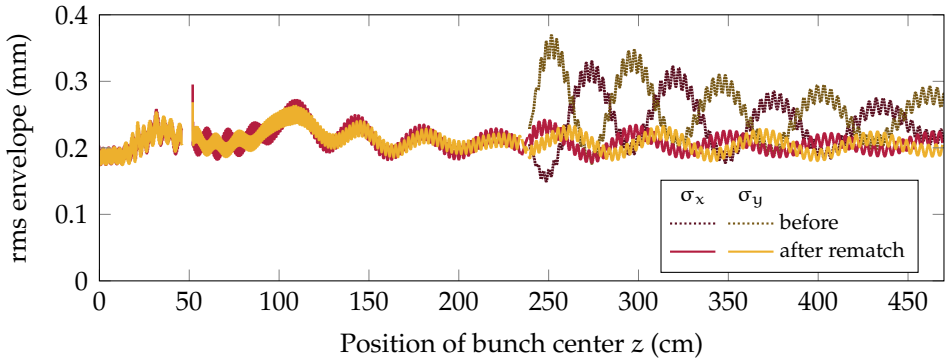

Figure 5.21: Beam envelopes of the Carbon-RFQ split into two cavities before and after the rematch. By tuning the length of the two $m = 1$ quadrupole cells, the beam was rematched into RFQ2. The transverse envelope beating of the original design was almost completely recovered, avoiding particle losses at high energies.

5.5 RF Design

Both methodology and choices of the RF design of the four-vane Carbon-RFQ were adapted from the proton HF-RFQ [18, 27, 40, 42, 43] and PIXE-RFQ [27, 29–31]—the obvious exception being the novel dipole-mode detuning discussed in Section 5.4.1. In this section, the remaining RF design considerations, including cavity geometry, maximum surface electric field, auxiliaries and power couplers, as well as thermal simulations, are presented. As the RF design of the PIXE-RFQ has been covered in detail in the foregoing chapters, only features unique to the Carbon-RFQ are highlighted, while redundant explanations are significantly shortened or completely left out. For a deeper insight, the reader is referred to Chapter 3.

5.5.1 Cavity Geometry

Similar restrictions as for the PIXE-RFQ (Section 3.2.1) apply: Sufficiently thick vanes for heat conduction and mechanical stability, at least 4 mm of bulk copper between water cooling channels and cavity volume to avoid leakage, and as much as possible planar interior surfaces, of which the back wall should be wide enough to incorporate the apertures of the auxiliary flanges. The 2D cross section of the Carbon-RFQ is shown in Fig. 5.22, where the red zones indicate the above-mentioned restrictions. As for the PIXE-RFQ, the parameter c_c was chosen differently for each of the mechanical modules to tune the local TE_{210} cutoff frequency. Additionally, $b_c = (c_c + 19\,\mathrm{mm})/\sqrt{2}$ was chosen as a compromise between high unloaded quality factor Q_0 and a wide-enough back wall. The magnetic and electric field of the 2D cross section are shown in Fig. 5.23.

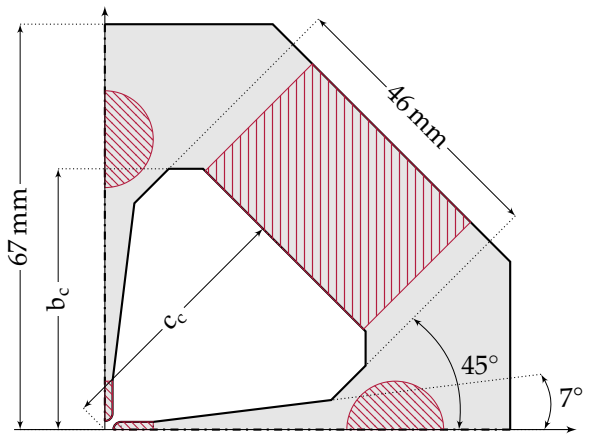

Figure 5.22: Quadrant of the Carbon-RFQ 2D cross section with restrictions to the optimization highlighted in red.

By simulating individual RFQ cells in Ansys HFSS® [90], an optimum cavity dimension c_c was obtained as a function of the longitudinal coordinate z. These simulations also delivered the quadrupole and dipole capacitance C', the dipole

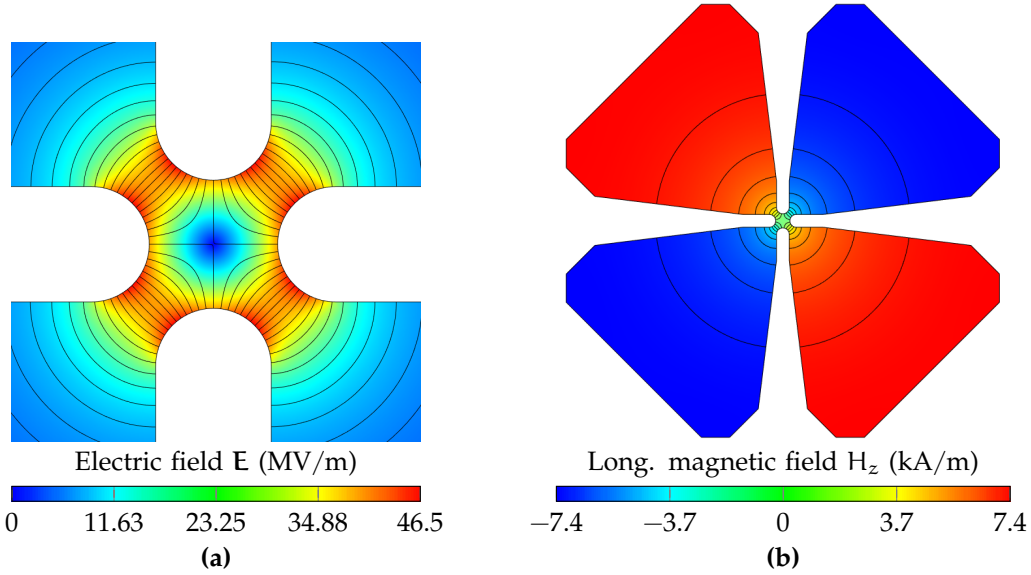

Figure 5.23: Transverse electric field lines at the equidistant vane tips of a cell without modulation are shown in Fig. (a). The peak values for an inter-vane voltage of $V_0 = 50\,\mathrm{kV}$ are shown, and the maximum surface electric field is 46.5 MV/m. The longitudinal magnetic field in the RFQ cavity of the 2D quadrupole mode is depicted in Fig. (b), where the lines connect points of equal amplitude.

cutoff frequency f_{co}, and the 2D quality factor $\tilde{Q}_0$, which are shown in Fig. 5.24. These parameters were used to construct the transmission line model consulted to estimate the cavity length for dipole-mode detuning (Section 5.4.1), as well as for the power loss calculation (Section 5.5.3).

Each of the two Carbon-RFQ cavities consists of four individually brazed modules (Fig. 5.25). The lengths of the copper pieces were chosen to be less than 60 cm to facilitate their machining [180]. The inter-module gaps (100 µm) are always placed in the center of an RFQ cell, which has been shown on the examples of HF-RFQ and PIXE-RFQ to have a minimum effect on the beam. The optimum cavity dimension c_c with respect to $f_0 = 750\,\mathrm{MHz}$ and maximum Q_0 was obtained by averaging the ideal $c_c(z)$ function (Fig. 5.24, upper plot) over each of the eight modules, such that module-wise constant cross sections were obtained. The stepwise changing cross section accounts for the significant inhomogeneity of the inter-vane capacitance (Fig. 5.24, second plot) by changing the shunt inductance accordingly, such that roughly a flat field is obtained without any tuning. The fine adjustment will be carried out by means of movable slug tuners.

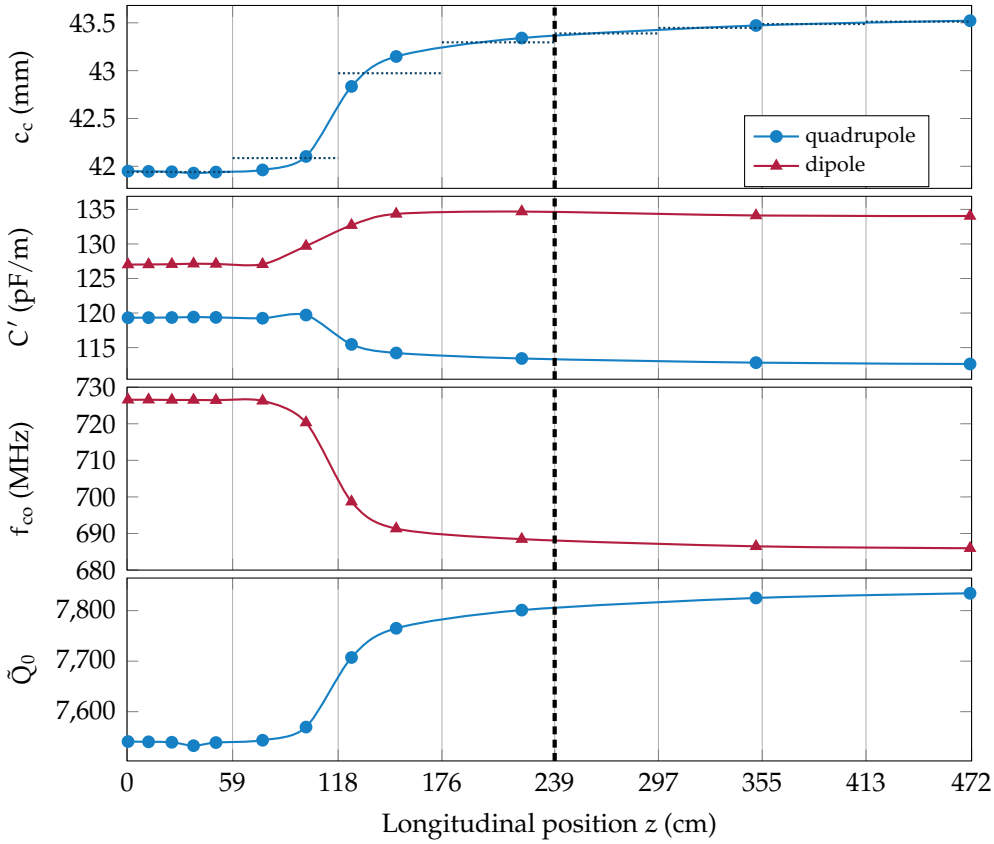

Figure 5.24: Optimum cavity dimension c_c for a local TE_{210} cutoff frequency of 750 MHz as a function of the longitudinal position z along the RFQ (upper plot). This parameter is averaged over each of the 2×4 RFQ mechanical modules (dotted lines). The other plots show the inter-vane capacitance C', local dipole cutoff frequency f_{co}, and quadrupole quality factor $\tilde{Q}_0$ in the resulting cavity. The vertical lines indicate the approximate dimensions of the modules (inter-cavity drift is neglected).

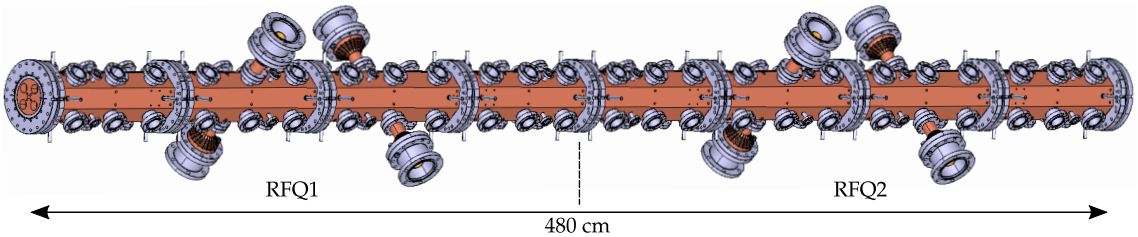

Figure 5.25: Preliminary CAD model of the two Carbon-RFQ cavities RFQ1 and RFQ2. Each cavity consists of four individually brazed modules and features four input power couplers, twelve vacuum pumping ports, as well as 32 slug tuners.

5.5.2 Surface Electric Fields

High surface electric fields may lead to electron emission and sparking, culminating in RF breakdown. Thus, the maximum peak surface electric field $E_{s,max}$ is an important quantity to consider, and a major performance limit for any linac [1].

The 2D cross section simulation, which assumes vane geometry without modulation, delivered an initial $E_{s,max} = 46.5\,\mathrm{MV/m}$ for a given $V_0 = 50\,\mathrm{kV}$. As known from the PIXE-RFQ studies (Section 3.2.2), this value is only an approximation of the actual maximum field driven by the 3D-curved vane-tip surface. Small geometric features at the inter-module gaps must be treated carefully, which can give rise to field values up to 20 % higher than the 2D estimate.

Taking the vane modulation into account, a value of 50.5 MV/m was obtained, located in the bunching section of the RFQ, depicted in Fig. 5.26(a). This value corresponds to the target value of 2.0 Kilpatrick, reflecting the HF-RFQ (see also Section 2.4). One advantage of the trapezoidal vane over standard vane is the reduced surface field in high-modulation cells in the accelerating section of the RFQ observed in this case. Although the maximum surface field is driven by the sinusoidal step in the center of the cell [Figs. 5.2(b), 5.3, 5.26(b)], it is still 7 % lower compared to a standard cell with otherwise same parameters (Fig. 5.10). However, the overall bottleneck—neglecting any later-introduced gaps—remains in the short high-modulation cells in the bunching section [Fig. 5.26(a)].

The inevitable subdivision of the Carbon-RFQ into several mechanical modules introduces gaps into the vane geometry. The gaps are placed in the center of a cell, minimizing effects on the beam. In both RFQ1 and RFQ2, three inter-module gaps are present each, driving the overall maximum electric field because of the small rounding radius. The field at the gap is shown in Fig. 5.26 for a bunching-section cell (c) and an accelerator-section cell (d). It amounts to 57.5 MV/m, independent of the particular cell. Although exceeding the initially targeted 50.6 MV/m by 14 %, the experience gained with the proton HF-RFQ gives confidence in these values: The HF-RFQ was successfully commissioned in 2018, featuring the same inter-module gap geometry and an only 3 % lower maximum surface electric field [Section 2.4.2, Fig. 2.14(a)].

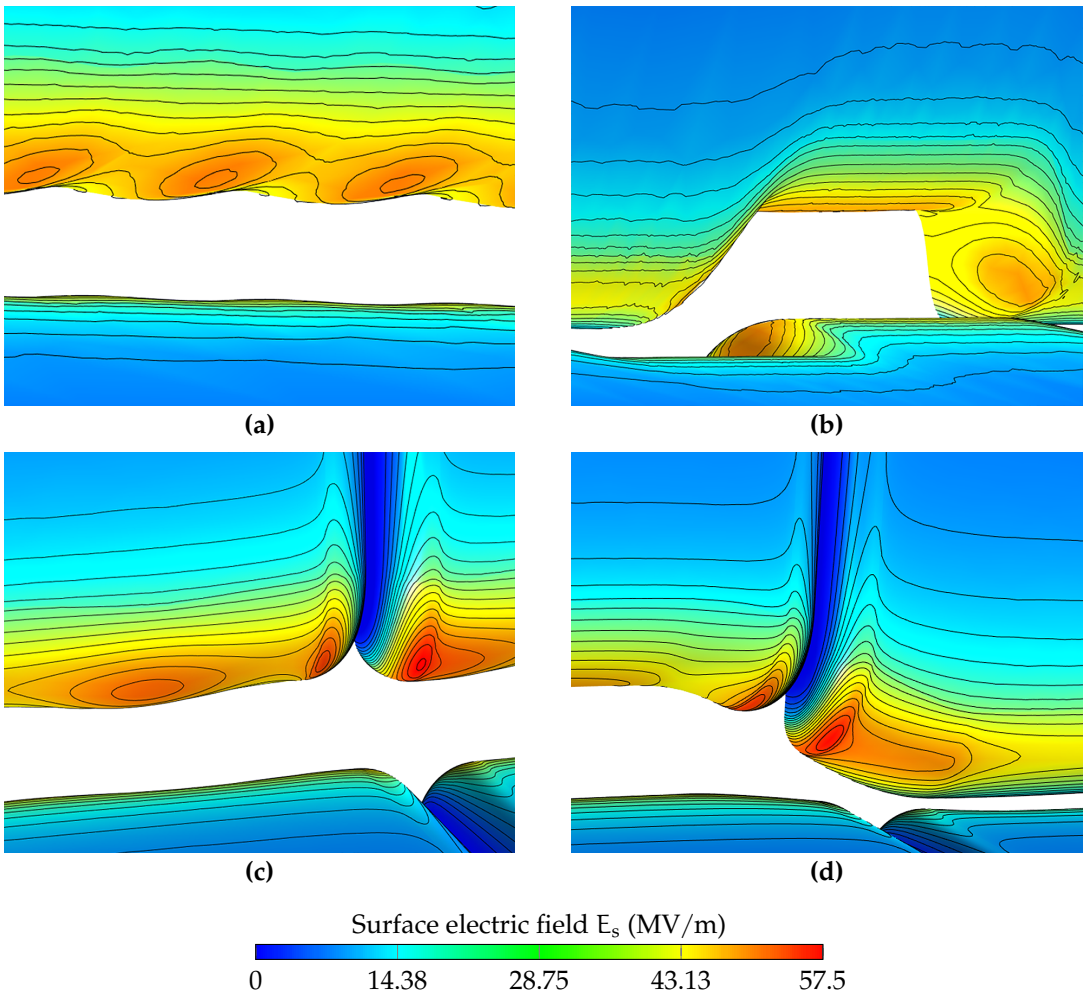

Figure 5.26: Surface electric field in normal cells of bunching section (a) and accelerating section (b), as well as in cells interrupted by the inter-module gap in bunching section (c) and accelerating section (d).

5.5.3 RFQ Auxiliaries and Input Power Couplers

Each of the two cavities features 32 slug tuners, twelve vacuum pumping ports, and four input power couplers. Additional eight ports are foreseen for diagnostic pickup antenna installation. The auxiliary geometries were directly adapted from those of the PIXE-RFQ. Except for the power coupler (see further below), only their penetrations into the cavity were modified to not perturb the operating mode resonant frequency. More details on the geometries can thus be found in Sections 3.2.5 and 3.2.6. Figure 5.27 shows the surface magnetic field H_t proportional to the surface current density on the tips of tuner (a), vacuum pumping port (b), and input power coupler (c). Unsurprisingly, the values of H_t in the Carbon-RFQ can be estimated with high accuracy as those of the PIXE-RFQ multiplied by the ratio inter-vane voltages (50 kV/35 kV), because the respective cavity geometries are very similar.

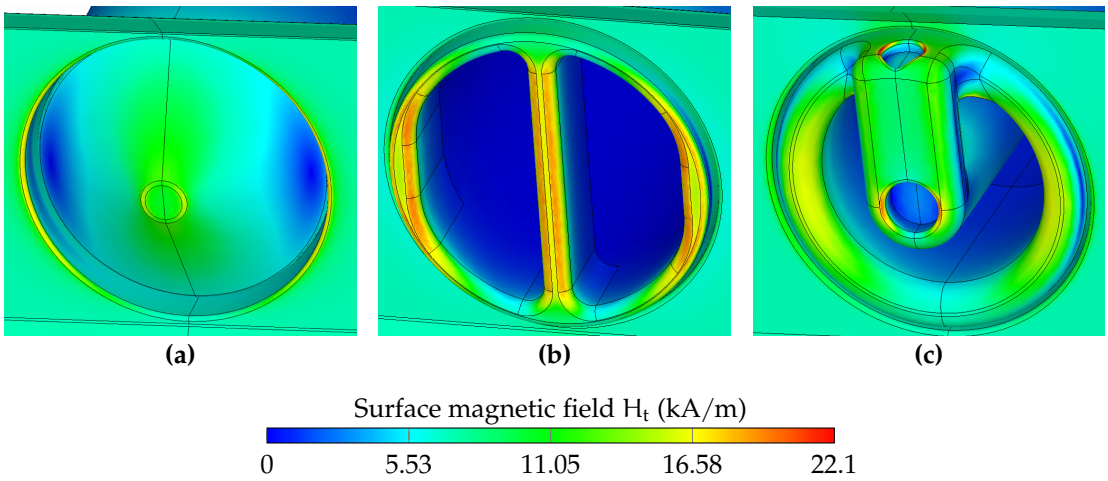

Figure 5.27: Surface magnetic field H_t on the tips of tuner (a), vacuum pumping port (b), as well as as input power coupler (c)

The Carbon-RFQ tuning system consists of 32 copper slug tuners mounted to each of the two roughly 2.4 m $= 6\lambda$ long RFQ cavities (Fig. 5.25), corresponding to 1.3 tuners/λ/quadrant. Although 6λ is considered in the limit of field stabilization using only piston tuners, the capabilities of this tuning system are considered to be sufficient with respect to the available spectral margins (Fig. 5.16). The slightly shorter (5λ) HF-RFQ has been successfully tuned with this configuration [42]. Each slug is foreseen to feature a movement range of ± 11 mm with respect to its nominal penetration into the cavity, such that the available frequency tuning range amounts to roughly ± 11 MHz. Because of the more inhomogeneous capacitance profile (Fig. 5.24, second plot), the field in RFQ1 will be more tilted when the tuners are in nominal position. Thus, RFQ1 is expected to pose a greater challenge for tuning. However, the necessary corrections are well within the piston movement range.

The power loss of both RFQ cavities was calculated by means of the method presented in Ref. [30] (detailed in Section 3.3.1), which has been demonstrated to agree with a full 3D eigenmode computation with an error of $\approx 1\,\%$. Each RFQ was considered as a concatenation of segments, which were chosen to coincide with the ports of tuners, pumping ports, couplers, and ends.[54] The nth segment contributes an RF power loss of $P_n = \omega_0 W_n / Q_{0,n}$, where the stored energy W_n is obtained by integrating the capacitance profile $C'(z)$ (Fig. 5.24, second plot). The unloaded quality factor of the nth segment $Q_{0,n}$ was calculated both from the contribution of the vane modulation (Fig. 5.24, bottom plot), and from 3D eigenmode computation of individual segments. The obtained RF quantities are summarized in Table 5.4.

Each cavity will be supplied by four magnetic loop couplers. While each coupler is strongly under-coupled on an individual basis (single-coupler $Q_{ex} = 20000$), combined they are over-coupled by a margin of approximately 30 %

[54] Again, the pickup antennas are neglected because of their marginal contribution.

Table 5.4: RF parameters of the Carbon-RFQ cavities.

		RFQ1	RFQ2	
Frequency	f_0	750		MHz
Inter-vane voltage	V_0	50		kV
Length	L_{RFQ}	235	233	cm
Average capacitance	$\langle C' \rangle$	117	113	pF/m
Stored energy	W	343	329	mJ
Surface power loss	P_0	244	230	kW
Unloaded quality factor	Q_0	6620	6750	
External quality factor, total	Q_{ex}	5000		
Loaded quality factor	Q_ℓ	2850	2870	
Coupling strength	β_c	1.32	1.35	
Number of couplers		4		
External quality factor, per coupler		20000		
Power per coupler ($\beta_c = 1$)		61	60	kW

($\beta_c = Q_0/Q_{ex} = 1.32$ in RFQ1 and 1.35 in RFQ2). Each of the two cavities thus features the same power coupler arrangement as the proton HF-RFQ [27, 42]. Size of the coupling loop and penetration into the cavity have been adjusted to match desired frequency and coupling strength, taking advantage of the methodology described in Section 3.3.2. The couplers will be mounted on rotatable flanges, allowing to fine-tune the coupling with the help of RF measurements after assembly. In the case of critical coupling ($\beta_c = 1$), each coupler will supply a (peak) power of approximately 60 kW. High-power tests with the HF-RFQ have demonstrated that the coupler can transmit up to 100 kW [18].

5.5.4 Thermal Simulation

During operation, RF losses constitute a surface heat source on the copper structure. The resulting temperature increase causes a deformation of the cavity and a detuning of the resonant frequency. Thermal and structural simulations were conducted using COMSOL Multiphysics® [93] to study this behavior and determine the requirements of the cooling system.

Because of the low duty cycle of $d = t_{pls} f_{rep} = 0.1\,\%$, the cooling system must dissipate only 240 W per RFQ. It rather serves for frequency stabilization. In Fig. 5.28, the frequency shift Δf is shown as a function of the duty cycle d and the cooling water temperature T_w. The average water speed in the cooling channels amounts to 1 m/s, corresponding to a convection coefficient of 3900 $W/m^2/K$. Two possible configurations were assessed: a design with two channels per vane, used by the HF-RFQ and the PIXE-RFQ (see Refs. [29, 30] and Section 3.4), and a new design with only a single channel per vane. The plot highlights that the difference between the two options is marginal, such that the mechanically simpler design with one channel per vane was selected.

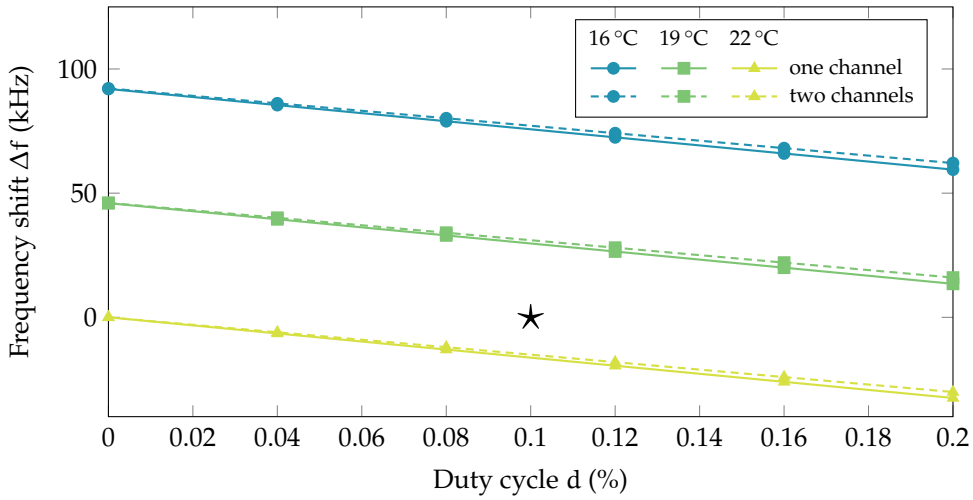

Figure 5.28: Resonance frequency shift Δf of the Carbon-RFQ cavities subject to heat-induced deformation as a function of duty cycle d and cooling water temperature T_w for the cases of one and two cooling channels per vane (estimated from 2D simulation). At nominal operation, the heating is compensated by reducing T_w by 1 K ($\star$).

Figure 5.28 visualizes the available frequency tuning range for a given water temperature range:

$$\frac{\partial f}{\partial T_w} = -15.3\,\mathrm{kHz/K}. \tag{5.13}$$

Furthermore, the frequency is a linearly decreasing function of the duty cycle with

$$\frac{\partial f}{\partial d} = -151\,\mathrm{kHz/\%}. \tag{5.14}$$

Thus, to recover the design resonance frequency at nominal operation, the cooling water temperature must be reduced by approximately 1 K ($\star$ in Fig. 5.28). Figure 5.29 shows the distributions of temperature T (b) and deformation field $\mathbf{u}$ (c) in the copper domain of the 2D cross section for this point of operation. Because of the temperature gradient in the vane, the vane tips move closer towards the beam axis and each other, increasing the capacitance C and thus lowering the frequency with increasing duty cycle. This is compensated by decreasing the overall temperature of the cavity, and thus its volume, by controlling the cooling water temperature. Hereby the inductance $\mathcal{L}$ is reduced. Since $\partial f/f = -(\partial\mathcal{L}/\mathcal{L} + \partial C/C)/2$, the design resonant frequency can be restored.

The peak RF power loss per unit length of the Carbon-RFQ (105 kW/m) is significantly higher than that of the PIXE-RFQ (65 kW/m) because of the increased inter-vane voltage. Relevant for thermal considerations however is the time-average of this quantity, which, because of the lower duty cycle, is by a factor of 15 smaller for the Carbon-RFQ (105 W/m compared to 1625 W/m). Extensive thermal simulations were carried out for the PIXE-RFQ including its auxiliaries. It was considered as sufficient to extrapolate from these data to the Carbon-RFQ by simple scaling laws, as the temperatures, deformation, and stresses in the

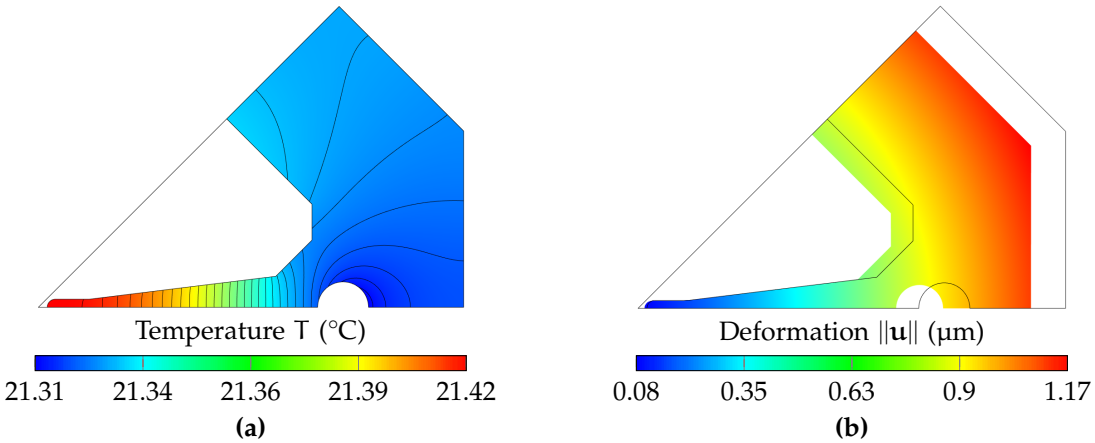

Figure 5.29: Thermal and structural simulation results for nominal operation parameters, namely $d = 0.1\,\%$, $T_w = 21\,°C$, and $v_w = 1\,m/s$ ($\star$ in Fig. 5.28). The water temperature T_w is reduced by 1 K with respect to the reference temperature, such that the cavity volume decreases. The hereby reduced inductance compensates for the increased vane capacitance, such that the frequency shift vanishes.

Carbon-RFQ are much smaller and less critical. For instance, the ΔT of the tip of the vacuum pumping port—with 38 °C the hottest part of the PIXE-RFQ—reads 16 K [Fig. 3.28(a)]. Scaling this value by the ratio of the average RF power losses per unit length delivers $\Delta T \approx 1\,K$ for the pumping port tip of the Carbon-RFQ. Considering that at nominal operation the cooling water temperature is reduced by 1 K, a maximum pumping port temperature of 22 °C arises. Table 5.5 summarizes the thermal calculation results, where the quantities extrapolated from PIXE-RFQ simulation data are marked with †.

Table 5.5: Summary of thermal simulation results for the Carbon-RFQ cavities. Values that were obtained by extrapolating the PIXE-RFQ simulation results are marked with †.

		PIXE	Carbon	
Peak surface power loss	P_0	65	each 240	kW
Length	L_{RFQ}	1.0	each 2.3	m
Duty cycle	d	2.5	0.1	%
Average surf. power loss		1625	105	W/m
Reference temperature	T_0	22	22	°C
Cooling water temperature	T_w	22	21	°C
Cooling water speed	v_w	1	1	m/s
2D vane temperature		25.7	21.4	°C
Vacuum port temperature†		38	22	°C
End plate temperature†		34	22	°C
Max. equivalent stress†	σ_{vM}	21	2	MPa

5.6 Conclusion

A 750 MHz RFQ for fully stripped carbon ions featuring trapezoidal vanes was designed. It represents the first RF accelerating structure of the "bent linac," a small-footprint linear accelerator recently proposed by Bencini [52] for cancer therapy by means of carbon ions. All of its components were optimized to match the requirements of compactness, low power consumption, and simplification of construction in view of industrialization.

The Carbon-RFQ was conceived and initially designed with standard (two-term potential) vanes by Bencini [52, 62] using the Los Alamos RFQ codes (PARMTEQ). The RFQ features a beam transmission of only 50 %—by design—and accelerates ions with a charge-to-mass ratio of 1/2 to 5 MeV/u. Particle losses at energies higher than a few 10 keV were minimized.

The standard-vane RFQ was then redesigned to feature trapezoidal vanes, reducing RF power consumption and length by 20 % because of the increased acceleration efficiency while preserving other beam parameters. A novel semi-analytic technique using sixteen terms of the well-known multipole potential function was proposed by the author of the thesis to determine the vane shape in a cell-by-cell manner. The beam dynamics design was validated by particle tracking simulation with both semi-analytic and FEM-based field maps, confirming that nearly the totality of particle losses occurs at or slightly above injection energy.

The particle tracking simulations showed that the sixteen-term potential function can describe both longitudinal and transverse beam dynamics for the Carbon-RFQ vanes in close agreement with an FEM simulation of the real geometry. As only one specific trapezoidal electrode type was considered (straight vanes with constant transverse curvature radius $\rho_t = 0.9r_0$ and sinusoidal step), future studies should challenge the applicability of the sixteen-term potential function with respect to other electrode types, for instance wedge-shaped vanes, vanes with variable transverse curvature radius, rods, and different step functions. Should the sixteen multipoles prove to be insufficient, more terms could be added easily. In the longer term, an extensive database providing multipole data for RFQ electrodes of various types could be created, as has been done for the PARMTEQ codes for conventional RFQ electrodes. It would provide a highly useful tool for rapidly designing RFQs with high acceleration efficiency featuring trapezoidal vanes.

The RF design of the Carbon-RFQ has been completed, focusing on minimized power loss and simplified construction. The geometries of cavity, auxiliaries, and power couplers were determined. A major feature is the subdivision into two fully decoupled RFQ cavities (RFQ1 and RFQ2). By 3D eigenmode simulation it was confirmed that the drift length of 4 cm, emerging from mechanical constraints, is sufficient to decouple the RFQ1 and RFQ2 without additional shielding. The rematching of the beam across the drift was accomplished by two quadrupole vane extensions, which were optimized for minimum beam envelope

oscillations in RFQ2 (joint effort between Bencini and the author [62]). The length of each of the two RFQ cavities was used as a mean of dipole-mode detuning. Simulations showed that the location of critical dipole modes can be precisely controlled by placing the splitting plane at discrete positions that correspond to the ends of the RFQ cells. Through this novel method, the spectral distances between TE_{210} operating mode and closest parasitic dipole modes were maximized, amounting to ± 8 MHz in RFQ1 and ± 11 MHz in RFQ2. Avoiding any additional geometric features dedicated to dipole-mode detuning, both RF power loss and construction complexity could be reduced.

The RF design was validated by accurately simulating the maximum surface electric field on the most critical surfaces, confirming that it does not significantly exceed the design value of 2.0 Kilpatrick. Thermal simulations of the 2D cross section were carried out to determine the frequency shift Δf as a function of duty cycle and cooling water temperature. The water temperature can be reduced by 1 K to compensate for RF losses at nominal operation (0.1 % duty cycle) such that $\Delta f \approx 0$ is achieved.

In the framework of a collaboration between CERN and Centro de Investigaciones Energéticas, Medioambientales y Tecnológicas (CIEMAT), Madrid, Spain, the Carbon-RFQ will be built as part of a demonstrator for the low-energy part of carbon ion therapy linacs. The demonstrator will include a copy of the TwinEBIS ion source, a LEBT, the Carbon-RFQ itself, and some further RF accelerating structure (studies are presently ongoing for the choice of the accelerating structure following the RFQ). It has the purpose of validating the beam quality at the end of the low-energy section, which is often the most critical part of a hadron linac, as it defines the beam characteristics that are then propagated along the accelerator.

6 General Conclusion and Outlook

The present thesis covers various aspects of the development of two compact radio-frequency quadrupole linear accelerators (RFQ) operating at 750 MHz. After providing the reader with the foundations forming the basis of the thesis in Chapter 2, the main thesis body is composed of two main parts that emerge from the two considered RFQs: Chapter 3 and 4 cover both RF design, low-power RF measurements, and tuning of the PIXE-RFQ, a one-meter long proton accelerator for ion beam analysis. Chapter 5 is dedicated to the design of the Carbon-RFQ for hadron cancer therapy.

Up front, an overview-study of field limitations in RFQs is presented at the end of the foundations chapter in Section 2.4. Various publications covering a range of commissioned or designed RFQs have been evaluated with regards to maximum surface electric field, frequency, and RF pulse lengths. Special focus was given to the maximum field that was achieved with short pulses during high-power RF conditioning. Several derived quantities have been analyzed to find a figure of merit suitable to predict the breakdown limit in RFQs besides the well-established but conservative Kilpatrick limit. While a pulse length-dependence can explain cases of exceptionally high fields, the Kilpatrick limit is the quantity with the overall highest consistency. However, it should be noted that this could just originate in the available data obtained at or close to the design values, which are dictated by (a multiple of) the Kilpatrick limit rather than by the breakdown limit. Moreover, it was found that quantities used for high-gradient accelerating structures operating in the X-band and with short pulses are not suited to describe the RFQ breakdown performance. The specific maximum surface electric fields of the two RFQs discussed in this thesis were justified with the example of the recently commissioned HF-RFQ [43].

Within the framework of the MACHINA collaboration [31, 32] between CERN and Istituto Nazionale di Fisica Nucleare, the PIXE-RFQ was developed as the heart of the first transportable system for *in situ* ion beam analysis (PIXE) of cultural heritage artifacts, allowing employment in museums, restoration centers, or even in the field. The RFQ features a frequency of 750 MHz—after the medical HF-RFQ [27] the second RFQ world-wide to operate at this frequency—and accelerates protons to 2 MeV over a length of just one meter. Prior to the research presented in this thesis, innovative beam dynamics were developed for

the PIXE-RFQ, sacrificing transmission in favor of short length and low power consumption [28, 40].

The complete RF design of the PIXE-RFQ is presented in Chapter 3. Geometrical dimensions of cavity, RFQ ends and dipole stabilization rods, tuners, vacuum pumping ports, diagnostic pickup antennas, and the input power coupler were determined for mechanical design and construction. The design value of the maximum surface electric field was confirmed, and the RF peak power loss was calculated. Both (semi-)analytical techniques such as a transmission line model or segment decomposition, as well as 3D eigenmode computations by means of FEM were utilized. The thermo-mechanical behavior of the structure was studied to anticipate temperature distribution and deformation as well as the shift on the resonant frequency for nominal operation parameters. A cost-efficient cooling system without frequency feedback will be used, resulting in an RFQ resonant frequency shift during operation which the RF power source has to follow to minimize reflected power. Moreover, it has been confirmed that a solely passive cooling of the RFQ auxiliaries is sufficient. The RF design was validated by means of beam dynamics studies: Particle tracking simulations showed that the frequency shift is acceptable for the beam. In this context, a comparison between the predicted phase spaces obtained from the RFQ design tools and from tracking through the RF field map was drawn, where very close agreement was observed. Lastly, it was confirmed that all particle losses—by design amounting to 70 % of the input beam in favor of compactness—occur at or close to injection energy, avoiding vane deterioration.

Chapter 4 reports the low-power RF measurements conducted during and after construction, as well as the tuning procedure of the PIXE-RFQ. Both manufactured power couplers—the actual installed one and its spare—were mounted "head-on" and the transmission was measured, confirming the quality of the constructed pieces. Likewise, the two mechanical modules composing the RFQ were measured individually before they were integrated into the full assembly. The RFQ electromagnetic field, decomposed into a quadrupole and two dipole contributions, was measured by means of bead-pull measurements. Machining imperfections and misalignments cause longitudinal and transverse field tilts that were compensated with the help of movable piston tuners. The necessary tuner adjustments were calculated by means of an augmented version of an algorithm previously introduced by other scientists [42]. This new variant allows for tuning both field and frequency at the same time. Evidence suggests that the algorithm convergence is also improved by the introduction of frequency and corresponding weights. With only two tuning steps, the PIXE-RFQ field could be corrected to an error of 1 % or less, and the frequency was tuned to the design value with a deviation of less than 30 kHz. Both values lie well within the requirements. After the RFQ was evacuated and its leak-tightness was confirmed, quality factors and coupling coefficients were measured, showing close agreement (error of 6 % at most) with the design parameters. With a final measurement the diagnostic

RF pickup antennas were calibrated, such that the field flatness may be assessed without exposing the RFQ cavity to ambient air, even during operation.

As of July 2020, low-level RF measurements and tuning of the PIXE-RFQ have been completed. The RFQ is now scheduled for high-power test and RF conditioning once the RF power source is connected. Afterwards, it will be integrated into the MACHINA setup and the proton beam will be commissioned. The RFQ is expected to commence operation towards the end of the year 2020. First PIXE measurements are expected in 2021 at the Opificio delle Pietre Dure, Florence, Italy.

The second part of the thesis is dedicated to the Carbon-RFQ for hadron therapy. The 750 MHz Carbon-RFQ was conceived as the first RF accelerating structure of the proposed "bent linac" [52] for cancer therapy by means of fully stripped carbon ions. It accelerates particles with a charge-to-mass ratio of 1/2 to 5 MeV/u. The development of the Carbon-RFQ stimulated two innovations: a semi-analytic description of the electric field of the trapezoidal vanes, and the detuning of parasitic dipole modes by length adjustment.

With the help of trapezoidal vanes, the acceleration efficiency of the RFQ was increased such that RF peak power consumption and overall length could be lowered by 20 % to 480 kW and 4.8 m, respectively. The demand of a semi-analytic description of the trapezoidal electrode field motivated an extension of the well-known eight-term potential to sixteen multipole coefficients to rapidly design the channel. While some discrepancies between the multipole approximation and FEM-based simulations were observed, the novel technique showed acceptable accuracy to design the Carbon-RFQ with its specific vane geometry. In future research, the sixteen-term potential function should be challenged with respect to other electrode geometries and RFQ designs. More coefficients could be easily added to the potential function without significantly increasing the computational effort, should the sixteen multipoles prove to be insufficient. It would provide a highly useful tool to rapidly design RFQs with trapezoidal vanes.

The RF design of the Carbon-RFQ was strongly inspired by the proton HF-RFQ [27] and the PIXE-RFQ (Chapter 3 of the present thesis and Ref. [30]). A particularity is the splitting into two fully decoupled RFQ cavities, which was applied for the first time at a frequency as high as 750 MHz. The vane geometry was modified to facilitate beam rematching across the drift. The detuning of parasitic dipole modes was accomplished solely by selecting the length of each of the two RFQ cavities in steps given by the RFQ cells. No dedicated detuning features were implemented, reducing construction effort and RF power loss. While originally studied by the author on the example provided by the PIXE-RFQ [30], this technique was implemented here for the first time. The RF design of the Carbon-RFQ was concluded by a range of FEM simulations, confirming maximum surface electric field and thermo-mechanical behavior.

In spring 2020, the Carbon-RFQ entered the mechanical design stage in the framework of a collaboration between CERN and CIEMAT. The projects aims at constructing a demonstrator accelerator comprising the low-energy part of a

carbon ion therapy linac—including the RFQ—which is generally the most critical section. It is important to evaluate the beam parameters at the end of the low-energy section, as they are propagated through the downstream accelerating structures and ultimately to the patient.

Linear particle accelerators operating at high frequencies fulfill the requirements of many present and future applications in industry and medicine—high beam quality, smaller footprint, and lower power consumption. Compact RFQs in turn are crucial components of high-frequency linacs, as they capture the beam after the particle source and dominate the beam quality of the entire accelerator. This thesis addresses the development of two 750 MHz RFQs for two particular accelerator applications: The Carbon-RFQ represents a critical component of a proposed linac for cancer treatment. The application of particle accelerators in oncotherapy is sometimes considered as *"the most significant spin-off of high-energy and nuclear physics research for the benefit of mankind"* (Wangler, 2008 in Ref. [1]), and only expected to grow in the future. The PIXE-RFQ on the other hand attends to a more niche application: ion beam analysis of cultural heritage artwork. However, an ion beam analysis RFQ could find a broad range of applications in other fields, such as chemistry, medicine, material sciences, or forensics, to name only a few. Last but not least, the PIXE-RFQ in its compactness offers a unique opportunity for education and public presentation of the accelerator community: A duplicate of the PIXE-RFQ, called ELISA-RFQ (Experimental Linac for Surface Analysis), is currently under construction at CERN, planned to be exhibited in the Science Gateway, CERN's upcoming scientific education and outreach center [223]. It will allow the general public to approach within a few centimeters a live proton beam injected into air, which is visible to the naked eye.

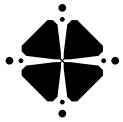

A Self-compensating Thermal Design for the PIXE-RFQ

This appendix presents a conceptual study on a self-compensating thermal design that was carried out for the PIXE-RFQ. During operation, RF power losses heat up the cavity and lead to thermal deformation, resulting in a resonance frequency shift. The shift is induced by changes of the cavity capacitance and inductance (see Section 3.4). Generally this is compensated by changing the cooling water temperature and/or flow rate (e.g. Refs. [42, 224–226]). Self-compensating in this context means that the relative changes in capacitance and inductance are equal in magnitude but of opposite sign. Then, the resulting frequency shift $\partial f/f = -(\partial\mathcal{L}/\mathcal{L} + \partial C/C)/2$ would approximately vanish. Thus, no or only very little compensation by means of the cooling water temperature (or flow rate) would be necessary, and nearly constant cooling system parameters could be maintained.

While in the PIXE-RFQ—representing a stand-alone accelerator—no compensation is required, the RFQ served as an example for the study in view of other possible applications. In the implemented thermal design discussed in Section 3.4.1, the frequency decreases with the duty cycle [Fig. 3.27(b)]. The vanes heat up such that the vane tips move closer together ($\partial C > 0$). Moreover, the tank size increases slightly, such that $\partial\mathcal{L} > 0$, but not enough as to compensate the increased length of the vanes. If one wishes to keep a constant cooling water temperature—ideally at the reference temperature, such that no deformation occurs at zero duty cycle—a positive $\partial\mathcal{L}$ is unavoidable, since the RF power losses are predominantly located at the cavity back wall, increasing the temperature [Fig. 3.26(a)].

Hence, in this case the only way to achieve a self-compensating design is by means of a negative ∂C, meaning that the vane tips need to retract from the beam axis. This can be accomplished by moving the cooling channels from the outer bulk copper into the vanes. Then, the vanes are kept close to the cooling water temperature, increasing their length only marginally. On the contrary, the tank expands considerably ($\partial\mathcal{L} > 0$), because the cooling channels are now no longer located there and the temperature increases compared to the implemented design. The expanding tank pulls the vanes and their tips away from the beam axis, such that $\partial C < 0$ is achieved.

Figure A.1 reports a possible (nearly) self-compensating cooling channel configuration based on the PIXE-RFQ cavity in the bottom row. The top row presents the channel layout implemented in the constructed PIXE-RFQ as a reference. The left plots show temperature distribution in the 2D octant and the deformation is presented by the right plots. Note that the same scalings are used in both cases. Both bulk temperature and deformation in the self-compensated design are intentionally higher, such that $\partial C/C \approx -\partial \mathcal{L}/\mathcal{L}$.

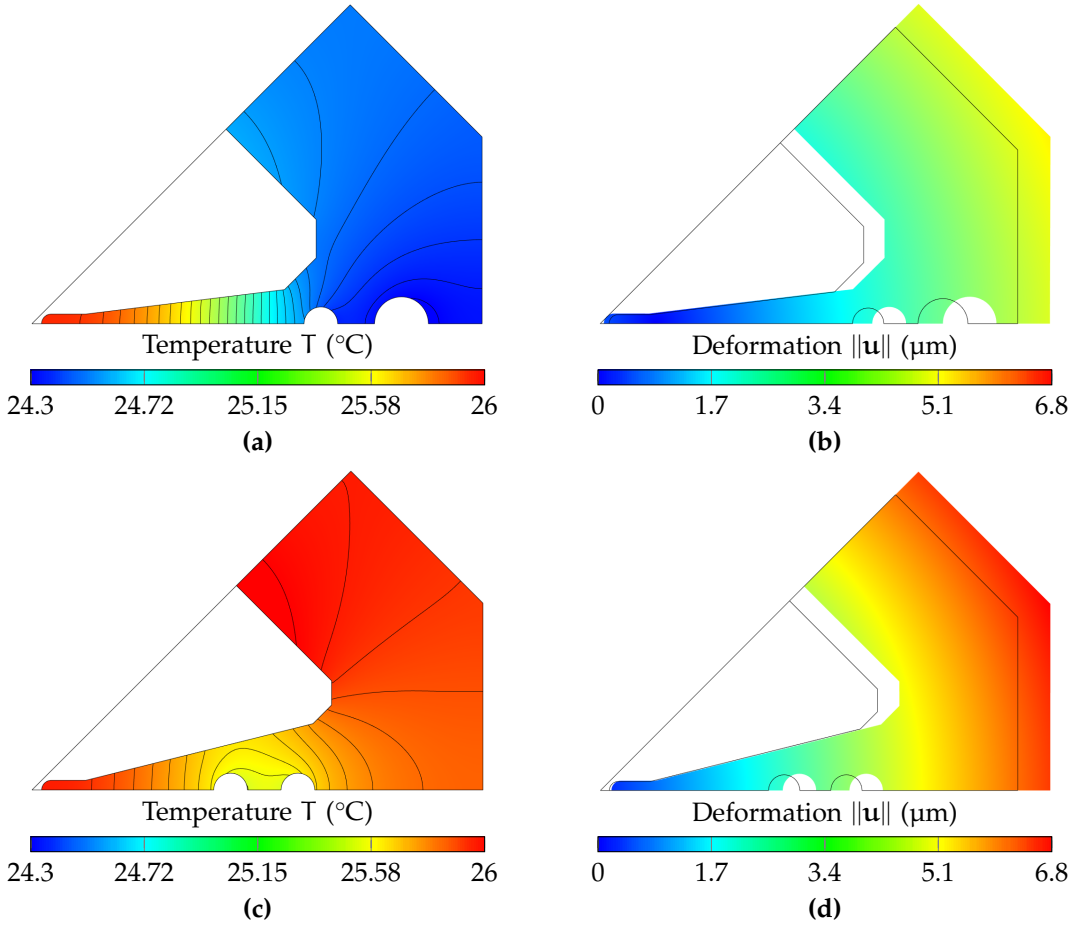

Figure A.1: 2D thermo-mechanical simulation results for the PIXE-RFQ implemented design, serving as reference (upper plots), and a self-compensating cooling channel layout (lower plots). The distributions of temperature T are shown on the left, while the right plots depict the mechanical deformation $\mathbf{u}$. The simulations were carried out with the PIXE-RFQ nominal operation parameters: $d = 2.5\,\%$, $T_w = 22\,°C$, $v_w = 1\,m/s$.

In Fig. A.2, the frequency shift Δf is shown as a function of the duty cycle d for different convection coefficients h between copper and water in the cooling channel. The case $h = 3900\,W/m^2/K$ corresponds to an average water flow speed of $v_w = 1\,m/s$, the configuration used for the PIXE-RFQ. It becomes clear that the self-compensation—and the frequency shift in general—strongly depend on the flow rate. The frequency shift is roughly linear with respect to $1/h$. This fact can

be used for fine-tuning during operation, such that $\Delta f = 0$ independent of duty cycle.

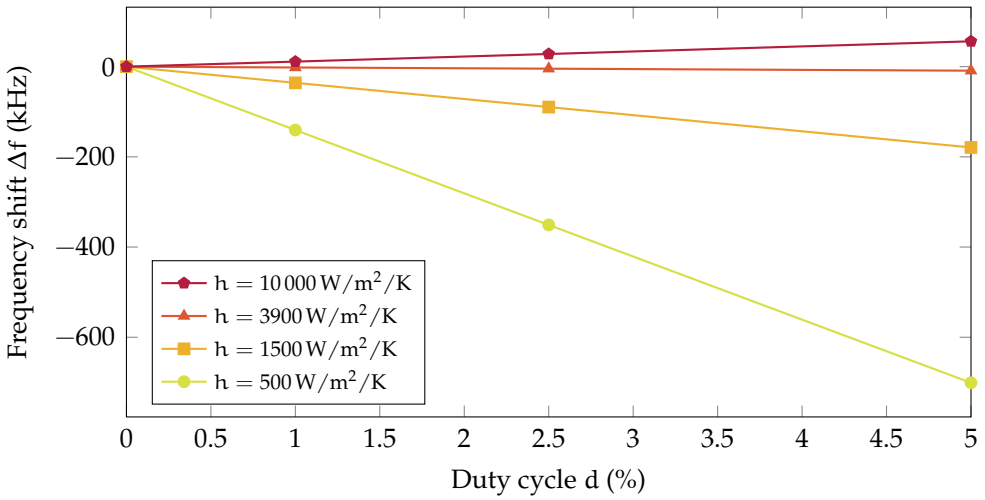

Figure A.2: Frequency shift Δf as a function of the duty cycle d for varying heat transfer coefficients h. With $h = 3900\,W/m^2/K$, the frequency shift nearly vanishes and becomes independent of the duty cycle.

Figure A.3 reports a parametric study that was carried out to estimate the sensitivity of the frequency shift with respect to the placement of the cooling channels: Δf is shown as a function of the distance of the inner cooling channel from the beam axis (where the outer cooling channel is kept at a constant distance to the inner one) for different heat transfer coefficients. The data were computed with 5 % duty cycle. The frequency shift is observed as a linear function of the cooling channel position whose slope does not depend on the heat transfer coefficients h. A larger h allows for placing the cooling channels further outwards for the same self-compensation effect, because the cooling of the vane is more effective and the bulk copper needs to expand less to compensate for the increase in vane length. The plot visualizes that a sub-millimeter precision would be required with respect to the cooling channel positions. However, in view of the high uncertainty with respect to the heat transfer coefficients—which strongly affect the frequency shift—one would need to fine-tune the compensation by means of flow speed adjustments during operation. This would significantly mitigate the drilling precision requirements.

As one can see from Fig. A.1 (compare top row to bottom row), the placement of the cooling channels closer to the beam axis demands a considerable modification of the cavity shape. Because a minimum thickness is required between water and vacuum domains, the so-called vane slope angle [α_c in Fig. 3.3(b)] had to be doubled from 7° to 14°. Moreover, a straight back wall to incorporate the auxiliary ports is kept. This results in an almost triangular quadrant cross section that is disadvantageous with respect to the quality factor, which decreased from $Q_{2D} = 7280$ to 6980 (nearly 5 % increased RF power consumption).

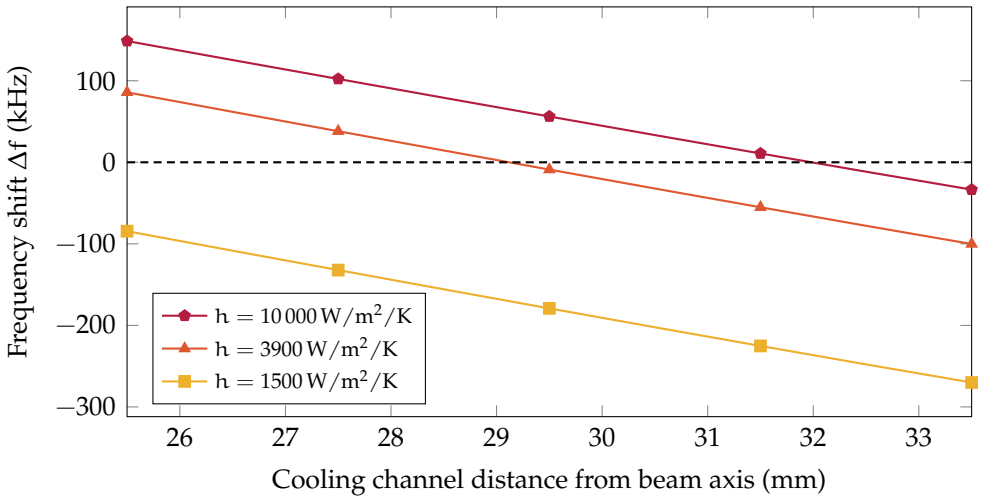

Figure A.3: Frequency shift Δf as a function of cooling channel distance from beam axis for varying heat transfer coefficients h. The data points were computed with 5 % duty cycle.

A possibility for improvement is given by decreasing the diameter of the auxiliary ports—and thus of tuners, vacuum pumping ports, and power couplers—from 36 mm to 30 mm, which corresponds to a smaller vacuum flange standard. The proposed cavity shape and its thermo-mechanical behavior are reported in Fig. A.4. Virtually no difference to the previously discussed design is observed, whereas the quality factor is restored to the value of the PIXE-RFQ reference design. Major drawbacks of a smaller flange diameter, however, are reduced tuning and pumping capability as well as a decreased effectiveness of the power coupler. One would need to ensure that for all auxiliaries feasible solutions are found before realizing this design.

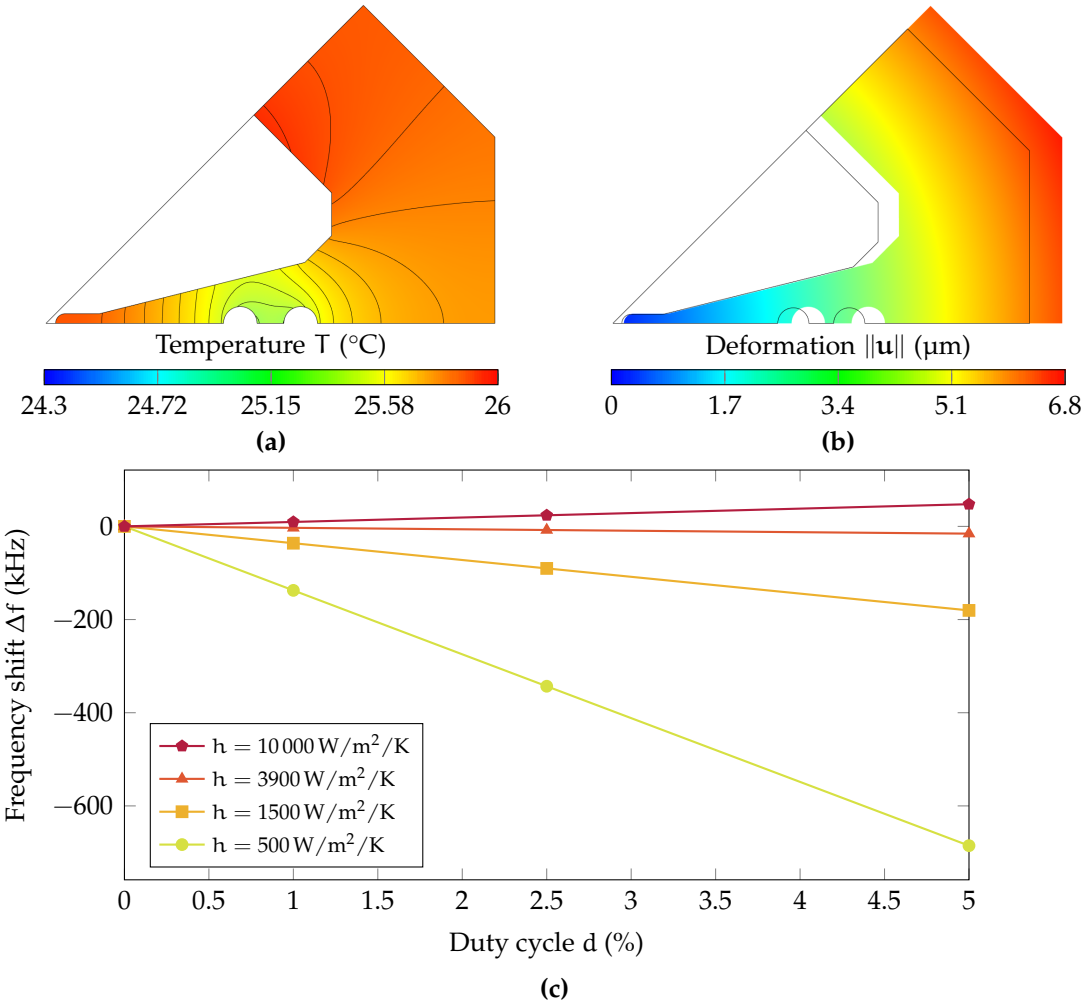

Figure A.4: 2D thermo-mechanical simulation results for the self-compensating design with a smaller auxiliary flange diameter of 30 mm. The distributions of temperature T and deformation $\mathbf{u}$ are shown in (a) and (b), respectively. These simulations were carried out with the PIXE-RFQ nominal operation parameters: $d = 2.5\,\%$, $T_w = 22\,°C$, $v_w = 1\,m/s$. The frequency shift Δf is plotted in (c) as a function of duty cycle for varying heat transfer coefficients.

B Formulae Related to the Multipole Potential Function

The multipole potential function introduced by Kapchinsky and Teplyakov [11] to describe the RFQ electric fields reads (in the notation of Section 2.3.1):

$$\frac{\Phi(r,\vartheta,z)}{V_0/2} = \sum_{\nu=0}^{\infty} A_{0,\nu} \left(\frac{r}{r_0}\right)^{2\nu} \cos(2\nu\vartheta) + \sum_{\mu=1}^{\infty}\sum_{\nu=0}^{\infty} A_{\mu,\nu} \mathcal{I}_{2\nu}(\mu k r) \cos(2\nu\vartheta)\cos(\mu k z). \tag{2.42}$$

This Appendix lists the corresponding electric field components (Section B.1) and describes how the expansion coefficients can be extracted from a given potential field (Section B.2).

B.1 Electric Field Components

In the cylindrical coordinate system, the electric field is given as the negative gradient of the potential:

$$\mathbf{E}(r,\vartheta,z) = -\boldsymbol{\nabla}\Phi(r,\vartheta,z) = -\left[\frac{\partial}{\partial r}\Phi\ ,\ \frac{1}{r}\frac{\partial}{\partial\vartheta}\Phi\ ,\ \frac{\partial}{\partial z}\Phi\right]^{\mathrm{T}}. \tag{B.1}$$

The radial, azimuthal, and longitudinal field components amount to

$$\begin{aligned}\frac{E_r(r,\vartheta,z)}{V_0/2} =& -\sum_{\nu=0}^{\infty} A_{0,\nu}\frac{2\nu}{r}\left(\frac{r}{r_0}\right)^{2\nu}\cos(2\nu\vartheta) \\ & -\sum_{\mu=1}^{\infty}\sum_{\nu=0}^{\infty} A_{\mu,\nu}\left[\frac{2\nu}{r}\mathcal{I}_{2\nu}(\mu k r) + \mu k \mathcal{I}_{2\nu+1}(\mu k r)\right]\cos(2\nu\vartheta)\cos(\mu k z),\end{aligned} \tag{B.2}$$

$$\frac{E_\vartheta(r,\vartheta,z)}{V_0/2} = \sum_{\nu=0}^{\infty} A_{0,\nu}\frac{2\nu}{r}\left(\frac{r}{r_0}\right)^{2\nu}\sin(2\nu\vartheta) + \sum_{\mu=1}^{\infty}\sum_{\nu=0}^{\infty} A_{\mu,\nu}\frac{2\nu}{r}\mathcal{I}_{2\nu}(\mu k r)\sin(2\nu\vartheta)\cos(\mu k z), \tag{B.3}$$

and

$$\frac{E_z(r,\vartheta,z)}{V_0/2} = \sum_{\mu=1}^{\infty}\sum_{\nu=0}^{\infty} A_{\mu,\nu}\mu k\mathcal{I}_{2\nu}(\mu k r)\cos(2\nu\vartheta)\sin(\mu k z). \tag{B.4}$$

Note that E_r and E_ϑ are undefined on the beam axis at $r = 0$, but approach zero in the limit.

While the longitudinal component E_z is shared by the Cartesian and cylindrical coordinate systems, E_x and E_y are obtained from the radial and azimuthal components as

$$\begin{aligned} E_x &= E_r\cos\vartheta - E_\vartheta\sin\vartheta, \\ E_y &= E_r\sin\vartheta + E_\vartheta\cos\vartheta, \end{aligned} \tag{B.5}$$

where the Cartesian and cylindrical coordinates are connected by $r^2 = x^2 + y^2$ and $\tan\vartheta = y/x$. Equations (B.5) are predominantly used to generate a Cartesian electric field map, as it is required by the particle tracking programs used throughout this thesis, from the potential function [Eq. (2.42)].

B.2 Extraction of Multipole Coefficients from Given Potential Field

The lookup table of the sixteen-term potential function (Section 5.2.2) was generated by simulating the electrostatic field of many different cell geometries. This section derives the formula used to extract the multipole coefficients $A_{\mu,\nu}$ from the given potential field Φ.

Since the potential function [Eq. (2.42)] represents a multipole expansion with respect to the azimuthal and longitudinal, but not radial direction, it can be written in the form

$$\Phi(r,\vartheta,z) = \sum_{\mu=0}^{\infty}\sum_{\nu=0}^{\infty} A_{\mu,\nu}R_{\mu,\nu}(r)F_{\mu,\nu}(\vartheta,z), \tag{B.6}$$

where

$$F_{\mu,\nu}(\vartheta,z) = \cos(2\nu\vartheta)\cos(\mu k z) \tag{B.7}$$

are the mutually orthogonal basis functions and

$$R_{\mu,\nu}(r) = \frac{V_0}{2} \begin{cases} (r/r_0)^{2\nu} & \text{if } \mu = 0, \nu \geqslant 1, \\ \mathcal{J}_{2\nu}(\mu k r) & \text{if } \mu \geqslant 1, \nu \geqslant 0, \end{cases} \tag{B.8}$$

is a radially dependent scaling factor. For the extraction of a particular $A_{\mu,\nu}$, the computed potential is multiplied by the basis function of interest $F_{\tilde{\mu},\tilde{\nu}}(\vartheta, z)$, and integrated over the lateral area $\mathcal{S}$ of a coaxial cylinder. The integration surface is sketched in Fig. B.1. The radius $\tilde{r}$ of the cylinder should be slightly smaller than the minimum aperture a—large enough to provide sufficient accuracy on the given FEM mesh, and small enough such that the result is not compromised by possible mesh artifacts close to the boundary given by the electrode surface. The cylinder length is identical to the cell length L. For convenience, the double integral is treated as two separate integrals aligned with the longitudinal and azimuthal coordinate axes, respectively, i.e. $d\mathcal{S} = \tilde{r} d\vartheta dz$:

$$\begin{aligned} &\iint_{\mathcal{S}} \Phi(r = \tilde{r}, \vartheta, z) F_{\tilde{\mu},\tilde{\nu}}(\vartheta, z) d\mathcal{S} \\ &\qquad = \sum_{\mu=0}^{\infty} \sum_{\nu=0}^{\infty} A_{\mu,\nu} \tilde{r} R_{\mu,\nu}(\tilde{r}) \int_0^L \int_0^{2\pi} F_{\mu,\nu}(\vartheta, z) F_{\tilde{\mu},\tilde{\nu}}(\vartheta, z) d\vartheta dz \end{aligned} \tag{B.9}$$

where sum and integrals may be exchanged. The area integral on the right hand side can be separated into a product of two integrals:

$$\begin{aligned} &\int_0^L \int_0^{2\pi} F_{\mu,\nu}(\vartheta, z) F_{\tilde{\mu},\tilde{\nu}}(\vartheta, z) d\vartheta dz \\ &\qquad = \underbrace{\int_0^L \cos(\mu k z) \cos(\tilde{\mu} k z) dz}_{\substack{L \text{ for } \mu = \tilde{\mu} = 0, \\ (L/2)\delta_{\mu,\tilde{\mu}} \text{ otherwise}}} \cdot \underbrace{\int_0^{2\pi} \cos(2\nu\vartheta) \cos(2\tilde{\nu}\vartheta) d\vartheta}_{\substack{2\pi \text{ for } \nu = \tilde{\nu} = 0, \\ \pi\delta_{\nu,\tilde{\nu}} \text{ otherwise}}}, \end{aligned} \tag{B.10}$$

where $\delta_{i,j}$ denotes the Kronecker delta. Because of the mutual orthogonality of the basis functions, the only nonzero summand is $\mu = \tilde{\mu}, \nu = \tilde{\nu}$, and Eq. (B.9) can be rearranged to obtain the corresponding multipole coefficient:

$$A_{\mu,\nu} = \frac{2}{\pi V_0 L \tilde{r}} \iint_{\mathcal{S}} \Phi(r = \tilde{r}, \vartheta, z) F_{\mu,\nu}(\vartheta, z) d\mathcal{S} \cdot \begin{cases} (r_0/\tilde{r})^{2\nu} & \text{for } \mu = 0, \nu \geqslant 1 \\ 1/\mathcal{J}_{2\nu}(\mu k \tilde{r}) & \text{for } \mu \geqslant 1, \nu = 0 \\ 2/\mathcal{J}_{2\nu}(\mu k \tilde{r}) & \text{for } \mu \geqslant 1, \nu \geqslant 1 \end{cases} \tag{B.11}$$

The three cases in Eq. (B.11) account for longitudinally independent, azimuthally independent, and full 3D field-patterns, respectively.

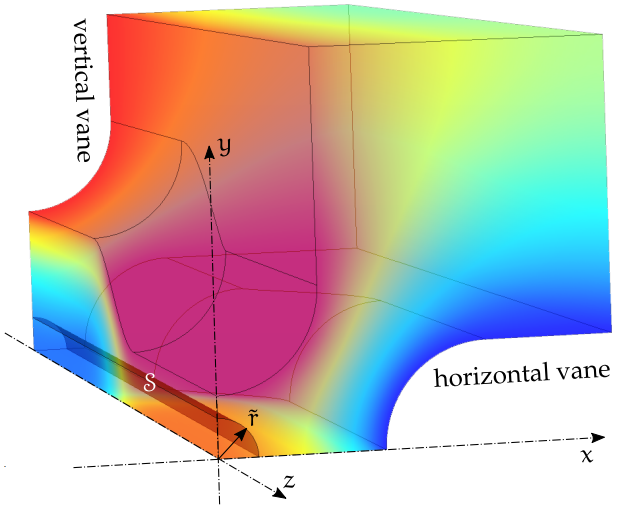

Figure B.1: Trapezoidal RFQ cell with cylindrical surface $\mathcal{S}$ with radius $\tilde{r}$ over which the potential is integrated to extract the multipole coefficients. In practice only one quarter is computed since the RFQ cell features two symmetry planes.

In the case of an RF eigenmode simulation, the potential Φ is undefined, as it can only be defined for curl-free electric fields. Instead, the electric field $\mathbf{E}$ is obtained directly as a computation result. To compute the $A_{\mu,\nu}$, two possibilities emerge:

1. Compute the electric potential from the electric field as

$$\Phi(r,\vartheta,z) \approx \int_0^z E_z(0,0,z')dz' + \int_0^r E_r(r',\vartheta,z)dr', \tag{B.12}$$

   i.e. by integrating along the beam axis and then to the location (r,ϑ,z) of interest. Since the electric field between the RFQ electrodes can in fact be considered as curl-free [$\mathbf{E} = -\nabla\Phi\cos(\omega t)$], the integration path may be chosen arbitrarily and aligned with the coordinate axes for convenience.

2. Derive an expression similar to Eq. (B.11) from Eqs. (B.2)–(B.4) to compute the coefficients directly from the electric field components E_r, E_ϑ, or E_z. One may even use all available components to compute a specific coefficient to reduce the influence of the discretization error. The multipole coefficients of the PIXE-RFQ shown in Fig. 3.33 were in fact computed from the HFSS field using this method.

C Numerical Convergence Studies

Appendix C reports a selection of the convergence studies performed on the simulation models used throughout this thesis.

A considerable portion of the problems discussed were solved by means of numerical simulation, most notably FEM (see e.g. Ref. [85]), because closed analytic solutions do not exist for all but the simplest of geometries. Generally, the computational domain, be it space or time, is discretized by a finite number of mesh cells with associated ansatz functions. The continuous analytic problem is thereby converted into an algebraic one with a finite number of degrees of freedom, that can be solved on a computer.

The discretization introduces a so-called discretization error that depends on number, shape, size, and distribution of mesh cells. The discretization error should always be roughly one order of magnitude smaller than the manufacturing accuracy. The accuracy of numerical simulations is commonly assessed by means of convergence studies, because the exact solution values are not available as a reference. From the first solution, an error indicator is derived for determining which mesh cells contribute the most to the overall solution error. The mesh is then refined in these locations—a procedure known as adaptive mesh refinement—and a new solution is computed in a second pass. The procedure is repeated until the solution does no longer depend on the particular mesh—up to a desired accuracy. This means that the relative error δ_{pass} in the computed quantity, e.g. the frequency, must not exceed the desired error from one pass to the next. One defines

$$\delta_{\text{pass}} = \left| \frac{\text{solution value of current pass}}{\text{solution value of previous pass}} - 1 \right| \tag{C.1}$$

as the relative error, that can be plotted against the number of mesh cells from the second pass onwards.[55] The quantity δ_{pass} is used by many numerical tools as stopping criterion for the refinement [89–94]. It should decrease with increasing number of passes and mesh cells, indicating that the solution converges. Typical

[55] Alternatively, one may solve the problem on a very fine mesh to obtain a reference solution. Then, the convergence behavior can be studied in terms of the error with respect to this reference solution. However, for very complex geometries requiring large numbers of mesh cells even for the first pass, such as the full model of the RFQ (Fig. C.6), this is not feasible on commonly available hardware because of the immense memory requirements.

convergence criteria are $\delta_{\text{pass}} < 10^{-3} \cdots 10^{-5}$. In practice, δ_{pass} often does not decrease monotonically with a constant order of convergence (the slope of the curve in a logarithmic plot), and sometimes even shows oscillating behavior. This can be related to the matrix condition corresponding to a very inhomogeneous mesh and imperfect geometric approximation even with curved mesh elements, especially of 3D curved surfaces.

In the following, some of the convergence studies performed on the simulation models used to design the two RFQs are presented. Section C.1 shows RF eigenmode simulations, Section C.2 reports on the multipoles and surface electric field in a trapezoidal cell, and Section C.3 presents the convergence behavior of particle tracking results as functions of the time step.

Most computations were performed on a workstation computer with an Intel® Xeon®E5-1620 v2 processor with eight virtual cores at 3.7 GHz and 16 GB memory. Larger models with their immense numbers of mesh cells, such as the full 3D eigenmode simulation shown in Fig. C.6, were simulated on a considerably more powerful computer with two Intel® Xeon®E5-2650 v4 processors with a total of 48 virtual cores at 2.2 GHz and 500 GB memory.

C.1 RF Eigenmode Computations

Figures C.1–C.6 show RF eigenmode simulations carried out with CST Microwave Studio® [91] or Ansys HFSS® [89, 90]. Such simulations were performed for the RF designs of PIXE-RFQ (Chapter 3) and Carbon-RFQ (Section 5.5).

The majority of the geometries required manual adjustments of the mesh by enforcing certain properties in (parts of) the computational domain and on its surfaces. Most notably, the mesh cell length between the vane tips was set to a fraction of the minimum aperture. A coincidence of 1 µm—a factor of five smaller than the machining accuracy [31]—was enforced between the mesh cells and the actual vane tip geometry. More detailed mesh refinement studies lie beyond the scope of this thesis.

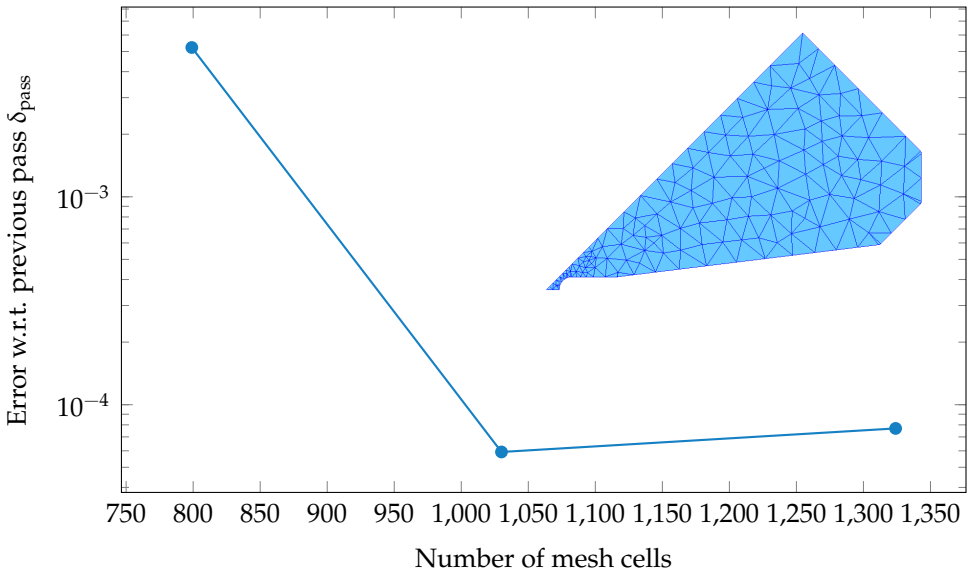

Figure C.1: Convergence study of an eigenmode simulation of the 2D RFQ cross section (shown in octant-symmetry), carried out with Ansys HFSS®. The relative change δ_{pass} of the resonant frequency from the previous to the current pass is shown as a function of the number of tetrahedral mesh cells in the current pass. The mesh of the last pass is depicted.

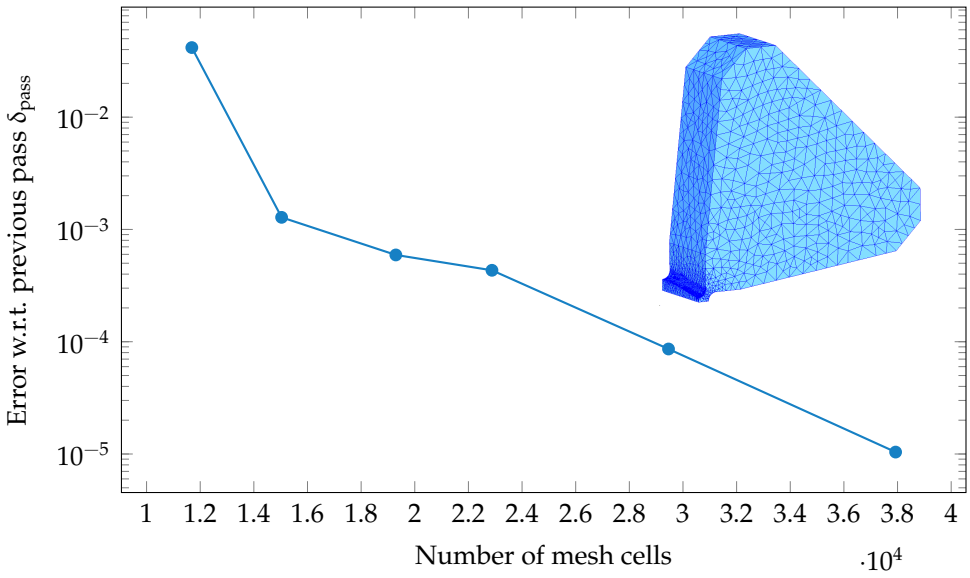

Figure C.2: Convergence study of an eigenmode simulation of an RFQ cell with modulated vanes (shown in quarter-symmetry), carried out with Ansys HFSS®. The relative change δ_{pass} of the resonant frequency from the previous to the current pass is shown as a function of the number of tetrahedral mesh cells in the current pass. The mesh of the last pass is depicted.

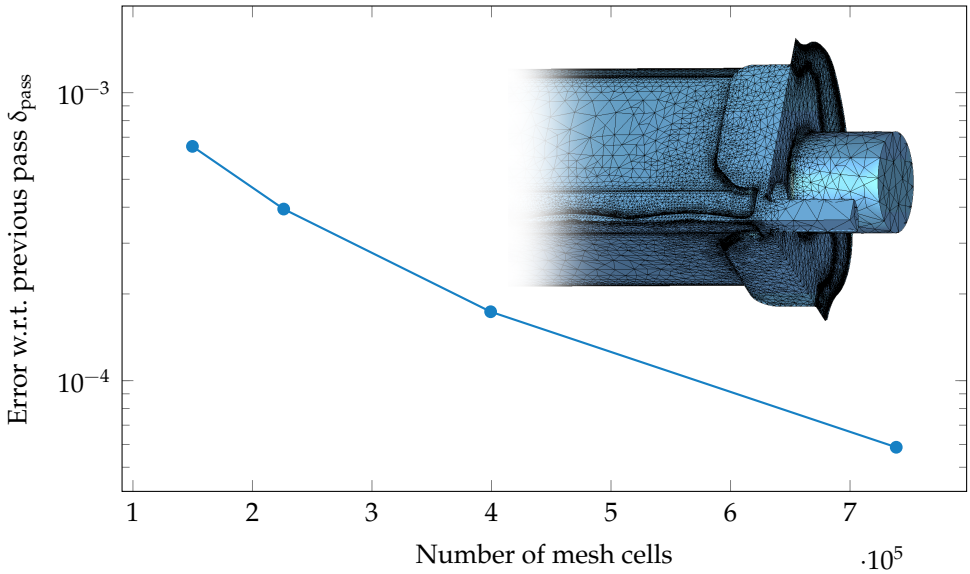

Figure C.3: Convergence study of an eigenmode simulation of the PIXE-RFQ downstream end (shown in quarter-symmetry), carried out with CST Microwave Studio®. The relative change δ_{pass} of the resonant frequency from the previous to the current pass is shown as a function of the number of tetrahedral mesh cells in the current pass. The mesh of the last pass is depicted.

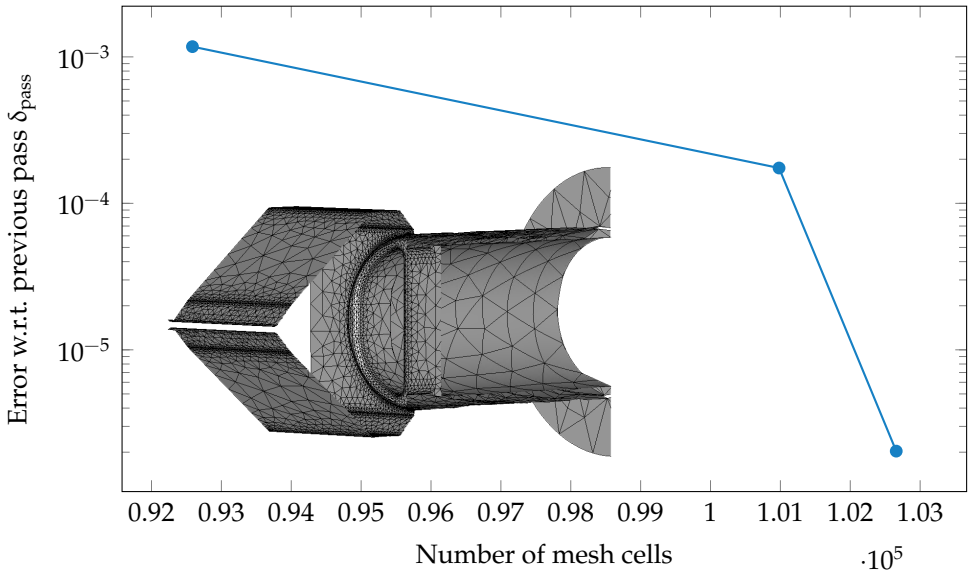

Figure C.4: Convergence study of an eigenmode simulation of a vacuum pumping port (shown in half-symmetry), carried out with CST Microwave Studio®. The relative change δ_{pass} of the resonant frequency from the previous to the current pass is shown as a function of the number of tetrahedral mesh cells in the current pass. The mesh of the last pass is depicted.

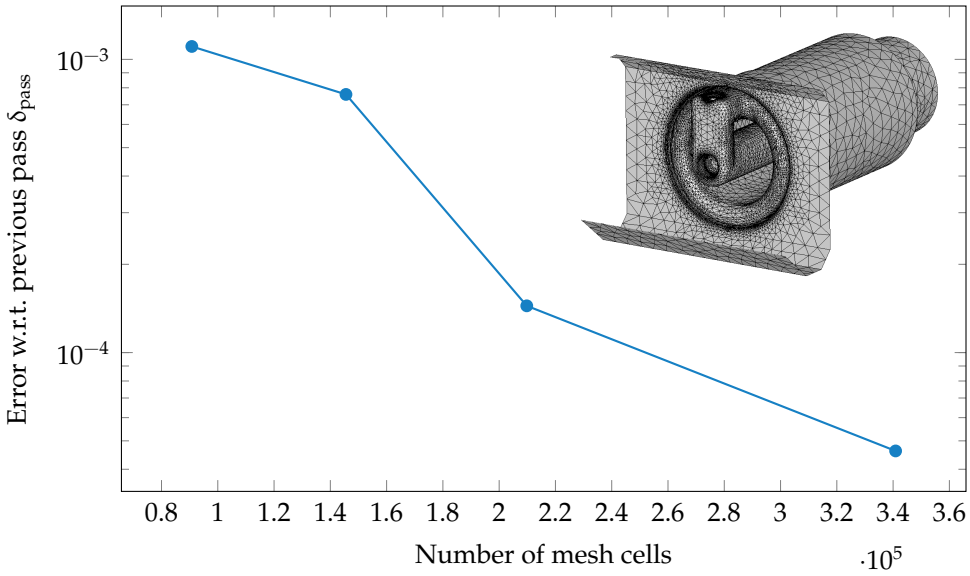

Figure C.5: Convergence study of an eigenmode simulation of an RFQ input power coupler, carried out with CST Microwave Studio®. The relative change δ_{pass} of the resonant frequency from the previous to the current pass is shown as a function of the number of tetrahedral mesh cells in the current pass. The mesh of the last pass is depicted.

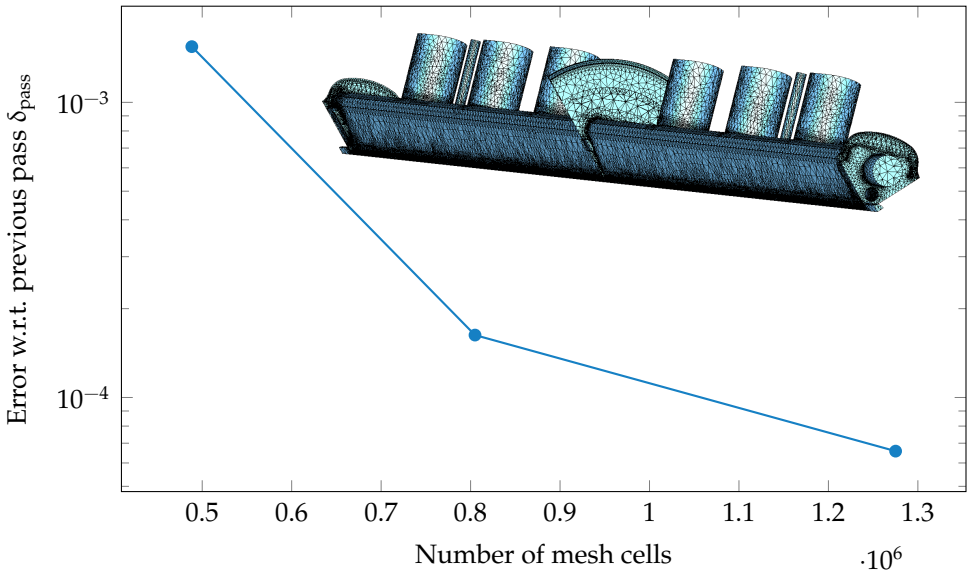

Figure C.6: Convergence study of an eigenmode simulation of the full 3D cavity of the PIXE-RFQ (shown in quarter-symmetry), carried out with Ansys HFSS®. The relative change δ_{pass} of the resonant frequency from the previous to the current pass is shown as a function of the number of tetrahedral mesh cells in the current pass. The mesh of the last pass is depicted.

C.2 Surface Electric Field and Multipoles in a Trapezoidal Cell

Figures C.7 and C.8 show the convergence behavior of the most important multipole coefficients and the maximum surface electric field $E_{s,max}$, respectively, in an electrostatic model of a trapezoidal RFQ cell simulated in COMSOL Multiphysics® [93]. Such models where used to compute the lookup tables of the sixteen-term potential function used in Section 5.2.

The accuracy achieved for $E_{s,max}$ strongly depends on the order of the FEM ansatz functions: in Fig. C.8, results obtained with linear, quadratic, and cubic continuous Lagrange elements [85, 93] are reported, where the latter show the best convergence behavior. Figure C.8(b) highlights that the lower-order models not only converge slower, but also against slightly different values that differ from the cubic ansatz by nearly 4 %. The maximum electric field is shown as the field enhancement κ in units of V_0/r_0 [Eq. (5.2)].

The computation of $E_{s,max}$ is—quite generally—intricate because it represents a local field quantity that is susceptible to local mesh artifacts. In contrast, the multipole coefficients are integral quantities for which local errors hardly play a role because of the implicit field averaging. In electrostatic FEM, the Poisson or Laplace equation [see Eq. (2.19)] is solved for the potential, from which the electric field emerges as the negative gradient. Thus, if the potential is approximated by a cubic ansatz, the electric field is still described in terms of quadratic functions. With respect to $E_{s,max}$ more accurate results could be obtained by means of the boundary element method, which solves for the surface charge density and thus the surface electric field directly [85].

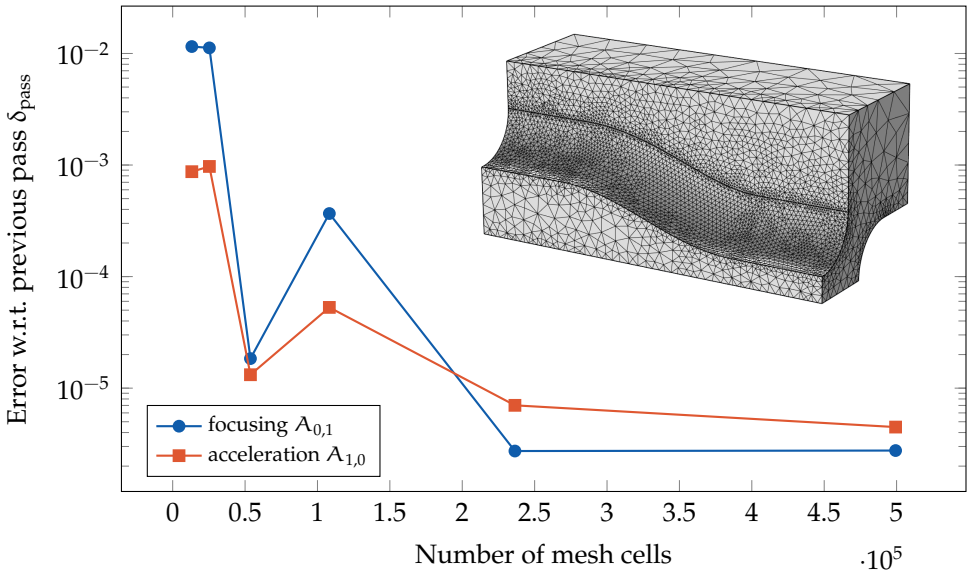

Figure C.7: Convergence study of an electrostatic simulation of a trapezoidal cell (shown in quarter-symmetry), carried out with COMSOL Multiphysics®. The relative change δ_{pass} of the multipole coefficients $A_{0,1}$ and $A_{1,0}$ from the previous to the current pass is shown as a function of the number of tetrahedral mesh cells in the current pass. The mesh of the last pass is depicted.

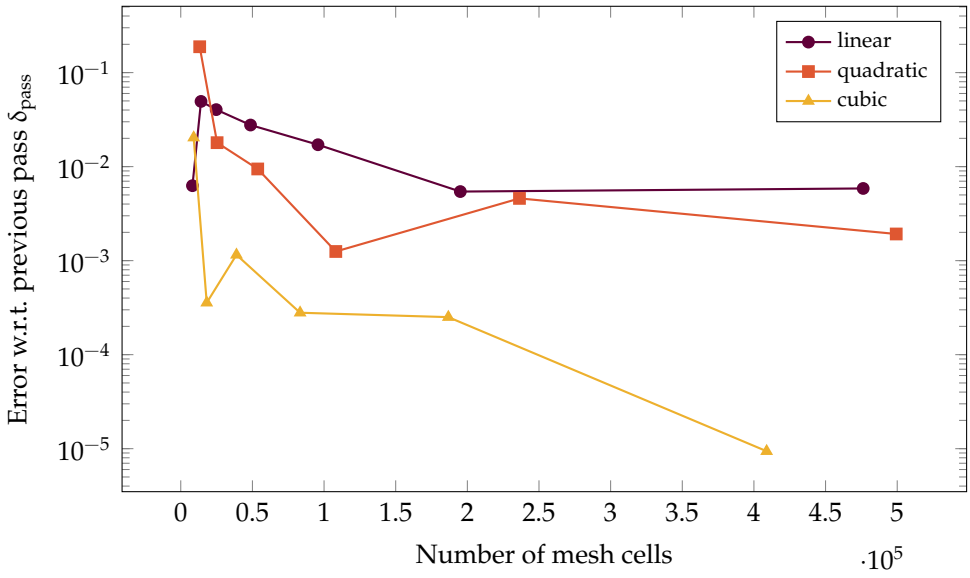

(a) Relative errors

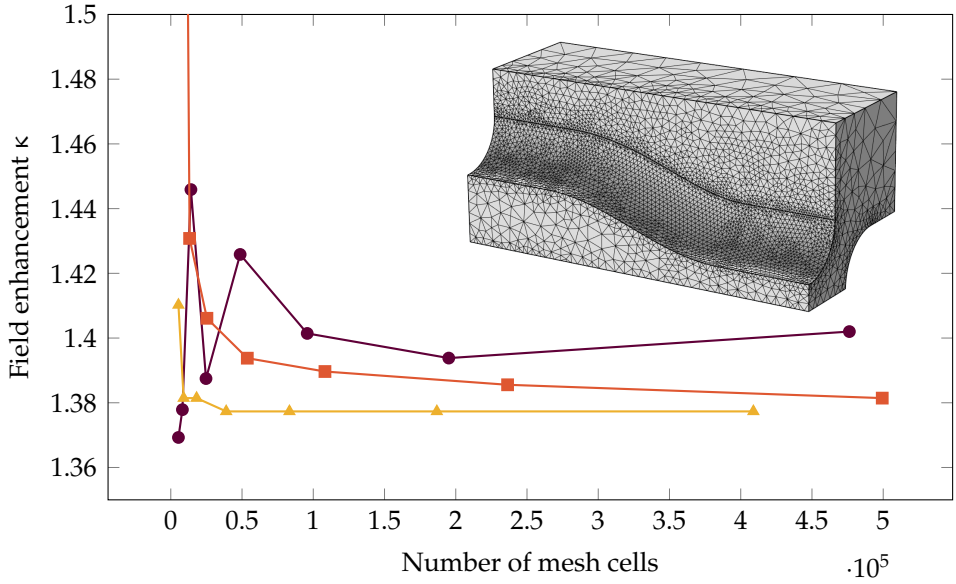

(b) Absolute values

Figure C.8: Convergence study of an electrostatic simulation of a trapezoidal cell (shown in quarter-symmetry), carried out with COMSOL Multiphysics®. The relative change δ_{pass} of the maximum surface electric field $E_{s,max}$ from the previous to the current pass is depicted in (a). The absolute value of $E_{s,max}$, shown in terms of the field enhancement κ [Eq. (5.2)], is reported in (b). All quantities are shown as functions of the number of tetrahedral mesh cells in the current pass, as well as for linear, quadratic, and cubic FEM ansatz functions. The mesh of the last pass is depicted.

C.3 Particle Tracking

Most of the particle tracking simulations reported throughout the present thesis were carried out using the leapfrog algorithm (see e.g. Ref. [95]) of the particle tracking tool RF-Track [99]. The stability and convergence of this explicit time-stepping iteration strongly depend on the step sizes in space (of the electric field map) and time.

Here, only the time-dependence is plotted, although other dependencies were investigated. Notably, an increase of spatial resolution of the tracking field map from 100 µm to 70 µm step size changes the output longitudinal emittance by 20 %, whereas transmission and beam sizes are virtually unaffected. Differences between tracking simulations conducted with 10^4 and 10^5 macroparticles are of the order of 1 %. More detailed convergence studies lie beyond the scope of this thesis, as the achieved results were acceptable for the RFQ designs.

Figure C.9 depicts the error of various output phase space parameters as functions of the step size in time. The time step is given as the number of leapfrog steps per RFQ cell. Doubling this value delivers the number of steps per RF period (assuming synchronous acceleration), which is reciprocal to the time step. Acceptable accuracies are achieved with 30 to 40 steps per RFQ cell.

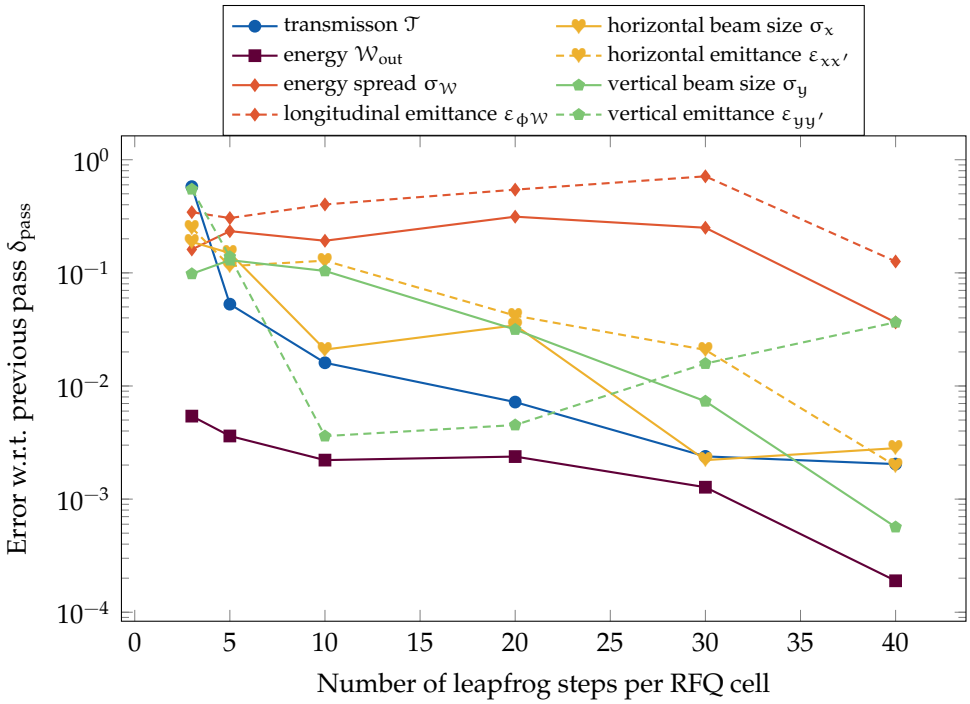

Figure C.9: Convergence study of the time step size of a particle tracking simulation carried out with RF-Track using the leapfrog algorithm. Various output phase space parameters are depicted. For all quantities, the relative change δ_{pass} from the previous to the current pass is shown as a function of the number of steps per RFQ cells in the current pass.

References

[1] T. P. Wangler. *RF Linear Accelerators*. 2nd ed. John Wiley & Sons, 2008. ISBN: 9783527406807. DOI: 10.1002/9783527623426.

[2] G. Ising. "Prinzip einer Methode zur Herstellung von Kanalstrahlen hoher Voltzahl". In: *Ark. Mat. Astr. Fys.* 18 (1924), 1–4.

[3] R. Widerøe. "Über ein neues Prinzip zur Herstellung hoher Spannungen". In: *Arbeiten aus dem Elektrotechnischen Institut der Technischen Hochschule Aachen*. Springer, 1929, pp. 157–176.

[4] R. J. Van de Graaff, K. T. Compton, and L. C. Van Atta. "The Electrostatic Production of High Voltage for Nuclear Investigations". In: *Physical Review* 43.3 (1933), pp. 149–157. DOI: 10.1103/physrev.43.149.

[5] J. D. Cockcroft and E. T. S. Walton. "Experiments with high velocity positive ions". In: *Proceedings of the Royal Society of London. Series A, Containing Papers of a Mathematical and Physical Character* 129.811 (1930), pp. 477–489. DOI: 10.1098/rspa.1930.0169.

[6] D. H. Sloan and E. O. Lawrence. "The Production of Heavy High Speed Ions without the Use of High Voltages". In: *Physical Review* 38.11 (1931), pp. 2021–2032. DOI: 10.1103/physrev.38.2021.

[7] L. W. Alvarez. "The design of a proton linear accelerator". In: *Physical Review* 70.9–10 (1946), pp. 799–800.

[8] L. W. Alvarez et al. "Berkeley proton linear accelerator". In: *Review of Scientific Instruments* 26.2 (1955), pp. 111–113.

[9] H. Padamsee, J. Knobloch, and T. Hays. *RF Superconductivity: Science, Technology and Applications*. Wiley-VCH, 2008. ISBN: 9783527408429. DOI: 10.1002/9783527627172.

[10] H. Wiedemann. *Particle Accelerator Physics*. Graduate Texts in Physics. Springer International Publishing, 2015. ISBN: 9783319183176. DOI: 10.1007/978-3-540-49045-6.

[11] I. M. Kapchinsky and V. A. Teplyakov. "A linear ion accelerator with spatially uniform hard focusing". In: *Prib. Tekh. Eksp. USSR* 4 (1970), pp. 19–22.

[12] I. M. Kapchinsky and V. A. Teplyakov. “Possibility of reducing the injection energy and increasing the limit current in an ion linear accelerator”. In: *Prib. Tekh. Eksp. USSR* 2 (1970), pp. 17–19.

[13] R. H. Stokes and T. P. Wangler. “Radiofrequency quadrupole accelerators and their applications”. In: *Annual Review of Nuclear and Particle Science* 38.1 (1988), pp. 97–118.

[14] European Organization for Nuclear Research (CERN). *The Large Hadron Collider*. URL: https://home.cern/science/accelerators/large-hadron-collider (visited on 07/22/2020).

[15] G. A. Loew. “The SLAC linear collider and a few ideas on future linear colliders”. In: *1984 Linear Accelerator Conference (LINAC1984), Seeheim, Germany*. Gesellschaft für Schwerionenforschung m.b.H., Darmstadt, Germany, 1984, pp. 282–287.

[16] European X-Ray Free-Electron Laser Facility GmbH. *European X-FEL Facts and Figures*. URL: https://www.xfel.eu/facility/overview/facts_amp_figures/index_eng.html (visited on 07/21/2020).

[17] W. Scharf. *Particle Accelerators and Their Uses*. Harwood Academic, New York, 1985.

[18] M. Vretenar et al. “A compact high-frequency RFQ for medical applications”. In: *27th Linear Accelerator Conference (LINAC2014), Geneva, Switzerland*. JACoW, Geneva, Switzerland, 2014, pp. 935–938.

[19] S. A. E. Johansson, J. L. Campbell, K. G. Malmqvist, J. D. Winefordner, et al. *Particle-induced X-ray Emission Spectrometry (PIXE)*. Vol. 133. John Wiley & Sons, 1995.

[20] K. Ishii. “PIXE and its applications to elemental analysis”. In: *Quantum Beam Science* 3.2 (2019), p. 12. DOI: 10.3390/qubs3020012.

[21] K. Sera et al. “Bio-PIXE at the Takizawa facility (Bio-PIXE with a baby cyclotron)”. In: *International Journal of PIXE* 2.3 (1992), pp. 325–330. DOI: 10.1142/s0129083592000348.

[22] M. J. Flores, F. Aldape, R. V. Díaz, and D. Crumpton. “Set-up and improvements of the PIXE facility at ININ, Mexico”. In: *Nuclear Instruments and Methods in Physics Research Section B: Beam Interactions with Materials and Atoms* 75.1-4 (1993), pp. 116–119. DOI: 10.1016/0168-583x(93)95624-e.

[23] S. Iwasaki et al. “Facility of PIXE analysis at Tohoku University”. In: *International Journal of PIXE* 06.01n02 (1996), pp. 117–125. DOI: 10.1142/s0129083596000120.

[24] P. A. Mandò, M. E. Fedi, N. Grassi, and A. Migliori. "Differential PIXE for investigating the layer structure of paintings". In: *Nuclear Instruments and Methods in Physics Research Section B: Beam Interactions with Materials and Atoms* 239.1-2 (Sept. 2005), pp. 71–76. DOI: 10.1016/j.nimb.2005.06.181.

[25] S. Limandri, C. Olivares, L. Rodriguez, G. Bernardi, and S. Suárez. "PIXE facility at Centro Atómico Bariloche". In: *Nuclear Instruments and Methods in Physics Research Section B: Beam Interactions with Materials and Atoms* 318 (Jan. 2014), pp. 47–50. DOI: 10.1016/j.nimb.2013.06.058.

[26] M. Vadrucci et al. "A new small-footprint external-beam PIXE facility for cultural heritage applications using pulsed proton beams". In: *Nuclear Instruments and Methods in Physics Research Section B: Beam Interactions with Materials and Atoms* 406 (Sept. 2017), pp. 314–317. DOI: 10.1016/j.nimb.2017.02.045.

[27] M. Vretenar et al. "High-frequency compact RFQs for medical and industrial applications". In: *28th Linear Accelerator Conference (LINAC2016), East Lansing, MI, USA*. JACoW, Geneva, Switzerland, 2016, pp. 704–709. DOI: 10.18429/JACoW-LINAC2016-TH1A06.

[28] A. Lombardi, M. Vretenar, S. Mathot, and A. Grudiev. "High frequency compact low-energy linear accelerator design". US Patent 10,051,721. Current assignee: CERN (European Organization for Nuclear Research). 2018.

[29] H. W. Pommerenke et al. "RF design of a high-frequency RFQ linac for PIXE analysis". In: *29th Linear Accelerator Conference (LINAC2018), Beijing, China*. JACoW, Geneva, Switzerland, 2018, pp. 822–825. DOI: 10.18429/JACoW-LINAC2018-THPO058.

[30] H. W. Pommerenke et al. "rf design studies on the 750 MHz radio frequency quadrupole linac for proton-induced x-ray emission analysis". In: *Physical Review Accelerators and Beams* 22.5 (2019). DOI: 10.1103/physrevaccelbeams.22.052003.

[31] S. Mathot et al. "The CERN PIXE-RFQ, a transportable proton accelerator for the machina project". In: *Nuclear Instruments and Methods in Physics Research Section B: Beam Interactions with Materials and Atoms* 459 (2019), pp. 153–157. ISSN: 0168-583X. DOI: 10.1016/j.nimb.2019.08.025.

[32] L. Giuntini et al. "MACHINA: movable accelerator for cultural heritage in-situ non-destructive analysis". In: *16th International Conference on Nuclear Microprobe Technology and Applications (ICNMTA2018), Guilford, Surrey, England*. 2018.

[33] K. L. Brown and G. W. Tautfest. "Faraday-Cup Monitors for High-Energy Electron Beams". In: *Review of Scientific Instruments* 27.9 (1956), pp. 696–702. DOI: 10.1063/1.1715674.

[34] C. Rossi et al. “The radiofrequency quadrupole accelerator for the Linac4”. In: *24th Linear Accelerator Conference (LINAC2008)), Victoria, BC, Canada*. JACoW, Geneva, Switzerland, 2008, pp. 157–159.

[35] S. Mathot et al. “Mechanical design, brazing and assembly procedures of the Linac4 RFQ”. In: *1st International Particle Accelerator Conference (IPAC2010), Kyoto, Japan*. ICR, Kyoto, Japan, 2010, pp. 807–809.

[36] O. Piquet et al. “The RF design of the Linac4 RFQ”. In: *1st International Particle Accelerator Conference (IPAC2010), Kyoto, Japan*. ICR, Kyoto, Japan, 2010, pp. 738–740.

[37] C. Rossi et al. “Assembly and RF tuning of the Linac4 RFQ at CERN”. In: *26th Linear Accelerator Conference (LINAC2012), Tel-Aviv, Isreal*. JACoW, Geneva, Switzerland, 2012, pp. 939–941.

[38] O. Piquet et al. “RF tuning of the Linac4 RFQ”. In: *4th International Particle Accelerator Conference (IPAC2013), Shanghai, China*. JACoW, Geneva, Switzerland, 2013, pp. 3761–3763.

[39] C. Rossi et al. “Commissioning of the Linac4 RFQ at the 3 MeV test stand”. In: *4th International Particle Accelerator Conference (IPAC2013), Shanghai, China*. JACoW, Geneva, Switzerland, 2013, pp. 3951–3953.

[40] A. M. Lombardi et al. “Beam dynamics in a high-frequency RFQ”. In: *6th International Particle Accelerator Conference (IPAC2015), Richmond, VA, USA*. JACoW, Geneva, Switzerland, 2015, pp. 2408–2412.

[41] B. Koubek, Y. Cuvet, A. Grudiev, C. Rossi, and M. Timmins. “Tuning of the CERN 750 MHz RFQ for medical applications”. In: *28th Linear Accelerator Conference (LINAC2016), East Lansing, MI, USA*. JACoW, Geneva, Switzerland, 2016, pp. 763–766. DOI: 10.18429/JACoW-LINAC'16-THOP09.

[42] B. Koubek, A. Grudiev, and M. Timmins. “rf measurements and tuning of the 750 MHz radio frequency quadrupole”. In: *Physical Review Accelerators and Beams* 20.8 (2017). DOI: 10.1103/physrevaccelbeams.20.080102.

[43] V. A. Dimov et al. “Beam commissioning of the 750 MHz proton RFQ for the LIGHT prototype”. In: *9th International Particle Accelerator Conference (IPAC2018), Vancouver, BC, Canada*. JACoW, Geneva, Switzerland, 2018, pp. 658–660. DOI: 10.18429/JACoW-IPAC2018-TUPAF002.

[44] G. P. Benincasa et al. “High frequency proton linac”. In: *The RITA network and the design of compact proton accelerators*. TERA Foundation, 1996, pp. 215–256. ISBN: 9788886409087.

[45] W. Maciszewski and W. Scharf. “Particle accelerators for radiotherapy: present status and future”. In: *Astroparticle, Particle and Space Physics, Detectors and Medical Physics Applications*. World Scientific, 2004, pp. 402–410. DOI: 10.1142/9789812702708_0060.

[46] A. Kaiser et al. “Proton therapy delivery and its clinical application in select solid tumor malignancies”. In: *Journal of Visualized Experiments* 144 (2019). DOI: 10.3791/58372.

[47] H. A. Bethe and J. Ashkin. In: *Experimental nuclear physics*. Ed. by E. Segré. Wiley, New York, 1953, p. 253.

[48] P. Sigmund. *Particle Penetration and Radiation Effects*. Springer Series in Solid State Sciences 151. Springer Berlin Heidelberg, 2006. ISBN: 3540317139.

[49] U. Weber and G. Kraft. “Comparison of carbon ions versus protons”. In: *The Cancer Journal* 15.4 (2009), pp. 325–332. DOI: 10.1097/ppo.0b013e3181b01935.

[50] S. Wrobel. *Power & precision. Proton therapy arrives in Georgia*. URL: http://news.emory.edu/features/2018/11/proton-therapy-center/index.html (visited on 06/15/2020).

[51] U. Amaldi and G. Kraft. “European developments in radiotherapy with beams of large radiobiological effectiveness”. In: *Journal of Radiation Research* 48.Suppl_A (2007), A27–A41. DOI: 10.1269/jrr.48.a27.

[52] V. Bencini. “Design of a Novel Linear Accelerator for Carbon Ion Therapy”. Available as CERN-THESIS-2019-301. PhD thesis. Sapienza Università di Roma, 2020.

[53] Particle Therapy Co-Operative Group (PTCOG). URL: https://www.ptcog.ch/ (visited on 06/15/2020).

[54] R. W. Hamm, K. R. Crandall, and J. M. Potter. “Preliminary design of a dedicated proton therapy linac”. In: *Conference Record of the 1991 IEEE Particle Accelerator Conference, San Francisco, CA, USA*. IEEE, 1991. DOI: 10.1109/pac.1991.165037.

[55] U. Amaldi, S. Braccini, and P. Puggioni. “High frequency linacs for hadrontherapy”. In: *Reviews of Accelerator Science and Technology* 02.01 (2009), pp. 111–131. DOI: 10.1142/s179362680900020x.

[56] C. Ronsivalle et al. “The TOP-IMPLART project”. In: *The European Physical Journal Plus* 126.7 (2011). DOI: 10.1140/epjp/i2011-11068-x.

[57] A. Degiovanni, P. Stabile, D. Ungaro, and A.D.A.M. SA. “LIGHT: a linear accelerator for proton therapy”. In: *2016 North American Particle Accelerator Conference (NAPAC2016), Chicago, IL, USA*. JACoW, Geneva, Switzerland, 2016, pp. 1282–1286.

[58] A. Degiovanni et al. “Status of the Commissioning of the LIGHT Prototype”. In: *9th International Particle Accelerator Conference (IPAC2018), Vancouver, BC, Canada*. JACoW, Geneva, Switzerland, 2018, pp. 425–428. DOI: 10.18429/JACoW-IPAC2018-MOPML014.

[59] P. Ostroumov, L. Faillace, A. Goel, S. Kutsaev, and B. Mustapha. "Compact Carbon Ion Linac". In: *2nd North American Particle Accelerator Conference (NAPAC2016), Chicago, IL, USA*. JACoW, Geneva, Switzerland, 2016, pp. 61–63. DOI: 10.18429/JACoW-NAPAC2016-MOA4CO04.

[60] M. Breitenfeldt, R. Mertzig, J. Pitters, A. Shornikov, and F. Wenander. "The TwinEBIS setup: machine description". In: *Nuclear Instruments and Methods in Physics Research Section A: Accelerators, Spectrometers, Detectors and Associated Equipment* 856 (2017), pp. 139–146. DOI: 10.1016/j.nima.2016.12.037.

[61] H. Pahl et al. "A low energy ion beamline for TwinEBIS". In: *Journal of Instrumentation* 13.08 (2018), P08012. DOI: 10.1088/1748-0221/13/08/p08012.

[62] V. Bencini, H. W. Pommerenke, A. Grudiev, and A. M. Lombardi. "750 MHz radio frequency quadrupole with trapezoidal vanes for carbon ion therapy". In: *Physical Review Accelerators and Beams* 23.12 (2020), p. 122003. DOI: 10.1103/PhysRevAccelBeams.23.122003.

[63] B. Koubek, A. Grudiev, and M. Timmins. *RF measurements and tuning of the 750 MHz HF-RFQ*. Tech. rep. CERN-ACC-NOTE-2017-0006. CERN, Geneva, Switzerland, 2017.

[64] H. P. Li et al. "Novel deuteron RFQ design with trapezoidal electrodes and double dipole four-vane structure". In: *Journal of Instrumentation* 15.2 (2020). DOI: 10.1088/1748-0221/15/02/t02006.

[65] K. Simonyi. *Theoretische Elektrotechnik*. 8th ed. Hochschulbücher für Physik. VEB Deutscher Verlag der Wissenschaften, 1980.

[66] M. Kummer. *Grundlagen der Mikrowellentechnik*. VEB Verlag Technik Berlin, 1986. ISBN: 3341000887.

[67] R. E. Collin. *Foundations for Microwave Engineering*. 2nd ed. McGraw-Hill, 1992. ISBN: 0070118116. DOI: 10.1109/9780470544662.

[68] R. P. Feynman, R. B. Leighton, and M. Sands. *The Feynman Lectures on Physics: New Millenium Edition*. 3 vols. Originally published 1963–1965. Basic Books, 2010. ISBN: 9780465023820.

[69] G. Lehner. *Elektromagnetische Feldtheorie*. Springer Berlin Heidelberg, 2010. ISBN: 9783642130427. DOI: 10.1007/978-3-662-56643-5.

[70] J. C. Maxwell. *A Treatise on Electricity and Magnetism*. Clarendon Press, 1873. ISBN: 9780511709333. DOI: 10.1017/cbo9780511709333.

[71] I. N. Bronshtein, K. A. Semendyayev, G. Musiol, and H. Mühlig. *Handbook of Mathematics*. Springer Berlin Heidelberg, 2015. ISBN: 9783662462218. DOI: 10.1007/978-3-662-46221-8.

[72] L. M. Young. “Operations of the LEDA resonantly coupled RFQ”. In: *2001 Particle Accelerator Conference (PAC2001), Chicago, IL, USA*. IEEE, 2001, pp. 309–313. DOI: 10.1109/pac.2001.987501.

[73] P. Fischer, A. Schempp, and J. Hauser. “A CW RFQ accelerator for deuterons”. In: *2005 Particle Accelerator Conference (PAC2005), Knoxville, TN, USA*. IEEE, 2005, pp. 794–795. DOI: 10.1109/pac.2005.1590566.

[74] E. Fagotti, L. Antoniazzi, A. Palmieri, F. Grespan, and M. Desmons. “High-power RF conditioning of the TRASCO RFQ”. In: *26th Linear Accelerator Conference (LINAC2012), Tel-Aviv, Isreal*. JACoW, Geneva, Switzerland, 2012, pp. 828–830.

[75] B. Pottin, M. Desmons, A. France, R. Gobin, and O. Piquet. “Status report on the French high-intensity proton injector project at Saclay (IPHI)”. In: *26th Linear Accelerator Conference (LINAC2012), Tel-Aviv, Isreal*. JACoW, Geneva, Switzerland, 2012, pp. 921–923.

[76] J. Knaster, P. Cara, A. Kasughai, Y. Okumura, and M. Sugimoto. “Challenges of the high current prototype accelerator of IFMIF/EVEDA”. In: *7th International Particle Accelerator Conference (IPAC2016), Busan, Korea*. JACoW, Geneva, Switzerland, 2016, pp. 52–57. DOI: 10.18429/JACOW-IPAC2016-MOZB02.

[77] Q. Fu et al. “Design and cold model experiment of a continuous-wave deuteron radio-frequency quadrupole”. In: *Physical Review Accelerators and Beams* 20.12 (2017). DOI: 10.1103/PhysRevAccelBeams.20.120101.

[78] Y. W. Kang et al. “Construction, test, and operation of a new RFQ at the Spallation Neutron Source (SNS)”. In: *9th International Particle Accelerator Conference (IPAC2018), Vancouver, BC, Canada*. JACoW, Geneva, Switzerland, 2018, pp. 1113–1116. DOI: 10.18429/JACoW-IPAC2018-TUPAL046.

[79] S. Groiss, I. Bardi, O. Biro, K. Preis, and K. R. Richter. “Parameters of lossy cavity resonators calculated by the finite element method”. In: *IEEE Transactions on Magnetics* 32.3 (1996), pp. 894–897. DOI: 10.1109/20.497385.

[80] L. Boltzmann. *Vorlesungen über die Principe der Mechanik*. Vol. 2. JA Barth, 1904.

[81] P. Ehrenfest. “A mechanical theorem of Boltzmann and its relation to the theory of energy quanta”. In: *Royal Netherlands Academy of Arts and Sciences (KNAW), Proceedings*. Vol. 16. 591. 1913, pp. 591–597.

[82] W. R. MacLean. “The resonator action theorem”. In: *Quarterly of Applied Mathematics* 2.4 (1945), pp. 329–335.

[83] J. C. Slater. “Microwave electronics”. In: *Reviews of Modern Physics* 18.4 (1946), p. 441.

[84] L. C. Maier Jr. and J. C. Slater. "Field strength measurements in resonant cavities". In: *Journal of Applied Physics* 23.1 (1952), pp. 68–77. DOI: 10.1063/1.1701980.

[85] A. Bondeson, T. Rylander, and P. Ingelström. *Computational Electromagnetics*. Texts in Applied Mathematics. Springer New York, 2005. ISBN: 9780387261584. DOI: 10.1007/978-1-4614-5351-2.

[86] T. Weiland. "A discretization model for the solution of Maxwell's equations for six-component fields". In: *Archiv für Elektronik und Übertragungstechnik* 31.3 (1977), pp. 116–120.

[87] U. van Rienen. *Numerical Methods in Computational Electrodynamics: Linear Systems in Practical Applications*. Lecture Notes in Computational Science and Engineering. Springer Berlin Heidelberg, 2012. ISBN: 9783642568022.

[88] A. Logg, K.-A. Mardal, and G. N. Wells. *Automated Solution of Differential Equations by the Finite Element Method. The FEniCS Book*. Springer Berlin Heidelberg, 2011. ISBN: 9783642230981. DOI: 10.1007/978-3-642-23099-8.

[89] ANSYS Inc. *Electromagnetics Suite®, release 18.2*. 2017.

[90] ANSYS Inc. *Electronics Desktop®, release 2019 R1*. 2019.

[91] Computer Simulation Technology. *CST Studio Suite®, release 2018*. 2018.

[92] COMSOL AB. *COMSOL Multiphysics®, version 5.3a*. 2017. URL: http://www.comsol.com.

[93] COMSOL AB. *COMSOL Multiphysics®, version 5.4*. 2018. URL: http://www.comsol.com.

[94] ANSYS Inc. *Mechanical®, release 18.2*. 2017.

[95] C. K. Birdsall and A. B. Langdon. *Plasma Physics via Computer Simulation*. 1st ed. Series in Plasma Physics. CRC Press, 2004. ISBN: 9780750310253.

[96] H. S. Deaven and K. C. D. Chan. *Computer codes for particle accelerator design and analysis: A compendium*. Tech. rep. LA-UR–90-1766. Los Alamos National Laboratory, 1990.

[97] V. Smirnov. "Computer codes for beam dynamics analysis of cyclotronlike accelerators". In: *Physical Review Accelerators and Beams* 20.12 (2017). DOI: 10.1103/physrevaccelbeams.20.124801.

[98] A. Perrin, J.-F. Amand, T. Mütze, and J.-B. Lallement. *Travel v4.07 user manual*. CERN. 2017.

[99] A. Latina. "RF-Track: beam tracking in field maps including space-charge effects, features and benchmarks". In: *28th Linear Accelerator Conference (LINAC2016), East Lansing, MI, USA*. JACoW, Geneva, Switzerland, 2016, pp. 104–107. DOI: 10.18429/JACoW-LINAC2016-MOPRC016.

[100] K. R. Crandall. *Effects of vane tip geometry on the electric fields in radio frequency quadrupole linacs*. Tech. rep. Los Alamos National Laboratory, 1983.

[101] K. R. Crandall. *Computation of charge distribution on or near equipotential surfaces*. Tech. rep. Los Alamos Scientific Laboratory, 1996.

[102] K. R. Crandall and T. P. Wangler. "PARMTEQ - a beam dynamics code for the RFQ linear accelerator". In: *AIP Conference Proceedings*. AIP, 1988, pp. 22–28. DOI: 10.1063/1.37798.

[103] R. Ferdinand, R. Duperrier, J.-M. Lagniel, P. Mattei, and S. Nath. "Field description in an RFQ and its effect on beam dynamics". In: *19th Linear Accelerator Conference (LINAC1998), Chicago, IL, USA*. 1998. URL: https://cds.cern.ch/record/740859.

[104] A. Letchford and A. Schempp. "A comparison of 4-rod and 4-vane RFQ fields". In: *6th European Particle Accelerator Conference (EPAC1998), Stockholm, Sweden*. 1998, pp. 1204–1206. URL: https://accelconf.web.cern.ch/e98/PAPERS/THP11E.PDF.

[105] J. Maus, R. A. Jameson, and A. Schempp. "Development of PteqHI". In: *25th Linear Accelerator Conference (LINAC2010), Tsukuba, Japan*. JACoW, Geneva, Switzerland, 2010, pp. 923–925.

[106] R. A. Jameson. *RFQ designs and beam-loss distributions for IFMIF*. Tech. rep. ORNL/TM-2007/001. Oak Ridge National Laboratory, 2007.

[107] N. J. Diserens. "Progress in the development of a 3D finite element computer program to calculate space and image charge effects in RF quadrupoles". In: *IEEE Transactions on Nuclear Science* 32.5 (1985), pp. 2501–2503. DOI: 10.1109/tns.1985.4333960.

[108] R. Duperrier. *Calcul du champ électrique maximum dans une cellule RFQ*. Tech. rep. CEA/DSM/SEA/9843. CEA Saclay, 1998.

[109] R. Duperrier. "TOUTATIS: a radio frequency quadrupole code". In: *Physical Review Accelerators and Beams* 3.12 (2000).

[110] B. Mustapha, A. A. Kolomiets, and P. N. Ostroumov. "Full 3D modeling of a radio-frequency quadrupole". In: *25th Linear Accelerator Conference (LINAC2010), Tsukuba, Japan*. JACoW, Geneva, Switzerland, 2010, pp. 542–544. URL: https://inspirehep.net/literature/1363849.

[111] S. Jolly et al. "Novel integrated design framework for radio frequency quadrupoles". In: *Nuclear Instruments and Methods in Physics Research, Section A: Accelerators, Spectrometers, Detectors, and Associated Equipment* 735 (2014), pp. 240–259. DOI: 10.1016/j.nima.2013.08.072.

[112] A. S. Plastun and P. N. Ostroumov. "Practical design approach for trapezoidal modulation of a radio frequency quadrupole". In: *Physical Review Accelerators and Beams* 21.3 (2018). DOI: 10.1103/physrevaccelbeams.21.030102.

[113] O. K. Belyaev et al. “IHEP experience on creation and operation of RFQs”. In: *20th Linear Accelerator Conference (LINAC2000), Monterey, CA, USA*. SLAC, Menlo Park, CA, USA, 2000, pp. 259–261.

[114] A. S. Plastun and A. A. Kolomiets. “RFQ with improved energy gain”. In: *26th Linear Accelerator Conference (LINAC2012), Tel-Aviv, Isreal*. JACoW, Geneva, Switzerland, 2012, pp. 966–968.

[115] B. Mustapha, A. A. Kolomiets, and P. N. Ostroumov. “Full three-dimensional approach to the design and simulation of a radio-frequency quadrupole”. In: *Physical Review Accelerators and Beams* 16.12 (Dec. 2013). DOI: 10.1103/physrevstab.16.120101.

[116] C. Li, Y. He, and Z. Wang. “Optimization design of the RFQ trapezoidal electrode”. In: *13th International Conference on Heavy Ion Accelerator Technology (HIAT2015), Yokohama, Japan*. 2015. DOI: 10.18429/JACoW-HIAT2015-WEPB06.

[117] Y. Iwashita, Y. Fuwa, and R. A. Jameson. “RFQ vane shapes for efficient acceleration”. In: *28th Linear Accelerator Conference (LINAC2016), East Lansing, MI, USA*. JACoW, Geneva, Switzerland, 2016, pp. 581–583. DOI: 10.18429/JACoW-LINAC'16-TUPLR054.

[118] F. Hinterberger. *Physik der Teilchenbeschleuniger und Ionenoptik*. Springer Berlin Heidelberg, 2013. ISBN: 9783662093122. DOI: 10.1007/978-3-540-75282-0.

[119] M. Vretenar. “The radio frequency quadrupole”. In: *CAS - CERN Accelerator School: Course on High Power Hadron Machines, Bilbao, Spain*. Available as CERN-2013-001. CERN, Geneva, Switzerland, 2011, pp. 207–223. DOI: 10.5170/CERN-2013-001.207.

[120] K. R. Crandall, R. H. Stokes, and T. P. Wangler. “RF quadrupole beam dynamics design studies”. In: *10th Linear Accelerator Conference (LINAC1979), Montauk, NY, USA*. 1979, pp. 205–216.

[121] M. Abramowitz and I. A. Stegun. *Handbook of Mathematical Functions with Formulas, Graphs, and Mathematical Tables*. Vol. 55. Applied Mathematics. US Government printing office, 1945.

[122] H. Klein. “Development of the different RFQ accelerating structures and operation experience”. In: *IEEE Transactions on Nuclear Science* 30.4 (1983), pp. 3313–3322.

[123] L. M. Young. “25 years of technical advances in RFQ accelerators”. In: *2003 Particle Accelerator Conference (PAC2003), Portland, OR, USA*. IEEE, 2003, pp. 60–64. DOI: 10.1109/pac.2003.1288841.

[124] A. Schempp. “Radio-frequency quadrupole linacs”. In: *CAS - CERN Accelerator School: Radio Frequency Engineering, Seeheim, Germany*. Available as CERN-2005-003. CERN, Geneva, Switzerland, 2000, pp. 305–314. DOI: 10.5170/CERN-2005-003.305.

[125] A. Fabris, A. Massarotti, and M. Vretenar. "A model of 4-rods RFQ". In: *Seminar on New Techniques for Future Accelerators, Erice, Sicily, Italy*. 1986, p. 265.

[126] G. P. Bezzon et al. "Construction and commissioning of the RFQ for the CERN lead-ion facility". In: *17th Linear Accelerator Conference (LINAC1994), Tsukuba, Japan*. KEK, Tsukuba, Japan, 1994, pp. 722–724.

[127] A. M. Lombardi, W. Pirkl, and Y. Bylinsky. "First operating experience with the CERN decelerating RFQ for antiprotons". In: *2001 Particle Accelerator Conference (PAC2001), Chicago, IL, USA*. IEEE, 2001.

[128] M. Schütt, M. A. Obermayer, U. Ratzinger, and M. Syha. "Status of the modulated 3 MeV 325 MHz Ladder-RFQ". In: *8th International Particle Accelerator Conference (IPAC2017), Copenhagen, Denmark*. JACoW, Geneva, Switzerland, 2017, pp. 2249–2251. DOI: 10.18429/JACoW-IPAC2017-TUPVA074.

[129] J. R. Delayen and W. L. Kennedy. "Design and modeling of superconducting RFQ structures". In: *16th Linear Accelerator Conference (LINAC1992), Ottawa, ON, Canada*. 1992, pp. 692–694.

[130] V. A. Andreev and G. Parisi. "90°-apart-stem RFQ structure for wide range of frequencies". In: *International Conference on Particle Accelerators, Washington, DC, USA*. IEEE, 1993. DOI: 10.1109/pac.1993.309574.

[131] H. J. Podlech. "Entwicklung von normal- und supraleitenden CH-Strukturen zur effizienten Beschleunigung von Protonen und Ionen". Habilitation thesis. Johann Wolfgang Goethe-Universität Frankfurt am Main, 2008.

[132] U. Ratzinger, K. Kaspar, E. Malwitz, S. Minaev, and R. Tiede. "The GSI 36 MHz high-current IH-type RFQ and HIIF-relevant extensions". In: *Nuclear Instruments and Methods in Physics Research Section A: Accelerators, Spectrometers, Detectors and Associated Equipment* 415.1–2 (1998), pp. 281–286. DOI: 10.1016/s0168-9002(98)00395-7.

[133] M. Olivier. "First heavy ion acceleration in SATURNE at 1 GeV/amu using the CRYEBIS-RFQ preinjector Hyperion II". In: *1984 Linear Accelerator Conference (LINAC84), Seeheim, Germany*. Gesellschaft für Schwerionenforschung m.b.H., Darmstadt, Germany, 1984, pp. 59–64.

[134] C. E. Hill, A. M. Lombardi, W. Pirkl, E. Tanke, and M. Vretenar. "Performance of the CERN Linac 2 with a high intensity proton RFQ". In: *17th Linear Accelerator Conference (LINAC1994), Tsukuba, Japan*. Available as CERN-PS-94-37. CERN, Geneva, Switzerland, 1994.

[135] L. M. Young, D. E. Rees, L. J. Rybarcyk, and K. A. Cummings. "High power RF conditioning of the LEDA RFQ". In: *1999 Particle Accelerator Conference (PAC1999)*. IEEE, 1999, pp. 881–883. DOI: 10.1109/pac.1999.795387.

[136] Y. Kondo et al. “Recent progress with the J-PARC RFQs”. In: *26th Linear Accelerator Conference (LINAC2012), Tel-Aviv, Isreal*. JACoW, Geneva, Switzerland, 2012, pp. 972–974.

[137] Y. Kondo, K. Hasegawa, T. Morishita, and R. A. Jameson. “Beam dynamics design of a new radio frequency quadrupole for beam-current upgrade of the Japan Proton Accelerator Research Complex linac”. In: *Physical Review Accelerators and Beams* 15.8 (2012). DOI: 10.1103/physrevstab.15.080101.

[138] T. Morishita et al. “High-power test results of the RFQ III in J-PARC linac”. In: *27th Linear Accelerator Conference (LINAC2014), Geneva, Switzerland*. JACoW, Geneva, Switzerland, 2014.

[139] P. Balleyguier. “3D design of the IPHI RFQ cavity”. In: *20th Linear Accelerator Conference (LINAC2000), Monterey, CA, USA*. SLAC, Menlo Park, CA, USA, 2000.

[140] D. Chirpaz-Cerbat et al. “Status of the ESS RFQ”. In: *7th International Particle Accelerator Conference (IPAC2016), Busan, Korea*. JACoW, Geneva, Switzerland, 2016, pp. 974–976. DOI: doi:10.18429/JACoW-IPAC2016-MOPOY054.

[141] F. Senée et al. “Increase of IPHI beam power at CEA Saclay”. In: *9th International Particle Accelerator Conference (IPAC2018), Vancouver, BC, Canada*. JACoW, Geneva, Switzerland, 2018, pp. 694–696. DOI: 10.18429/JACOW-IPAC2018-TUPAF016.

[142] M. Di Giacomo et al. “RF commissioning of the SPIRAL2 RFQ in CW mode and beyond nominal field”. In: *10th International Particle Accelerator Conference (IPAC2019), Melbourne, Australia*. JACoW, Geneva, Switzerland, 2019, pp. 2804–2806. DOI: 10.18429/JACOW-IPAC2019-WEPRB007.

[143] Y. Kondo, T. Morishita, and R. A. Jameson. “Development of a radio frequency quadrupole linac implemented with the equipartitioning beam dynamics scheme”. In: *Physical Review Accelerators and Beams* 22.12 (2019). DOI: 10.1103/physrevaccelbeams.22.120101.

[144] S. Ikeda, Y. Otake, T. Kobayashi, and N. Hayashizaki. “Design of 500 MHz RFQ linear accelerator for a compact neutron source, RANS-III”. In: *Nuclear Instruments and Methods in Physics Research Section B: Beam Interactions with Materials and Atoms* 461 (2019), pp. 186–190. DOI: 10.1016/j.nimb.2019.09.051.

[145] T. P. Wangler. “Lumped-circuit model of four-vane RFQ resonator”. In: *1984 Linear Accelerator Conference (LINAC84), Seeheim, Germany*. Gesellschaft für Schwerionenforschung m.b.H., Darmstadt, Germany, 1984, pp. 332–334.

[146] A. Simoens, A. France, and O. Delferrière. "An equivalent 4-wire line theoretical model of real RFQ based on the spectral differential theory". In: *21st Linear Accelerator Conference (LINAC2002), Gyeongju, Korea*. Pohang Accelerator Laboratory, Pohang, Korea, 2002.

[147] F. Grespan, A. Pisent, and A. Palmieri. "Dipole stabilizers for a four-vane high current RFQ: theoretical analysis and experimental results on a real-scale model". In: *Nuclear Instruments and Methods in Physics Research, Section A: Accelerators, Spectrometers, Detectors, and Associated Equipment* 582.2 (2007), pp. 303–317. DOI: 10.1016/j.nima.2007.08.149.

[148] A. Palmieri, F. Grespan, and A. Pisent. "Perturbation analysis on a four-vane RFQ". In: *1st International Particle Accelerator Conference (IPAC2010), Kyoto, Japan*. ICR, Kyoto, Japan, 2010, pp. 606–608.

[149] D. D. Armstrong, W. D. Cornelius, F. O. Purser, R. A. Jameson, and T. P. Wangler. *RFQ development at Los Alamos*. Tech. rep. LA-UR–84-498. Los Alamos National Laboratory, 1984.

[150] L. M. Young. "Tuning and stabilization of RFQs". In: *15th Linear Accelerator Conference (LINAC1990), Albuquerque, NM, USA*. 1990, pp. 530–534.

[151] M. Vretenar. "Low-beta structures". In: *CAS - CERN Accelerator School: RF for Accelerators, Ebeltoft, Denmark*. Available as CERN-2011-007. CERN, Geneva, Switzerland, 2010, pp. 319–340. DOI: 10.5170/CERN-2011-007.319.

[152] D. Howard and H. Lancaster. "Vane coupling rings: a simple technique for stabilizing a four-vane radiofrequency quadrupole structure". In: *IEEE Transactions on Nuclear Science* 30.2 (1983), pp. 1446–1448. DOI: 10.1109/tns.1983.4332556.

[153] D. Schrage et al. "BEAR rfq-beam experiment aboard a rocket". In: *Nuclear Instruments and Methods in Physics Research Section B: Beam Interactions with Materials and Atoms* 40-41 (Apr. 1989), pp. 949–953. DOI: 10.1016/0168-583x(89)90514-4.

[154] A. Kolomiets, D. Liakin, and A. Plastun. "Asymmetric four-vane RFQ". In: *28th Linear Accelerator Conference (LINAC2016), East Lansing, MI, USA*. JACoW, Geneva, Switzerland, 2016, pp. 592–594. DOI: 10.18429/JACoW-LINAC2016-TUPLR059.

[155] L. Yang et al. "Design and optimization of a novel bent-vane type radio frequency quadrupole". In: *Physical Review Accelerators and Beams* 23.2 (2020). DOI: 10.1103/physrevaccelbeams.23.021301.

[156] C. Zhang, H. Podlech, and E. Tanke. "Realizing long radio-frequency quadrupole accelerators with multiple shorter and independent cavities". In: *Physical Review Accelerators and Beams* 23.4 (2020). DOI: 10.1103/physrevaccelbeams.23.042003.

[157] A. Grudiev, S. Calatroni, and W. Wuensch. "New local field quantity describing the high gradient limit of accelerating structures". In: *Physical Review Accelerators and Beams* 12.10 (2009). DOI: 10.1103/physrevstab.12.102001.

[158] W. D. Kilpatrick. "Criterion for vacuum sparking designed to include both RF and DC". In: *Review of Scientific Instruments* 28.10 (Oct. 1957), pp. 824–826. DOI: 10.1063/1.1715731.

[159] T. J. Boyd Jr. *Kilpatrick's Criterion*. Tech. rep. LANL group AT-1 report. Los Alamos National Laboratory, 1982.

[160] R. B. Palmer. "Prospects for High Energy e^+e^- Linear Colliders". In: *Annual Review of Nuclear and Particle Science* 40.1 (1990), pp. 529–592. DOI: 10.1146/annurev.ns.40.120190.002525.

[161] S. Döbert et al. "High gradient performance of NLC/GLC X-band accelerating structures". In: *2005 Particle Accelerator Conference, Knoxville, TN, USA*. IEEE, 2005, pp. 372–374.

[162] C. Zhang et al. "HSI RFQ Upgrade for the UNILAC Injection to FAIR". In: *7th International Particle Accelerator Conference (IPAC2016), Busan, Korea*. JACoW, Geneva, Switzerland, 2016, pp. 877–879. DOI: 10.18429/JACOW-IPAC2016-MOPOY016.

[163] G. Amendola, J. M. Quesada, and M. Weiss. "Beam dynamics studies for the CERN lead-ion RFQ". In: *3rd European Particle Accelerator Conference (EPAC1992), Berlin, Germany*. Atlantica Séguier Frontières, 1992, pp. 973–975.

[164] W.-P. Dou et al. "Beam dynamics and commissioning of CW RFQ for a compact deuteron–beryllium neutron source". In: *Nuclear Instruments and Methods in Physics Research Section A: Accelerators, Spectrometers, Detectors and Associated Equipment* 903 (2018), pp. 85–90. DOI: 10.1016/j.nima.2018.06.044.

[165] M. Comunian, L. Bellan, E. Fagotti, and A. Pisent. "IFMIF-EVEDA RFQ, measurement of beam input conditions and preparation to beam commissioning". In: *57th ICFA Advanced Beam Dynamics Workshop on High-Intensity, High-Brightness and High-Power Hadron Beams (HB2016), Malmö, Sweden*. JACoW, Geneva, Switzerland, 2016, pp. 338–341.

[166] E. Fagotti et al. "Beam commissioning of the IFMIF EVEDA very high power RFQ". In: *9th International Particle Accelerator Conference (IPAC2018), Vancouver, BC, Canada*. JACoW, Geneva, Switzerland, 2018, pp. 2902–2907. DOI: 10.18429/JACOW-IPAC2018-THXGBF2.

[167] R. Gaur and V. Kumar. "Beam dynamics and electromagnetic studies of a 3 MeV, 325 MHz radio frequency quadrupole accelerator". In: *European Physics Journal - Nuclear Sciences and Technologies* 4 (2018), p. 9. DOI: 10.1051/epjn/2018004.

[168] Q. Z. Xing et al. "Field tuning and RF measurements of the four-vane radio frequency quadrupole with ramped inter-vane voltage". In: *Physical Review Accelerators and Beams* 22.2 (2019). DOI: 10.1103/physrevaccelbeams.22.020102.

[169] S. Gupta et al. "RF conditioning and beam experiments on 400 keV RFQ accelerator at BARC". In: *2014 International Symposium on Discharges and Electrical Insulation in Vacuum (ISDEIV), Mumbai, India*. IEEE, 2014. DOI: 10.1109/deiv.2014.6961608.

[170] D. P. Pritzkau. "RF Pulsed Heating". Available as SLAC-Report-577. PhD Thesis. Stanford University, 2001.

[171] D. P. Pritzkau and R. H. Siemann. "Experimental study of rf pulsed heating on oxygen free electronic copper". In: *Physical Review Accelerators and Beams* 5.11 (2002). DOI: 10.1103/physrevstab.5.112002.

[172] P. B. Wilson. "Scaling linear colliders to 5 TeV and above". In: *AIP Conference Proceedings*. Vol. 397. 1. AIP, 1997. DOI: 10.1063/1.52986.

[173] V. F. Kovalenko. *Physics of Heat Transfer and Electrovacuum Devices*. Sovetskoe Radio, Moscow, 1975.

[174] J. Bannantine, J. Comer, and J. Handrock. *Fundamentals of Metal Fatigue Analysis*. Prentice Hall, Englewood Cliffs, NJ, 1990.

[175] O. A. Nezhevenko. "On the limitations of accelerating gradient in linear colliders due to the pulse heating". In: *Proceedings of the 1997 Particle Accelerator Conference, Vancouver, BC, Canada*. IEEE, 1997, pp. 3013–3014. DOI: 10.1109/pac.1997.753092.

[176] L. Laurent et al. "Experimental study of rf pulsed heating". In: *Physical Review Accelerators and Beams* 14.4 (2011). DOI: 10.1103/physrevstab.14.041001.

[177] M. J. Boland et al. *Updated baseline for a staged Compact Linear Collider*. Tech. rep. CERN-2016-004. CERN, 2016. DOI: 10.5170/CERN-2016-004.

[178] R. Zennaro et al. "Design and fabrication of CLIC test structures". In: *24th Linear Accelerator Conference (LINAC2008), Victoria, BC, Canada*. JACoW, Geneva, Switzerland, 2008, pp. 533–535.

[179] A. Grudiev. Personal communication. 2017–2020.

[180] S. Mathot. Personal communication. 2017–2020.

[181] G. V. Romanov, M. D. Hoff, D. Li, J. W. Staples, and S. P. Virostek. "Project X RFQ EM design". In: *3rd International Particle Accelerator Conference (IPAC2012), New Orleans, LA, USA*. IEEE, 2012, pp. 3883–3885.

[182] J.-P. Berenger. "A perfectly matched layer for the absorption of electromagnetic waves". In: *Journal of Computational Physics* 114.2 (1994), pp. 185–200. DOI: 10.1006/jcph.1994.1159.

[183] Electronic Components Industry Association (ECIA). *EIA-225. Rigid Coaxial Transmission Lines and Connectors – 50 Ohms*. Version Revision A. 2018.

[184] V. A. Kirillin, V. V. Syčev, and A. E. Sheĭndlin. *Engineering Thermodynamics*. Mir, 1982. ISBN: 9780828502566.

[185] F. Kreith and R. M. Manglik. *Principles of Heat Transfer*. 8th ed. Cengage Learning, 2017. ISBN: 9781337516921.

[186] M. G. Cooper, B. B. Mikić, and M. M. Yovanovich. "Thermal contact conductance". In: *International Journal of Heat and Mass Transfer* 12.3 (1969), pp. 279–300. DOI: 10.1016/0017-9310(69)90011-8.

[187] B. Snaith, S. D. Probert, and P. W. O'Callaghan. "Thermal resistances of pressed contacts". In: *Applied Energy* 22.1 (1986), pp. 31–84. DOI: 10.1016/0306-2619(86)90073-5.

[188] C. V. Madhusudana. *Thermal Contact Conductance*. Springer New York, 1996. ISBN: 9781461239789. DOI: 10.1007/978-1-4612-3978-9.

[189] R. Dou, T. Ge, X. Liu, and Z. Wen. "Effects of contact pressure, interface temperature, and surface roughness on thermal contact conductance between stainless steel surfaces under atmosphere condition". In: *International Journal of Heat and Mass Transfer* 94 (2016), pp. 156–163. DOI: 10.1016/j.ijheatmasstransfer.2015.11.069.

[190] I. V. Leitão. "Development, validation and application of a novel method for estimating the thermal conductance of critical interfaces in the jaws of the LHC collimation system". In: *4th International Particle Accelerator Conference (IPAC2013), Shanghai, China*. 2013, pp. 3430–3432.

[191] B. B. Mikić. "Thermal contact conductance; theoretical considerations". In: *International Journal of Heat and Mass Transfer* 17.2 (1974), pp. 205–214. DOI: 10.1016/0017-9310(74)90082-9.

[192] Kurt J. Lesker Company. *CF flanges technical notes*. URL: http://www.lesker.com/newweb/flanges/flanges_technicalnotes_conflat_1.cfm (visited on 11/13/2019).

[193] F. W. Guy. "Three-dimensional space charge and image charge effects in radio frequency quadrupole accelerators". In: *1991 IEEE Particle Accelerator Conference*. IEEE, 1991. DOI: 10.1109/PAC.1991.165177.

[194] P. M. Lapostolle. "Possible emittance increase through filamentation due to space charge in continuous beams". In: *IEEE Transactions on Nuclear Science* 18.3 (1971), pp. 1101–1104. DOI: 10.1109/tns.1971.4326292.

[195] D. Uriot and N. Pichoff. *TraceWin documentation*. CEA Saclay. 2011.

[196] Keysight Technologies. *E5061B ENA Vector Network Analyzer*. URL: https://www.keysight.com/en/pdx-x201771-pn-E5061B/ena-vector-network-analyzer (visited on 07/19/2020).

[197] Keysight Technologies. *85032F Standard Mechanical Calibration Kit, DC to 9 GHz, Type-N, 50 ohm*. URL: https://www.keysight.com/en/pd-1000003537%3Aepsg%3Apro-pn-85032F/standard-mechanical-calibration-kit-dc-to-9-ghz-type-n-50-ohm (visited on 07/22/2020).

[198] Hanna Instruments. *Checktemp®1 Digital Thermometer*. URL: https://www.hannainst.com/hi98509-checktemp-1-digital-thermometer.html (visited on 07/19/2020).

[199] L. G. Hector and H. L. Schultz. "The dielectric constant of air at radiofrequencies". In: *Physics* 7.4 (1936), pp. 133–136. DOI: 10.1063/1.1745374.

[200] M. Santo Zarnik and D. Belavic. "An experimental and numerical study of the humidity effect on the stability of a capacitive ceramic pressure sensor". In: *Radioengineering* 21.1 (2012), pp. 201–206.

[201] A. L. Buck. "New equations for computing vapor pressure and enhancement factor". In: *Journal of Applied Meteorology* 20.12 (1981), pp. 1527–1532.

[202] Buck Research Instruments LLC. *Model CR-1A hygrometer with autofill, operating manual*. Ed. by A. L. Buck. 2012. URL: http://www.hygrometers.com/wp-content/uploads/CR-1A-users-manual-2009-12.pdf (visited on 06/29/2020).

[203] C. W. Steele. "A nonresonant perturbation theory". In: *IEEE Transactions on Microwave Theory and Techniques* 14.2 (1966), pp. 70–74. DOI: 10.1109/tmtt.1966.1126168.

[204] A. Savitzky and M. J. E. Golay. "Smoothing and differentiation of data by simplified least squares procedures." In: *Analytical Chemistry* 36.8 (1964), pp. 1627–1639. DOI: 10.1021/ac60214a047.

[205] W. H. Press, S. A. Teukolsky, W. T. Vetterling, and B. P. Flannery. *Numerical Recipes 3rd Edition: The Art of Scientific Computing*. Cambridge University Press, 2007. ISBN: 9780521880688.

[206] A. Heidary. "A Low-cost Universal Integrated Interfacefor Capacitive Sensors". PhD thesis. Tehran University, 2010.

[207] Copper Mountain Technologies. *TR1300/1 2-Port 1.3 GHz Analyzer*. URL: https://coppermountaintech.com/vna/tr1300-1-2-port-1-3-ghz-analyzer (visited on 07/22/2020).

[208] F. Caspers. "RF engineering basic concepts: the Smith chart". In: *CAS - CERN Accelerator School: RF for Accelerators, Ebeltoft, Denmark*. Available as CERN-2011-007. CERN, Geneva, Switzerland, 2010.

[209] W. Altar. "Q Circles-A Means of Analysis of Resonant Microwave Systems". In: *Proceedings of the IRE* 35.5 (1947), pp. 478–484. DOI: 10.1109/jrproc.1947.232938.

[210] D. Kajfez. “Linear fractional curve fitting for measurement of high Q factors”. In: *IEEE Transactions on Microwave Theory and Techniques* 42.7 (1994), pp. 1149–1153. DOI: 10.1109/22.299749.

[211] D. Kajfez. “Random and systematic uncertainties of reflection-type Q-factor measurement with network analyzer”. In: *IEEE Transactions on Microwave Theory and Techniques* 51.2 (2003), pp. 512–519. DOI: 10.1109/tmtt.2002.807831.

[212] V. A. Goryashko et al. “High-precision measurements of the quality factor of superconducting cavities at the FREIA laboratory”. In: *17th International Conference on RF Superconductivity (SRF2015)*. JACoW, Geneva, Switzerland, 2015, pp. 810–813.

[213] L. Picardi et al. “Experimental results on SCDTL structures for protons”. In: *5th International Particle Accelerator Conference (IPAC2014), Dresden, Germany*. JACoW, Geneva, Switzerland, 2014, pp. 3247–3249. DOI: 10.18429/JACOW-IPAC2014-THPME016.

[214] M. J. Browman and L. M. Young. “Coupled radio-frequency quadrupoles as compensated structures”. In: *15th Linear Accelerator Conference (LINAC1990), Albuquerque, NM, USA*. 1990, pp. 70–72.

[215] O. Piquet, M. Desmons, and A. France. “Tuning procedure of the 6 meter IPHI RFQ”. In: *10th European Particle Accelerator Conference (EPAC2006), Edinburgh, Scotland*. 2006, pp. 291–293.

[216] F. D. McDaniel et al. “The tandem-RFQ linac booster at Sandia National Laboratories”. In: *17th International conference on the application of accelerators in research and industry, Denton, TX, USA*. Vol. 680. 1. AIP Conference Proceedings, 2003, pp. 986–990. DOI: 10.1063/1.1619874.

[217] G. Bisoffi et al. “Superconducting RFQ’s ready for ion beam operation at INFN-LNL”. In: *8th European Particle Accelerator Conference (EPAC2002), Paris, France*. JACoW, Geneva, Switzerland, 2002, pp. 266–268.

[218] A. Bechtold and H. Podlech. “Proposal of a normal conducting CW-RFQ for the EURISOL post-accelerator and a dedicated β-beam linac concept”. In: *10th European Particle Accelerator Conference (EPAC2006), Edinburgh, Scotland*. JACoW, Geneva, Switzerland, 2006, pp. 1580–1582.

[219] C. Zhang and H. Podlech. “Single-cavity and two-cavity solutions for a 120 emA, 3 MeV proton RFQ linac”. In: *Nuclear Instruments and Methods in Physics Research Section A: Accelerators, Spectrometers, Detectors and Associated Equipment* 976 (2020), p. 164259. DOI: 10.1016/j.nima.2020.164259.

[220] G. L. Matthaei, L. Young, and E. M. T. Jones. *Design of Microwave Filters, Impedance-matching Networks, and Coupling Structures*. Artech House, Inc., Norwood, 1963. DOI: 10.21236/ad0402852.

[221] K. R. Crandall. “RFQ radial matching sections and fringe fields”. In: *1984 Linear Accelerator Conference (LINAC1984), Seeheim, Germany*. Gesellschaft für Schwerionenforschung m.b.H., Darmstadt, Germany, 1984, pp. 109–111. URL: https://accelconf.web.cern.ch/l84/papers/tup0009.pdf.

[222] K. R. Crandall. “Ending RFQ vanetips with quadrupole symmetry”. In: *17th Linear Accelerator Conference (LINAC1994), Tsukuba, Japan*. 1994, pp. 227–229. URL: https://accelconf.web.cern.ch/l94/papers/mo-69.pdf.

[223] European Organization for Nuclear Research (CERN). *CERN unveils its Science Gateway project*. 2019. URL: https://home.cern/news/press-release/knowledge-sharing/cern-unveils-its-science-gateway-project (visited on 07/20/2020).

[224] L. M. Young and L. Rybarcyk. “Tuning the LEDA RFQ 6.7 MeV accelerator”. In: *19th Linear Accelerator Conference (LINAC1998), Chicago, IL, USA*. 1998, pp. 270–272.

[225] J. Wang et al. “Frequency tuning with RFQ temperature in China ADS injector II”. In: *Chinese Physics C* 40.3 (2016), p. 037003. DOI: 10.1088/1674-1137/40/3/037003.

[226] J. P. Edelen et al. “First principles modeling of RFQ cooling system and resonant frequency responses for fermilab’s PIP-II injector test”. In: *IEEE Transactions on Nuclear Science* 64.2 (2017), pp. 800–808. DOI: 10.1109/tns.2016.2644663.

Statement of Originality

Except for those parts in which it is explicitly stated to the contrary, this thesis titled *"Compact Radio-frequency Quadrupoles for Industrial and Medical Applications"* is my own work. I confirm that I have not used other than the declared references, and that I have explicitly marked all material which has been quoted either literally or by content from the used sources. This thesis has not been submitted for any degree at this or any other academic or professional institution.

Geneva, 16 August 2020 Hermann W. Pommerenke